eman ta zabal zazu

Universidad del País Vasco

Euskal Herriko Unibertsitatea

Design and development of a thermochemical energy storage system based on the redox couple Mn_2O_3/Mn_3O_4 for concentrated solar power plants

THESIS

Author: Daniel Bielsa Linaza[1]

Industrial Engineer

Director: Dr. Pedro Luis Arias Elgueta[2]

December 2021

[1]: *Centre for Cooperative Research on Alternative Energies (CIC energiGUNE), Basque Research and Technology Alliance (BRTA)*

[2]: *University of the Basque Country (UPV/EHU)*

Acknowledgements

I would like to take advantage of these next lines to thank all the people who have been involved somehow in this fascinating research process.

First of all, to my family. My parents Angel† and Begoña, who gave me everything. Thanks to Chon, an inspiring soul. Lastly, many thanks to my soulmate Mirenka, and my beloved daughters Sara and Leyre, who have so generously allowed me to dedicate part of the time that belonged to them to the development of this research, which, translated into their language, was called "*the balls for storing heat*".

To Nuria Gisbert, a professional inspiration, for encouraging me to carry out this work and giving me all the possible support to do so.

To a group of top-level researchers and technicians, without whom it would not have been possible to carry out this work successfully. Thanks to Pedro Luis, Abdo, Ali, Mikel O., Stefania, Jean Luc, Cesar, Cristina, Yagmur, Mikel I. and Imanol.

Last but not least, thanks to the Department of Economic Development and Infrastructures of the Basque government for their economical support through the funding of the ELKARTEK CIC Energigune-2017 research program.

Abstract

The future energy grid based on renewable energy sources will require strong support from energy storage systems since renewable energy cannot be managed. Concentrated solar power is one of the leading technologies to produce electrical energy from the sunlight and thermal energy storage systems helps this technology to keep producing electricity in a cloudy day or after sunset. In order to increase the penetration of this technologies, decreasing the cost of concentrated solar power plants becomes of paramount importance to compete with fossil fuel-based energy sources. Advanced thermal energy storage technologies can play an important role in this challenge. Current commercial thermal energy storage systems store the energy using sensible heat with an energy storage density that can be multiplied by 10 if a thermochemical energy storage technology is properly developed. Thermochemical energy storage uses endothermic/exothermic reversible chemical reactions to store and release heat and in addition to their high energy density, they would allow increasing the operation temperatures of the plant and consequently, its efficiency, improving significantly the competitiveness of the technology. Nevertheless, they are still at an early stage of development, requiring mainly to avoid material degradation during cycling, proper design of high temperature components and design an optimal integration into the operation of the plant. Among high temperature thermochemical candidate materials, metal oxides can use air both as heat transfer fluid and reactant, avoiding the use of intermediate heat exchangers or the complexity derived of using other gases such as steam or CO_2 required for other type of thermochemical materials. These advantages facilitate their integration into the concentrated solar power plants and therefore, they are one of the most studied thermochemical materials.

Within this challenge, we have studied a new approach, for the first time to the best of our knowledge, based on Mn_2O_3/Mn_3O_4 thermochemical material. This material has been selected since it is nontoxic and rather available. The objective is mainly focused on improving the thermochemical material behavior during repetitive charge and discharge cycles, as it has been identified as the main drawback of the technology at material scale. The novelty consisted in finding a doping agent that properly mixed with the active material, creates a protective layer around the particles that prevent them from agglomeration and at the same time, contributes to improve the chemical reaction kinetics. Furthermore, a granulation technique has been developed to produce granules of several mm, with enough chemical and mechanical stability, which have been tested and validated in a packed bed configuration within a lab-scale thermochemical reactor.

Resumen

La futura red eléctrica basada en fuentes de energía renovables necesitará un gran apoyo de sistemas de almacenamiento de energía, ya que la energía renovable no puede ser gestionada. La energía solar de concentración es una de las principales tecnologías para producir energía eléctrica a partir de la luz solar. Su principal ventaja es que esta tecnología facilita almacenar grandes cantidades de energía térmica a un coste competitivo, que permite seguir produciendo electricidad en un día nublado o después de la puesta de sol. Para aumentar el despliegue de este tipo de tecnologías y competir con las plantas de generación de energía basadas en combustibles fósiles, es de vital importancia la disminución del coste de inversión. Las tecnologías de almacenamiento de energía térmica avanzadas pueden desempeñar un papel importante en este reto. Los actuales sistemas comerciales de almacenamiento de energía térmica almacenan la energía mediante calor sensible, con una densidad de almacenamiento de energía que puede multiplicarse por 10 si se desarrolla adecuadamente una tecnología de almacenamiento de energía termoquímica. El almacenamiento termoquímico de energía utiliza reacciones químicas reversibles endotérmicas/exotérmicas para almacenar y liberar calor. Además de contar con una mayor densidad de energía, permitirían aumentar las temperaturas de funcionamiento de la planta y, en consecuencia, su eficiencia, mejorando sustancialmente la competitividad de la tecnología. Sin embargo, aún se encuentran en una fase preliminar de desarrollo, requiriendo principalmente evitar la degradación de los materiales durante su operación, diseñar adecuadamente los componentes de alta temperatura y diseñar su óptima integración en el funcionamiento de la planta. Entre los materiales termoquímicos de alta temperatura más prometedores se encuentran las reacciones redox con óxidos metálicos. Su principal ventaja es que estos materiales pueden utilizar aire atmosférico tanto como fluido de transferencia de calor como reactivo. De esta manera se evita el uso de intercambiadores de calor intermedios o la complejidad derivada de utilizar otros gases como el vapor o el CO_2, que se requiere para otro tipo de materiales termoquímicos. Estas ventajas facilitan su integración en las centrales de concentración solar y consecuentemente, son unos de los materiales más estudiados.

Dentro del presente trabajo de investigación, hemos estudiado un nuevo enfoque, por primera vez hasta donde sabemos, basado en el material termoquímico Mn_2O_3/Mn_3O_4. Este material se ha seleccionado principalmente por ser un material no tóxico y bastante abundante. El objetivo se centra principalmente en mejorar el comportamiento del material termoquímico durante los ciclos repetitivos de carga y descarga, ya que se ha identificado como el principal inconveniente de la tecnología a escala de material. La novedad ha consistido en encontrar un agente dopante que, mezclado adecuadamente con el material activo, crea una capa protectora alrededor de las partículas que impide su aglomeración y, al mismo tiempo, contribuye a mejorar la cinética de la reacción química. Además, se ha desarrollado una técnica de granulación que permite producir gránulos de varios mm, con suficiente estabilidad química y mecánica, que se ha ensayado y validado en una configuración de lecho compacto dentro de un reactor termoquímico a escala de laboratorio.

Laburpena

Energia-iturri berriztagarrietan oinarritutako etorkizuneko sare elektrikoak energia biltegiratzeko sistemen laguntza handia beharko du, energia berriztagarria ezin baita kudeatu. Kontzentraziozko eguzki-energiam, eguzki-argitik energia elektrikoa sortzeko teknologia nagusietariko bat da. Bere abantaila nagusia da teknologia honek kostu lehiakor batean energia termikoko kantitate handiak biltzea errazten duela, egun lainotsu batean edo eguzkia sartu ondoren elektrizitatea ekoizten jarraitzea ahalbidetzen duena. Horrelako teknologien hedapena areagotzeko eta erregai fosiletan oinarritutako energia sortzeko instalazioekin lehiatzeko, ezinbestekoa da inbertsio-kostua murriztea. Energia termikoa biltegiratzeko teknologia aurreratuek zeregin garrantzitsua izan dezakete erronka honetan. Energia termikoa biltegiratzeko egungo merkataritza-sistemek energia biltegiratzen dute bero sentikorraren bitartez, energia biltegiratzeko dentsitatea 10ez biderkatu daiteke energia termokimikoa behar bezala biltegiratzeko teknologia bat garatzen bada. Energiaren biltegiratze termokimikoak erreakzio kimiko itzulgarri endotermiko/exotermikoak erabiltzen ditu beroa biltegiratzeko eta askatzeko. Energia-dentsitate handiagoa izateaz gain, instalazioaren funtzionamendu-tenperaturak igotzea ahalbidetuko luke, eta, ondorioz, haren eraginkortasuna, teknologiaren lehiakortasuna nabarmen hobetuz. Hala ere, oraindik garapenaren atariko fase batean daude, batez ere, materialen degradazioa saihestu behar da operazioan zehar, tenperatura altuko osagaiak behar bezala diseinatu behar dira eta landarearen funtzionamenduan ahalik eta hobekien integra daitezen diseinatu behar da. Tenperatura handiko material termokimiko oparoenen artean, oxido metalikoen erredox erreakzioak daude. Abantaila nagusia da material horiek aire atmosferikoa erabil dezaketela, bai beroa transferitzeko fluido gisa, bai erreaktibo gisa. Horrela, saihestu egiten da tarteko bero-trukagailuak erabiltzea edo beste gas batzuk erabiltzearen ondoriozko konplexutasuna, hala nola lurruna edo CO_2, beste material termokimikoko mota batzuetarako behar dena. Abantaila horiek eguzki-kontzentrazioko zentraletan integratzea errazten dute, eta, ondorioz, gehien aztertutako materialetako batzuk dira.

Ikerketa lan honen barruan, dakigun punturaino, Mn_2O_3/Mn_3O_4 material termokimikoan oinarritutako ikuspegi berri bat aztertu dugu lehen aldiz. Material hau material ez-toxikoa eta nahiko ugaria izateagatik hautatu da nagusiki. Helburua nagusiki, zamalanetako ziklo errepikakorretan material termokimikoaren portaera hobetzea da, material eskalako teknologiaren eragozpen nagusitzat jo baita. Berritasuna izan da agente dopatzaile bat aurkitzea, material aktiboarekin behar bezala nahastuta, partikulen inguruan geruza babesle bat sortzen duena, bere aglomerazioa eragozten duena eta, aldi berean, erreakzio kimikoaren zinetika hobetzen laguntzen duena. Gainera, granulazio-teknika bat garatu da, hainbat mm-ko pikorrak ekoizteko aukera ematen duena, egonkortasun kimiko eta mekaniko nahikoarekin, ohe trinkoko konfigurazio batean saiatu eta balioztatu dena laborategi eskalako erreaktore termokimiko baten barruan.

Index

CHAPTER 1. Introduction

1.1 Concentrated Solar Power Plants

According to SolarReviews, each square meter of our upper atmosphere receives around 1.367 kWh every hour [1], which means that the energy coming from the sun is more than enough to satisfy the whole energy demand of the current world population, the only limitation is our ability to collect it by means of a cost-effective way and therefore, this is our mission.

Solar photovoltaic and concentrated solar power (CSP) technologies are the most widespread technologies aiming to collect the energy coming from the sun and convert it into useful energy. Nevertheless, the energy source is the only thing they have in common, since photovoltaic technologies converts the light directly into electricity by means of semiconductors, while CSP uses the sunlight to increase the temperature of a fluid, which later is used to generate steam and produce electricity in a turbogenerator.

The first CSP plant entered into operation in 1968 [2], capable of delivering 1MWe and since then, it has evolved considerably, especially during the first part of the present century. As evidence, the CSP installed power was multiplied by 10 times in the period from 2006 to 2016, from 500 MW to almost 5 GW, reaching an expected annual growth rate of 22% from 2008 to 2022 [3] (Fig. 1). Another example is the brand-new CSP plant recently commissioned in Ouarzazate (Morocco), which is an impressive solar complex reaching an electric production power up to 580 MWe.

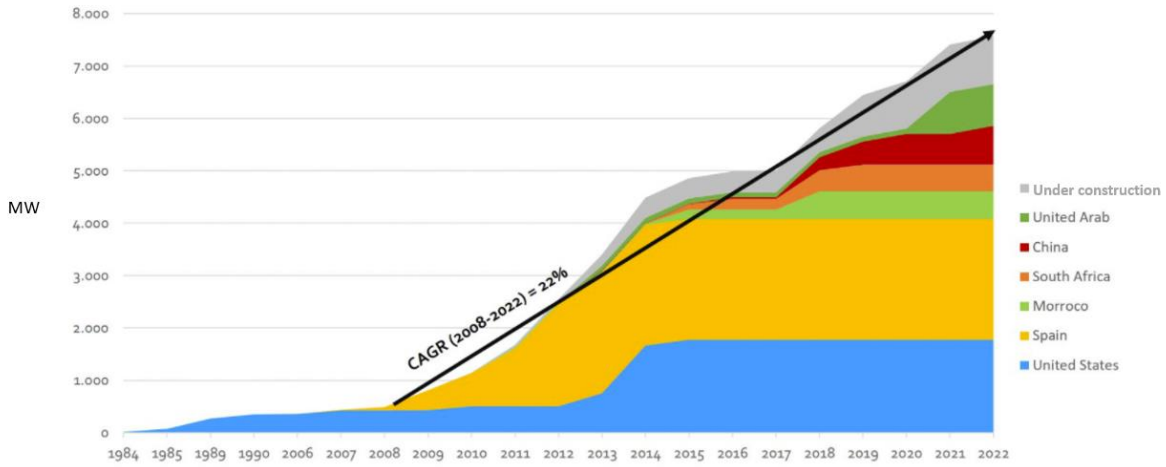

Figure 1. CSP installed and under construction worldwide between 1984 and 2022 **[3]**

CSP takes advantage of the well-known Rankine thermodynamic cycle, commonly used in conventional power plants. The process consists in several steps: i) concentrate the sunlight onto a receiver through which a fluid is flowing, increasing its temperature, ii) subsequently, the fluid is pumped to a heat exchanger where steam at high pressure is produced and iii) finally, the steam is introduced in a steam turbine connected to an electrical power generator which produces electricity. The singular advantage of this technology is that the hot fluid can be easily stored in thermally insulated tanks so that the electrical energy supply can be extended beyond sunset. This fact represents an important advantage of CSP compared to other technologies, since large amount of

energy can be stored at a reasonable cost. The energy is usually stored in a two-tank technology system, using a fluid that is a mixture of nitrates, with energy densities of around 250 kJ/kg [1], which can increase solar power availability from 25% to 65% [2].

The most widespread CSP technology is known as parabolic through power plant (Fig. 2), accounting for more than 80% of the total CSP installed, which to some extent can be considered as a mature technology. These systems consist of a series of parabolic mirrors oriented in such a way that the solar radiation is concentrated at their focus. The concentrator, located at this focus, consists of a tube through which a heat transfer fluid (HTF) is flowing. This HTF is commonly a thermal oil that can be heated up to 400°C. The solar field is composed of several parabolic mirrors located in series and parallel in order to get the required amount of HTF at the targeted temperature, which sets the power output of the plant. Subsequently the HTF is pumped to the steam boiler where steam at more than 100 bar is produced. This steam is introduced into the power block to produce electricity and the condensate fluid is reintroduced into the circuit to close the loop. In regular operation mode, part of the hot HTF is derived to the TES system, composed of an indirect two tank system, which transfer the heat through a heat exchanger (HX) to a nitrate salt, stored in the so-called hot tank, which is flowed back after sunset to extend the electricity production. Once the hot nitrate salt delivers its energy to the HTF, the cold salt is stored in the cold tank waiting to start the next charging cycle. Most of the parabolic through CSP plants in operation have an extended production capacity after sunset of 7.5 hours, which requires almost 20,000 tons of salt, stored in tanks of 15 m height and 39 m of diameter.

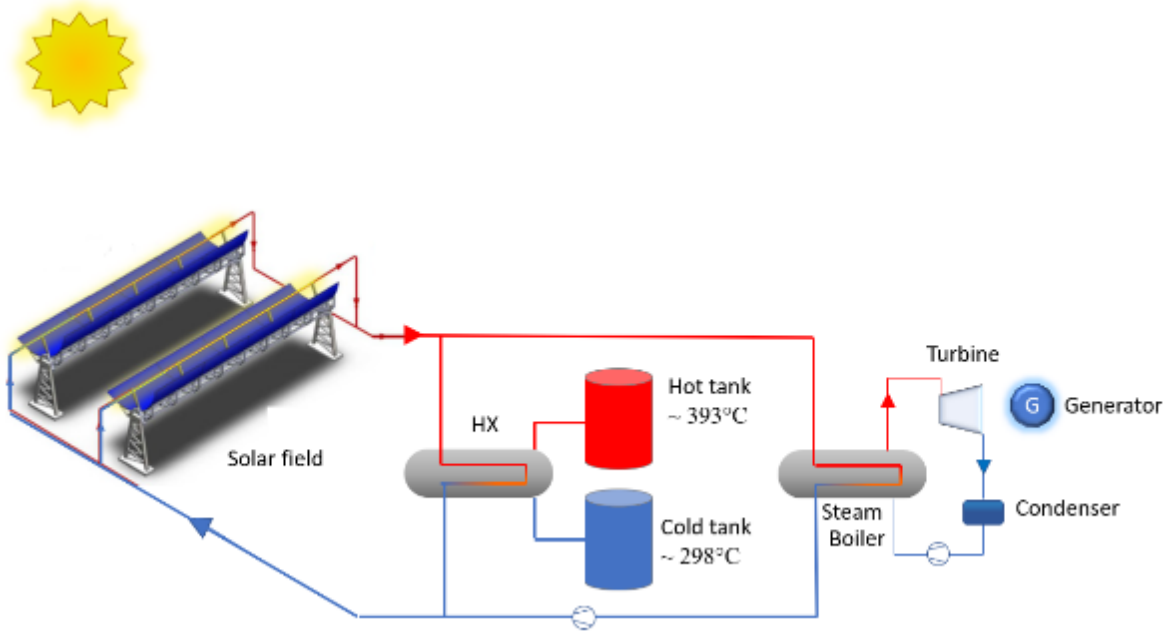

Figure 2. Parabolic through power plant concept

2011 became a significant breakthrough in the CSP world with the commissioning and start-up of Gemasolar CSP plant. Barely after one month in operation, Gemasolar achieved 24 h of continuous operation being the first CSP supplying electricity uninterruptedly during a whole day. Gemasolar was a First of a Kind CSP plant, nowadays known as 'Solar Power Tower' and proposed a meaningful change on the plant configuration, which set the basis for current CSP competitiveness (Fig. 3). Solar tower plants are composed of a field of mirrors called 'Heliostats' which concentrate the solar radiation at the top of a tower, in a critical component called receiver. These heliostats can be flat or slightly concave and follow the direction of the sun in two axes. At the concentration point in the tower,

temperatures of 800°C to 1000°C may be reached because the solar radiation reaching the heliostats is multiplied by 600-800 times [4]. This temperature is used to heat a HTF flowing through the receiver, which is then used alike in the parabolic through plants to generate electricity. The heat-to-electricity conversion efficiency increases with temperature, so the tower concept uses nitrate salt as HTF to take advantage of the high temperature reached in the receiver to increase the efficiency of the plant. In addition, this fact facilitates the operation of the two-tank TES system, which is installed in series without the need of a heat exchanger, known as direct TES configuration. Gemasolar has a power output of 20 MWe, with almost 9 tons of nitrate salts, operating between 290 and 565°C, capable of extending its operation during 15 h without sunlight. Solar tower plants may reach plant efficiencies between 23-35%, which compared to the 14-20% efficiencies of the parabolic through plants, constitutes a huge improvement of the CSP technology [5].

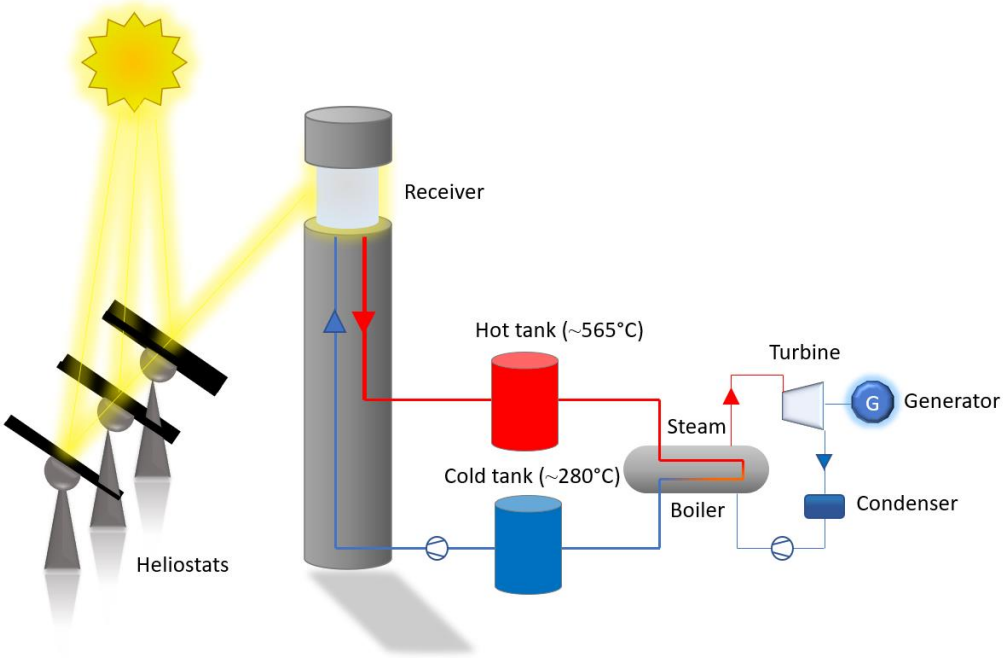

Figure 3. Solar power tower plant concept

Alike most renewable energy technologies, in order to compete with fossil fuel energy sources, the greatest challenge the CSP community is facing is to keep reducing the levelized cost of electricity (LCOE) of the CSP plant, which represents the average cost of electricity generation over the entire lifetime of the plant. A CSP plant is a complex operation of millions of euros where many factors apart from the investment costs may have a significant impact on the LCOE, namely, financial costs, expected lifetime of the plant, solar resource availability or the possibility to take advantage of the TES system to access the high price electricity market during peak hours. Recent power purchase agreements (PPAs) in Australia and Dubai came to demonstrate the possibilities of CSP technology getting an extremely competitive LCOE of 0.07 $/kWh [6]. However, after many years of cost-reduction activities and research, there is a general feeling that CSP technology needs a breakthrough to definitively evolve from a promising candidate to a real player on the future green energy grid. In this regard, the CSP research community is mainly focused in trying to increase the actual low efficiency of the solar-to-electricity conversion by increasing the HTF operation temperature, currently limited by the maximum temperature allowable by the nitrate-based solar salt (~600°C). Either using a Rankine cycle or a Bryton cycle a significant working temperature increase would have a direct positive impact on the overall efficiency of the plant, likely becoming the long-awaited improvement

and a new generation of CSP pants. The thermodynamic analysis carried out by Schrader et al. showed that an efficiency of 44% can be reached using a Bryton cycle with temperatures around 777°C [7]. However, increasing the working temperature imposes many engineering challenges, which are currently under study (e.g. alternative HTF [8], high temperature receivers [9] and TES systems [10], implementing sCO_2 cycle [11]). It should be pointed out that nowadays TES has been identified as the cornerstone of the competitiveness of CSP technology since it is one of the most cost-effective ways to achieve higher penetration of renewable energy sources and enable energy dispatchability, especially at large power levels. Consequently, it has become the main focus of the research activity in regard of CSP technologies, as evidenced by being the CSP related term with the highest number of scientific publications during the last years (Fig. 4).

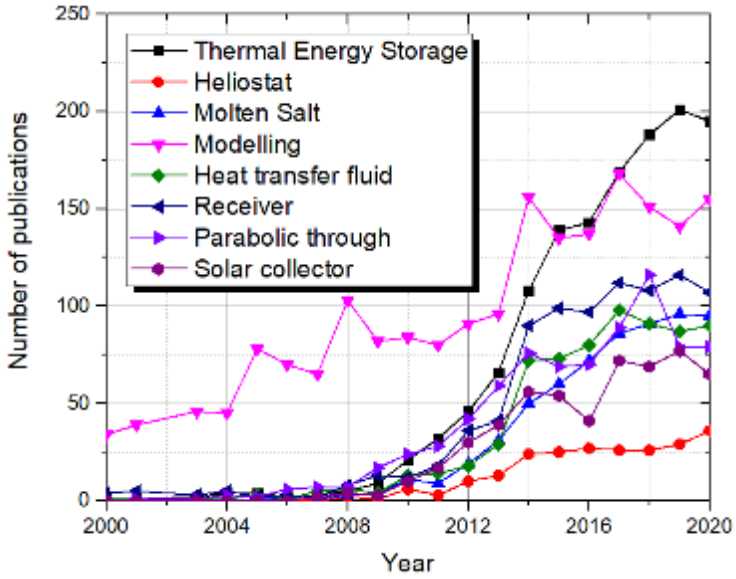

Figure 4. Nº of publications in Scopus between 2000 and 2020 with the term 'CSP' adding the following keywords: 'Thermal Energy Storage', 'Heliostat', 'Molten Salt', 'Modelling', 'Heat Transfer Fluid', 'Receiver', 'Parabolic through' and 'Solar collector'

1.2 Thermal energy storage technologies

Since the discovery of electricity, huge efforts have been made to develop appropriate systems to storage energy for use on demand, but the complexity of reaching to a both technical and economical proper solution turned it out even these days as a relatively unsolved issue.

Over the last century, the growing concern regarding the protection of the environment has led to a significant political change, with important international agreements that boost the electricity generation based on renewable energy sources. Within this challenge, energy storage becomes even more important and essential to take advantage of these energy sources which can not be easily managed and are at some extent unpredictable.

Energy storage systems have been properly studied and therefore provide a wide array of technological approaches to manage the power supply. Among them, the most well-known technologies can be classified as electrochemical energy storage, pumped hydro storage and thermal energy storage. While electrochemical storage and pumped hydro storage are the most spread energy

storage technologies, thermal energy storage is especially appropriate when the power source delivers the energy as heat, such as in CSP plants, since a relevant amount of energy can be stored at a very competitive cost.

Within the thermal energy storage systems, three different technologies can be identified: **sensible heat storage, latent heat storage** and **chemical heat storage.**

In **sensible heat storage systems,** the heat is used to increase the temperature of a solid or a fluid, which is stored at a reference temperature until it is discharged on demand. The storage energy can be expressed as follows:

$$Q = mCp\Delta T \quad \text{Eq. 1}$$

Where m is the mass of the storage material (kg), C_p the specific heat (kJ/kg K) and ΔT the variation of the temperature.

In **latent heat storage systems,** the heat is used to induce a phase change in the storage material (kwown as PCM), which is then stored in its new phase and discharged on demand in an isothermal process, recovering its previous phase. The thermal energy stored is related to the latent heat of the material and can be expressed as follows:

$$Q = mL \quad \text{Eq. 2}$$

Where m is the mass of the storage material (kg) and L the latent heat of the storage material (kJ/kg).

Chemical heat storage systems take advantage of the energy exchange in some chemical processes and reactions and can be divided into two different systems: sorption and thermochemical systems.

In a sorption system the heat is used to break the binding force between the sorbent and the sorbate and includes: adsorption process, where the adsorptive accumulates on the surface of an adsorbent and absorption process, where a substance is distributed into a liquid or solid and forms a solution.

The thermochemical systems are based on reversible chemical reactions, where in general the heat applied to a reactant (A) is used to dissociate it into two different products (B and C) through an endothermic reaction and the heat can be recovered later if the products (B and C) are mixed again, resulting in the initial product (A) through an exothermal reaction.

$$A + Heat \leftrightharpoons B + C \quad \text{Eq. 3}$$

The stored heat is related to the reaction enthalpy and can be expressed as follows:

$$Q = n_A \Delta H_r \quad \text{Eq. 4}$$

Where n_A is the mol number of the reactant (mol) and ΔH_r the reaction enthalpy (kJ/mol_A or KWh/mol_A).

Nowadays, the main aspects of the three thermal energy storage systems present huge differences, especially those related to the heat storage capacity and the maturity of the technology. All of them are listed in Table 1 [12] and some examples are given in Table 2.

Table 1. Main aspects of thermal energy storage technologies

	Thermal storage technology		
	Sensible heat	Latent heat	Chemical
Energy density (kWh/m^3)	50	100	500
Storage temperature	Reference temperature	Reference temperature	Any
Storage time	Limited (losses)	Limited (losses)	Ilimited
Transport	Small distances	Small distances	Ilimited
Technological maturity	Commercial	Industrial pilots	Lab pilots
Technological complexity	Simple	Médium	High

Table 2. Examples of thermal energy storage technologies

Material	Storage technology	Energy density (kWh/m^3)	Storage temperature (°C)	Maturity	Applicability
Water	Sensible	93	<100	Commercial	Seasonal
Solar Salt	Sensible	250	565	Commercial	CSP
Solar Salt	Latent	155	225	Commercial	CSP
$Na_2S{\cdot}5H_2O$	Chemical	780	80	Lab scale	Building
MgH_2	Chemical	1110	350-450	Lab scale	Industrial/CSP

Current TES technologies in most commercial CSP plants involve the use of molten nitrate salts as the storage medium, because they are low-cost materials with good energy storage density. Nevertheless, these salts present some drawbacks such as their high freezing point and limited maximum allowable temperature, that impose maintaining the temperature of the salt continuously above 290˚C and not exceeding 565˚C to avoid its degradation [13]. Current research efforts are mainly focused on reducing the cost of these systems to improve their competitiveness. TES cost represents approximately 9% of the total capital costs of a parabolic through 50 MWe power plant with 7.5 h of storage [14], which represents several tens of millions of euros. After the solar field, TES optimization has been reported to have the greatest impact on LCOE reduction [15], and therefore, many TES research lines are ongoing. The research community is making great efforts to work with materials with a higher thermal energy storage density, proposing technologies based on improved sensible heat storage (SHS), latent heat storage (LHS) or thermochemical energy storage (TcES) [3]. It has been reported that TcES might increase the thermal energy storage density of the system between 5 and 10 times, reaching 3600 kJ/m^3 [4], with the possibility of operating at higher temperatures and thus, achieving greater plant efficiencies. Even though they are still in a preliminary research phase to be used in CSP, TcES are considered to be the most promising technology for the TES systems of the new CSP generation [5].

1.3 Thermochemical energy storage at high temperature

The first reference regarding the use of thermochemical energy systems for storage purposes found was published in 1961 by Goldstein [16], giving a list of chemical reactions with the potential to be used as TES and setting the starting point of the technology development that came immediately after.

TcES systems for high temperature (300°C < T < 1200°C) are of interest mainly for industrial waste heat recovery and concentrated solar power plants (CSP), in which the temperature of the heat source is as high as possible in order to improve the efficiency of the heat-to-electricity conversion process. These thermochemical energy storage systems are currently being investigated due to their obvious advantages: energy density 5 to 10 times higher than latent and sensible heat storage systems, their storage period is theoretically unlimited due to the lack of thermal losses during storage, the system can be easily transported and at some extent, the temperature and kinetics of the reaction controlled. On the other hand, nowadays these systems still present some drawbacks that must be solved before reaching to a commercial stage, regarding mainly to their poor reversibility and kinetics, undesirable side reactions, cost, system components design (e. g. reactors) and system integration into the power plant [17]. At present, there are little experience and only some small pilots at laboratory or pre-industrial scale. Their technical complexity still requires a lot of effort and investment to get definitive results to envisage pilots at industrial real scale. Nevertheless, despite its complexity, there are many studies that can be found in the literature and some international projects that are pushing the state of the art and achieving some promising results.

The equilibrium temperature of the reaction is defined when the free-energy change is equal to 0 according to the following equations given by W. E. Wentworth and E. Chen in 1976 [18].

$$dG = dH - TdS \rightarrow dG = 0 \rightarrow T = \frac{dH}{dS} \qquad \text{Eq. 5}$$

This particular result becomes important to select the appropriate candidate for heat storage, considering that ΔH defines the heat storage capacity and thus, it should be as high as possible, and the temperature of the heat source is fixed, so there will be no many high enthalpy reversible systems that match the required ΔS.

In the wide range of candidate reactions available, the vaporization reactions simplify the system due to the simple separation of products and even with the disadvantage of volume increase, although they have not been the unique researched systems, they are generally considered as the most suitable for heat storage purposes.

The thermochemical storage systems presented in the literature can be classified by the reactant family that share the nature of the reactants and products and at some extent, the reaction enthalpy. The general classification presented in the literature and the most studied reactions are showed in Fig. 5 [19]. Within the different families there is an extensive research in materials that turn into reactions, which may have significative differences in activation temperatures and reaction enthalpies. An attempt to include the whole reported range for each family among the most studied materials is presented in Table 3, together with some research references.

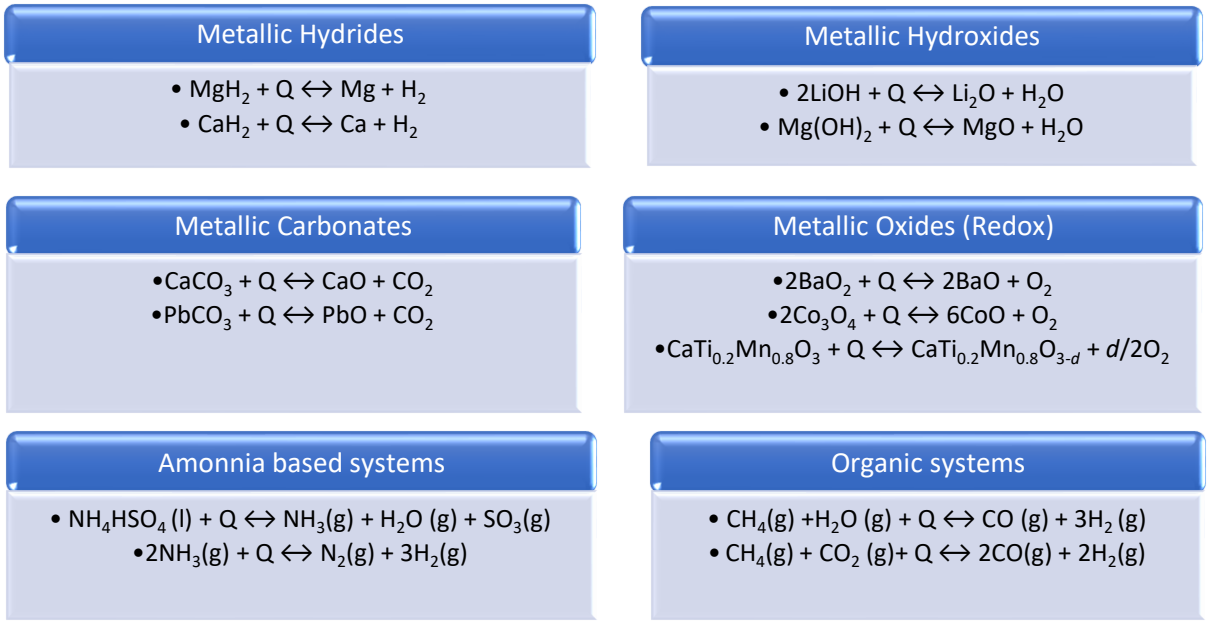

Figure 5. Families of thermochemical energy storage systems for high temperature **[19]**

Table 3. Main features of high temperature thermochemical systems

System	Enthalpy (kJ/mol)	Onset temperature (°C)	Nature
Metallic Hydrides [20] [21]	76-181	400-1100	Solid-Gas
Metallic Hydroxides [22] [23]	60-100	125-1000	Solid-Gas
Metallic Carbonates [24] [25]	178-234	400-1300	Solid-Gas
Metallic Oxides [26] [27]	30-202	885-1300	Solid-Gas
Ammonia based [28] [18]	66,9-336	400-740	Gaseous
Organic [29] [18]	98-247	300-1000	Gaseous

Among the different thermochemical materials for high temperature, metal oxides have been some of the most studied materials for next generation of CSP. One of the main advantages of the redox systems is the possibility of working in open conditions, using natural air both as reactant and heat transfer fluid, without the necessity of intermediate storage for the gas phase (oxygen), simplifying the integration of the system. This fact, together with the total availability of air, its unlimited operation temperature range and its negligible cost, makes metal oxides a very promising candidate for future CSP TcES. On the other hand, their main drawback at material scale is associated to the high temperatures used for the reactions, which may cause some grade of sintering, reducing the cyclability of the system and limit the heat sources that can be used to those at high temperatures.

1.4 Research context, scope and objectives of the thesis

1.4.1 Research context

Most redox systems are based on thermochemical reactions using metal oxides, which absorb heat through an endothermic reaction releasing oxygen (charge step) and give the heat back through an exothermic reaction (discharge step) when oxygen is again put into contact with the reduced species under specific conditions. Most research efforts in the temperature range up to 1100°C have been focused on the following redox pairs: BaO_2/BaO, Fe_2O_3/Fe_3O_4, CuO/Cu_2O, Co_3O_4/CoO and Mn_2O_3/Mn_3O_4. Wong et al. [15] carried out the first major screening of redox candidates. Within this study, most of reactions mentioned above were discarded due to their slow reaction kinetics or poor reversibility, except the one involving Co_3O_4 and some mixed oxides, where the negative effect observed was less severe. Hereinafter, several studies confirmed the profound tendency of these metal oxides materials to sinter when subjected to repetitive charge and discharge cycles, becoming the main reason of cyclability loss in a long-term operation scenario.

1.4.2 Research scope

B. Wong was one of the first researchers presenting a comprehensive study regarding the redox behaviour of several metal oxides for TcES. In this work, he stated a relationship between the grain growth and the decrease in the re-oxidation fraction over cycling, in most of the metal oxides he studied [30]. Later, Carrillo et al. studied the effect of the initial particle size on the cyclability of Mn_2O_3, obtaining incomplete re-oxidation of the samples with the smallest particle sizes, while the largest ones presented complete cyclability during 30 redox cycles. Nevertheless, all the samples presented some re-oxidation kinetics deterioration over cycling. This deterioration was greater in the case of the smallest particles, having higher surface energy. This energy promotes mass diffusivity among grains, which causes higher densification degree. This densification was presented as the main reason of the observed cyclability loss, representing a physical barrier, which hinders the diffusion of O_2 into Mn_3O_4 molecules during the re-oxidation reaction [31]. Overall, all metal oxides seem to be affected at some extent by sintering, which in the long-term operation required by the CSP application may turn into a significant decrease on the heat storage efficiency.

Sintering is a well-known process in the manufacturing of metallurgical products to produce density-controlled materials. The main effects of sintering are densification and grain growth. Densification involves reducing the porosity of the powder, whereas grain growth, also known as coarsening, involves that the smaller grains are consumed by the larger ones [32].

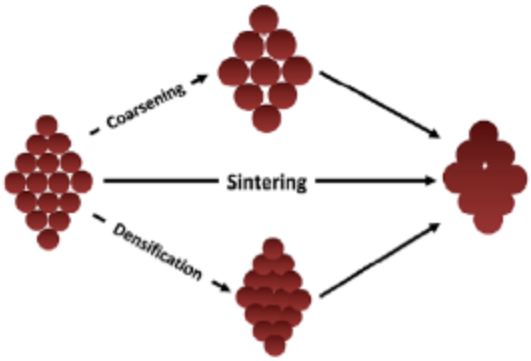

Figure 6. The two main effects of sintering: Coarsening and densification **[31]**. Copyright Elsevier 2014

Among all the metal oxides studied for high temperature TcES, both Co_3O_4 and Mn_2O_3 present operation temperatures that become attractive for the next generation of CSP, being higher than the actual limit temperature of the molten salt (~600°C) and not too high that might require the use of very expensive structural materials and components. Therefore, they have been extensively studied in this regard. **In order to study the hypothesis of the present thesis, the redox pair Mn_2O_3/Mn_3O_4 has been selected because even though Co_3O_4 presents higher reaction enthalpy and kinetics, the lower cost and toxicity of Mn_2O_3 turns this material into a promising candidate for these systems**. The redox reaction of Mn_2O_3 is as follows:

$$6Mn_2O_3 + Q \leftrightarrow 4Mn_3O_4 + O_2 \qquad \text{Eq. 6}$$

In the comprehensive study carried out by B. Wong, he already observed that Mn_2O_3 presented slow oxidation reaction kinetics, reaching only a re-oxidation of 6 %, and the resulting structure was dense and highly sintered [30]. However, he came to demonstrate that 10-15 % of iron addition might improve the redox performance of the oxide, obtaining a lower sintering degree and maintaining almost 90 % of the TES capacity after a 500 cycles test. Considering these results, Mn_2O_3 was further investigated by other authors, following the iron addition approach to improve the oxidation rate, considered as a key factor to ensure long-term viability. In this regard, Carrillo et al. studied the cycling performance of several samples with different quantities of iron, ranging from 0 to 40 %, finding a similar improvement in the cycling response. However, it was observed that the reaction onset temperature increases with iron addition, from 948°C to 1008°C for an iron content of 40 %. In general, the samples showed a slight oxidation rate decay during cycling, which was attributed to the high degree of sintering, counteracted at some extent by the iron addition [33]. In a following work, the same authors attributed this oxidation rate improvement to an enlargement and weakening of the Mn-O bonds, due to lattice distortion caused by the smaller Fe^{2+} radius [34]. The cycling improvement and the reaction temperature increase due to iron addition were also confirmed later by T. Block and M. Schmücker [27], André et al. [35] and Wokon et al. [36], identifying materials with different iron contents in each work as the best candidates by assessing the reaction enthalpy and reversibility. These differences might be caused by using different testing instruments and temperature programs. Another interesting approach was reported by Varsano et al. consisting in using lithium manganese oxides, which presented a remaining 90 % TES capacity after 45 redox cycles with a slight increase on the reaction temperatures, but with no substantial changes in the structural morphology of the grains [37]. Overall, it has been shown that **a mixed oxide structure based on doping the redox material with cations of smaller radius than Mn^{3+} contributes to improve the reaction kinetics of Mn_2O_3/Mn_3O_4 redox couple** for TcES. However, none of the previous research approaches were

focused in diminishing the material sintering and its negative effects. Therefore, it is very likely that over the expected life-time of a CSP plants (>20 years), the material is completely deactivated. In a nutshell, sintering and its effects are of paramount importance to be addressed in order to reach the next development step of TcES systems.

In this regard, doping of ceramic materials have been proven to be an effective technique to modify the grain growth and particle shrinkage in manufacturing of metallurgical products. When the amount of doping agent is higher than the bulk solubility limit, the excess cations may segregate forming dopant-rich phases at the grain boundaries, contributing to change the grain boundary diffusivity and thus, the sintering conditions [38]. However, the main goal of this research was to accelerate the sintering effects and obtain dense body structures with better mechanical properties, which is just the opposite required for TcES, since this morphology changes contributes to hinder oxygen diffusion decreasing the reaction kinetics. Even so, because of this research, the key parameters that govern grain diffusivity have been identified, making it possible to try to get the contrary effects. **It was observed that when cations of higher valence than the major component are segregated at the grain boundaries, oxygen interstitials are created in the structure and consequently, ion diffusion mechanisms are hindered, decreasing the sintering effects**.

Therefore, a convenient combination of these findings led to the formulation of the following hypothesis of the present thesis: **if an appropriate dopant is found for Mn_2O_3/Mn_3O_4 redox couple, it can be possible to contribute both to improve the reaction kinetics and to decrease the sintering effects**, extending the life-time of these type of TcES materials.

1.4.3 Objectives

The proposed thesis work aims to develop the research, design and development of a TES technology based on thermochemical materials, oriented towards new generation of CSP plants, i.e., capable of operating with fluids that reach higher temperatures than the current commercially available (565°C). This fact may improve significantly the competitiveness of CSP technology by increasing the efficiency of the thermodynamic cycle of this type of power plant. The research will try to provide new insights into redox reactions based on mixed manganese metal oxides and their upscaling to a thermochemical reactor. The main objective is to improve the cycling chemical stability of the material, overcoming the negative effects of sintering presented by the materials investigated to date and consequently, laying the foundations that will enable the next step to the pre-industrial phase.

The specific objectives are the following:

- **OB01. Study of the state of the art.** With the aim of acquiring knowledge and identifying the state of development of all thermochemical materials and high temperature reactors investigated by the scientific community, with the target of identifying the main problems encountered by the research activity to date.

- **OB02**. **Design, synthesis and characterization of materials**. The aim is to select and synthesize new materials that will form the basis on which important aspects such as the cyclability (>100 cycles) or energy density of the system will be based. The influence of different synthesis techniques, grain size or composition on the behavior of the material will also be studied. The

work will be carried out with compounds based on pure and mixed compositions of Mn_2O_3 with different amounts of other metals.

- **OB03. Modelling, simulation and evaluation of a kinetic model for both the reduction and oxidation reactions**. The aim of this task is to find the mathematical model that allows obtaining operating results that are close to the real ones, so that it can be used to define the optimal geometry of the reactor that allows maximizing the efficiency and cyclability of the reaction, for which theoretical simulations will be developed. The aim is to achieve an error of less than 5%.

- **OB04**. **Design and fabrication of a laboratory scale reactor (≈1 Wh).** In this case, the design, manufacture and assembly of a laboratory-scale reactor will be carried out, allowing tests to be carried out on a larger scale than that used for characterization (>5gr). For this reason, a synthesis process will be developed, capable of producing pellets of the thermochemical material starting from powder.

- **OB05**. **Laboratory-scale experimental tests of the developed system**. During this task, the system will be subjected to real service conditions: loading and unloading cycles, with the aim of studying the behavior of the material on a larger scale and at conditions similar to the real ones. The objective is subjecting the material to multiple cycles (≈100). and check the mechanical and chemical stability of the developed solution.

1.4.4 Thesis overview

The thesis is structured as follows: After a general introduction included in Chapter 1, Chapter 2 describes the research carried out to date regarding redox reactions using metal oxides, the material upscaling and the especial TcES requirements for their integration into CSP plants. Subsequently, Chapter 3, 4, 5, 6, 7 and 8 contain the experimental activity carried out in this research work, subdivided as follows:

- Chapter 3 describes the characterization techniques used and the first experiments concerning the characterization of the redox couple Mn_2O_3/Mn_3O_4;
- Chapter 4 explores the effects of doping Mn_2O_3 with other metals in order to improve the thermochemical behavior of the material;
- Chapter 5 explains the first findings concerning the new thermochemical material developed in the present thesis, based on doping Mn_2O_3 with Si;
- Chapter 6 provides new insights into the Si-doped Mn_2O_3 doping route, analyzing different synthesis processes, the material behavior over multiple redox cycles and discusses more precisely the reasons behind the cyclability improvement observed;
- Chapter 7 contains the elaboration of the mathematical model describing the reduction and oxidation kinetics of the new material;
- Chapter 8 comprises a comprehensive study of a synthesis route to elaborate granules of the new material, their characterization and testing in a lab-scale packed bed reactor.

Finally, Chapter 9 includes the main conclusions of the research work proposing future research lines to keep analyzing and improving the present findings in order to get closer to the pre-industrial stage.

CHAPTER 2. State of the art

2.1 Redox reactions

The Redox systems are based on thermochemical reactions using mainly metallic oxides, which release heat when O_2 is absorbed through an exothermic reaction and in the other direction, they can be dissociated applying heat at high temperatures by means of an external source in an endothermic reaction, working as the following reversible reaction.

$$X_mO_n(s) + Heat \leftrightharpoons mX(s) + \frac{n}{2}O_2(g) \qquad \text{Eq. 7}$$

Where X is the metal

The first reference found in the literature regarding metallic oxides for thermal energy storage purposes was published by G. Ervin in 1977 [23], since then, there are many other reported references in the literature regarding redox materials for high temperature heat storage, among them, the most studied ones are BaO_2, Mn_2O_3, Co_3O_4 and CuO and the mixture of some of them. All of them presenting different behavior in terms of reaction onset temperature and kinetics. The reaction equilibrium of those reactions as a function of temperature and oxygen partial pressure is given in the following Van't Hoff diagram [27]. The intersection of the dotted line corresponds to 0,21 bar of O_2 with the different lines representing the equilibrium temperature of the reactions.

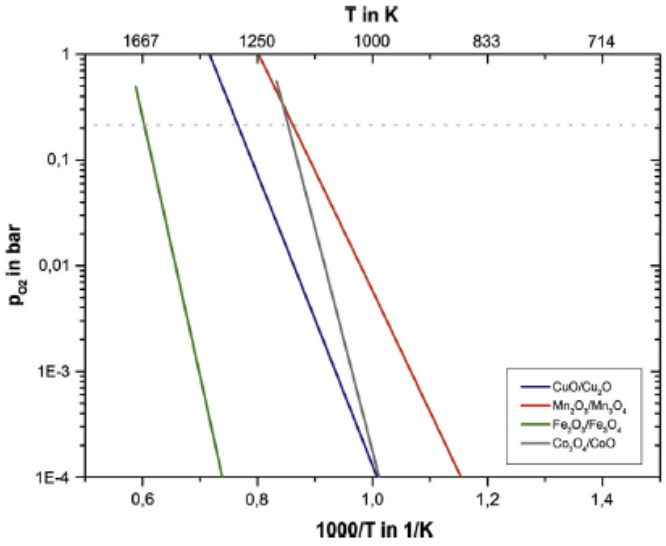

Figure 7. Van't Hoff diagram of main redox materials **[27]**

Among the many reported references in the literature regarding redox systems for high temperature TcES, the materials presented are by far the most studied thermochemical compounds. Their main characteristics may slightly differ from one research study to another, likely ascribed to the nature of the different materials, characterization techniques or equipment used. A summary of their main characteristics extracted from some review papers is given in Table 4 [39] [40] .

Table 4. Main characteristics of the most studied redox systems for high temperature TES [39] [40]

Compound	Enthalpy ($\frac{kJ}{mol}$)	Storage capacity ($\frac{kJ}{kg}$)	Red./Ox. Temperature (°C)	Nº of cycles tested	Cost (€/kg)
BaO_2	77,3	390-526	885/550	30	116
Mn_2O_3	31,9	202	1000/550	30	100
Co_3O_4	202	816-844	900/700	100	250
CuO	51,8	811	1100/700	20	60
Fe_2O_3	79,2	485	1345	3	40
Co_3O_4/Fe_2O_3	99,6	460	1298	40	222
CuO/Co_3O_4	107.8	800	894	40	236
CuO/Mn_2O_3	24.41	150	915	40	98
Mn_2O_3/Fe_2O_3	26.23	267	999	75	80

Taking into account the experimental results reported, TcES based on redox reactions are at an early stage of development, and it is necessary, mainly, to avoid the reversibility losses under repetitive charge and discharge cycles and to upscale the materials preserving their mechanical stability for their correct operation within thermochemical reactors.

2.1.1 Barium oxide

Ba_2O/BaO was the first redox reaction investigated for thermal storage purposes. It is abundant in nature, has low toxicity, high enthalpy, medium cost (116 €/kg) and lower activation temperatures compared to other investigated redox systems. Its main drawbacks are the high reactivity of BaO with elements commonly present such as CO_2 or H_2O and the degradation at high temperatures.

Within the different works found, the authors identified a reaction enthalpy of 77.3 kJ, where 2 mol of BaO_2 decompose into 2 mol of BaO and 1 mol of O_2 in the range between 550°C and 885°C at pressures between 0 and 0.5 bar, in a single, endothermic and reversible reaction step, with a storage capacity between of 390 and 526 kJ/kg and a maximum weight loss of 9.45 wt%, as follows:

$$2BaO_2(s) + 77.3\,\frac{kJ}{mol} \leftrightharpoons 2BaO(s) + O_2(g) \qquad \text{Eq. 8}$$

The BaO_2 dissociation reaction has been deeply studied since the late 1800s up to the beginning of 1970s with slightly different results regarding the activation temperature, which depending on the authors falls in the range between 740°C and 844°C at 1 bar, the reaction enthalpy between 79,9 kJ/mol and 148 kJ/mol and the relationship between the temperature and the pressure, which has been subjected to the following different proposals by Le Chatelier in 1892, J. M. Hildebrand in 1912 [41] and L. Till in 1971 [42], respectively.

$$logP_{O_2} = -\frac{6850}{T} + 1.75logT + 2.8 \quad \text{Eq. 9}$$

$$logP_{O_2} = -\frac{5800}{T} + 1.75logT + 2.8 \quad \text{Eq. 10}$$

$$logP_{O_2} = -\frac{4170}{T} + 3.4 \quad \text{Eq. 11}$$

The first kinetic study of the reaction was published in 1983 by M A Fahim and J D Ford who assumed that it was controlled by surface intrinsic kinetics, within a first order kinetics with E_a of 52 kJ/mol and proposed the following rates for decomposition and oxidation, respectively.

$$k_1 = 2.81 \cdot 10^5 e^{\left(-\frac{33600}{RT}\right)} \quad \text{(650°C -800°C)} \quad \text{Eq. 12}$$

$$k_2 = 141.84 e^{\left(-\frac{12400}{RT}\right)} \quad \text{(450°C -580°C)} \quad \text{Eq. 13}$$

The cyclability of the system was tested under 20 cycles between 850°C and 550°C by M. A. Fahim and J D Ford in 1983. After these cycles in the capacity of the system was hugely decreased up to 80%. The authors explained it due to the formation of a thick layer of BaO_2 which blocked the accessibility to BaO particles and thus, stopping the completion of the oxidation reaction [43].

The first proposal for energy storage purposes was publish by J. A. Simmons in 1976 and immediately tested in 1978 by R. G. Bowrey and J. Jutsen, who confirmed the minimum activation temperature of 750°C identified in previous works at which there is acceptable rates of reaction, and carried out five oxidation/reduction cycles obtaining no decrease in the global performance of the system. The acceptable performance of the system, in opinion of the authors, rely upon not exceeding the heating rate of 8°C/min and the maximum temperature of 850°C [44].

General Atomics carried out in 2011 a wide study of redox candidates for thermal storage for concentrated solar power plants, published by B. Wong [26]. Within the study, BaO_2 was proposed as a candidate although its low cyclability was known. To face this problem, they proposed to form mixed oxides that have been successfully used previously to increase the electrical conductivity in ceramics, but no improvement was found regarding BaO_2.

During the last years, DLR (German Aerospace Center) has been focused in the study of several redox candidates for thermal energy storage, among them BaO_2. Agrafiotis et al. published in 2016 a TGA study and some experiments covering several candidates, aimed to identify their limitations and advantages. BaO_2 showed poor cyclability due to its tendency to react with CO_2 and moisture, considering that they are commonly present in real conditions they suggested this material as inappropriate for its use as thermal storage [45] [46].

In order to improve the performance of the system, there has been some related work in the field of O_2 production that could be applied also to thermochemical heat storage. In 2005 Jin et al. focused their work in the mixture of BaO_2 and MgO. Using different proportions of the reactants they carried out over 100 cycles and thermal stability was demonstrated [47]. The Kyung Hee University of Korea

has been recently working in a new multicomponent formed by (BaSrMg)O, also in the field of O_2 extraction. They found a way to be able to decide the % of each component to be present into the system and succeed in getting high thermal stability over 5 cycles [48].

Following these promising results, Carrillo et al. carried out in 2016 a deep study concerning the oxidation/reduction cycles of BaO_2 [49]. They confirmed over a 30 redox cycles at temperatures between 900°C and 500°C and 5°C/min, that the oxidation reaction was much slower than the reduction one and thus, it is the limiting step of the system, attaining a maximum conversion of 85%. They checked how both processes were accelerated increasing the heating or cooling rates testing 2°C/min, 5°C/min and 10°C/min and this contributes to minimize the sintering effect. Even more, they verified how a pre-treatment of the sample, aimed to eliminate impurities of $BaCO_3$, helped to maintain the conversion rate stable and realized that inappropriate storage of the sample could lead to undesirable side reactions, especially with moisture to form barium hydroxides. They measured an E_a of 96.2 kJ/mol, quite different to the one calculated by M. A. Fahim and J. D. Ford, and determined that the oxidation reaction fitted quite well to a zero-order kinetics.

2.1.2 Manganese oxide

Mn_2O_3 is a chemical compound which is abundant in nature, a low cost material (100 €/kg), with a low level of toxicity.

Within the different works found, the authors identified a reaction enthalpy of 31.9 kJ, where 6 mol of Mn_2O_3 decomposes into 4 mol of Mn_3O_4 and 1 mol of O_2 in the range between 550°C and 1000°C, in a single, endothermic and reversible reaction step, with a storage capacity of 202 kJ/kg and a maximum weight loss of 3.38 wt%, as follows:

$$6Mn_2O_3(s) + 31.9\,\frac{kJ}{mol} \leftrightharpoons 4Mn_3O_4(s) + O_2(g) \qquad \text{Eq. 14}$$

General Atomics carried out in 2011 a wide study of redox candidates for thermal storage in concentrated solar power plants published by B. Wong [26], obtaining for the Mn_2O_3/Mn_3O_4 system a reaction enthalpy of 31.9 kJ/mol, corresponding to 202 kJ/mol and an equilibrium temperature of 1000°C. Within the study, Mn_2O_3 was subjected to a 3 cycles test at 30°C/min, achieving a poor conversion of 6% during re-oxidation. To face this problem, they proposed to form mixed oxides that have been successfully used previously to increase the electrical conductivity in ceramics.

In 2013 Karagiannakis et al. considering that for a practical use in CSP plants, the material in the form of powders would not have any chance, they compared the performance of Mn_2O_3 and Co_3O_4 in the form of pellets. They confirmed during a 6 cycles test, between 1000°C and 500°C, the slow oxidation kinetics of Mn_2O_3 and achieved a low average energy density of 110 kJ/kg, five time lower than the one of Co_3O_4 [50].

Within the scope of the last projects of DLR, Agrafiotis et al. published in 2016 a TGA study and some experiments covering several candidates, aimed to identify their limitations and advantages, among them, they carried out some experiments with pure Mn_2O_3 [46]. They identified reduction temperatures of 940°C and oxidation temperatures around 690°C-750°C, during a 3 cycles test

between 1000°C and 550°C at 10°C/min, 5°C/min and 2°C/min, with an oxidation reaction rate slower than the reduction reaction rate, achieving a re-oxidation conversion after the 3rd cycle of approximately 90%. To solve this problem a cascaded configuration system was proposed, comprising both Mn_2O_3 and Co_3O_4, which could operate in a wider range of temperatures.

The institute IMDEA Energia has been also interested in the redox performance of Mn_2O_3, although they have been focused mainly in the improvement of its performance by metal co-doping. The relevant publications regarding the characterization and performance of Mn_2O_3 are covered in two publications in 2014 by Carrillo et al.. The first one concerning the study of the influence of the particle size on the cyclability, in which the results of a 30 cycles test over several samples of different size, between 1000°C and 650°C at 5°C/min, were presented. It was found that the particle size influenced not only to the % of conversion, being lower for the smallest particles, but also to the re-oxidation temperature, which decreased with the size of the particles [31]. The second one concerning the comparison of the performance of pure Mn_2O_3 with different Co-doped samples [51].

In addition, S. Alvarez de Miguel designed and constructed a test rig capable to generate between 10-60 m^3/h (165-1000 L/min) of hot air up to 1100°C, aimed to study fixed and fludized bed thermochemical reactor configurations. The work was developed under the scope of TCS power project where manganese oxide and iron-doped manganese oxide redox reactions were studied in a 100 Wh thermochemical reactor. Almost 3 kg of active material in the form of pellets of 2-5 mm were cycled 25 times, observing better kinetic performance of the doped sample although worse mechanical properties compared to the pure sample. In some of the experiments the temperatures in the bed did not reach the reaction onset temperature and incomplete material conversion was observed, besides no significant effect on the bed temperatures was observed during the reactions and the reactions kinetics were studied based on the oxygen concentration variation measured with a gas analyzer [52].

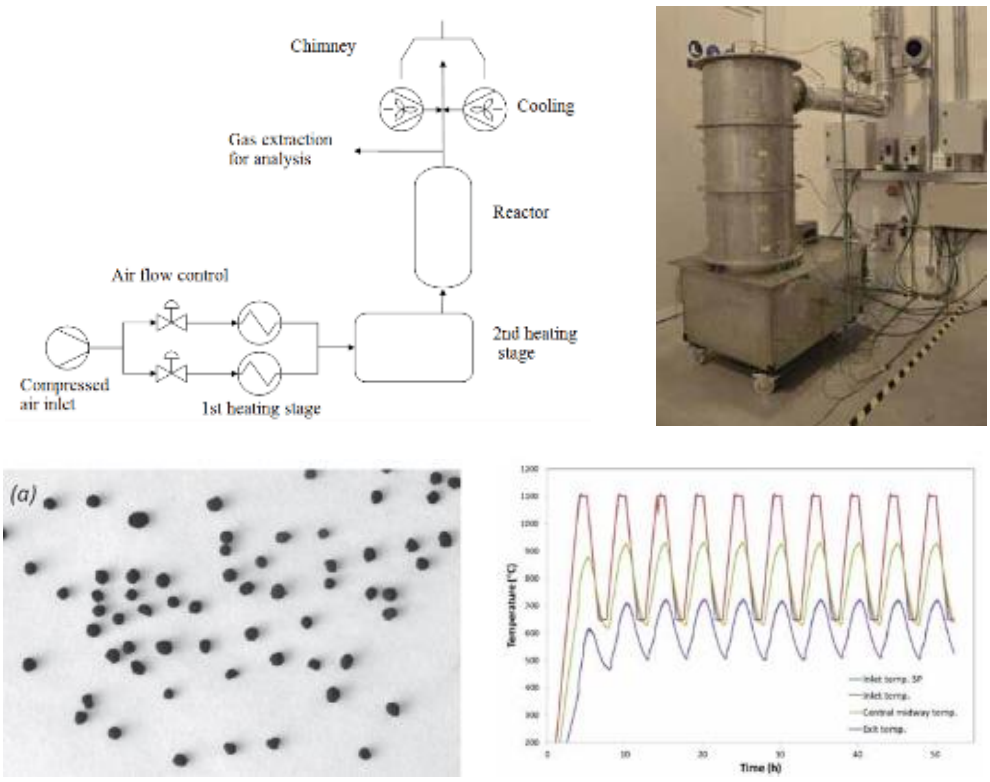

Figure 8. 100 Wh fuidized bed reactor of manganese oxide by S. Alvarez de Miguel [52]. Copyright 2017 Elsevier

2.1.3 Cobalt oxide

Cobalt oxide is an inorganic compound with the formula of Co_2O_3, most commonly used for bleaching. It is the most studied redox compound for thermal energy storage although it has some important drawbacks such as its cost (258 €/kg), higher than other metallic oxides potentially suitable for thermal storage purposes, and being potentially carcinogenic.

Within the different works found, the authors identified the highest reaction enthalpy of all the redox materials, 202 kJ/mol, where 2 mol of Co_3O_4 decompose into 6 mol of CoO and 1 mol of O_2 within the range between 800°C and 1000°C, in a single, endothermic and reversible reaction step, with a theoretically storage capacity of 844 kJ/kg with a maximum weight loss of 6.64 wt%, as follows:

$$2Co_3O_4(s) + 202\frac{kJ}{mol} \leftrightharpoons 6CoO(s) + O_2(g) \qquad \text{Eq. 15}$$

The oxidation reaction kinetics was studied since the end of the 1930s by several authors. W. R. Ott and D. T. Rankin measured in 1979 the rate of oxidation of sintered pellets, concluding that the oxidation is nuclei-growth controlled around 800°C [53]. Another approach was made in 1982 by H. S. Hsu and G. J. Yurek regarding the influence of the O_2 pressure in the rate of oxidation, performing some tests that involved pressures between 0 and 1 bar and temperatures between 600°C and 800°C and found an oxidation process that followed a parabolic rate law [54]. K. N. Hutchings arrived to a similar conclusion in the work published in 2006 which involved 100 cycles between the range from 870°C and 955°C at 20°C/min, obtaining a reaction enthalpy of 200 kJ/mol, an equilibrium temperature of 891°C and no degradation after the last cycle [55].

General Atomics carried out in 2011 a wide study of redox candidates for thermal storage in concentrated solar power plants published by B. Wong [26]. Within the study, Co_3O_4 showed the fastest kinetics among all of them, and it was used in a packed bed proof of concept reactor. They submitted the sample to a 500 redox cycles between 700°C and 900°C and with several temperature rates (1°C/min, 10°C/min and 30°C/min) confirming that the sintering effect decreased the re-oxidation capacity to 70% and discovering that the addition of another oxide such as Cr, added by chance during the tests, could improve the performance.

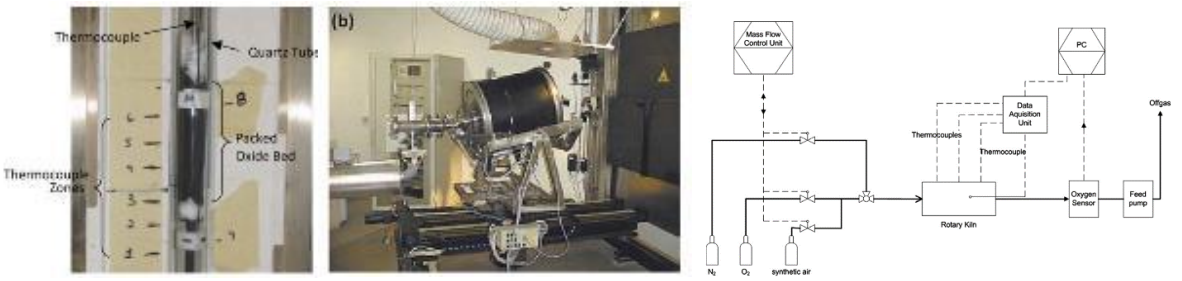

Figure 9. Packed bed and Rotary kiln reactors used by B. Wong **[30]**. Copyright 2010 US Department of Energy.

The following years, an intense work in the validation and optimization of thermochemical heat storage systems based on the Co_3O_4 reduction/oxidation reactions were developed, mainly by the German Aerospace Center (DLR) and the Center for Research and Technology-Hellas.

Belonging to the work carried out in the Center for Research and Technology-Hellas, in 2013 Karagiannakis et al. considering that for a practical use in CSP plants, the material in the form of

powders would not have any chance, they compared the performance of Mn_2O_3 and Co_3O_4 in the form of pellets [50] [56]. They first submitted the commercial powder of Co_2O_3 to a 6 cycles test in a fixed bed reactor, identifying a reduction and oxidation temperature of 930°C and 800°C, respectively and obtaining only a 60% of the maximum theoretical conversion, which corresponds to a heat storage capacity of 495 kJ/kg. When they repeated the tests with pellets made of the same powder, they found faster kinetics and was attributed to the better heat transfer capability of the pellets, which added to a lower pressure drop in a fixed bed configuration turned this proposal into a promising solution for thermochemical storage.

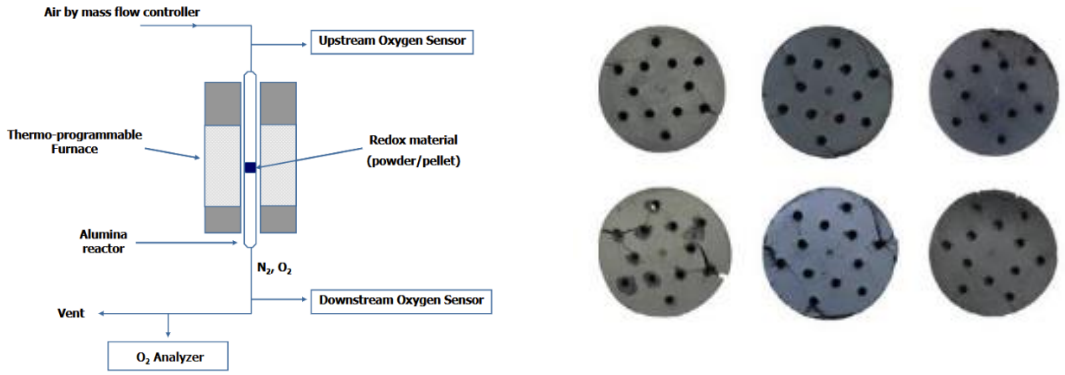

Figure 10. Experimental set-up and samples for validation of flow-through pellets of Co_3O_4 and Mn_2O_3 by G. Karagiannakis **[57] [56]**. Copyright 2014 Elsevier.

Being aware of the notable advantages of monolithic bodies compare to pure powders, in 2014 Pagkoura et al. extended the previous work and tested the redox performance of pellets made of four different grades of pure Co_3O_4, in a 5 cycles test [58]. They identified a huge variation in the energy density, from the minimum value obtained of 365 kJ/kg to a maximum value of 609 kJ/Kg. These differences are mainly associated to the powder available surface area, the amount of impurities present and the morphologic homogeneity, and the authors concluded that in-house manufactured powders can achieve better performance than commercial ones. They also investigated the effect of a second oxide addition, finding a general decrease in redox performance but in the other hand, this addition allows to adjust the reduction and oxidation temperatures and increase the thermomechanical stability. Among all the tested compositions, the pellets with alumina and iron oxide ($CoFe_2O_4$ and $CoAl_2O_4$) presented the best performance comprising thermomechanical stability, kinetics and redox cyclability that need to be further investigated.

The next step in the investigation was related to the performance of Co_3O_4 honeycomb structures, published in 2015 by Pagkoura et al. [59]. For this study they prepared three different samples, two by the extrusion of pure Co_3O_4 and a mixture of Co_3O_4 and alumina and the third one by coating commercial cordierite segments with Co_3O_4, and subjected all of them to 10 redox cycles from 800°C to 1000°C. Extruded Co_3O_4 and coated samples performance were good but in the other hand, the sample with alumina presented the worst redox performance due to formation of cobalt aluminate spinel phase, with a poor 51% of O_2 released when compared to the theoretical one. This percentage was 69% for the pure Co_3O_4 sample, which corresponds to a heat density of 549 kJ/kg Co_2O_3. In the case of cordierite coating the maximum value reached 539 kJ/kg Co_2O_3, in which the total mass of Co_2O_3 was 1.3-2.9 g, compared to the 14-14.8 g of the extruded samples. However, the addition of alumina contributes to reduce the temperature hysteresis from 30°C to 10°C and increase the thermomechanical stability, so reduced quantities of alumina could be an optimal approach to solve

the stability problems of pure cobalt oxide. Regarding the kinetics of the reaction, it shall be noted that the time required for the reactions was 12% shorter compare to the ones obtained in previous works with pellets.

Figure 11. Honeycomb extrusion and coated structures of Co_2O_3 in the Center for Research and Technology-Hellas **[59]**. Copyright Elsevier 2015

Corresponding to the work developed in the German Aerospace Center, in 2012 Neises et al. reported a work concerning the validation of a solar heated rotary kiln concept, using the reduction/oxidation reaction of pure Co_3O_4 and a mixture with 5% of aluminum oxide [60]. They used between 125 g and 250 g of reactants and achieved a poor average conversion during the reduction reaction of 40-50% during 30 cycles between 800°C and 900°C, that means a real heat storage capacity of 400 kJ/kg. In opinion of the authors, although some sintering and agglomeration appeared, it was mainly produced due to poor surface contact between powder and gas inside the kiln. Increase the loading levels, the rotational speed or adding fins inside the kiln were some of the suggestions to increase the conversion rate.

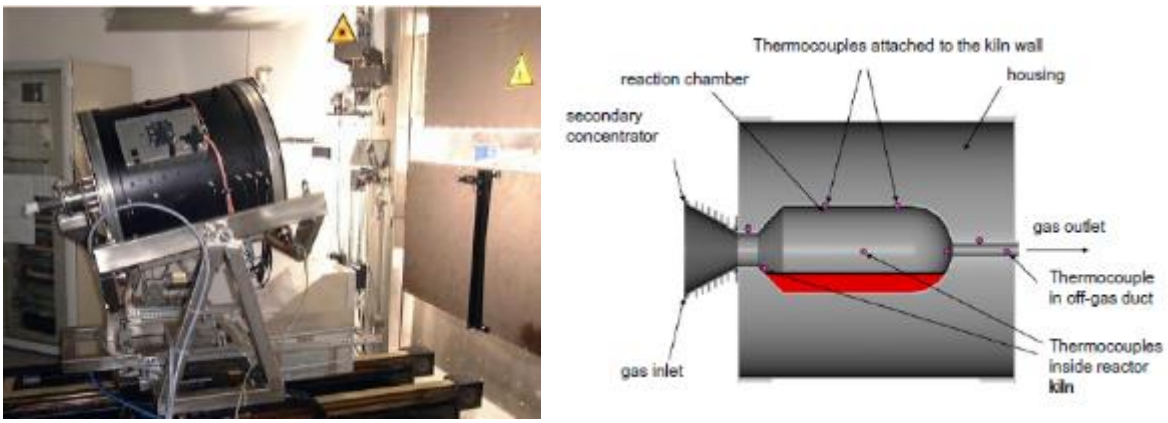

Figure 12. Solar rotary kiln reactor of DLR with Co_2O_3 **[61]**. Copyright Elsevier 2012

In 2014 Tescari et al. proposed two different reactor concepts based on the use of the Co_3O_4 reversible chemical reaction, a rotary kiln reactor and a honeycomb reactor [62].

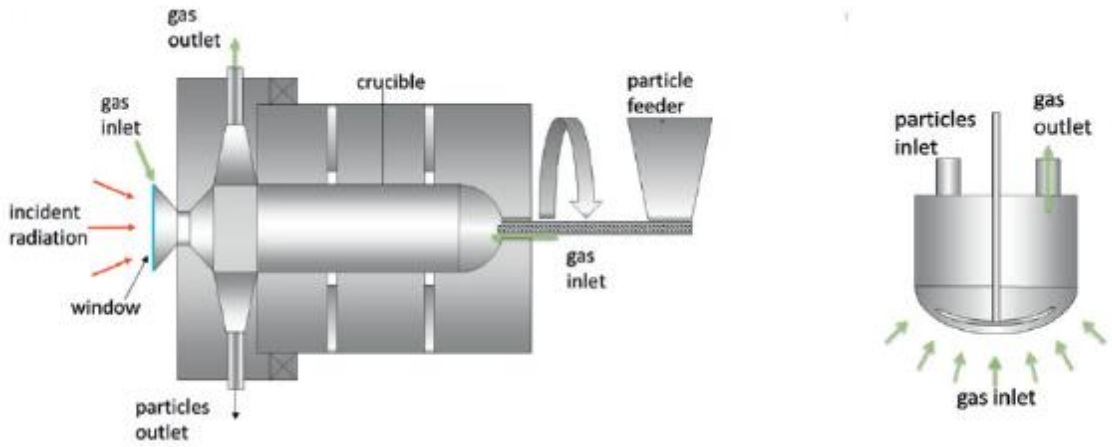

Figure 13. Rotary kiln reactor for Co_3O_4 in DLR [62]. Copyright Elsevier 2014

Firstly, they submitted pure samples of Co_3O_4 to a two cycles test in which they confirmed full conversion, with an oxidation temperature of 885°C and a reduction temperature of 900°C, very close to the value reported in the literature by K. N. Hutchings, B. Wong and C. Agrafiotis. The concept of a rotary kiln reactor using Co_3O_4 powder was presented previously by Neises et al., with a poor rate of conversion. In this work, S. Tescari suggested an optimization of this concept consisting in a reactor in which the reduction and oxidation reactions took place in different chambers, so that the sensible heat needed to heat the principal reactor, where the reduction took place, is consumed just once. They presented a study covering different reactor lengths and radius. The concept of a honeycomb reactor involved an inert ceramic honeycomb coated with an active thermochemical material that during sunshine periods would storage both the sensible heat of the ceramic honeycomb and the enthalpy of the reduction reaction of the thermochemical oxide. They carried out 30 cycles to a sample consisting in honeycomb structures coated with 28 wt% Co_3O_4 powder, obtaining the same performance of the powder alone, without capacity loss during the whole test.

Following the previous work in DLR and with the aim of increasing the efficiency of the system, Agrafiotis et al. published between 2014 and 2016 a complete set of works that cover different approaches. The first one was published in 2014 and had the aim of optimizing the oxidation/reduction cycles of Co_3O_4. Agrafiotis et al. carried out several tests involving pure Co_3O_4 and some mixed oxides, comprising $NiCo_2O_4$, $CuCo_2O_4$ and $MgCo_2O_4$ [63]. They observed that the oxidation step is much slower than the reduction one and extending the cooling time turned out to be more effective to get full conversion than choosing the right temperature levels that were shifted from values around 785°C for oxidation to 985°C for reduction. The addition of Ni, Cu and Mg did not improve the redox performance, so the samples of pure Co_3O_4 were subjected to further study obtaining a maximum heat capacity of 561 kJ/kg, much higher than the one obtained by Karagiannakis et al.. They submitted the pure samples to a 30 cycles test between 785°C and 985°C at 5°C/min, with a slight decrease in the weight loss (96%) that means just a minimum performance decrease, but they found different performances depending on the source of the powder which has larger impact than other aspects, such as the powder size or the available surface.

The following work, published in 2015, considered the preparation of several Co_3O_4 coated porous ceramic honeycomb and foams structures and the identification of their optimal operation conditions [64]. Several materials were considered within the study, namely Al_2O_3, ZrO_2, cordierite, SiC and SiSiC. With loadings between 14 wt% and 200 wt%, they submitted the samples to a 2 cycles experiment in

which they found the maximum weight loss of 6.64%, independently of the loading amount, corresponding to full reaction, with no capacity reduction during the whole test, except for SiC-based supports. Among all the materials investigated for oxide supports they identified some side reactions with SiC-based oxide supports that reduced the weight loss and selected cordierite as the best option due to its better thermal properties and wide variety of commercial structures available. In order to measure the cyclic performance, they carried out a 100 cycles test to a cordierite foam loaded with 64 %wt of Co_3O_4 arriving to the same conclusion above, maintaining the redox performance at full capacity.

Giving continuity to the previous work, in 2015, the next proposals consisted in the use of inert Co_3O_4 coated honeycomb structures or foams made entirely of Co_3O_4 as the active material for a thermochemical reactor [65]. They manufactured several samples of honeycomb structures with different Co_3O_4 loading percentages, varying from 17 to 94 wt%, finding a similar performance than the powder itself during a two cycles test and finding no capacity and structural integrity loss during a 30 cycles test, which on the other hand, such loss was identified in the results showed for the pure powder. Same good results were obtained with the two foams made entirely of Co_3O_4 for a 2 and 15 cycles tests, demonstrating the feasibility of manufacturing small scale ceramic foams. They observed a weight increase during the first heat up due to the presence of some remaining reduced CoO. This was clarified with another set of tests using pellets made of Co_3O_4 powder and an organic binder, containing some traces of CoO. The study was completed in 2015 with the comparison of the results with a different approach, consisting in the use of pellets made completely of Co_3O_4, which offers higher active material density [66]. This proposal showed a similar cyclic performance but a weaker structural integrity, finding some cracks after the contracting and expansion processes during the reduction and oxidation reactions and for that reason, this proposal was not considered as a solution for future thermochemical storage system.

Subsequently, another research work was published in 2016 with the proposal of a hybrid system consisting in a thermochemical storage cascade system based on the use of honeycomb structures coated with Co_3O_4 and Mn_2O_3 which pretends to take advantage of the thermocline temperature distribution in some kind of reactors [67]. They investigated the effect of varying the air flow rate and compared the behavior of the system with and without the oxide coating. Finally, they demonstrated that the two oxides system can work in a consecutive way, due to their different reduction and oxidation temperatures, but no application has been found yet.

After deep research on the optimal redox material allocation inside the thermochemical reactor, S. Tescari constructed a laboratory set-up at a relevant scale, capable of testing up to 88 kg of Co_3O_4-coated blocks of cordierite honeycombs. A pronounced heating or cooling rate decrease were observed when reaching the reaction onset temperatures, followed by a slight temperature plateau under an air flow of 0.05 kg/s. The thermochemical reactor demonstrated an increased thermal energy storage capacity 4 times higher compare to its counterpart sensible heat storage. They performed up to 22 redox cycles without no significant cycle-to-cycle capacity degradation, setting the basis for future reactor optimization [68].

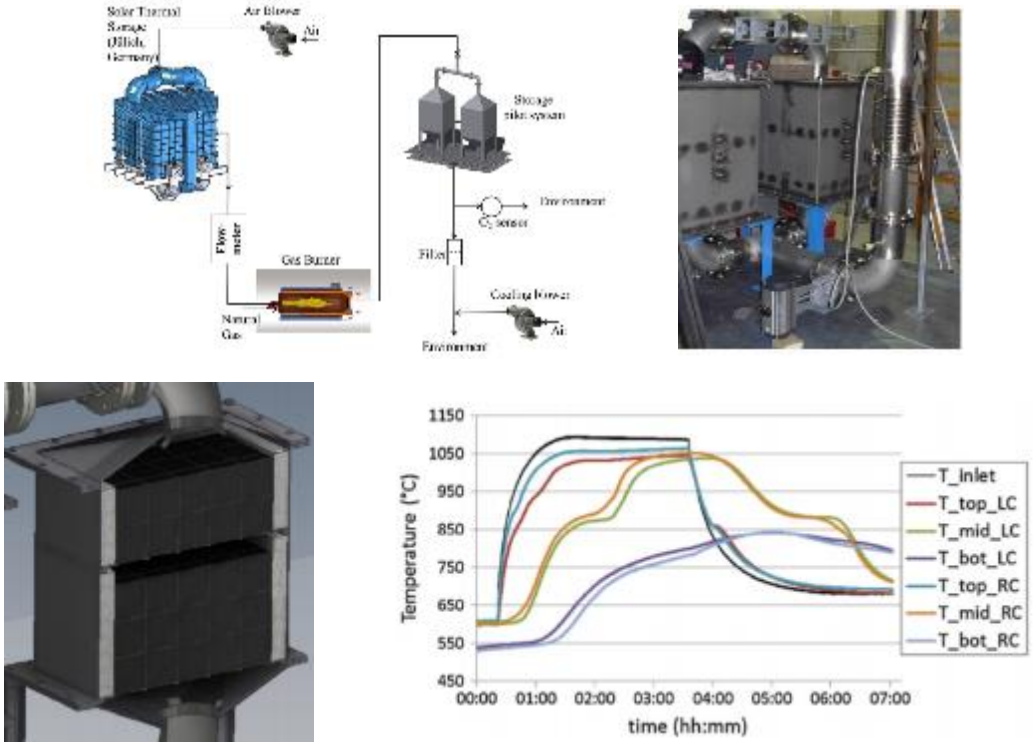

Figure 14. Experimental set-up of a TcES reactor containing 88 kg of Co3O4 by S. Tescari **[68]**. Copyright 2017 Elsevier.

Completing the work developed in DLR, in 2016 T. Block and M. Schmücker published another proposal regarding the use of several binary metal oxide systems, comprising cobalt oxide/iron oxide, copper oxide/cobalt oxide, copper oxide/manganese oxide and manganese oxide/iron oxide [27]. In this proposal pure metals were also tested, obtaining an enthalpy for Co_3O_4 of 576 kJ/kg, which was much lower than the theoretical one and was attributed to a change of a Co^{3+} spin state. They carried out a 3 cycles test with temperatures between 915°C and 879°C at 10°C/min, finding a clear decrease in reaction rates and concluding that being also a high cost material, new proposals must be found to use the pure metal oxide as a thermochemical heat storage material.

The institute IMDEA Energia has been also interested in the redox performance of Co_3O_4, although they have been focused mainly in the improvement of its performance by Mn co-doping. In the scope of this study, published in 2014 by A. J. Carrillo, they have measured the performance of pure Co_3O_4, obtaining full re-oxidation in a two cycles test between 985°C and 785°C at 5°C/min [51].

2.1.4 Copper oxide

Copper oxide is an inorganic compound which may refer to Cu_2O (copper (I) oxide), CuO (copper (II) oxide), CuO_2 (copper peroxide) and Cu_2O_3 (copper (III) oxide). The most studied compound for thermal heat storage is CuO. It is a black solid and one of the two stables oxides of copper, the other being Cu_2O. As a mineral, it is known as Tenorite and paramelaconite. It is a product of copper mining and it is by far, the highest cost material among all the studied oxides for thermal storage purposes (948 €/kg).

Within the different works found, the authors identified a reaction enthalpy of 51.8 kJ, where 4 mol of CuO decomposes into 2 mol of Cu_2O and 1 mol of O_2 in the range between 1000°C and 1100°C, in a

single, endothermic and reversible reaction step, with a theoretically storage capacity of 652 kJ/kg with a maximum weight loss of 10.01 wt%, as follows:

$$4CuO(s) + 51.8\frac{kJ}{mol} \leftrightharpoons 2Cu_2O(s) + O_2(g) \qquad \text{Eq. 16}$$

General Atomics carried out in 2011 a wide study of redox candidates for thermal storage applications in concentrated solar power plants, published by B. Wong [26], obtaining a reaction enthalpy for CuO/Cu_2O reaction of 64.5 kJ/mol, corresponding to 811 kJ/kg and an equilibrium temperature of 1030°C. As a conclusion of the study, they rejected CuO as a suitable thermal storage material, due to the fact that its transition temperature of 1030°C was too close to its melting temperature of 1232°C, and this turned into difficulties to manage this reaction without having some material melted which decrease the re-oxidation conversion due to sintering.

In 2015 Alonso et al. published a study concerning the performance of the copper oxide in a rotary kiln reactor [69]. The tests involved the use of 10 g of CuO powder. They achieved an 80% conversion with 900°C in a reduction test with argon. In a cyclability test with air, under a reduction temperature of 1000°C and an oxidation temperature of 700°C, the sintering effect was so high that the total conversion during reduction was only 40% and from this quantity only 9% was reached for re-oxidation. In opinion of the authors, the feasibility of the materials could be reached and relies on a fine reaction temperature control.

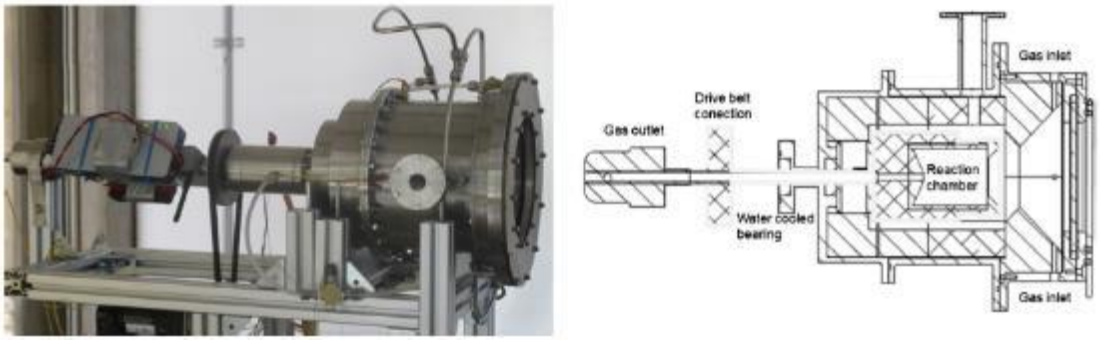

Figure 15. Rotary kiln reactor of CuO in the National University of Mexico **[69]**. Copyright Elsevier 2015

In 2016 Agrafiotis et al. carried out some tests with two samples of CuO powder, between 1090°C and 1000°C at 1°C/min and 5°C/min [46]. They got full reduction conversion but no complete re-oxidation was possible, even increasing the re-oxidation temperature to 1020°C at 5°C/min, although in such conditions, a re-oxidation conversion up to 80% was achieved with one of the samples. The dwelling time was not enough to complete the re-oxidation reaction and an increasing weight loss rate was observed during a 5 cycles test.

Completing the work developed in DLR, in 2016 T. Block and M. Schmücker published another proposal regarding the use of several binary metal oxide systems, comprising cobalt oxide/iron oxide, copper oxide/cobalt oxide, copper oxide/manganese oxide and manganese oxide/iron oxide [27]. In this proposal pure metals were also tested, obtaining a reaction enthalpy for CuO of 51.7 kJ/mol, corresponding to 650 kJ/kg, being the fastest reduction reaction among all the metallic oxides but

again, strong grain growth was found when submitted to a 3 cycles test between 1042°C and 1021°C at 10°C/min, which reduced the re-oxidation step significantly.

Recently, M. Gigantino developed a synthesis method to prepare spheres of 1-2 mm of CuO and tested their redox performance into a packed bed reactor. 107 g of active material where place inside a quartz tube of 50 mm of diameter, reaching 40 mm height. The granules incorporated a sintering inhibitor based on Y_2O_3/ZrO_2 stabilized material which got a stable charging and discharging processes under 30 redox cycles using 18-20 L/min of gas flow, both at isobaric and isothermal conditions, unlike previous studies with CuO [70].

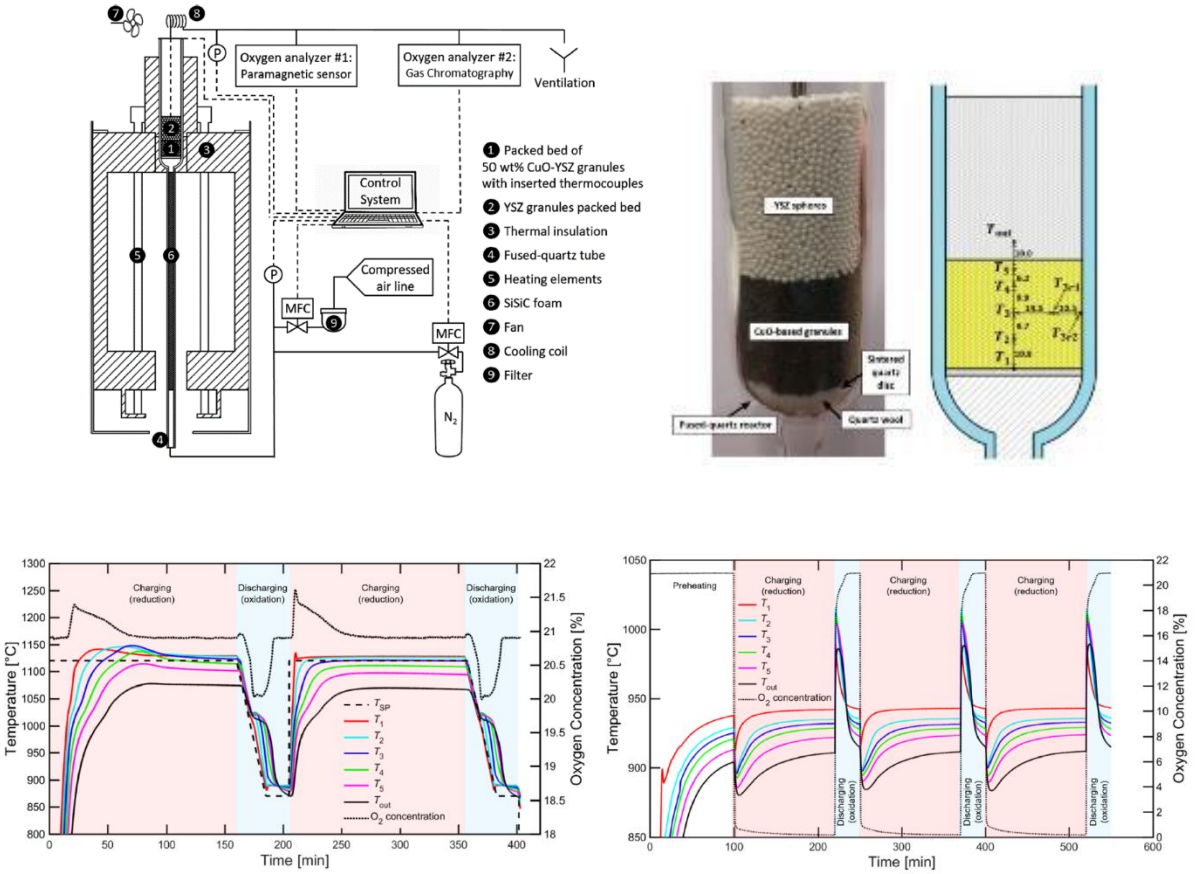

Figure 16. Packed-bed CuO thermochemical reactor bench by M. Gigantino **[70]**. Copyright 2020 ACS Publications

2.1.5 Iron oxide

Iron oxide is the inorganic compound with the formula Fe_2O_3. It is one of the three main oxides of iron, the other two being FeO and Fe_3O_4 (mineral magnetite). Fe_2O_3 is the main source of iron for the steel industry and it is also known as hematite. Fe_2O_3 is ferromagnetic, dark red, and readily attacked by acids. Due to its availability, it is the cheapest material among all the considered oxides (40€/kg).

Within the different works found, the authors identified a reaction enthalpy of 79.2 kJ, where 6 mol of Fe_2O_3 decomposes into 4 mol of Fe_3O_4 and 1 mol of O_2 in the range between 1300°C and 1400°C, in

a single, endothermic and reversible reaction step, with a theoretically storage capacity of 599 kJ/kg, as follows:

$$6Fe_2O_3(s) + 79.2\frac{kJ}{mol} \leftrightharpoons 4Fe_3O_4(s) + O_2(g) \quad \text{Eq. 17}$$

General Atomics performed in 2011 a wide study of redox candidates for thermal storage in concentrated solar power plants published by B. Wong [26], in which they found for the Fe_2O_3/Fe_3O_4 system a reaction enthalpy of 79.2 kJ/mol, corresponding to 496 kJ/kg, and an equilibrium temperature of 1400°C, but it was not subjected to further study due to the severe attrition problems identified caused by cracks during the reduction step.

Completing the work developed in DLR, in 2016 T. Block and M. Schmücker published a proposal regarding the use of several binary metal oxide systems, comprising cobalt oxide/iron oxide, copper oxide/cobalt oxide, copper oxide/manganese oxide and manganese oxide/iron oxide [27]. In this proposal pure metals were also tested, identifying 1392°C as the reaction temperature of Fe_2O_3, with an enthalpy of 560 kJ/kg, finding strong sintering effects after three redox cycles at 10°C/min. Taking advantage of the low cost of the material, the authors suggest lowering the oxygen partial pressure as a way to reduce the equilibrium temperature and its sintering effect.

2.1.6 Mixed oxides

Among the two types of possible mixed oxides reactions, solid-solid and solid solutions, only the solid solutions behavior is suitable for thermal cycling as the reaction develops similar to pure oxides without attrition effects that can be found in the solid-solid mixed oxides. In this kind of mixed oxides the primary cation is replaced by a secondary cation in the oxide lattice, it can be totally or partially substituted.

- Solid-solid reaction (resulting in a single phase oxide):

$$Mn_2O_3 + 2Fe_2O_3 + heat \rightarrow 2MnFe_2O_4 + O_2 \quad \text{Eq. 18}$$

- Solid solution reaction:

$$Co_2NiO_4 + heat \leftrightarrow Co_2NiO_3 + \frac{1}{2}O_2 \quad \text{Eq. 19}$$

The performance of mixed oxides has been widely studied for thermal energy storage purposes. One of the first studies comprising the analysis and proposal of mixed oxides as a thermochemical material for heat storage was published by B Wong in 2011, within the work developed in General Atomics with DLR, oriented to CSP applications [26]. Firstly, they analyzed the performance of several pure oxides, finding Co_3O_4, Mn_3O_4 and BaO_2 as the most promising ones, so they were selected to further investigation regarding their performance in a mixed compound with other oxides.

Once they confirmed in a 500 cycles test that the sintering effect decreased the re-oxidation capacity of pure Co_3O_4 up to 70%, they worked in its performance improvement by the addition of another

oxide, which had been observed by chance in one of the tests, finding some amount of Cr in the tested sample. They prepared several samples using different quantities of Al_2O_3, Cr_2O_3 and Fe_2O_3 resulting in lower grain growth and thus, a noticeable improvement in cyclability. They found that the samples with 5% Al_2O_3 and 23.2% of Fe_2O_3 presented the better performance, achieving a re-oxidation conversion above 99% after 500 cycles. Considering the low cost of Fe_2O_3, this mixed oxide could be an excellent approach for a large scale storage system. They also tested the sample with Al_2O_3 in a rotary kiln reactor, finding a much faster re-oxidation compare to the packed bed reactor, due to a better heat transfer.

Several secondary oxides were proposed to improve the kinetics of Mn_2O_3 reaction, among them Fe_2O_3, ZrO_2, CuO, ZnO, TiO_2, NiO, Al_2O_3, Co_3O_4, Li_2O, Cr_2O_3 and $NiFeO_4$, finding that iron oxide was the most suitable one, with a composition in the range of 10-15% Fe_2O_3, which increased the total conversion by 20-fold. They submitted the samples to a 500 redox cycles with an activation temperature of 950°C, confirming that the sintering effect was lower in the iron mixture than in the pure manganese oxide. The authors explained this improvement as due to the iron oxide additions, which enable the oxygen diffusion inside the material.

Concerning the low cyclability found in the pure BaO_2 reaction, several mixtures with secondary oxides were tested, such as NiO, TiO_2, Fe_2O_3, SnO, ZnO and commercially available $BaTiO_3$ and $BaCuO_x$. The results showed that no cyclability improvement was achieved via these mixtures and thus, they rejected this material for thermal storage purposes.

During the last years, the IMDEA Energy Institute has developed an intense work aimed to find a suitable system able to withstand the long-term requirements of a thermochemical energy heat storage system. Carrillo et al. used in 2014 a different approach to improve the cyclability of the Mn_2O_3 system by mixing Mn_2O_3 with different quantities of Co [51]. They submitted pure Mn_2O_3 and Co-doped Mn_2O_3 to five redox cycles, between 1000°C and 500°C at 10°C/min, obtaining complete re-oxidation of pure Mn_2O_3, unlike to what B Wong reported some years before. Adding Co produced three different effects: it contributes to decrease the reaction rate due to sintering effect, it decreases the reduction and re-oxidation temperatures and finally, it contributes to increase the heat exchange during the reactions. They confirmed that the re-oxidation reaction is the slowest process, driven by the diffusion of the oxygen into the oxide, different of the heat transfer driven reduction process, and suggest decreasing the cooling rate to achieve complete conversion. In opinion of the authors, although Co-doping contributes to decrease the temperature difference between reduction and oxidation and increases the heat capacity it contributes to thermally stabilize the Mn_2O_3 and thus, it does not help to improve the cyclability of the system. Following this conclusion, and taking into account that the sintering effect could not be disregarded in a long-term use with high temperatures, even for pure Mn_2O_3, another strategy was suggested by the same authors concerning Fe addition to Mn_2O_3. The first work was published in 2015 by Carrillo et al. related to the effect in decreasing the thermal hysteresis [33]. They prepared several samples with Fe content from 0 to 40 % mol and submitted to 30 cycles, between 1050°C and 650°C, according the following redox reaction, with a reduction temperature of 979°C and an oxidation temperature of 828°C, the highest reached enthalpy was 202 kJ/kg with 20% of Fe.

$$6(MnFe)_2O_3 + 18.6\,\frac{kJ}{mol} \leftrightharpoons 4(MnFe)_3O_4 + O_2 \qquad \text{Eq. 20}$$

They found a complete re-oxidation of all the doped materials, but a decrease in the total conversion of the pure material down to 87%, unlike the full re-oxidation presented in a previous work. In opinion

of the authors due to the increase in the cycling temperature, being 1000°C in the previous work. Another improvement was related to the decrease in the temperature hysteresis between the reduction and oxidation temperature, which was 281°C for the pure material and decrease progressively with Fe addition down to 105°C when the content of Fe was 40% mol.

The second work was published in 2016 and was aimed to give understanding to the redox kinetics of the Fe-doped Mn_2O_3 material [34]. It was proven that the Fe addition contributes to stabilize and increase the oxidation rate, for which the Fe counteracts the sintering effect still present even with high quantities of Fe. The main reason for that is related to crystallographic changes, which would explain the best performance got with 20 % mol instead of that for higher contents. This faster kinetics led to an increase in the reaction enthalpy from a value of 184 kJ/kg of pure Mn_2O_3 to a maximum value of 219 kJ/kg for a 20 % mol composition. Fe addition also reduces the temperature hysteresis from 200°C of pure Mn_2O_3 to 105°C with 40% mol of Fe, mainly due to the increase in the oxidation temperature.

Another approach published by Carrillo et al. in 2015 was related to Fe and Cu co-doping to Mn_2O_3 [71]. They had confirmed that Fe doping contributes to increase the activation temperature, while Cu doping had the opposite effect. Using different quantities of Cu and Fe they achieved a temperature hysteresis decrease in all of them, from the 225°C original value up to 98°C for a sample with 10% mol Fe and 5% mol Cu. All the samples showed stability after 30 cycles, between 1000°C and 650°C at 5°C, except the ones which have 5% mol of Cu, which exhibited a high degree of sintering and slower kinetics so they suggested the sample with 5% mol Fe and 1% mol Cu as the ideal candidate for thermal energy storage.

Finally, as a result of the European project TCSPower, IMDEA published in 2016 the first results concerning the design and construction of a Mn_2O_3 based thermochemical reactor that can work as a fixed or fluidized bed reactor and presented the comparison of the numerical model developed and the experimental results which deviated only a maximum of 5,6% [72].

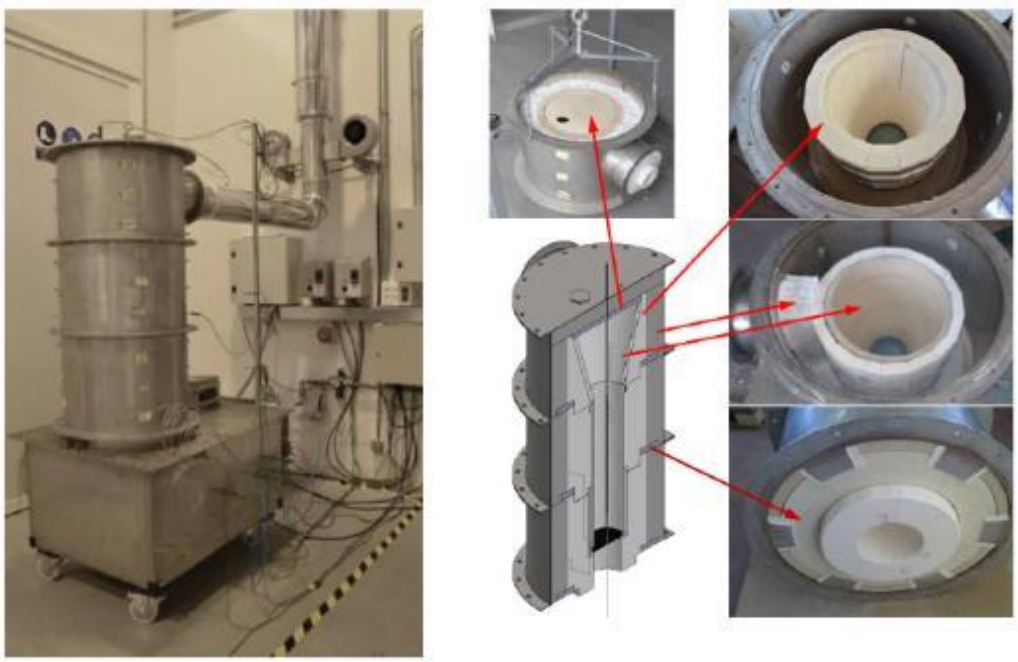

Figure 17. Design and construction of a thermochemical reactor in IMDEA **[72]**. Copyright AIP Conference Proceedings 2016

In 2014, T. Block investigated the performance of a mixed oxide comprising Co_3O_4 and Fe_2O_3 with the aim of achieving a thermochemical material with high capacity but with lower activation temperatures than pure cobalt oxide [73]. They carried out a 3 cycles test to several samples with different quantities of cobalt oxide, from x=0 to x=1, between 1100°C -1400°C and 500°C at 10°C/min. The amount of cobalt oxide has a strong influence on the reduction temperature, decreasing from an initial value of 1392°C for x=0 to 1017°C for x=0.2. The same decrease was observed regarding the enthalpy and mass change, which strongly decrease in the range between x= 0 to x=0.533 to a minimum value of 72,4 kJ/kg and increase again from x=0.533 to x=1 up to the final value of 578 kJ/kg. They noticed that in the range from x=0,3 to x=0,47 no reaction took place below 1400°C. Finding that cobalt oxide with little amounts of iron oxide could be the most promising material, they carried out a cyclability test with mixed oxides with x=0,867 and x=1, and confirmed that although they both experimented some reduction in the conversion rate with the number of cycles, the effect was lower in the sample of x=0.87, providing that the addition of iron contributes to improve the microstructural stability with just a slight decrease in the reaction enthalpy which reached 433.3 kJ/kg.

Completing the work developed in DLR, in 2016 T. Block and M. Schmücker published another proposal regarding the use of eight different binary metal oxide systems, finding several promising materials comprising cobalt oxide/iron oxide, copper oxide/cobalt oxide, copper oxide/manganese oxide and manganese oxide/iron oxide [27]. In principle all the systems presented a general decrease in reaction enthalpies counteracted by an improvement in their cyclability performance. Regarding the performance of the cobalt oxide/iron oxide system, the same conclusions of the previous work were presented. In the case of copper oxide/cobalt oxide, the compositions with higher quantities of Co, between x=0,1 and x=0,33 of Cu, seemed to be the most suitable ones, with higher enthalpies, kinetics and reduction temperatures around 866°C, 470 kJ/kg was reached with 0.07 CuO. In this case the CuO present, although it did not react, was demonstrated in a 40 cycles test that it contributed to stabilize the material and thus, reduce the sintering effect compare to pure Co_2O_3. The authors suggested that to take advantage of a higher proportion of CuO in the material, lower O_2 partial pressures might be used. Copper oxide/Iron oxide system showed good performance in copper rich compositions, but with reduction temperatures of 1037°C, which was very close to the melting point of copper oxide, so this mixture is only useful if there is a fine temperature control in the system. Copper oxide/Manganese oxide system presented high enthalpies in manganese rich compositions, up to 157 kJ/kg for x=0.03, decreasing the reaction temperature of pure Mn_2O_3 from 942°C to 913°C and increasing the reaction kinetics. Another promising system was manganese oxide/Iron oxide, which presented enthalpies around 232.7 kJ/kg at 999°C for manganese rich compositions around x=0.67. The copper oxide/chrome oxide and aluminum oxide/manganese oxide systems were rejected. The first one due to the fact that one of the two reactions that take place is not reversible and the other one happens too close to the melting point. The second one, due to a really slow re-oxidation reaction.

To determine the influence of the main operating parameters in the storage system performance at a reactor scale, M. Wokon designed a test ring with 500 g of manganese iron oxide particles of 1-3 mm using a packed bed configuration. The reactor tube dimensions were 195 mm height and 54.3 mm of diameter. The experiments revealed the heat exchange capacity between the thermochemical material and the HTF as the main limiting factor to charge and discharge the storage reactor. The reactor thermocouples output plots during charging and discharging showed a clear temperature plateau at 983.5°C during the reduction reaction, completed after 125 min and at 915°C during the oxidation reaction, completed after 69 min. The reactions evolution was confirmed by oxygen

concentration measurements using 5, 10 and 15 NL/min flow rates. The material suffered from some degree of sintering over 17 complete redox cycles, decreasing its mechanical strength which may compromise its long-term stability [36].

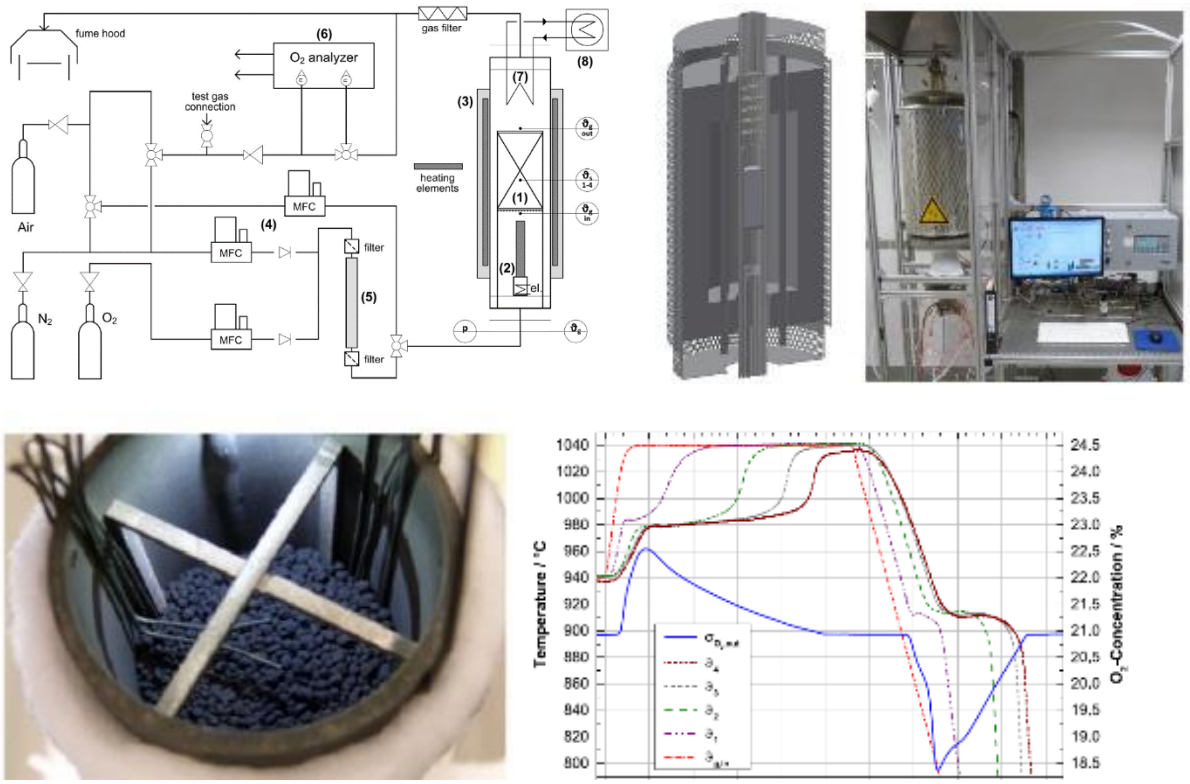

Figure 18. Packed bed test ring for 500 g of manganese iron oxide by M. Wokon **[36]**. Copyright 2017 Elsevier.

More recently, N. Carina assessed experimentally for the first time the behavior of manganese-iron oxide in a moving bed reactor. The experiments demonstrated the feasibility of oxidizing 3 g/s of falling particles of the thermochemical material under a countercurrent flow of oxygen, reaching a 80.2% conversion extent, which together with increasing particles flowability represents the main challenges [74].

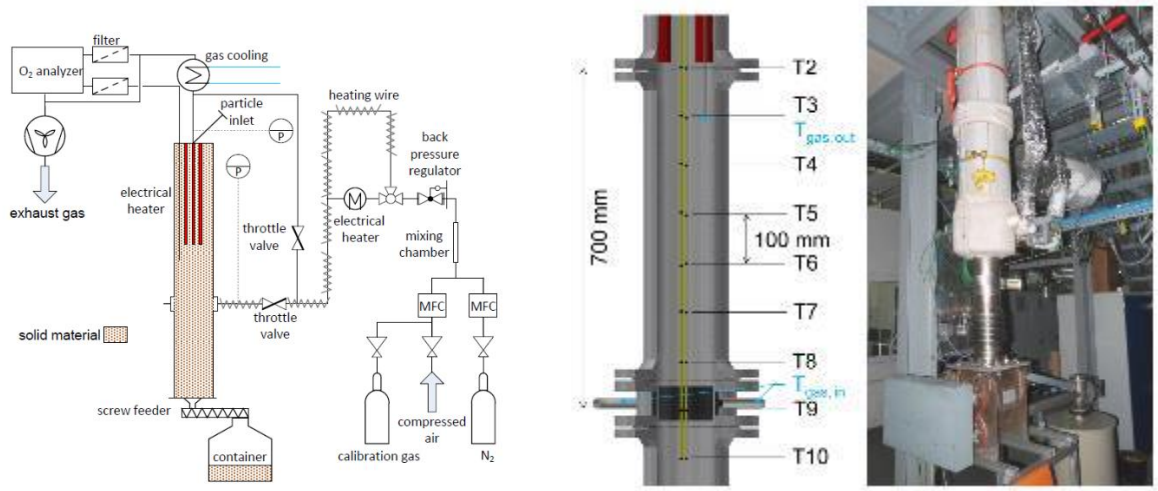

Figure 19. Moving bed thermochemical reactor by N. Carina **[74]**. Copyright 2020 MDPI.

In regard of the manganese-iron oxide approach, Hamidi et al. studied the reduction of iron-manganese oxide using a small packed-bed reactor of 3 cm height and 21 mm of diameter (around 35 g), heated inside an electric IR furnace with a gas flow rate of 100 mL/min. The experimental results were used to validate an O_2 concentration prediction model in MATLAB. The model results were accurate, even though some discrepancies were observed at the beginning of the reaction, where the experimental results were higher than the predictions and was attributed to higher flux of infrared radiation over the top of the bed, leading to an accelerated heat absorption [75].

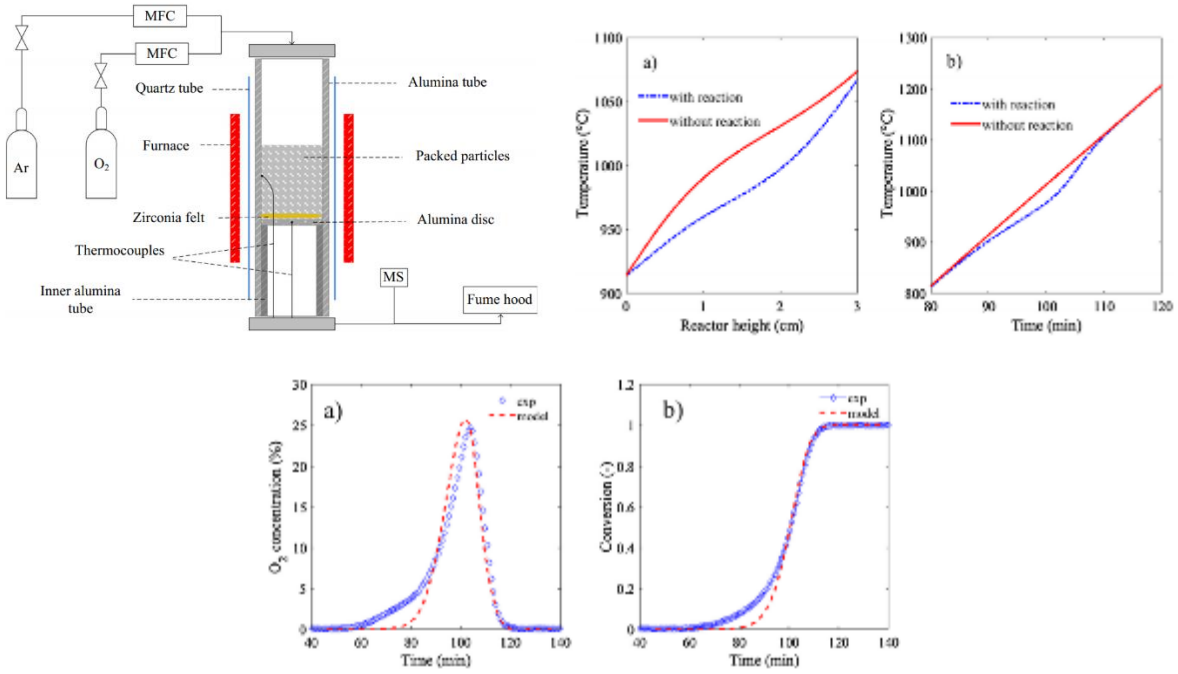

Figure 20. Small packed-bed thermochemical reactor by M. Hamiodi **[75]**. Copyright 2020 Elsevier

Finally, N. C. Preisner studied the effect on the mechanical strength of manganese-iron oxide by adding 20 wt% of different supporting materials, namely of ZrO_2, CeO_2 and TiO_2 in a packed bed reactor. 21-26 g of material was subjected to 30 redox cycles between 1050 and 850°C with 3 l/min of air flow. The results showed quasi-stable redox performance and an increase in particle stability with ZrO_2 and CeO_2 supports.

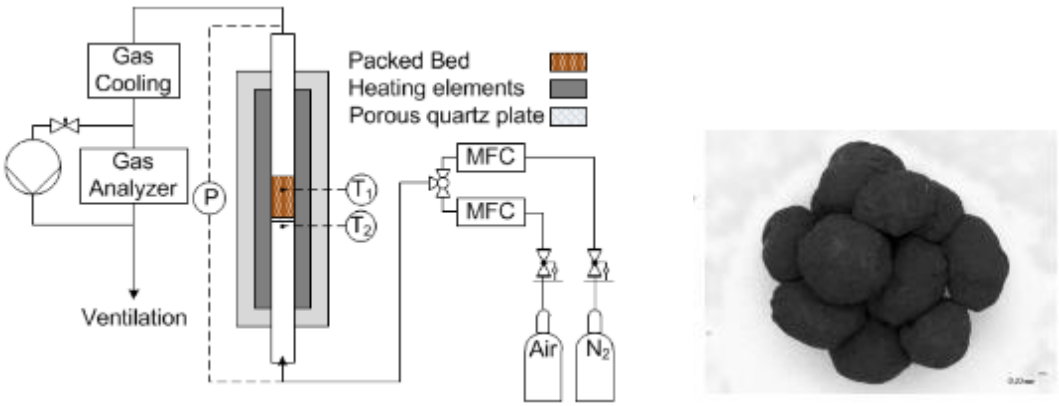

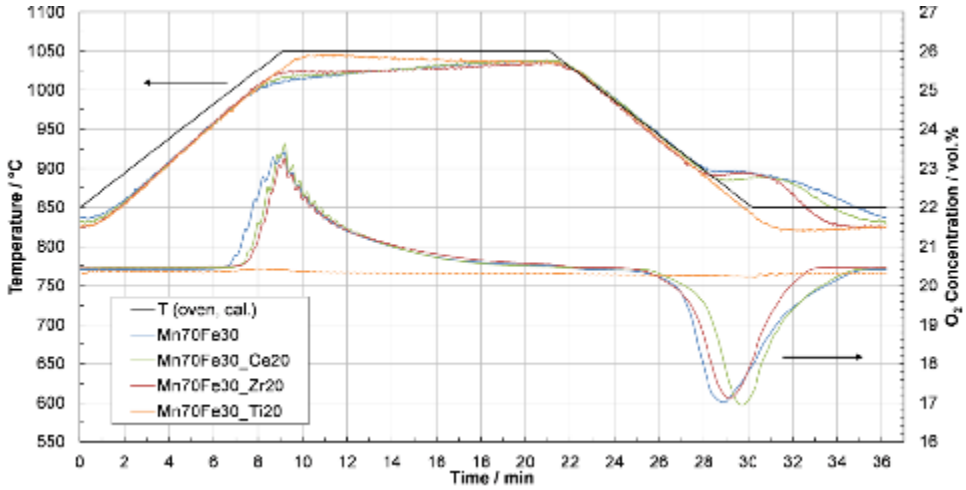

Figure 21. Manganese-iron oxide stabilized particles for packed bed reactor [76]. Copyright 2020 Wiley

2.1.7 Perovskite oxides

Perovskite oxides refers to rare-earth/transition metal mixed oxides which have the same crystal structure than $CaTiO_3$ with the formula ABO_{3-d}, where A and B are alkaline earth metal and transition metal, respectively and oxygen in a non-stoichiometry composition.

$$\boldsymbol{ABO_3 + heat \leftrightharpoons ABO_{3-d} + \frac{d}{2}O_2} \qquad \textbf{Eq. 21}$$

The potentiality of the perovskite oxides lies on their octahedral arrangement structure, which is larger than the one of a pure metal oxide and quite stable. In this structure, the endothermic reduction introduces oxygen vacancies into the crystal lattice without a crystallographic change, which added to the high porosity for oxygen transport and the wide range of A and B materials turn these compounds into a wide range of promising materials for thermochemical heat storage. The performance of the system may be easily tuned due to the fact that oxygen variation is temperature and O_2 partial pressure dependant, and the wide range of A and B elements available or even co-doping may contribute to increase the system stability maintaining the same O_2 exchange rate. They have fast kinetics but in the other hand, they require complex processing which poses their suitability for real scale application.

Perovskites redox performance has been studied for many applications apart from thermochemical heat storage. One of these applications is chemical loop combustion with the aim of CO_2 production or capture, which have been focused mainly in $CaMnO_{3-d}$ doping, with the main advantage of being a low cost material. Hallberg et al. have been working during the last decade with calcium manganite $CaMn_{0.9}Mg_{0.1}O_{3-d}$, $CaMn_{0.775}Ti_{0.125}Mg_{0.1}O_{3-d}$ and $CaMn_{0.8}Fe_{0.2}O_{3-d}$, and confirmed the good performance of these materials first in a small fluidized bed reactor [77] and some years after, during 99 h of operation in a 10 kW_{th} reactor [78]. In the same way, Galinsky et al. published a work in 2015 related to find the effect of Sr and Ba doping to $CaMnO_{3-d}$ in a fluidized bed reactor, finding no improvement with Ba doping and an excellent stability for Sr doped samples. The most promising one was $Ca_{0.75}Sr_{0.25}MnO_{3-d}$, subjected to 100 redox cycles at 850°C without losing oxygen desorption capacity [79].

With the aim of oxygen sorption/desorption, $Ca_{0.5}Sr_{0.5}FeO_{3-d}$, $Ca_{0.5}Ba_{0.5}FeO_{3-d}$ and $Sr_{0.5}Ba_{0.5}FeO_{3-d}$ were also subjected to further studies by Masunaga et al. in 2012 [80]. They showed a good stability in the range of 450°C-500°C during a 10 cycles test. In the same way, Shen et al. studied in 2016 the effect of Co-doping in the cyclability of $SrCo_{1-x}FeO_{3-d}$ in a fixed bed arrangement, finding $SrCo_{0.8}Fe_{0.2}O_{3-d}$ as the most promising material, with absortion/desorption temperatures between 750°C and 850°C, an improvement of cyclic stability during a 20 cycles test and larger O_2 desorption amount, compare to $La_{0.1}Sr_{0.9}Co_{0.5}Fe_{0.5}O_{3-d}$ and $Sr_{0.5}Ca_{0.5}Co_{0.5}Fe_{0.5}O_{3-d}$ [81].

Another different application in which perovskite oxides has been studied is H_2O and CO_2 splitting. Scheffe et al. published in 2016 the results of the collaboration of ETH and PSI in the experimental study of lanthanum-based perovskites $La_{1-x}Sr_xMnO_{3-d}$, looking of an alternative to cerium oxide-based systems. The results showed not a clear advantage but set the base for further development with other materials [82].

In the field of thermal storage application, Babiniec et al. published in 2015 a characterization and thermodynamic wide study of $La_xSr_{1-x}Co_yMn_{1-y}O_{3-d}$ and $La_xSr_{1-x}Co_yFe_{1-y}O_{3-d}$ compositions, as a starting point due to the available studies of these materials for other applications [83] [84]. The best redox performance was found with compositions with low La, and the largest reaction enthalpy achieved was 250 kJ/kg, corresponding to $La_{0.3}Sr_{0.7}Co_{0.9}Mn_{0.1}O_{3-d}$, showing sufficient redox stability during a 100 cycles test between 400°C and 1050°C.

Following the previous work and with the goal of increasing the reaction enthalpy whilst reducing the cost of the materials, Babiniec et al. carried out a work in 2015 concerning Ti-doped and Al-doped calcium manganite perovskites, taking advantage of the low cost of calcium for A-site and using cations for B-site difficult to reduce, which contributes to increase the reaction enthalpy [85]. Within the family of compounds studied, $CaTi_{0.2}Mn_{0.8}O_{3-d}$ and $CaAl_{0.2}Mn_{0.8}O_{3-d}$ presented the best performance, with a reaction enthalpy that reached 370-390 kJ/kg cycled at 1250°C.

Agrafiotis et al. presented in 2016 a thermogravimetric study of different materials for a cascade operation system. The work involved the study of $La_{0.3}Sr_{0.7}FeO_3$, which was submitted to two reduction and oxidation cycles between 1200°C and 800°C, finding a reaction enthalpy of 250 kJ/kg and complete reversibility [46].

Z. Zhang published in 2016 the results of a wide study regarding the effects of Ba and Sr A-doping into Fe, Co and Mn B-based perovskites. From the no-doped perovskites analyzed, $BaCoO_{3-d}$ presented the highest reaction enthalpy, reaching 292.1 kJ/kg at 900°C and 10^{-6} bar and complete re-oxidation at 600°C and 0.2 bar. They found different effects testing part substitution in A-site, B-site and both kinds of substitutions, proposing $BaCoO_3$, $BaFeO_3$ and $Ba_{0.5}Sr_{0.5}CoO_3$ as the best candidates for further research in the field of thermal energy storage [86].

2.2 TcES technology upscaling

2.2.1 Integration of high temperature thermochemical storage in CSP

Many efforts have been dedicated to research on redox thermochemical reactions during the last decades, focusing mainly in energy storage for the next generation of CSP plants. Nevertheless, their integration into the plant operation has been scarcely studied and it may represent a complex issue that shall be further developed.

The integration of a thermochemical energy storage based on $Ca(OH)_2/CaO$ in a conventional CSP using a Rankine cycle is one of the most studied systems, taking advantage on the fact that the gas phase driving the exothermic reaction and the fluid driving the Rankine turbine is water steam. M. Smitch and M. Linder showed that, compared to a molten salt storage system working between 290 and 565°C, in a realistic scenario the maximum amount of thermochemical energy storage using $Ca(OH)_2/CaO$ may only reach 42%, due to the lowest allowable reaction temperature, limited at 445°C [87]. The thermochemical storage efficiencies were studied including several steam extracting steps at the low-pressure turbine, not commercially available, reaching up to 73-87%. In order to improve this efficiency, another receiver with operation temperatures within the reaction equilibrium temperatures shall be designed. Considering the same thermochemical material, Pelay et al. studied different TcES integration possibilities into CSP plant driven by a Rankine cycle, presenting an energy and exergy analysis of all the proposals [88]. The best configuration in terms of efficiency is the so-called 'turbine integration concept', composed of a second turbine in an independent circuit for the storage (Fig. 22), achieving an overall efficiency of 0.392.

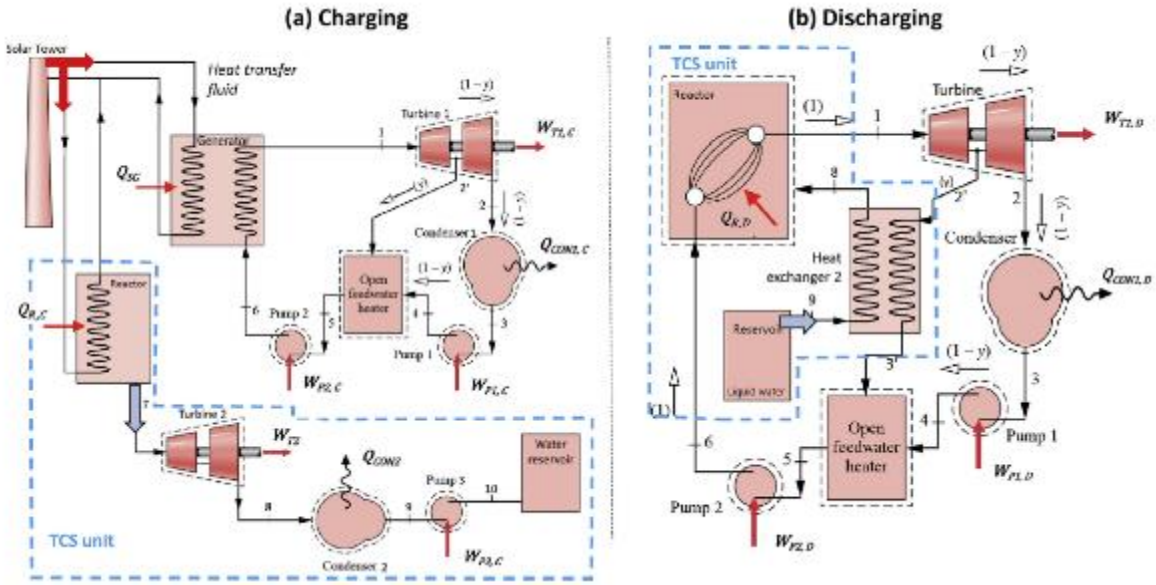

Figure 22. TcES integration into Rankine CSP during storage charge and discharge, 'turbine integration' concept [88]. Copyright 2019 Elsevier

The integration of a redox system using air as HTF has been scarcely studied. Sthröle et al. investigated the optimal arrange of a packed bed and fluidized bed reactor configurations based on Mn_2O_3/Mn_3O_4 redox couple in a CSP plant [89]. Series and parallel configurations are presented, dependent on the

maximum allowable temperature entering the solar field and the minimum useful temperature for the power block (Fig. 23a and 23b). Their findings showed how the material properties, such as particle size, reaction temperatures or specific heat, may have a significant influence on the optimal reactor technology. In the case of the study concerning the packed bed configuration, most of the material did not react during the charging step (86%), since the outlet temperature was limited by the maximum temperature allowable in the solar field and most of the energy was stored as sensible heat (91%). Nevertheless, in the case of the fluidized bed reactor, it is possible to connect the outlet of the reactor to the power block inlet, since the outlet temperature of the reactor was closer to the reaction temperatures. In that case, most of the stored energy was in chemical form (63%), although both the gravimetric and volumetric energy density remains lower than in the packed bed configuration due to the higher specific weight of the sensible heat.

a) b)

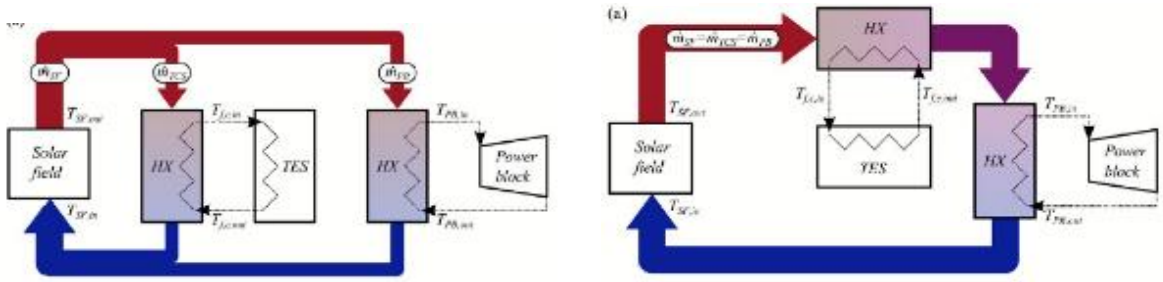

Figure 23. Different TQS configurations in a CSP: a) parallel configuration and b) series configuration. Copyright 2016 Royal Society of Chemistry

X. Peng studied the integration of a fixed-bed TQS reactor in a CSP considering the interaction between plant components and an operation subjected to dynamic input conditions [90]. They considered a s-CO_2 Bryton cycle and evaluated three thermochemical systems: carbonates, hydroxides and redox. In their study they found that Mn_2O_3/Mn_3O_4 provide the highest energy efficiency while $CaCo_3$/CaO has the highest LCOE potential reduction. In terms of cost, the thermochemical reactor represents the most expensive component, since they considered a shell and tube configuration with a very small tube diameter to increase the heat exchange area.

More recently, Buck et al. presented a techno-economic analysis of a 125 MW_e CSP with 12 h of storage using the particle receiver concept [91]. This approach consists on a moving particle stream which is transported from a cold tank to a hot tank after passing through a cavity receiver, where the endothermic reaction takes place, subsequently the particles are stored in the hot tank until they are discharged by means of introducing the heat transfer fluid, which once hot, feds the steam generator (Fig. 24). In their study they considered different metal oxides thermochemical materials, obtaining similar LCOE of 64.9 €/MWh, even though the effect of the material reaction kinetics was not taken into consideration.

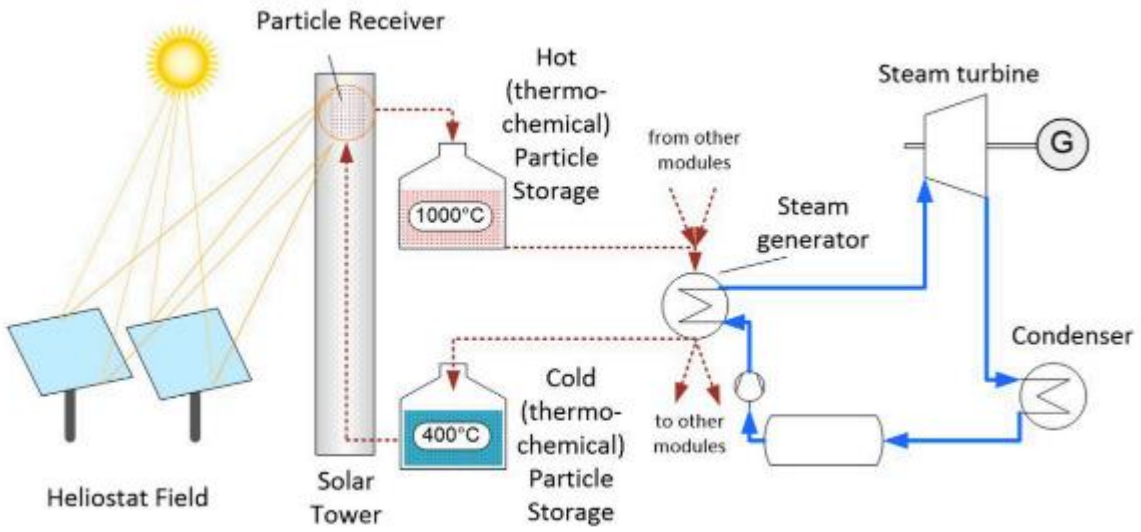

Figure 24. Scheme of a CSP based on particle moving thermochemical reactor. Copyright Frontiers in energy research. 2021

All these findings lead to interesting conclusions. First of all, it seems clear that a thermochemical energy storage cannot directly substitute a conventional thermal energy storage system in a CSP based on commercial molten salt system. Despite its higher energy storage density, the following issues must be considered: i) the isothermal nature of the thermochemical reactions may represent a disadvantage against the sensible heat stored within the common 290 - 565°C temperature range of the molten salt for conventional CSP plants and thus, the specific heat of the material may become an important material property; ii) there is a temperature drop between the charging temperature and the discharging one, meaning that the temperature outlet in the discharge mode may be 100-200°C lower than the charging temperature and this fact shall be appropriately tackled to avoid any efficiency loss in the power block and iii) in case of HTF different from the thermochemical gas product, the latter shall be appropriately extracted during the charging step and its energy content recovered for the overall system efficiency.

2.2.2 High temperature thermochemical reactors

One of the most critical components of the TcES system that must be properly design is the thermochemical reactor. According to the system operation, two existing possibilities have been principally considered: direct use of solar radiation, where the thermochemical material absorb the solar thermal energy in a receiver acting at the same time as a reactor and indirect use, where the thermochemical material is stored in a reactor and the heat exchange is carried out by means of an intermediate heat transfer fluid [92]. In terms of reactor technology, four different reactor design technologies have been found in the literature for thermochemical solid-gas research:

- **Fixed bed reactors**: Also known as packed bed reactors, they are the widest spread technology in the chemical industry to conduct chemical reactions. It consists on a random packaging of catalyst particles inside a pressurized tank (Fig. 25a). The gas flows throughout the particles interstices and the reaction takes place over the surface of the catalyst. They are easy to build and operate but their main drawbacks are the pressure drop inside the bed, that may induce

preferred gas channeling and the limited available surface of the reactants, which may compromise the thermal power output [36].

- **Fluidized bed reactors**: In this type of reactors, a fluid (gas or liquid) is passed through a solid granular material at a given enough velocity to suspend the particles, making it to behave as it was a fluid [93] (Fig. 25b). In order to avoid particles spouting and carry out an uniform mixing between the gas and the particles, it is indicated that the size of the particles should remain below 1 mm. This technology has been considered specially for volumetric directly irradiated tower receivers.

- **Moving bed reactors**: As can be inferred by its name, moving bed reactors implies that the reactives located inside the reactor are traveling from one tank (reactor) to another (refrigerator) whilst the reaction takes place [74] (Fig. 25c).

- **Rotary kiln reactors**: in this case, the reactives are placed inside the reactor, which rotates and forces the reactives to move, increasing the reactant available surface [61].

The main advantages and disadvantages of the most studied reactors for thermochemical energy storage are presented in Table 5 [94].

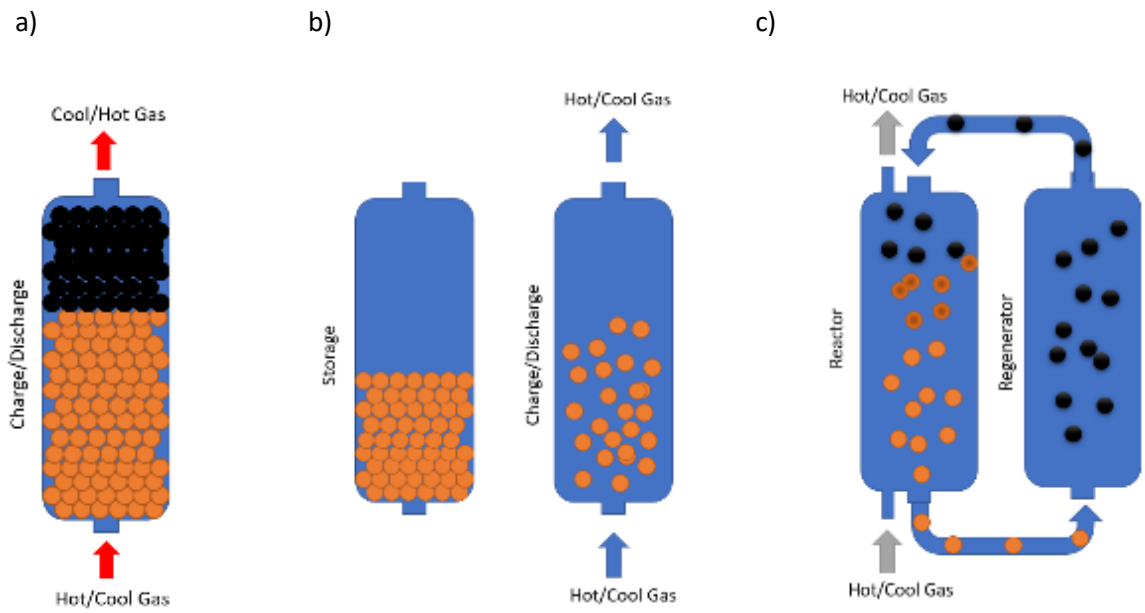

Figure 25. a) Packed bed reactor, b) Fluidized bed reactor and c) Moving bed reactor

Table 5. Main advantages and disadvantages of the most studied reactors for thermochemical energy storage

Reactor type	Advantages	Disadvantages
Packed bed	☺ Reduced maintenance ☺ Reduced complexity ☺ Particles >1-2 mm	☹ Pressure drop may require extra pumping cost ☹ Heat exchange capacity material/HTF becomes limiting factor ☹ Mass transfer limitations ☹ High particle mechanical strength is required
Moving/Fluidized bed	☺ Better contact between particles and HTF ☺ Low mechanical stress in the particles ☺ Enables continuous operation	☹ Particle agglomeration ☹ Bad reaction control ☹ Particles < 0.5mm
Rotary kiln	☺ High heat transfer coeficients ☺ Good thermal homogeneity	☹ Erosion of particles and reactor walls ☹ Difficulties to model the thermodynamic behavior

2.2.3 Material preparation for thermochemical reactors

The thermochemical material properties, namely, its shape, size and structural composition and stability may have a significant impact on the performance of a thermochemical reactor and thus, it may become one of the most important challenges of this technology. Nevertheless, most of the scientific studies aimed to assess the behaviour of metal oxides use several mg in the form of powder made of micro-sized particles at lab-scale [61] [95], whereas the technology upscaling on a thermochemical reactor for a real application might require kg or even tons of material. This material amount, in the shape of fine powder, may cause extremely high pressure drop and extra pumping power. In addition, fine powder is more prone to agglomerate, which may contribute to enhance channelling and hinder re-oxidation kinetics [96]. Therefore, studies on technology up-scaling consider different material preparation approaches (e. g. material pelletization or granulation, adding supports), looking for particles in the scale of mm or cm, with sufficient mechanical and chemical stability capable of withstand a great number of thermal cycles. Other interesting approaches involved experiments with extruded metal oxides composites [97] and with a support structure coated with the active redox material, through which the fluid can flow, often honeycomb structures, corderites or foams [98] [99] [100] [101] [102]. The coated structures presented better integrity over repetitive redox cycles, although the volumetric energy storage is limited by the capacity of active material loading and thus, the storage energy density decreases substantially.

In the case of an indirect thermochemical reactor, the particles suffer from several kinds of stresses, namely, chemical, mechanical, and thermal stresses. The volume changes due to both phase transition and thermal expansion and shrinkage, together with the pressure induced by the weight of the upper particle layers cause particle-wall or particle-particle friction, known as ratcheting. In

addition, particle movement in fluidized or moving bed reactors may enhance particle attrition. Furthermore, pore reduction caused by sintering may create overpressure during gas release in solid-gas thermochemical materials. As a result of this, particles may crack, or their surface may be eroded due to friction, leading to a decrease on the void fraction due to reallocation of particles, especially significant on the lower layers, which are subjected to higher weight loads. If this process is maintained, it would lead to a significant increase on the pressure drop or to a collapse of the container wall. Therefore, the metal oxide granules prepared for a real application, together with chemical stability, should demonstrate sufficient mechanical strength to ensure reliable stability during the lifetime of these TES systems, which may last several decades.

Particle strength can be increased by designing a proper synthesis route (e. g. sol-gel, spray-drying), applying a pretreatment (e. g. high temperature sintering) or by adding binders or support materials (e. g. Al_2O_3, TiO_2 or ZrO_2), provided that they do not react with the active material that may lead to thermochemical deactivation. Another possibility is strengthening the particle surface by encapsulation in a strong porous material or by rapid heating and cooling of particles, avoiding changes in the core of the granules that might damage the thermochemical material properties.

The addition of support materials in manganese-based oxides has been deeply studied both for CO_2 capture through chemical looping and for thermochemical energy storage. The attrition resistance of manganese-iron oxide with the addition of Al_2O_3, $MgAl_2O_4$, CeO_2, ZrO_2 and Y_2O_3–ZrO_2 was investigated by G. Azimi in a fluidized bed reactor. The materials were prepared by spray-drying and calcinated up to 1200°C during 4 h. The research showed that the crushing strength does not improve substantially with the addition of these supports, with the exception of ZrO_2, where a slight improvement was observed [103] [104]. Looking at chemical looping applications, M. Abian observed that the addition of TiO_2 may double the crushing strength of manganese-iron oxides, reporting values of 3-5 N compared to the 1-2 N of the undoped samples [105].

Taking into account previous result but focusing in thermal energy storage working conditions, N. C. Preisner studied the effect on the mechanical strength of manganese-iron oxide by adding 20 wt% of different supporting materials, namely of ZrO_2, CeO_2 and TiO_2 for a moving bed reactor. The material was prepared by VITO using a build-up granulation technique at 800°C during 10 h. Pure manganese-iron oxide particles showed a clear tendency to agglomerate and to break into fines when subjected to thermal cycling in air. Furthermore, the bed volume was increased by 17 % after 30 cycles in a packed bed reactor containing 21 g of material, meaning that some extent of coarsening happened. Nevertheless, both ZrO_2 and CeO_2 contribute to improve the attrition strength, with a slight particles agglomeration and no coarsening was observed. TiO_2 react to form another stable phase and thus, it can not be considered for thermochemical energy storage [76].

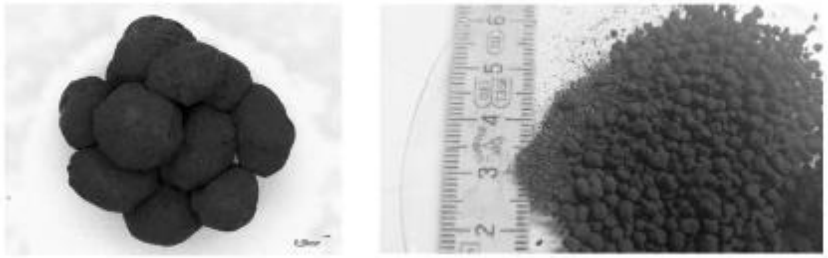

Figure 26. Manganese-iron oxide granules agglomeration and fines after 30 redox cycles [76]. Copyright 2020 Wiley

In addition, spherical shape particles are prone to suffer less agglomeration issues than particles of other shapes and thus, it has been the most targeted shape for the research concerning lab-scale thermochemical reactor testing. Spray drying is a commonly used method to make high-performance, fluidizable particles for chemical looping combustion applications, which have been shown to withstand long exposure for high temperature cycling. I. A. Al-Shankiti studied the effect on the redox behavior and sintering of spray-dried particles of manganese oxide with Al_2O_3, ZrO_2, and Fe_2O_3. All the materials showed very poor mass change during redox cycling, since they have undergone significant sintering during calcination at 1200°C. Nevertheless, ZrO_2 and Al_2O_3 samples demonstrated enough structural stability under the temperatures tested, although Al_2O_3 addition tends to form $MnAl_2O_4$ phase, which is stable at the tested temperatures [106].

M. Wokon studied the kinetic performance of manganese-iron oxide granules of 1-3 mm prepared by a build-up granulation technique without any support or binder in a thermobalance. The corresponding amounts of Mn_3O_4 and Fe_3O_4 powders were mixed in an Eirich mixer, based on the principle of intensive mixing by an inclined arranged rotating mixing pan, providing mixing effect in vertical and horizontal and application of a rotating micro-granulator mixing tool. A significant particles volume increase after 100 redox cycles was observed, which turned into lower density and more fragile particles, that might not withstand continuous redox cycling at a real scale and therefore, their mechanical stability shall be enhanced [107].

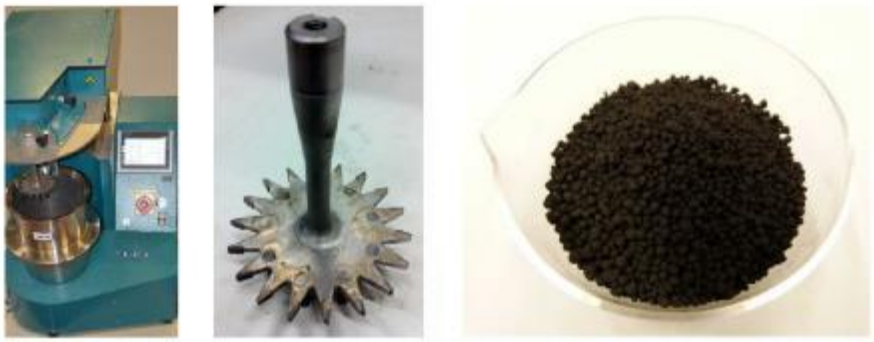

Figure 27. Manganese-iron oxide granules fabrication using an Einrich mixer [107]. Copyright Elsevier 2017

The granules of manganese-iron oxide synthetized by M. Hamidi were obtained by intensive mixing in an Einrich mixer, introducing maltodextrin solution organic binder at the end of the mixing process. Particle sizes of 0.5-1 mm were used to study the reduction reaction of manganese-iron oxide in a small packed bed reactor containing approximately 35 g of thermochemical material. No data regarding the mechanical properties and stability of the particles under cycling was provided [108].

Considering that adding a support material decreases the volumetric energy storage density and may deactivate the thermochemical material by undesired chemical reactions, another approach considers increasing the material strength through designing a proper granules production process. M. Gigantino modified a lab-scale granulation process, known as drop technique, to obtain CuO particles of 1-2 mm of diameter [70]. The process consisted in dissolving an organic polymer with the active material to create a paste that is dropped to a bath where the immiscibility leads to particle sphericity (Fig. 28). Different combinations of polymers, solvents and surfactants were studied, selecting the best combination which led to the highest particle strength and sphericity, even though no data regarding the influence on the reaction kinetics and storage density was reported. In order to

reduce the sintering effect, the CuO powder was mixed with Y_2O_3/ZrO_2 stabilized powder, turning into less agglomeration after 100 redox cycles, for amounts of Y_2O_3/ZrO_2 above 50 wt%.

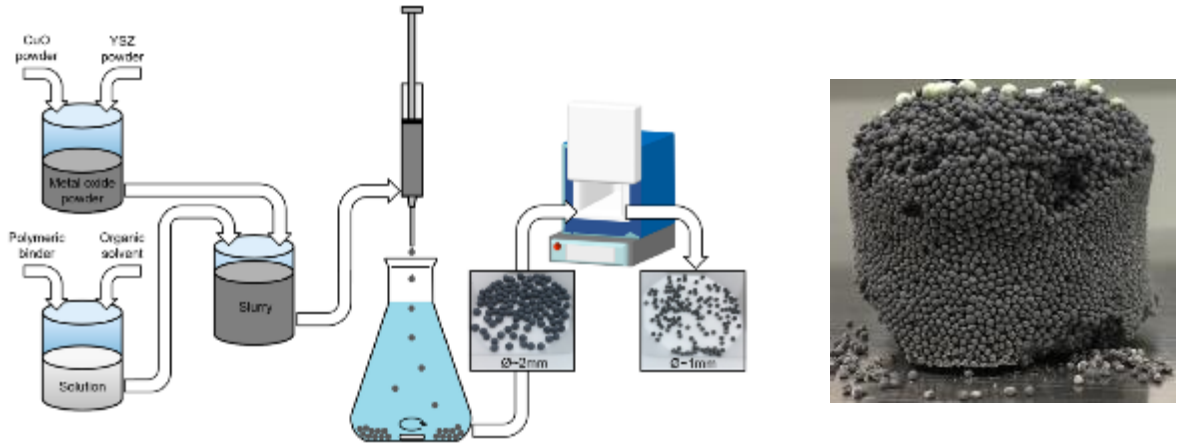

Figure 28. Drop technique used to produce granules of CuO and granules state after cycling in a packed bed lab-scale reactor [70]. Copyright 2020 Elsevier

2.3 Conclusions

Among the redox thermochemical materials reported in the scientific literature, the redox couple Co_3O_4/CoO and Mn_2O_3/Mn_3O_4 present attractive reaction temperatures which make them suitable for next generation of CSP plants. Firstly, the reaction onset temperatures are above the maximum temperature of the molten salt system, which can improve the overall efficiency of the plant. Secondly, the temperature required to complete the reactions are below 1000°C, which does not impose critical stresses to the components and materials of the plant, which can compromise the overall cost.

Comparing the redox performance of both materials, Co_3O_4 presents higher reaction enthalpy and kinetics. Nevertheless, cobalt is a material used for electrochemical batteries, with an increasing demand which is increasing significantly its price. Besides, cobalt is toxic and can cause health problems. On the other hand, Mn_2O_3 is an abundant material, non-toxic and therefore, it has been selected to study the hypothesis of the present thesis. In any case, this does not prevent the conclusions from being applied to other metal oxide.

Considering material upscaling and testing, the granulation technique and the packed bed reactor represent the simplest technology and even though, the research work on other type of synthesis routes and thermochemical reactors reports better performance, they has been selected as a first approach to test the material chemical and physical stability at a larger scale.

CHAPTER 3. Introduction to Mn_2O_3/Mn_3O_4 redox material characterization for CSP plants

3.1 Characterization techniques

The following techniques and laboratory instruments have been used throughout the whole research work:

The structural analysis of the material was carried out by X-ray powder diffraction (XRD) using a Bruker D8 Discover X-ray diffractometer equipped with a LYNXEYE detector using CuKα1 radiation (λ= 1.5406 Å) and θ–2θ geometry. The data were collected at room temperature between 10° and 110° in 2θ with a step size of 0.02° and a counting time of 67 s per step. The Diffract. EVA v4.2.1 software was used to determine the phase composition of the material.

The prepared samples were imaged by means of a Quanta 200 FEG scanning electron microscope (SEM) operated in high vacuum mode at 30 kV and with a back scattered electron detector (BSED). In addition, energy-dispersive X-ray spectroscopy (EDX) analysis was carried out to obtain chemical composition maps of the different observed sample zones. In order to get images at nanosized scale, transmission electron microscopy (TEM) measurement was realized by using an FEI Tecnai F20 transmission electron microscope operating at 200kV. For TEM measurement, samples were grained and dispersed in ethanol and sonicated. The resulting solution was transferred onto a holey carbon film fixed on a 3mm copper grid (200 mesh).

Thermogravimetric analysis (TGA) measurements were performed with the vacuum-tight thermo-microbalance TG209 F1 Libra (Netzsch). In cyclability studies, samples of 20 mg were placed into 85 µl open alumina crucibles (Netzsch) and subjected to charging and discharging cycles under air atmosphere. After the experiments, the sample and crucible were analyzed, where no evidence of reaction was observed.

Simultaneous thermal analysis (STA) measurements were performed with the simultaneous thermal analyzer STA 449 F3 Jupiter (Netzsch). In these studies, samples of approximately 20 mg were placed into 85µl open platinum/rhodium crucibles (Netzsch) and subjected to different reduction and oxidation steps under different gas atmospheres.

The dimensional changes of materials versus temperature were determined in a NETZSCH DIL 402 C/4/G dilatometer by placing pellets with the different compositions, with a length of 6.5 mm and a diameter of 4 mm, inside an alumina holder in air atmosphere with a heating rate of 20°C/min.

The bulk density and true density of the different granules were measured using a helium pycnometer AccuPyc II 1340. For the measurements a reference volume of 1 cm^3 was completely filled with the different composition granules, resulting in total mass varying from 0.1 to 0.3 g.

3.2 Introduction to the redox behavior of Mn_2O_3/Mn_3O_4

The whole content of this subclause was presented in the conference SolarPACES 2018 and published in AIP Conference proceedings on the 26th of July of 2019, with the tittle:' Efficiency Improvement of Mn_2O_3/Mn_3O_4 Redox Reaction by Means of Different Operation Strategies, https://doi.org/10.1063/1.5117750.

3.2.1 Introduction

The redox pair Mn_2O_3/Mn_3O_4 has been studied for TcES since many years, reporting some controversy regarding its chemical stability. To evaluate the material behavior, usually a small quantity of powder was subjected to a number of heating up steps followed by cooling down steps aiming to get 100% of re-oxidized material after several cycles, considering this fact as the main indication of its ability to maintain the energy exchange over a quite number of operation cycles. The source of powder, morphology or particle size have been pointed out as the main reasons to explain the different behaviors of the studied materials [31] [51], showing most of them a particular reaction rate decrease in each cycle and proposing the incorporation of other metals to improve its behavior, finding out iron addition as one of the best approaches, although an increase in the reaction temperatures was noticed [33] [27]. Nevertheless, the effect of the different parameters used in the cycling programs such as temperature or heating/cooling rate cannot be neglected and this has not been fully investigated.

In order to evaluate the feasibility to use Mn_2O_3 as a TcES material for CSP, a better understanding of the reduction and oxidation reactions has been addressed in this work. In this sense, new operation strategies involving different charge and discharge modes of the TcES material has been studied and the conclusions are presented in this paper. In addition, this work presents the noticeable effect that different strategies may have on the overall efficiency of the system, which may be critical to push this technology one step forward.

3.2.2 Material preparation

The sample was synthetized by modified Pechini process, following the process described by Sunde et al. [109] and Jana et al. [110] in order to obtain a homogenous sample in which concern the crystallinity, particle size, porosity and surface area. For that purpose, aqueous solution of $Mn(NO_3)_2{\cdot}6H_2O$ was mixed with citric acid (CA) in a solution of a molar ratio 1:5. Afterwards, to promote the polymerization into a resin, ethylene glycol (EG) is used in a molar ratio EG:CA of 2:3.

The synthesis process was carried out according the following steps:

- The required amount of citric acid is dissolved in 50 ml of distilled water, stirred at 70°C during 30min.
- Manganese nitrate was added to the solution and stirred during 3h.

- The temperature is increased to 90°C and the required amount of ethylene glycol is added dropwise, the mixture kept stirring until it turns into a gel.

- The gel was dried at 200°C during 2 h and then calcinated in two steps at 450°C for 4h and 800°C for 15 h in static air, being grounded to fine powder after each calcination step by means of an agate mortar.

3.2.3 Results and discussion

3.2.3.1 Structure and Morphology

The X-Ray powder diffraction pattern of the sample is plotted in Fig. 29. The analysis of the synthetized sample shows the presence of a unique phase corresponds to Mn_2O_3 cubic structure, characteristic of bixbyite crystal phase.

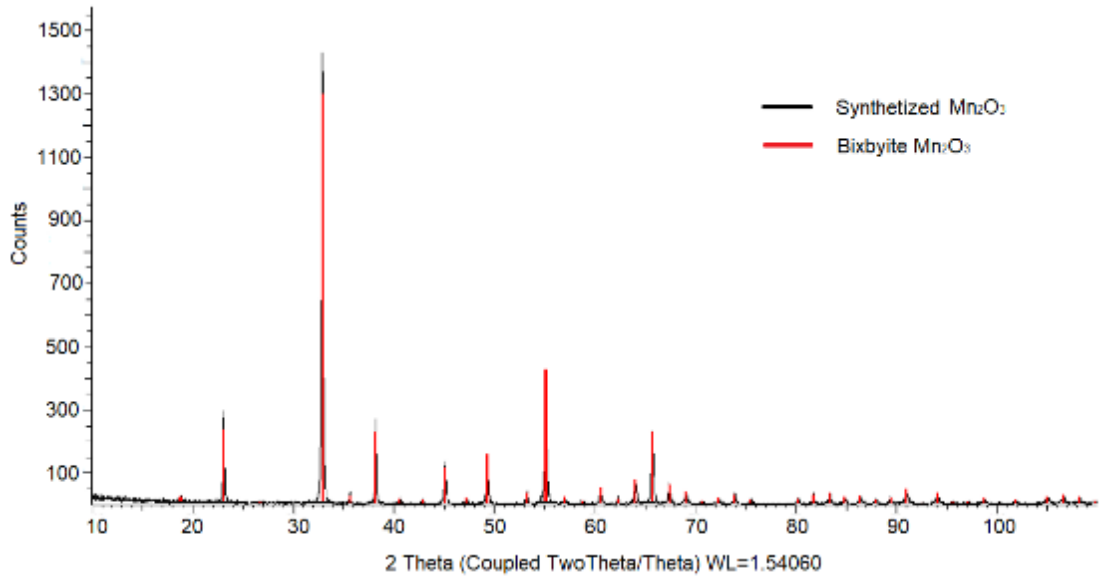

Figure 29. X-Ray powder diffractogram of the Mn_2O_3 sample.

Figure 30 depicts the SEM micrographs of the sample before being subjected to any cycling measurement. The sample are formed by micro clusters of irregular particles of an average size of 142 nm. Table 6 summarizes the obtained characteristics of Mn_2O_3 sample.

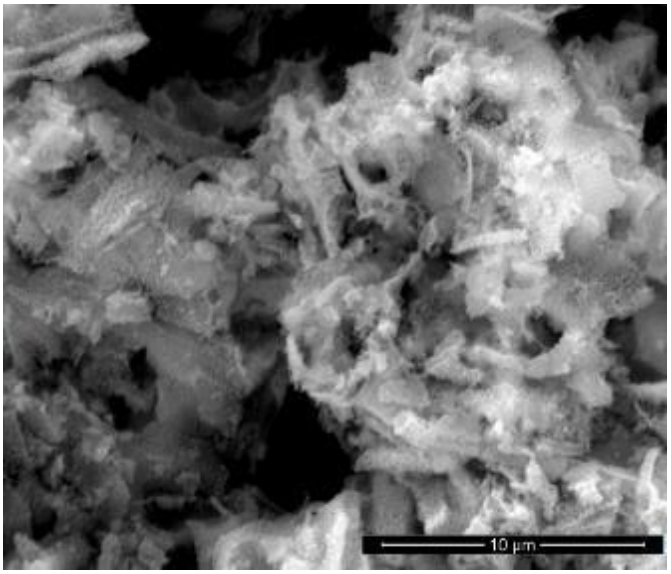

Figure 30. SEM image of the synthesized sample of Mn_2O_3.

Table 6. Material source, calcination temperature, crystal phase, crystallite size (d) and lattice parameter (α) of the synthesized sample

Material	Source	Calcination temperature	Crystal phase	d (nm)	α (Å)
Mn_2O_3	Shyntetized	800°C	Cubic Mn_2O_3	142	9.4146

3.2.3.2 Effects of the Temperature Testing Program in the Reduction and Oxidation Reactions

In order to find out the governor parameters affecting the reduction reaction several samples consisting on 20 mg of the synthetized Mn_2O_3 powder were tested. Three samples were subjected to the following heating up steps with a heating rate of 10°C/min: sample nº1 from 900°C to 950°C followed by a dwelling step at 950°C, then sample nº2 from 900°C to 1000°C and finally sample nº3 from 900°C to 1050°C (Fig. 31a). In all programs, when the temperature of 930°C is crossed, the material mass starts to decrease abruptly, identifying the starting point of the reaction, finishing when the temperature peak programmed is reached, even in the case of the program subjected to a dwelling step. This fact, unlike the published studies, caused incomplete reduction reactions, except in the case of a continuous heating up to 1050°C, reaching values beyond the stoichiometry mass loss, which might be attributable to the presence of some impurities (basically CO_2), resulted from the exposure of the sample to the atmosphere, which are lost in the first cycle as will be confirmed later. In addition, new samples were subjected to different heating rates up to 1050°C using 5, 10 and 20°C/min, obtaining no effect of the heating rate in the reduction extent, whereas the reduction rates were slightly higher in the range of 930°C - 950°C for lower heating up rates, while the opposite was observed in the range of 950°C -1050°C.

In the case of the oxidation reaction, most of the reported studies subjected the samples to a cooling down step just after a previous heating up step [46] [111] [31] [51], so the material is oxidized from higher temperatures to lower temperatures, within the range between 770°C and 650°C. Nevertheless, in real conditions, the discharge of the storage rarely goes immediately after the charge

process and in such a case, it might be more efficient to decrease the temperature of the material to avoid thermal losses during storage periods. If the temperature of the material decreases below the reaction temperature range, a heating up process is needed to activate the oxidation reaction and recover the stored heat. Taking this into account, the present study has evaluated the behavior of the oxidation reaction both during a heating up step and a cooling down step, finding considerable differences between the two procedures. For the oxidation reaction under a heating up, several samples have been subjected to a heating up to 1050°C, followed by a cooling down to 500°C, under Argon atmosphere, so after a complete reduction of the sample was achieved, the oxidation reaction was not activated during the cooling down, due to the absence of oxygen and therefore, Mn_3O_4 was obtained, which was further subjected to two different heating up programs from 500°C to 900°C with heating rates of 2°C/min and 10°C/min under air flow of 250 mL/min. The results show a noticeable improvement from those obtained using a cooling down step, obtaining the best reaction kinetics in the sample subjected to heating step from 500°C at 2°C/min (Fig. 31b), finding out that the oxidation reaction is properly conducted at temperatures below 600°C, lower than the ones reported in the published works.

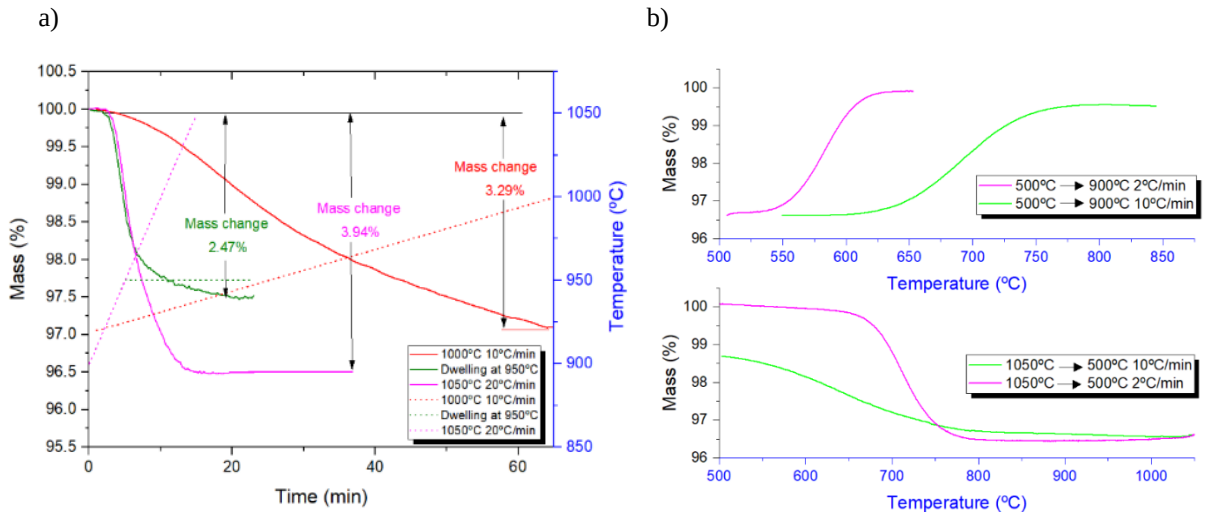

Figure 31. a) TG results of different reduction programs; and b) TG results of different oxidation programs.

3.2.3.3 Characterization of the Cycling Stability

Since the first work of Wong et al. [6], there has been some controversy regarding the cyclability of pure Mn_2O_3 and some of its mixed compounds for thermal energy storage, as it was mentioned in the introduction of this paper. To evaluate the cycling stability, in all the previous works, the material was subjected to different heating and cooling ramp rates aimed to maintain the full re-oxidization of the material over the cycles, considering this fact as the main indication of its ability to maintain the energy exchange over a quite number of operation cycles. Differences in the source of powder, morphology or particle size have been pointed out as the main reason to explain the different behaviors found in those studies [31]. Nevertheless, most of the studies show a particular reaction rate decrease in each cycle, increasing the re-oxidation time needed to complete the reverse reaction, which might turn into uncomplete material conversion in the long-term use.

To select the best cycling conditions for the Mn_2O_3 materials, the sample was subjected first to 10 cycles between 1050°C-550°C with 10°C/min and secondly, considering the results of the previous subclause, the sample was subjected to 10 cycles between 1000°C and 750°C, with a heating rate of

20°C/min for the reduction reaction and 2°C/min for the oxidation reaction, for practical reasons air was used both for heating and cooling, so the oxidation reaction started during the cooling down step. Cycle to cycle evolution as well as SEM images after cycling are depicted on Fig. 32 and Fig. 33. In the first case, the mass recovered after the 10th cycle was 94.69%, corresponding to a mass change of 1.35% and a storage capacity reduction of 64%, whereas in the second case the re-oxidized mass was 97.63%, corresponding to a mass change of 2.48%, which corresponds to a storage capacity decrease of only 9%. This effect has a correlation with the different grade of obtained sintering, although the grain size is similar in both cases, the degree of densification observed is lower in the sample subjected to cycles between 1000°C and 750°C, as one might expect.

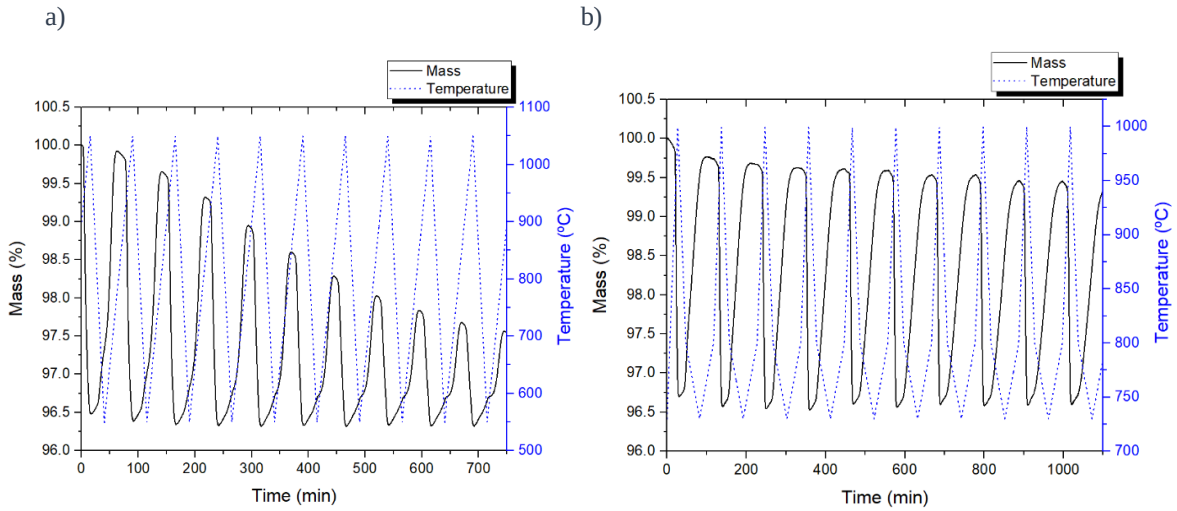

Figure 32. a) Weight change curves during 10 TGA cycles between 1050°C-550°C with 10°C/min, and b) between 1000°C-730°C with 20°C/min and 2°C/min

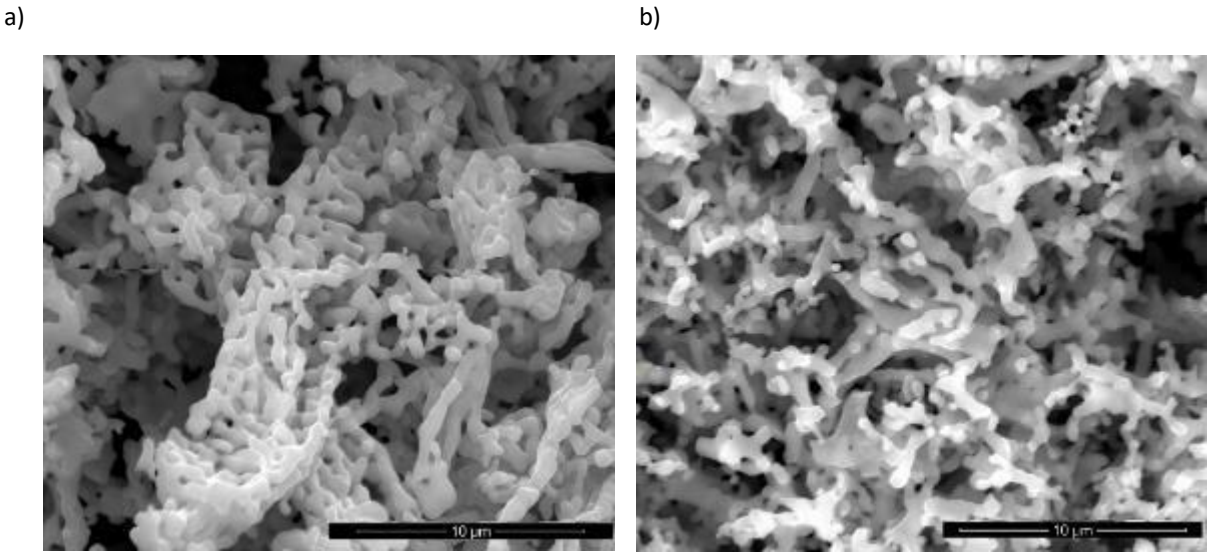

Figure 33. SEM images of the samples after 10 cycles between 1050°C-550°C with 10°C/min (a) and between 1000°C-730°C with 20°C/min and 2°C/min (b)

3.2 4 Conclusions

Reduction and oxidation reactions of Mn_2O_3 were investigated under different conditions aimed to improve the cycling behavior of the TES. The reduction reaction extent under air atmosphere showed a relationship with the percentage of the temperature range completed, in this particular case from 930°C to 1050°C, independently of the time exposed within this temperature range, providing that the higher the heating rate the faster the reaction, whereas the reduction rate is slightly affected. In the case of the oxidation reaction, the temperature range of the reaction is larger, from 550°C to 850°C, and in this case, unlike for the reduction reaction, its extent is time dependent. The oxidation reaction was analyzed for the first time both under a heating up and cooling down step, finding out that the reaction rate is clearly improved if it is displaced to temperatures below 600°C and discharged using a heating up step, which in addition, may increase the efficiency of the TES avoiding thermal losses if the system temperature is decreased to room temperature during long storage periods. In regard to the cycling ability of Mn_2O_3, this material presents a clear trend to sinter, which may be improved by lowering the maximum temperature of the cycles and increasing the heating rate at high temperatures. Considering the results of this work, the heat storage capacity loss after 10 cycles has been almost reduced to the half, concluding that the performance of the Mn_2O_3/Mn_3O_4 may be clearly improved by means of selecting properly the operating conditions.

CHAPTER 4. First approach to improve the Mn_2O_3/Mn_3O_4 behavior through metal doping

4.1 Introduction

Most research studies aimed to improve the reversibility and chemical stability of Mn_2O_3 consisted in forming a mixed structure using another metal, mainly iron [30]. In regard to Mn_2O_3, several researchers reported an impressive kinetics improvement mixing Mn_2O_3 with different quantities of iron [30] [33] [35] [112]. A. J. Carrillo attributed this improvement to Fe^{2+} cations, which tends to substitute Mn^{2+} into the cubic structure and its smaller ionic radius causes an enlargement of Mn-O bonds. This enlargement makes the bonds weaker, which facilitates oxygen intake and release [113]. Mn_2O_3 co-doping with Fe and Cu was another approach studied trying to reduce the temperature gap between reduction and oxidation reactions, getting complete reversibility over 30 redox cycles [71]. Nevertheless, in none of these studies the material sintering caused by the high temperatures was completely avoided and the long-term stability is then compromised. Overall, the behavior improvement found belongs entirely to the acceleration of the oxidation reaction kinetics caused by the lattice distortion. On the other hand, there are few studies considering doping Mn_2O_3 with other type of metals, so we consider an opportunity to explore other type of mixed oxides. Therefore, taking into account the phase diagrams of several promising mixed oxides, which show phase transitions around 900°C, namely Co-Mn-O [114], Ni-Mn-O [115], Cr-Mn-O [116] and Fe-Mn-O [117], the following work examines the effects on the chemical structure, kinetics and stability of doping Mn_2O_3 with different quantities of Co, Ni, Cr and Fe.

4.2 Material preparation

The samples were prepared following the so-called modified Pechini synthesis route. This process starts with a homogeneous aqueous solution containing the desired cation precursors in stoichiometric ratio and citric acid, which by evaporation and reactions is converted to a rigid cross-linked polymer hindering segregation of the cations. Then, the resulting polymer is calcined to obtain a homogeneous oxide powder. Sunde et al. developed a comprehensive review of the methodology [109].

The synthesis process was carried out following the steps:

- The required amount of citric acid is dissolved in 50 ml of distilled water, stirring at 70°C during 30 min.
- Stoichiometric amounts of metal nitrates were added to the solution and stirred during 3 h, namely $Co(NO_3)_2{\cdot}6H_2O$ (99,9% Sigma-Aldrich), $Ni(NO_3)_2{\cdot}6H_2O$ (99,9% Sigma-Aldrich), $Cr(NO_3)_2{\cdot}9H_2O$ (99,9% Sigma-Aldrich) and $Fe(NO_3)_2{\cdot}9H_2O$ (99,9% Sigma-Aldrich).
- The temperature is increased to 90°C and the required amount of ethylene glycol is added to the solution while stirring until it turns into a gel.
- The gel is dried at 200°C during 2 h and then calcinated at 450°C for 4 h.

The different samples synthesized are showed in the following table.

Table 7. Material identification, dopant, doping composition and crystal phase of the synthesized samples.

Material	Material	Dopant (at. %)*	Crystal phase
Mn_2O_3	-	0	Cubic Mn_2O_3
	Co	1.8	Cubic Mn_2O_3
		5	Cubic Mn_2O_3 and $CoMn_2O_4$
		10	Cubic Mn_2O_3 and $CoMn_2O_4$
		15	Cubic Mn_2O_3 and $CoMn_2O_4$
	Ni	1.8	Cubic Mn_2O_3
		5	Cubic Mn_2O_3
		10	Cubic Mn_2O_3 and $NiMn_2O_4$
		15	Cubic Mn_2O_3 and $NiMn_2O_4$
	Cr	1.8	Cubic Mn_2O_3
		5	Cubic Mn_2O_3
		10	Cubic Mn_2O_3
		15	Cubic Mn_2O_3 and $CrMn_2O_4$
	Fe	1.8	Cubic Mn_2O_3
		5	Cubic Mn_2O_3
		10	Cubic Mn_2O_3
		15	Cubic Mn_2O_3

*Dopant (at. %) = n(Dopant)/[n(Dopant)+n(Mn)]*100

4.3 Influence of the amount of dopant on the chemical structure

The different samples included in Table 7 were subjected to XRD measurements after synthesis (Fig. 34). For the highest dopant quantities used (>5-10 %), the Co, Ni and Cr-doped samples showed the formation of a secondary stable phase which is not desirable ($CoMn_2O_4$, $NiMn_2O_4$ and $CrMn_2O_4$), since it contributes to decrease the energy storage density of the material. Low quantities did not show any trace of this undesirable phase and thus, they are selected for further analysis in the TGA. In the case of iron-manganese oxide, as expected, all the samples presented a stable mixed structure, which according to previous studies should be completely reversible.

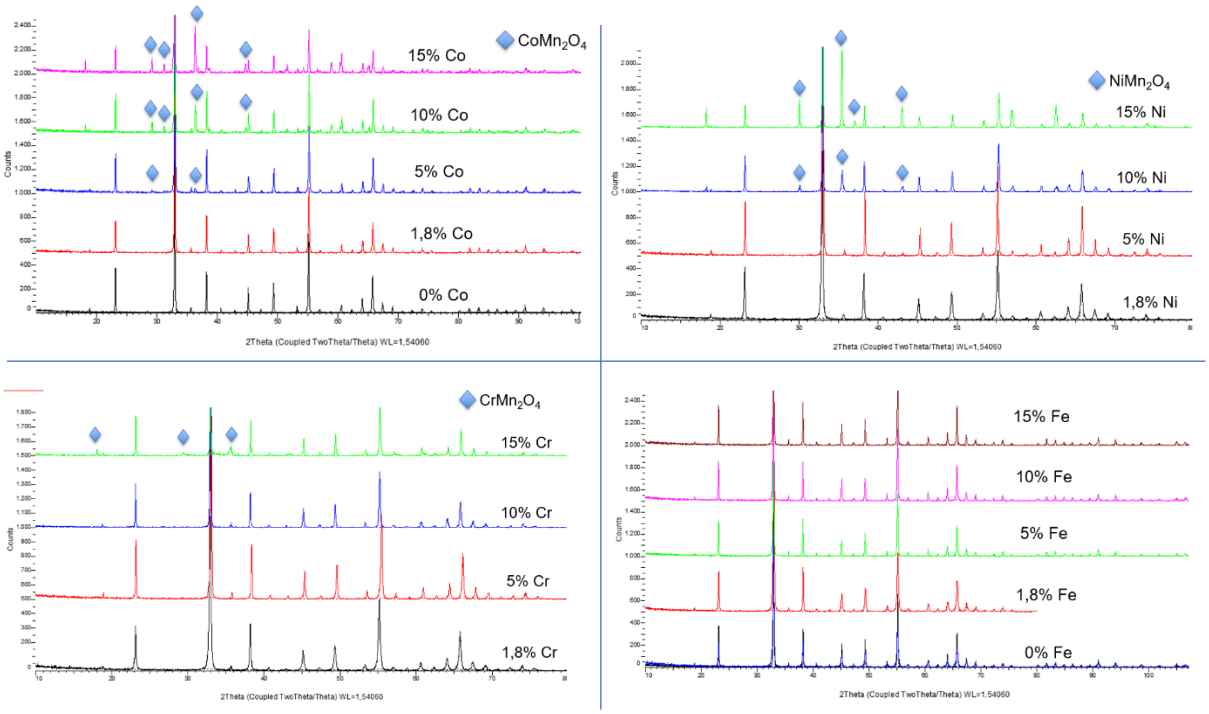

Figure 34. X-Ray powder diffractogram of the Mn_2O_3 Co/Ni/Cr/Fe doped samples

4.3 Effect of the dopant on the chemical kinetics and stability

Further kinetic analysis consisted in subjecting the samples doped with 1,8% metal, with no traces of secondary phases, to 1 redox cycle in the TGA. In order to reduce the material, it is subjected to a heating step up to 950°C with 10°C/min, followed by a cooling step to 700°C with 10°C/min and an isothermal step to completely oxidize the sample in an air flow of 100 mL/min (Fig. 35). The reduction reaction seems to not differ significantly from pure Mn_2O_3, independently of the metal dopant used. Nevertheless, the oxidation kinetics present greater differences. The first remarkable difference is the oxidation onset temperature, while Fe and Cr displace the temperature upwards, Ni and specially Co, displace the onset temperature downwards. Regarding oxidation kinetics, Fe and Cr contributes to accelerate the reaction, while Co decreases it substantially. Doping with Ni maintains similar oxidation kinetics than pure Mn_2O_3 sample. Furthermore, the mass loss of the Ni-doped sample is significantly lower compared to the rest of the samples, attributable to the undesirable formation of $NiMn_2O_4$ during the redox cycle, which must be confirmed by XRD measurements. As a preliminary conclusion, doping Mn_2O_3 with low quantities of Cr can be a promising candidate.

In order to study the chemical stability of the material, the samples were subjected to 3 redox cycles, consisting in a heating step up to 1000°C with 10°C/min, followed by a cooling step to 500°C with 10°C/min with an air flow of 100 mL/min. The results were overlapped and are shown in Fig. 36. It should be noted that the oxidation onset temperature of the Cr, Ni and Co doped samples is displaced to lower temperatures compared to the Fe-doped sample and in these cases, the oxidation is not completed when the temperature reached the lowest program value (500°C). Consequently, the oxidation reaction kinetics suffered a slowdown coinciding with the change from cooling to heating, before starting to oxidize again when the required temperature is reached. In any case, all the samples showed an oxidation kinetics deterioration each cycle, which is inferred from the evolution of the

slope of the curve. Even though Cr, Ni and Fe-doped samples get complete reoxidation over the whole cycling program, it is delayed each cycle, meaning that the reversibility of the material is suffering a continuous deterioration.

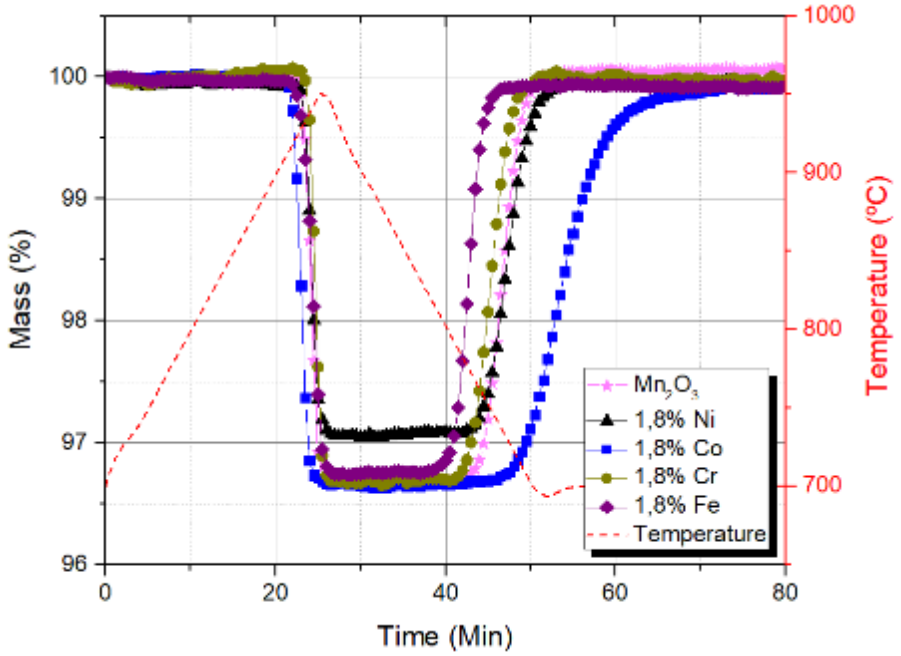

Figure 35. Mass loss/gain in the TGA of Mn_2O_3 Co/Ni/Cr/Fe doped samples during 1 redox cycle between 950°C and 700°C at 10°C/min with 100 mL/min of air

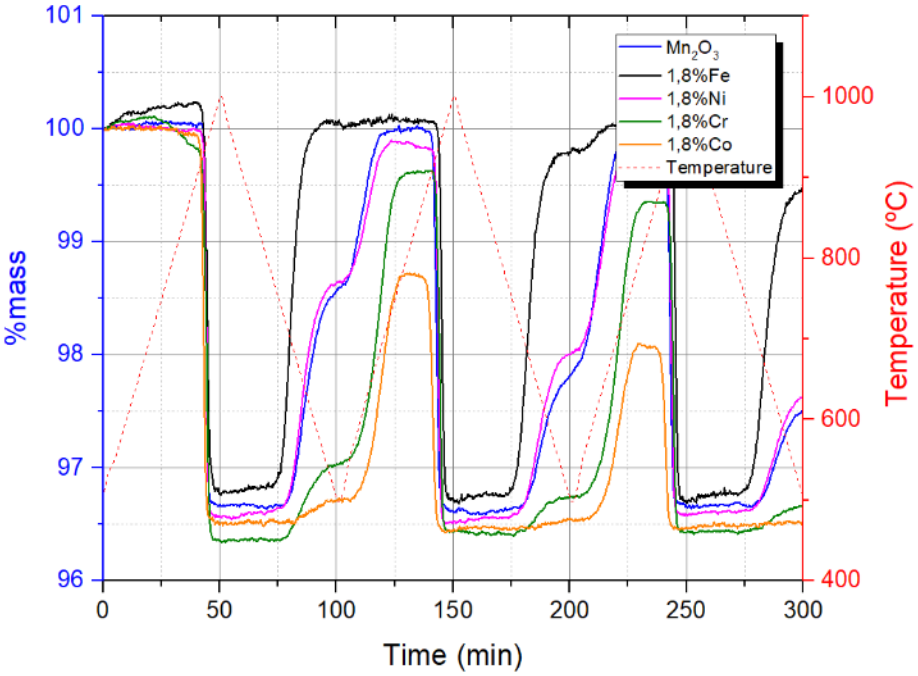

Figure 36. Mass loss/gain in the TGA of Mn_2O_3 Co/Ni/Cr/Fe doped samples during 3 redox cycles between 1000°C and 500°C at 10°C/min

4.3 Effect of the dopant on the particle morphology

The morphology evolution of the pure Mn_2O_3 sample and the doped samples particles after redox cycling was observed by SEM, in order to study if there is any effect on the particle sintering. SEM images of the samples after synthesis and after 30 redox cycles are shown in Fig. 37 for comparison. As can be inferred from the pictures, all the samples present a high degree of particle coarsening after being subjected to redox cycling, from the nanoscale to the microscale size. The sintering degree is slightly different in each sample but as a general conclusion, one can conclude that none of the dopants contribute to hinder the negative sintering consequences.

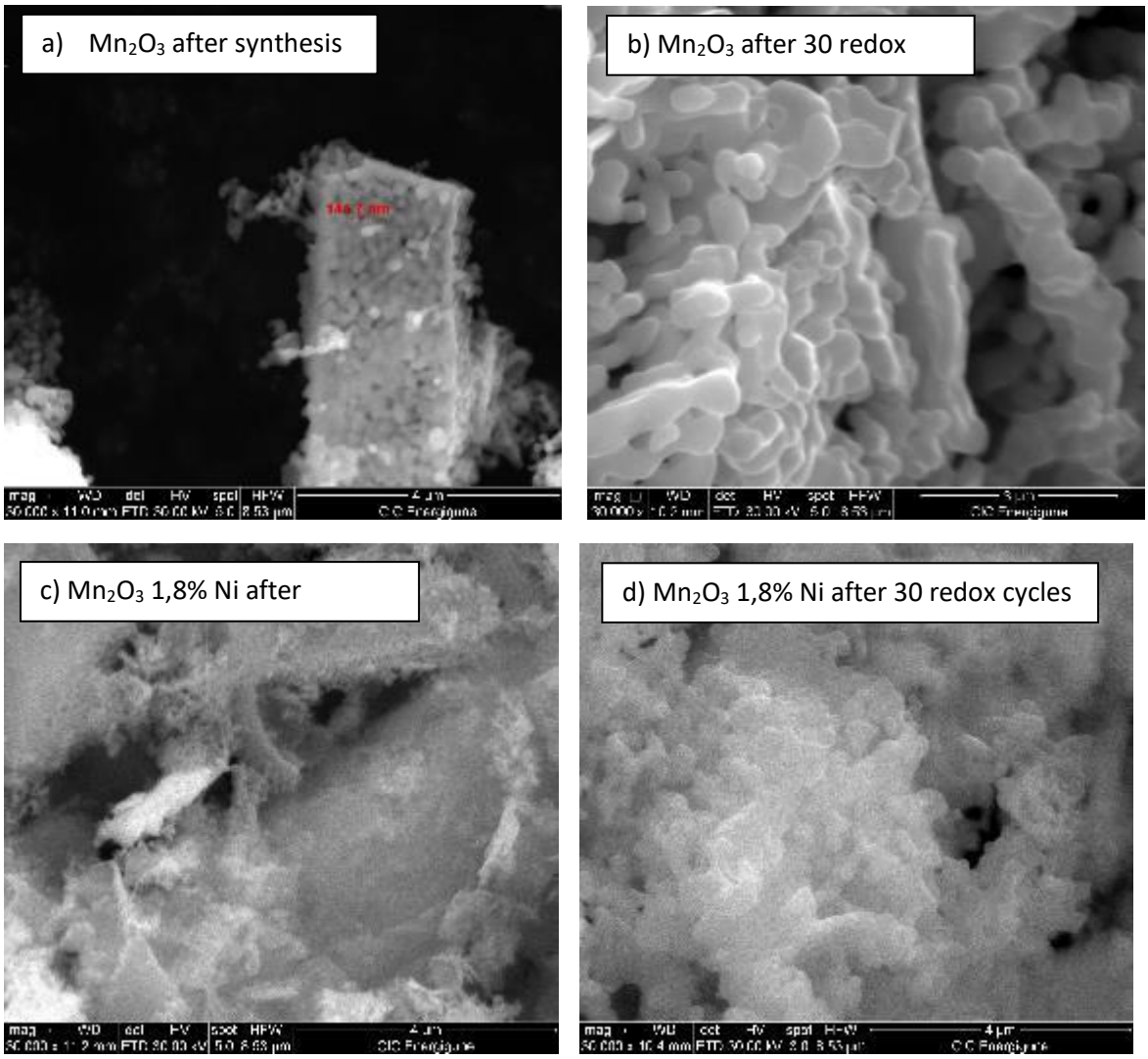

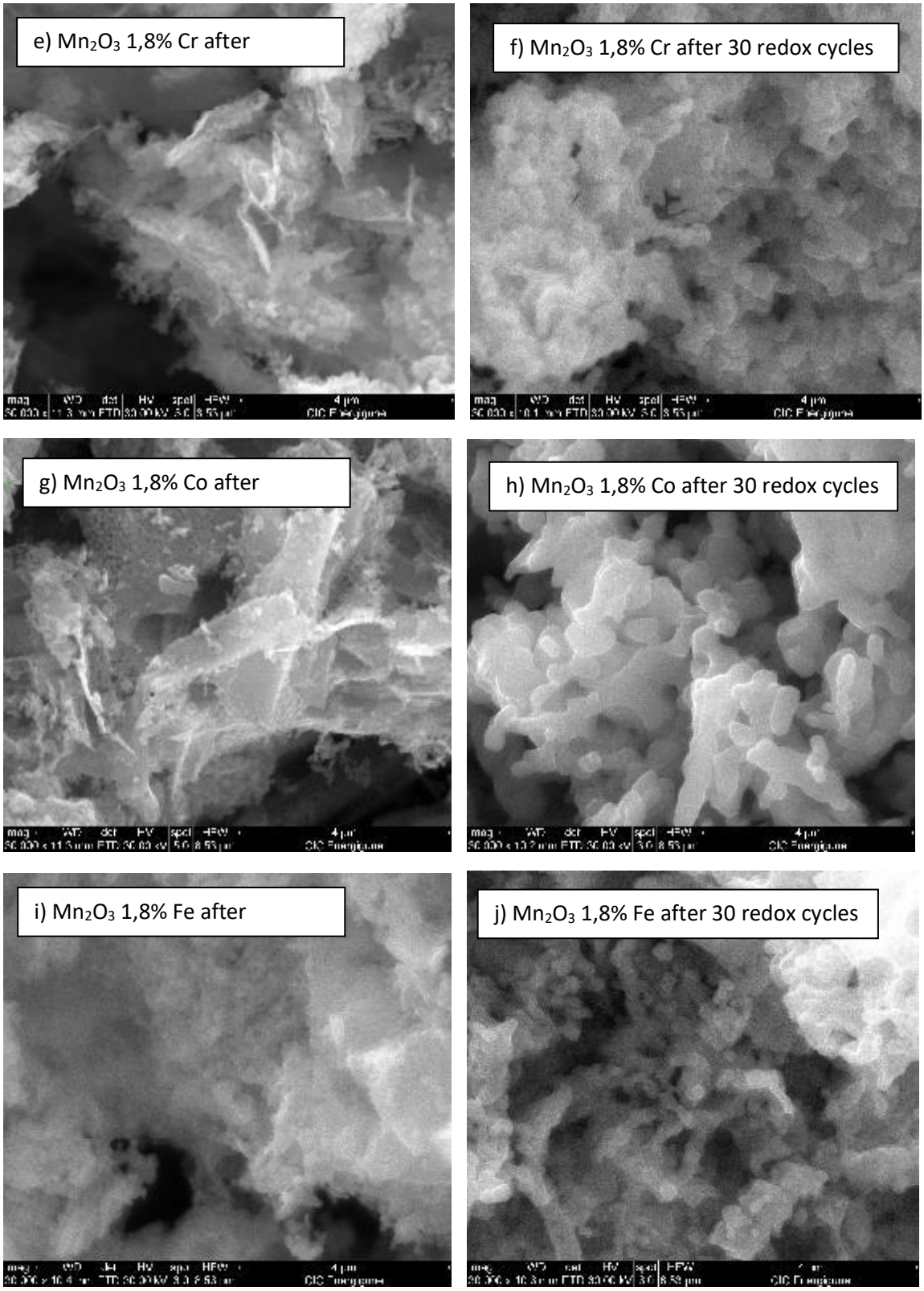

Figure 37. SEM images of the doped samples: a) Mn_2O_3 after synthesis, b) Mn_2O_3 after 30 redox cycles, c) Mn_2O_3 1,8% Ni after synthesis, d) Mn_2O_3 1,8% Ni after 30 redox cycles, e) Mn_2O_3 1,8% Cr after synthesis, f) Mn_2O_3 1,8% Cr after 30 redox cycles, g) Mn_2O_3 1,8% Co after synthesis, h) Mn_2O_3 1,8% Co after 30 redox cycles, i) Mn_2O_3 1,8% Fe after synthesis, j) Mn_2O_3 1,8% Fe after 30 redox cycles.

4.4 Conclusions

In order to find new routes to improve the thermochemical behavior of Mn_2O_3, a comprehensive study has been carried out comprising doping Mn_2O_3 with different quantities of Co, Ni, Cr and Fe. Subsequently, the effects on the chemical composition, kinetics, stability and particle morphology after redox cycling has been studied by XRD, TGA and SEM, respectively. The positive effect on the oxidation kinetics of iron addition has been confirmed, while none of the other studied metals provide any significant improvement. Moreover, the chemical deterioration caused by sintering was not avoided in none of the studied samples. Consequently, a new approach must be studied to obtain a Mn_2O_3-based thermochemical candidate for future CSP plants.

CHAPTER 5. Discovering a new path to improve the cyclability of Mn_2O_3/Mn_3O_4

The whole content of this subclause was presented in the conference SolarPACES 2019 and published in AIP Conference proceedings on the 11th of December of 2020, with the tittle:' Thermochemical Heat Storage for CSP Using Mn_2O_3/Mn_3O_4 : Effects of Si Doping in Cyclability Improvement', https://doi.org/10.1063/5.0028737.

5.1 Introduction

One common limitation among most of the redox materials studied is their tendency to sinter when high operating temperatures are applied. This sintering phenomenon increase the grain size and densification degree of the powder, and has been identified as the main reason of the kinetics decrease of the oxidation reaction. This fact might turn into a complete deactivation of the heat storage capacity of the TcES system in a long-term use. Within the first studies reported by B. Wong, the reversibility of Mn_2O_3 decreased down to 6% after the first redox cycle due to sintering [5]. Carrillo et al. observed the influence of the initial particle size in the reversibility of Mn_2O_3, getting complete reoxidation of the samples with the largest particles in a 30 redox cycles test. Nevertheless, all the samples presented some decrease in the oxidation reaction kinetics, which was attributed to pore shrinkage [6]. Most of the proposals to overcome this material weakness are based on mixing this material with 10-20% of Fe. Iron addition forms a mixed structure of the type $Mn_{2-x}Fe_xO_3$, with much faster reaction kinetics than pure Mn_2O_3. This improvement was attributed to an enlargement and weakening of the Mn-O bonds, due to lattice distortion caused by the smaller Fe^{2+} radius [7]. In addition, it has been shown in a 30 cycles test, that Fe doping contributes to increase the cycle stability. Nevertheless, the sintering effects are not completely avoided, causing a slight decay of the oxidation rate from one cycle to the next one [8].

Sintering is a well-known process in the manufacturing of metallurgical products to produce density-controlled materials, ideally with a fine grain size structure. In order to control the sintering effects, doping of ceramic materials have been proven to be an effective technique to modify the grain growth and particle shrinkage [9]. When the amount of doping agent is higher than the bulk solubility limit, the excess cations segregate at the grain boundaries, contributing to change the sintering conditions. Although most of the research has been focused in obtaining high dense ceramic materials, it has been found that the interaction between the dopant and the grain boundary mobility is dependent on three main factors: the charge, the size and the amount of dopant [10]. Therefore, selecting the appropriate doping agent it should be possible to decrease the sintering effects in Mn_2O_3, in order to obtain a redox stable material for a long-term application.

In this first approach, the Mn_2O_3 redox material has been doped with 1 wt% of Si, in order to overcome the sintering effects. The behavior of the material under 10 redox cycles has been measured and compared with pure Mn_2O_3 and a mixed oxide composed of Mn_2O_3 and 15 % Fe.

5.2 Material preparation

Mn_2O_3 and Mn_2O_3 15% Fe samples were synthetized by the modified Pechini process, following the process described by Sunde et al. [11] and Jana et al. [12] in order to obtain a homogenous sample in which concern the crystallinity, particle size, porosity and surface area. For that purpose, an aqueous solution of $Mn(NO_3)_2{\cdot}6H_2O$ was mixed with citric acid (CA) in a solution at a

molar ratio 1:5. Afterwards, to promote the polymerization into a resin, ethylene glycol (EG) is used in a molar ratio EG:CA of 2:3. After the drying process, the samples were calcined at 800°C for 15 h with 2°C/min.

The Mn_2O_3 1% Si doped sample was synthesized by mixing Mn_2O_3 with as received amorphous SiO_2 nanoparticles of 12 nm. An amorphous structure as well as nanosized particles have been proven to provide higher reactivity than crystalline or microsized particles, due to their higher surface to volume ratio, facilitating the introduction of Si into Mn_2O_3 structure [13]. Aiming to obtain the desired Mn_2O_3 Si doped structure, a dry synthesis method was used. The corresponding amount of synthesized Mn_2O_3 and as-received SiO_2 nanoparticles were placed in an aluminium bottle and then physically mixed during 15 min by means of milling equipment, obtaining a homogeneous mixture as can be observed in Fig. 38.

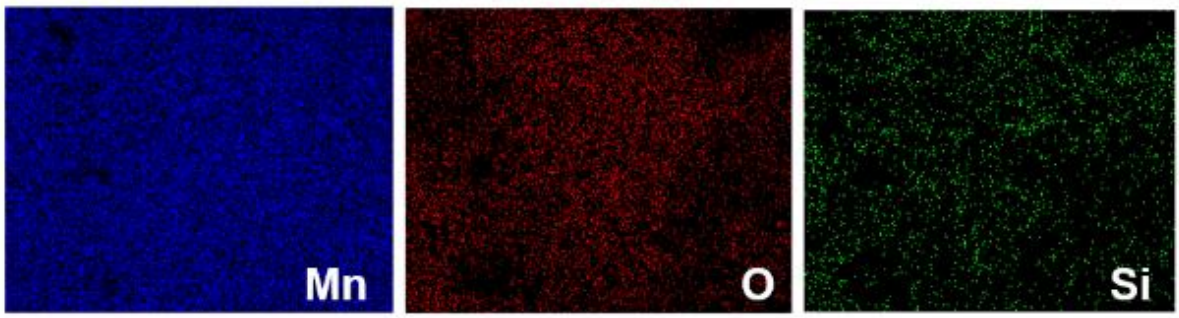

Figure 38. EDX mapping of Mn_2O_3 Si-doped sample

5.3 Results and discussion

5.3.1 Structure and Morphology

The X-Ray powder diffraction patterns of the samples are plotted in Fig. 39a. The analysis of the synthetized samples shows the presence of a unique phase corresponds to the Mn_2O_3 cubic structure. The addition of Fe did not change the XRD pattern of the sample. As Mn^{3+} and Fe^{3+} present the same ionic radius in six-fold coordination (0.645 Å) [14], Fe^{3+} replaces Mn^{3+} without any significant change in the lattice parameters. In the case of Si doped sample, it presents a slight shift of the peaks to higher 2θ angles compared to the Mn_2O_3 and $Mn_{1.7}Fe_{0.3}O_3$ samples (Fig. 39b). This shift is related to the slight reduction in the lattice parameters, attributed to the smaller ionic radius of Si^{4+} (0.4 Å) in six-fold coordination [14], confirming that Si has entered into the Mn_2O_3 structure.

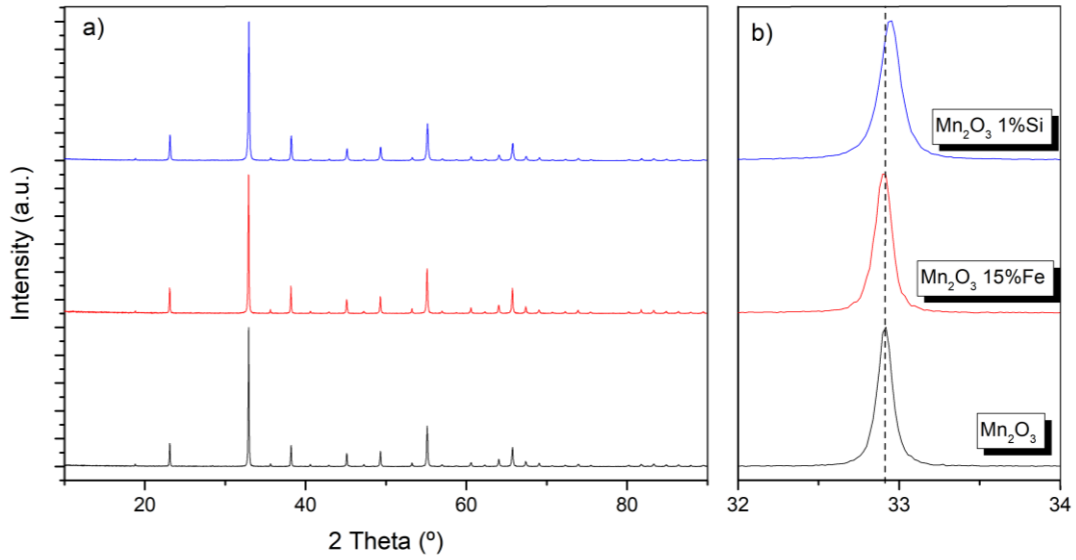

Figure 39. a) X-Ray powder diffractogram of the synthesized samples, b) XRD patterns magnification in the 32-34º region

Figure 40 depicts the SEM micrographs of the samples before being subjected to any temperature program. The samples are formed by micro clusters of irregular particles of a homogeneous average size. Table 8 summarizes the obtained characteristics of the synthesized samples.

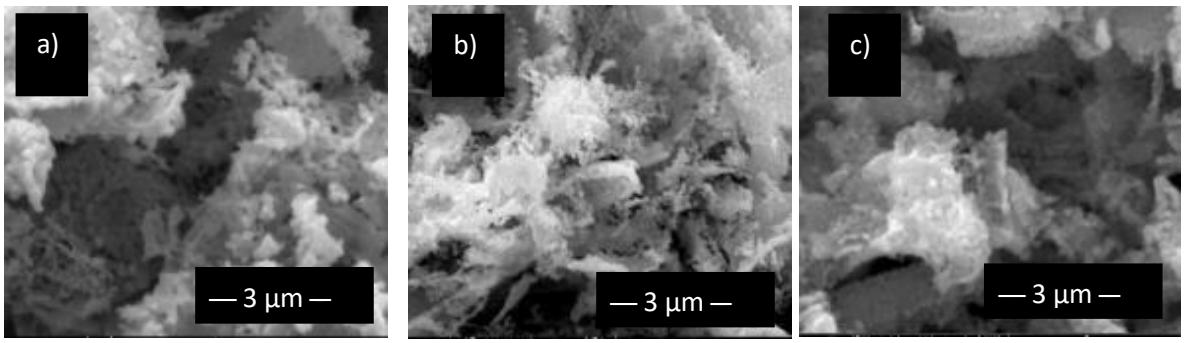

Figure 40. SEM images of the synthesized samples: a) Mn_2O_3, b) $Mn_{1.7}Fe_{0.3}O_3$ and c) $Mn_{1.98}Si_{0.02}O_3$

Table 8. Material composition, crystallite size (d), crystal phase and lattice parameter (α) of the synthesized samples

Sample	Dopants		$d_{average}$ (nm)	Crystal phase	α (Å)
	[at. %]*	Agent			
Mn_2O_3	0	-	150	Cubic Mn_2O_3	9.43
$Mn_{1.7}Fe_{0.3}O_3$	15	Fe	100	Cubic Mn_2O_3	9.43
$Mn_{1.98}Si_{0.02}O_3$	1	Si	150	Cubic Mn_2O_3	9.41

* at. % = n(M)/n(Mn) + n(M)

5.3.2 Cycling Stability

To evaluate the capacity of the materials to withstand numerous charge and discharge cycles, the samples were subjected to 10 redox cycles in a thermobalance between 1050°C and 700°C, with a heating/cooling rate of 20°C/min followed by a dwelling at 700°C for 35 min, in order to get a complete re-oxidation of the samples. The measurements were made using a TGA software from Netzsch which includes a mathematical procedure (TGA-BeFlat®) allowing for the removal from TGA measurement of the contribution of buoyancy effects and friction force from the vertically moving gas. The reduction and oxidation reactions onset temperatures of pure Mn_2O_3 sample and $Mn_{1.98}Si_{0.02}O_3$ sample were approximately in the same range, 940°C and 750°C, respectively. However, the $Mn_{1.7}Fe_{0.3}O_3$ sample presented a substantial increase in its reaction onset temperatures, up to 975°C for the reduction reaction and up to 919°C for the oxidation reaction. The three samples studied presented stable weight changes during the ten cycles (Fig. 41). The weight gain/loss observed for Mn_2O_3 and $Mn_{1.7}Fe_{0.3}O_3$ was 3.38%, corresponding to the stoichiometry value, while for $Mn_{1.98}Si_{0.02}O_3$ it was slightly lower (3.33%), attributable to the inactive nature of Si-O bonds compare to Fe-O bonds [7]. Nevertheless, there is a noticeable difference on the oxidation reaction kinetics behavior from one sample to another.

As stated in the introduction, the oxidation rate decay during cycling, represents the main drawback of these materials. In order to observe the oxidation rate evolution during the redox cycles, the mass loss in each cycle was overlapped and plotted in Fig. 42a, 42b and 42c. As can be observed in Fig. 42a, pure Mn_2O_3 sample suffered a noticeable slowdown in the oxidation reaction kinetics from the first cycle to the end of the temperature program. This reaction rate decrease is attributable to the particle morphological evolution, from the initial nano-sized particles to a coral-like array of interconnected micro-sized particles, which can be observed in the SEM image of Fig. 42d. In the case of $Mn_{1.7}Fe_{0.3}O_3$ sample, the oxidation rate was much faster than Mn_2O_3, which was in agreement with previous research [7], although a slight decrease was observed in the oxidation kinetics from one cycle to the following one (Fig. 42b). As it has been observed by other authors, iron addition does not prevent the sintering effects, shown in the SEM images of Fig. 42e, being similar to that of the pure Mn_2O_3 sample. Nevertheless, the reaction kinetics improvement mostly counteracted the negative sintering effects and the cycling behavior of the sample remains almost stable during the 10 cycles test. In the case of Si doped sample, the oxidation reaction rate during major part of the oxidation reaction was even faster than in $Mn_{1.7}Fe_{0.3}O_3$, although the oxidation rate decay at the end of the cycle was more pronounced (Fig. 42c). However, a slight oxidation reaction rate increase was observed at the beginning of the oxidation reaction from one cycle to the next one. This fact might be attributable to some unreacted SiO_2 nanoparticles that might continue reacting with Mn_2O_3 during the redox cycles, improving the redox behavior. As can be observed in the SEM image of Fig. 42f, the-particles remain at a nano-sized scale, confirming the effective sintering inhibition caused by Si doping and thus, considered as the main reason of the cyclability improvement found.

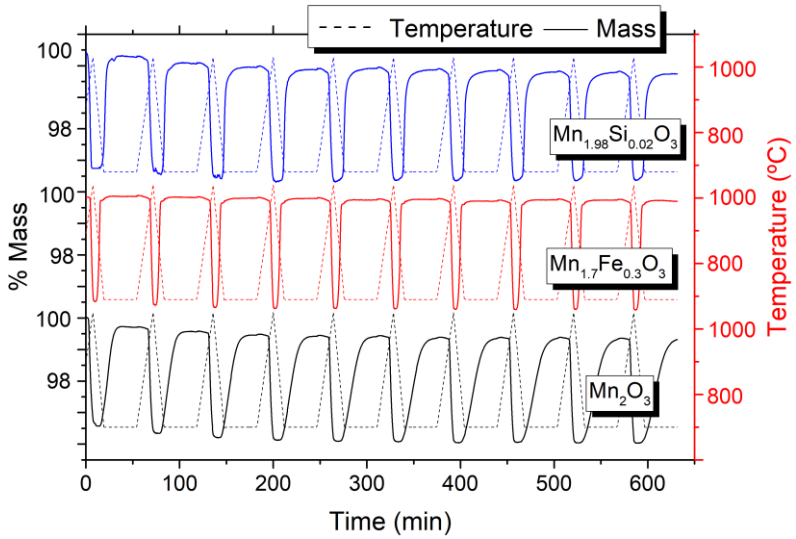

Figure 41. Weight variation versus time plots of 10 redox cycles between 1050˚C and 700˚C for the three studied materials

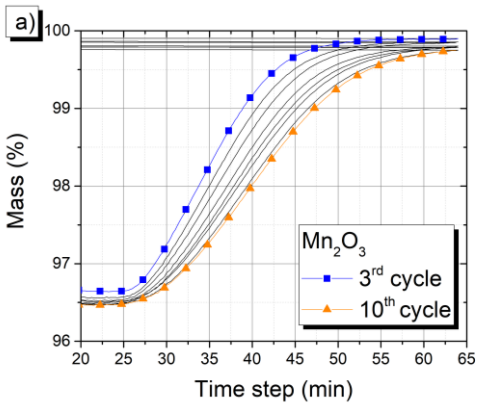

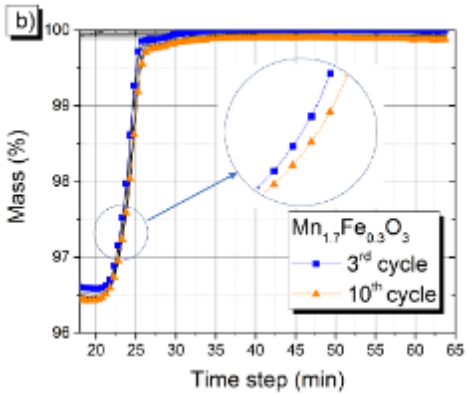

d)

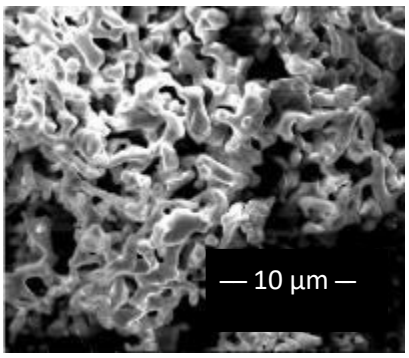

e)

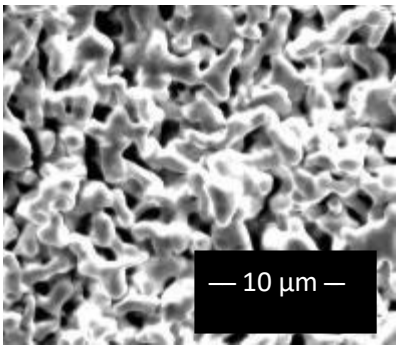

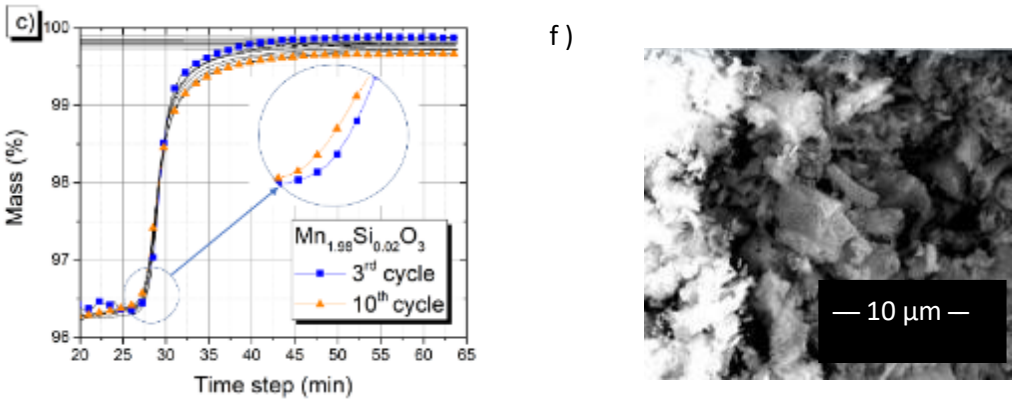

Figure 42. Weight gain versus time plot during oxidation, from the third cycle to the tenth cycle: a) Mn_2O_3, b) $Mn_{1.7}Fe_{0.3}O_3$ and c) $Mn_{1.98}Si_{0.02}O_3$. SEM micrographs of the samples after the 10 redox cycles: d) Mn_2O_3, e) $Mn_{1.7}Fe_{0.3}O_3$ and f) $Mn_{1.98}Si_{0.02}O_3$

5.4 Conclusions

Next generation of concentrated solar power plants requires a cheap and reliable thermal energy storage system. Thermochemical energy storage systems based on the Mn_2O_3/Mn_3O_4 redox couple are easy to manage and cheap, thus becoming a promising candidate. Nevertheless, it suffers pronounce reversibility decay during cycling, which was observed during a 10 redox cycles test in this work and it must be solved before reaching a commercial stage. Fe addition has been previously presented as a promising approach to improve the behavior of the material. The re-oxidation kinetics of a 15% Fe doped sample during 10 redox cycles have been measured, showing a considerably improvement in the redox behavior, although the sintering effects were not completely avoided, causing a slight decrease of the oxidation rate from one cycle to another. Taking into account that sintering has been identified as the main reason of cyclability loss, doping Mn_2O_3 with Si was successfully investigated to determine its role as a sintering inhibitor. The comparison between the thermogravimetric and SEM data of pure Mn_2O_3, $Mn_{1.7}Fe_{0.3}O_3$ and Mn_2O_3 doped with 1% Si, confirms the positive effect of Si doping, which unlike pure and Fe doped samples, led to a negligible grain growth after a 10 redox cycles test. Thus, the Si doped sample presents the fastest oxidation kinetics of the three tested samples, although the slight decay observed at the end of the oxidation reaction indicates an incomplete doping of the material, revealing a need to improve the synthesis route. This approach may be applicable not only to Mn_2O_3 but also, to other promising redox materials which make these materials a very interesting candidates for future concentrated solar power plants.

CHAPTER 6. Further insights into the chemical stability of the novel Mn_2O_3-based material

The whole content of this subclause was published in Solar Energy Journal on the 1st of July of 2020, with the tittle: 'Improving the redox performance of Mn_2O_3/Mn_3O_4 pair by Si doping to be used as thermochemical energy storage for concentrated solar power plants', https://doi.org/10.1016/j.solener.2020.04.073.

6.1 Introduction

In view of the previous results, we have investigated the effects of doping Mn_2O_3 with different quantities of Si, in order to determine the optimal doping content that provides the best material behavior for CSP application. At the same time, in order to find out an appropriate synthesis method, two different synthesis routes have been evaluated. In the first part of the work, the Si doping effects on the redox cycle have been investigated, and compared to pure Mn_2O_3, as the starting point for the proposed application. Subsequently, the material behavior in a 40th redox cycling test has been studied in a thermo-balance, in order to evaluate the capacity of the doped material to withstand the cycling conditions required for TCES in CSP. Finally, an explanation of the positive effect and improvement found in the reaction kinetics and cycling performance is proposed, opening new possibilities using the cation doping approach to improve the behavior not only of Mn_2O_3 material but other redox materials as well.

6.2 Material preparation

Manganese oxide powder was synthesized by the modified Pechini process, following the process described by Sunde et al. [109] and Jana et al. [110]. For that purpose, a solution of $Mn(NO_3)_2{\cdot}1H_2O$ (98%, Sigma Aldrich) was mixed with citric acid in a solution at a molar ratio 1:5. Afterwards, to promote the polymerization into a resin, ethylene glycol (99.8%, Sigma Aldrich) was used in a molar ratio EG:CA of 2:3. After the drying process, the sample was calcined at 700°C for 6 h with a heating/cooling rate of 2°C/min in air atmosphere, aimed to get complete crystallization of the sample with small particle size. Manganese Si-doped samples were synthesized using two different methods. The first one was a dry method and the second one was a wet method. For the dry method, as received amorphous SiO_2 nanoparticles of 12nm (99.8 %, Sigma Aldrich) were used as doping agent. An amorphous structure as well as nanosized particles have been proven to provide higher reactivity than crystalline or microsized particles, due to their higher surface to volume ratio [118]. Aiming to obtain an homogeneous mixture, the corresponding amounts of synthesized Mn_2O_3 and as-received SiO_2 nanoparticles were placed in an aluminium bottle and then physically mixed for 15 min by means of milling equipment (Prep 8000-series High-Energy Shaker Mill). For the wet method, the doped samples were synthesized by sol-gel method, which allow the preparation of porous materials with a homogeneous distribution of components on the atomic scale [119]. Manganese precursor was prepared by dissolving $Mn(NO_3)_2{\cdot}1H_2O$ (98%, Sigma Aldrich) and citric acid (99+%, Alfa Aesar) at a molar ratio 1:5 in a solution of 20 ml of deionized water and ethanol (96%. Scharlau). After stirring the solution for 10 min, the corresponding amount of $Si(C_8H_{20}O_4)$ (98%, Sigma Aldrich) was added and kept stirring for 2h. Then, the solution was dried and the obtained powder was calcined using the same

temperature program used for the dry method samples, aiming to avoid differences on the materials redox behaviour derived from the use of different calcination programs.

6.3 Results and discussion

6.3.1 Influence of the synthesis method on the composition of the samples

The composition and crystalline properties of the samples are summarized in Table 9. The expected composition of the samples was unclear, based in the aforementioned uncertainty related to the available Mn-Si-O phase diagrams. For the low concentrations of Si used in this work (< 0.14 %mol), preliminary studies in air reported the presence of a single phase below 877°C corresponding to a $Mn_{2-x}Si_xO_3$ solid solution [120]. According to a recent study by Rydén et al., bixbyite (Mn_2O_3) and braunite (Mn_7SiO_{12}) are expected below 800°C at p_{O2} of 0.05 atm [121]. Even though it has been reported the redox reversibility of all these phases, the presence of different phases is not desirable, as they present different reaction parameters.

The X-Ray powder diffraction (XRD) patterns of the synthetized samples are plotted in Fig. 43. The analysis of the diffractograms shows different compositions depending on the synthesis method used. The samples using SiO_2 nanoparticles (1Mc and 5Mc) show the presence of a single phase, corresponding to Mn_2O_3 cubic structure, with a slight shift of the peaks to higher 2θ angles compared to the un-doped sample. This shift is related to the slight reduction in the lattice parameters, as indicated in Table 9, attributed to the smaller ionic radius of Si^{+4} (0.4 Å) in six-fold coordination, compared to the Mn^{+3} ionic radius (0.645 Å) [122]. On the other hand, the samples synthesized using the sol-gel method (1Ms and 5Ms) presented two phases corresponding to Mn_2O_3 cubic structure and small amount of Mn_3O_4 tetragonal structure (Fig. 43). The Mn_2O_3 cubic structure presented lower lattice parameters than the samples obtained by the dry method, confirming the incorporation of more Si^{+4} atoms within its structure. It is worth to mention that the amorphous nature of the SiO_2 nanoparticles might hinder their detection by XRD technique. However, SEM and TEM techniques were used to study the morphology of the obtained materials and to detect the un-reacted nanoparticles. As an example, Fig. 44 shows the SEM and TEM micrographs obtained for 5Mc and 5Ms materials. On the first hand, it can be clearly seen in TEM micrographs (Fig. 44a and b) the presence of un-reacted nanoparticles in the case of 5Mc material, while no evidence of their presence was observed in the case of 5Ms sample. This result agrees with the XRD analysis that in the case of the sol-gel method a better diffusion of Si^{+4} within Mn_2O_3 structure was obtained compared to the case of ceramic method, where partial diffusion of Si^{+4} was observed.

SEM micrographs of the samples before being subjected to any cycling measurement show the formation of micro clusters of irregular particles. The particle size distribution presented in Fig. 44e and Fig. 44f has been calculated from SEM images using an image processing program (ImageJ). The average particle size of the samples presents different values depending on the synthesis route used, being in the range of 123-128 nm for the dry method and 78-81 nm for the wet method.

Table 9. Material identification, doping composition, composition of the synthesized samples, average particle size (d) and lattice parameter (a).

Sample	Material	Doping method	Si (at. %) *	Composition	$d_{average}$ (nm)	Mn_2O_3 a (Å)
0M	Mn_2O_3	-	0	Mn_2O_3	128	9.430(1)
1Mc	Mn_2O_3-1%Si	Ceramic	1	Mn_2O_3/ Amorphous SiO_2	123	9.416(1)
1Ms	Mn_2O_3-1%Si	Sol-gel	1	Mn_2O_3/Mn_3O_4	78	9.410(1)
5Mc	Mn_2O_3-5%Si	Ceramic	5	Mn_2O_3/ Amorphous SiO_2	123	9.415(1)
5Ms	Mn_2O_3-5%Si	Sol-gel	5	Mn_2O_3/Mn_3O_4	81	9.408(1)

*Si (at. %) = n(Si)/[n(Si)+n(Mn)]*100

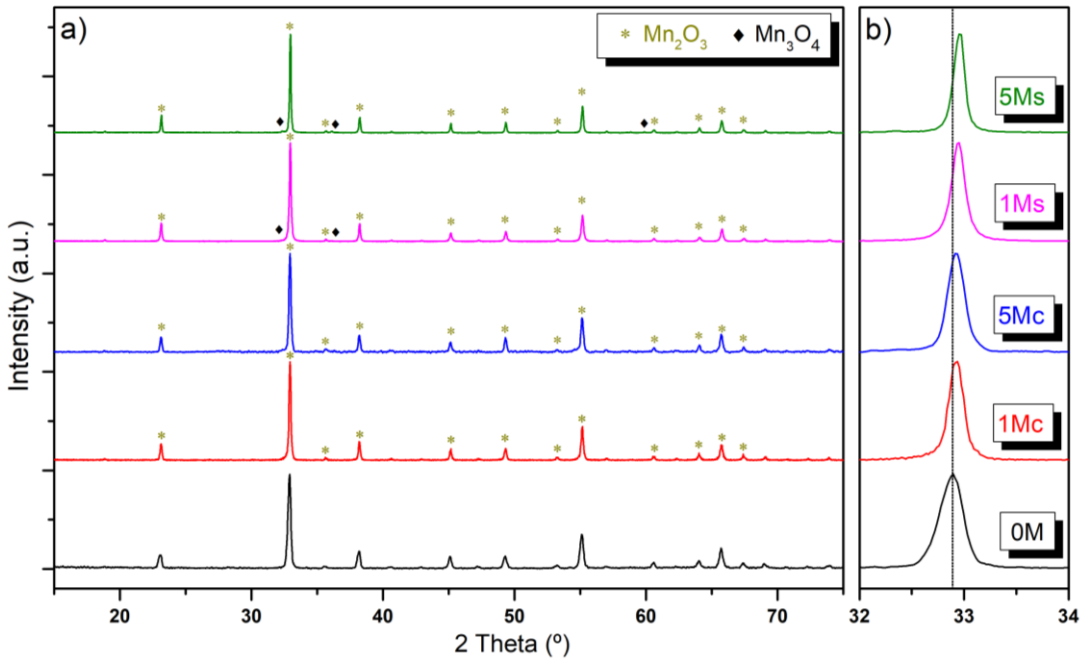

Figure 43. a) XRD patterns of the samples in the oxidized state, b) details of XRD patterns showing the evolution of the peak in 32-34° region.

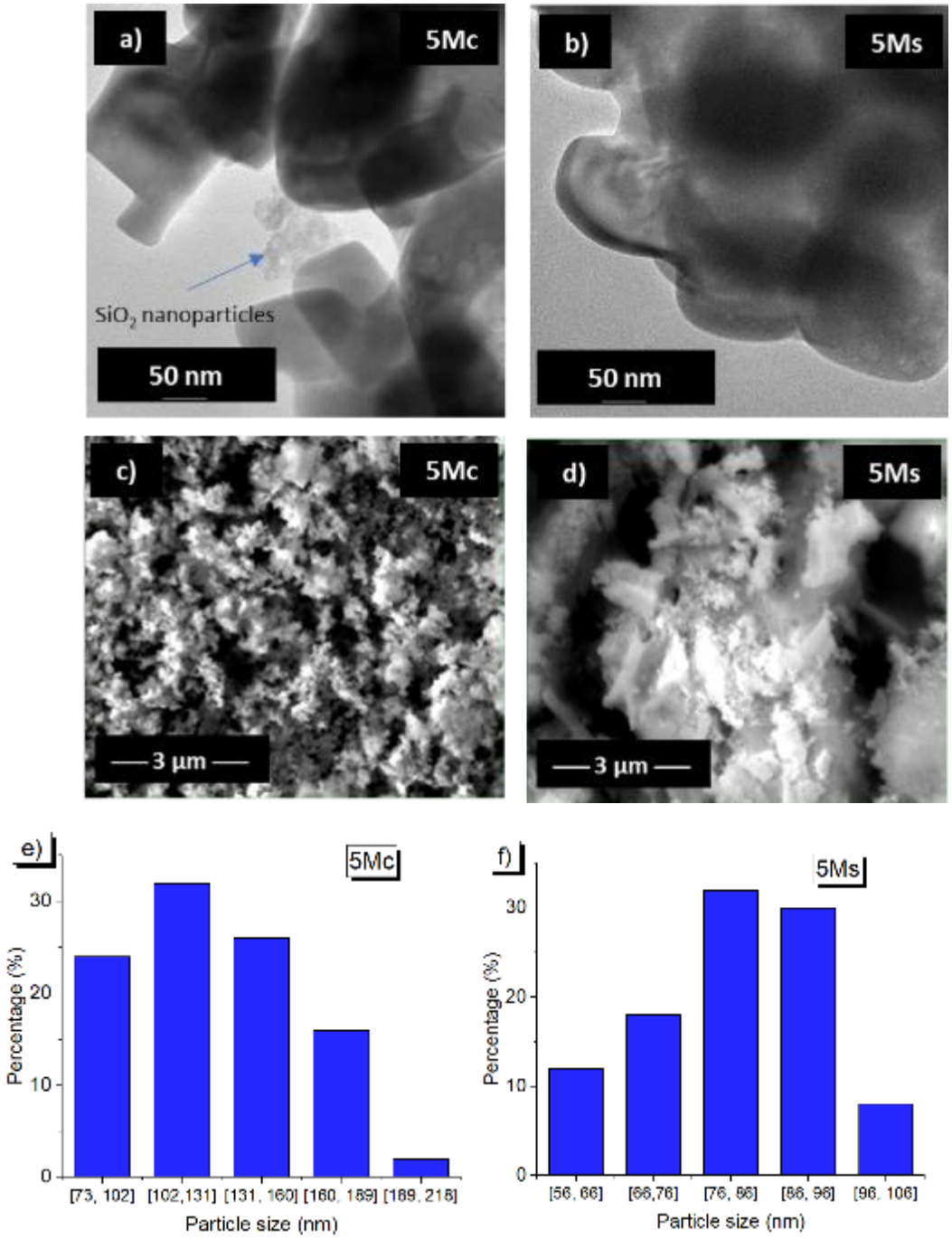

Figure 44. TEM (a and b) and SEM (c and d) images and particle size distribution (e and f) of as-synthetized 5Mc (a, c and e) and 5Ms (b, d and f) samples.

6.3.2 The effect of Si doping in the thermochemical cycle

The redox reversible reaction of Mn_2O_3 involves two steps: charge and discharge. In the first step, the sample is heated above the equilibrium temperature, which has been identified in the range from 940°C to 1000°C [31], triggering the endothermic reduction reaction with a theoretical stoichiometry mass loss of 3,38 %. The second step corresponds to the exothermic reaction, in which the reduced form is oxidized when the temperature is decreased below 840°C, releasing heat

corresponding to the reaction enthalpy, with a theoretical value of 202 kJ/kg [46]. The expected redox reaction in the studied samples is as follows (Eq. 22):

$$6Mn_{2-x}Si_xO_3(s) \leftrightarrow 4Mn_{3-x}Si_xO_4\,(s) + O_2\,(g) \qquad \text{Eq. 22}$$

Where x corresponds to 0, 0.02 (Si 1 at. %) and 0.1 (Si 5 at. %).

The thermogravimetric analysis of the reduction and oxidation reactions of the studied samples is reported in Fig. 45 and Table 10. To avoid the possible effect of impurities, present in the samples due to exposure to the atmosphere, the analysis corresponds to the last cycle of a three redox cycles program. Additionally, in order to avoid buoyancy effects, all the curves shown are blank curve corrected. The redox cycle starts with a heating step up to 1050°C, provided that it has been identified as the required temperature to reach complete reduction of Mn_2O_3 [Fig. 54]. After the temperature peak is reached, the sample is cooling down to 700°C and kept under isothermal conditions for 20 min, to complete the re-oxidation reaction.

The reaction onset temperatures of the doped samples presented a slight variation compared to pure Mn_2O_3, falling in the range 941°C - 954°C for the reduction reaction and 767°C -797°C for the oxidation reaction. This difference between reduction and oxidation onset temperatures, characteristic of this redox couple, has been observed in previous works [33] and presents an average temperature difference of 160°C, with slight changes due to Si doping. Nevertheless, the mass loss of the doped samples decreases compared to the pure Mn_2O_3, which might be attributed to both the presence of thermodynamically-stable secondary phases and oxygen partially trapped by the Si dopant inside the structure, and will be further analysed during cycling measurements. The main difference between the behaviour of pure Mn_2O_3 and the doped samples is the faster re-oxidation reaction kinetics of the doped samples, provided that the reduction reaction kinetics remains similar. This behaviour is similar to the effect identified by other authors with the addition of iron as dopant. In that case, the hypothesis stated that this effect may be attributable to an enlargement and weakening of Mn^{2+}-O bonds, being the main species involved in the re-oxidation process, due to the smaller radius of Fe^{2+} atoms (0.63 Å) compared to Mn^{2+} (0.66 Å) in fourfold coordination [34]. This hypothesis might be valid for the case of Si doping, taking into consideration that the ionic radius of Si^{4+} (0.4 Å) is even smaller.

Additionally, significant differences have been observed in the shrinking state of the different samples after the temperature cycle programs, while 0M sample changed from a dispersed powder to a compact pellet-shape sample, all the doped samples maintain their initial form (Fig. 55). Considering that mass transfer difficulties within the powder has been identified as the main reason of the oxidation reaction deterioration [31], the shrinkage degree might also have a significant effect in the oxidation kinetics improvement or deterioration. This shrinkage effect is temperature dependent [123] and thus, it will be much more severe when subjected to several redox cycles. For that reason, the shrinkage effect will be further addressed in the following section.

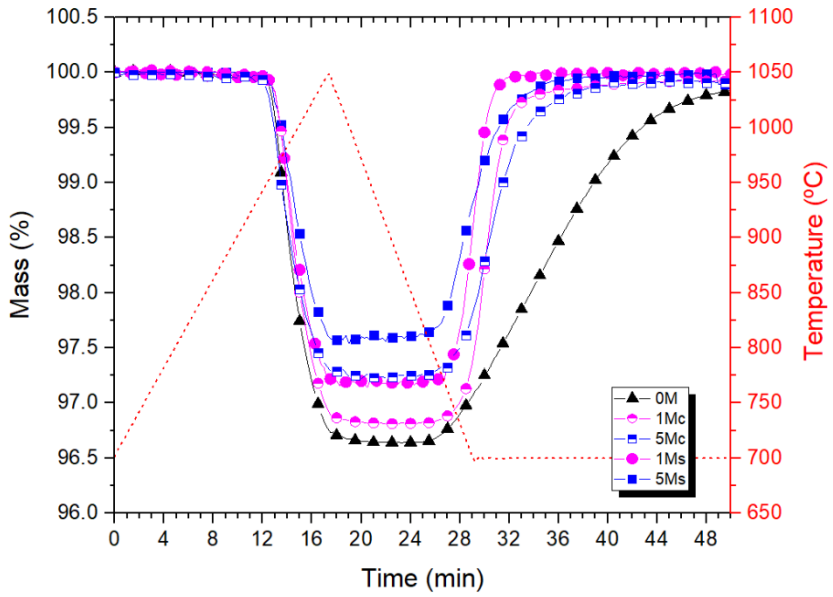

Figure 45. Thermogravimetric curves of the different samples, reduction at 20°C/min and oxidation at 700°C isothermal in air atmosphere (60ml/min).

Table 10. Reduction and oxidation reaction onset temperatures, reaction duration, thermal hysteresis, mass loss and theoretical stored heat of the studied samples.

Sample	T_{red} [°C]	$Time_{red}$ [min]	T_{ox} [°C]	$Time_{ox}$ [min]	ΔT [°C]	Mass loss [%]	Theoretical stored heat [kJ/kg]*
0M	940±1	11	793±5	23.5	147	3.36	200.8
1Mc	941±1	11	767±5	10	174	3.33	199.01
5Mc	943±1	12	787±5	15	156	2.778	166.02
1Ms	948±1	11	782±5	7	166	2.858	170.80
5Ms	954±1	12	797±5	13	158	2.46	147.02

*: this value is calculated based on the mass loss compared to the stoichiometry value

6.3.3 Effect of Si doping on the cycling behavior

In most applications, the TCES system is subjected to a great number of charging and discharging cycles during its lifetime. Therefore, its ability to maintain a high degree of reversibility under these severe conditions must be satisfactorily fulfilled. It has been reported different behaviors of pure Mn_2O_3 when subjected to a relevant number of reduction and oxidation cycles. There is a common agreement regarding the high tendency of this material to sinter, causing mainly a slowdown of the oxidation reaction which leads to a certain reversibility deterioration in a long-term use [31]. Carrillo et al. have shown that iron addition helps to improve the oxidation rate, although the sintering effects could not be avoided and the oxidation rate decreased in most of the samples [33].

This sintering effect is caused by the high temperatures used to conduct the redox reactions, which in most of the works reached 1000°C and it is shown even from the first cycle. In this work, the reduction reaction of synthetized Mn_2O_3 powder was not completed until 1040°C is reached [Fig. 54]. So, in order to evaluate the cycling stability, the samples were subjected to 40 cycles in a thermobalance between 1050°C and 700°C, with a heating/cooling rate of 20°C/min followed by a

dwelling at 700°C for 20 min, in order to get a complete re-oxidation of the samples. The measurements were made using a TGA software from Netzsch which includes a mathematical procedure (TGA-BeFlat®) allowing for the removal from TGA measurement of the contribution of buoyancy effects and friction force from the vertically moving gas.

The weight change in all the samples over 40 redox cycles is plotted in Fig. 46a, 46c, 46e, 46g and 46i. It should be pointed out that during the first 5 cycles, there is an irreversible mass loss which was not recovered in the subsequent cycles. Taking into consideration that no evidences of MnO_2 was observed and that the oxidation of Mn_2O_3 under ambient conditions is not favoured (B. Wong, 2010), this mass loss was attributable to some impurities present in the samples due to exposure to the atmosphere. The same observation was also reported by Carrillo et al. [31]. In order to provide a clear evolution of the oxidation rate over the cycles, the weight of the sample at the beginning of the 5th cycle was set to 100% and the mass change during the subsequent 35 cycles was overlapped and plotted in Fig. 46b, 46d, 46f, 46h and 46j.

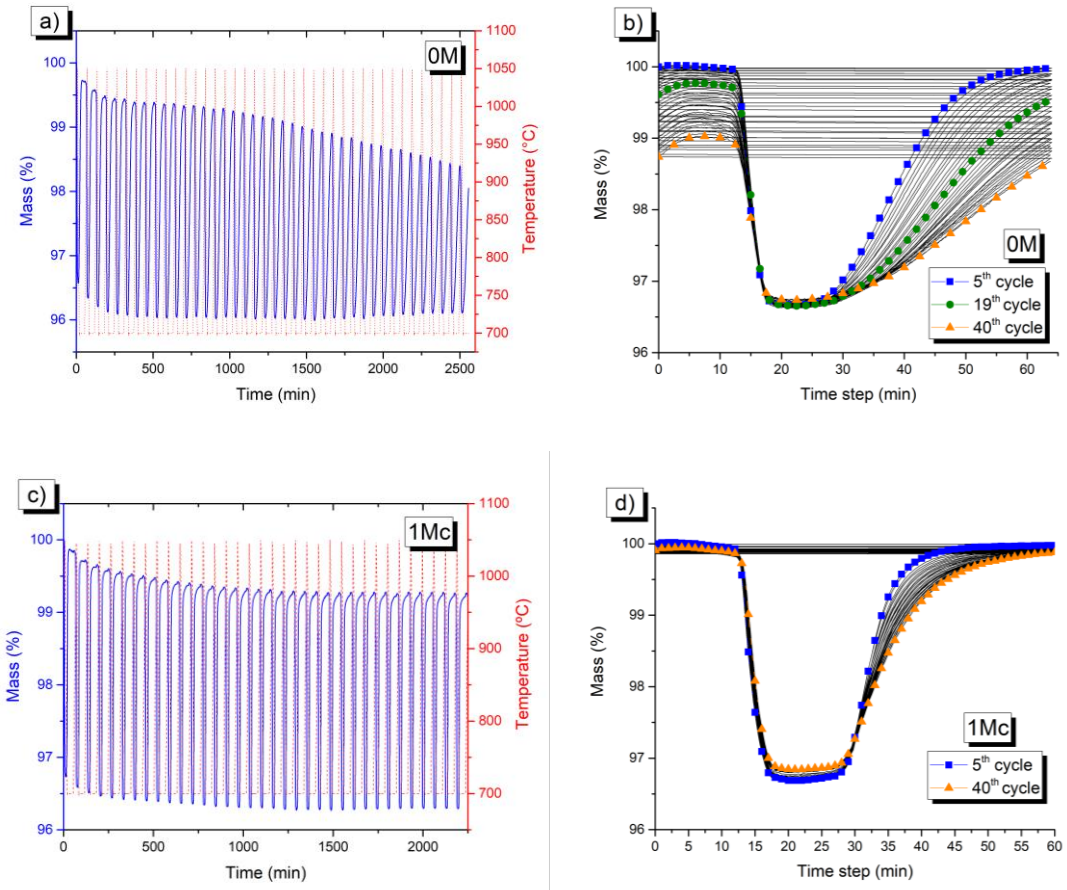

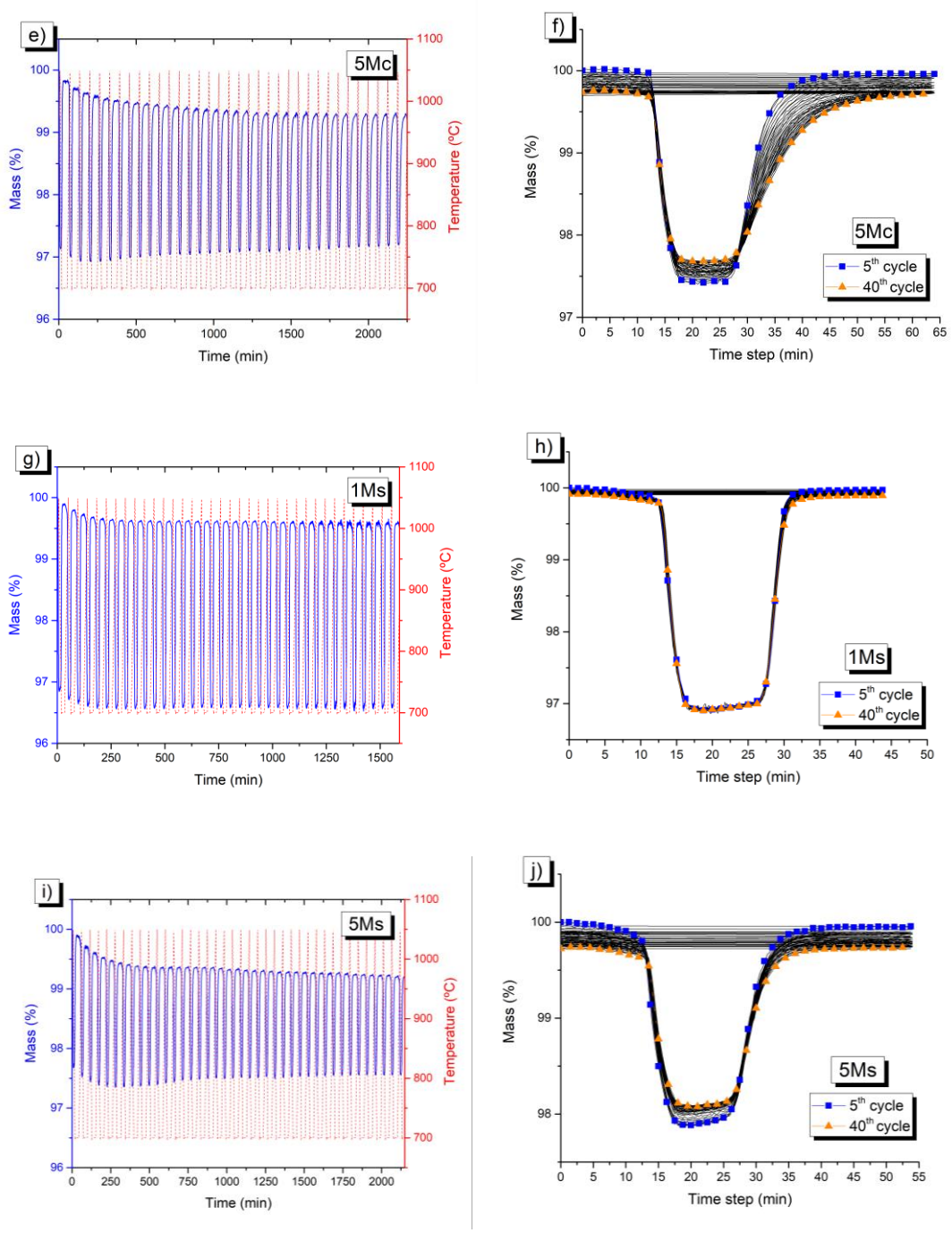

Figure 46. Weight change curves during TGA 40 cycles program between 1050°C-700°C: 0M (a and b), 1Mc (c and d), 5Mc (e and f), 1Ms (g and h) and 5Ms (i and j).

In agreement with previous works, the pure Mn_2O_3 sample suffered a noticeable slowdown in the oxidation reaction kinetics from the first cycle to the end of the temperature program. The 3.38 % mass loss corresponding to the stoichiometry value was only maintained during the first three cycles, decreasing gradually in each cycle. Additionally, the slowdown of the oxidation reaction rate led to insufficient time within the temperature range in which the oxidation reaction is favored, and from the 20th cycle, the recovered mass suffered a more intense decrease, being reduced to 1.94 % at the end of the 40 cycles program. The 1Mc and 5Mc samples exhibited better behavior than pure Mn_2O_3 sample, reaching 3,05 % recovered mass in 1Mc and 2,03 % in 5Mc, after the 40th cycle. Taking into account the mass loss observed in the first cycle, the remaining reversibility at the end of the

cycling program corresponds to 93,39% and 77.07% for 1Mc and 5Mc, respectively. The evolution of the re-oxidation kinetics remains faster than the one showed by the 0M sample during the whole program, although it shows a slight and gradual slowdown at the end of each re-oxidation cycle, which becomes greater in the case of 5Mc sample and represents the main cause of the observed reversibility deterioration.

In the SEM images of Fig. 47, the samples present a non-uniform morphological evolution of the grains, where part of the grains remains stable and others present some degree of sintering. This fact might explain the faster re-oxidation of the non-sintered grains at the starting of the re-oxidation reaction, while the sinterable grains presents slower kinetics, being oxidized at the end of the cycle, becoming worse each cycle, as they are continuously affected by sintering. Taking into account that Si doping has been proven to improve the re-oxidation kinetics of Mn_3O_4, these results might confirm that SiO_2 nanoparticles have not completely reacted with all Mn_2O_3 particles, due to an ineffective synthesis method. In order to explain this behavior, the phase composition of the samples after cycling was determined by XRD (Fig. 48). All samples confirm the presence of small amounts of Mn_7SiO_{12}, which is stable in the temperature range of the measurements [121] and contributes to decrease the mass loss capacity of the samples after each redox cycle. The reduction extent at the end of the 40^{th} cycle did not reach a stable value, meaning that the new phase formation may continue in subsequent redox cycles.

On the other hand, the re-oxidation kinetics of 1Ms and 5Ms samples remains stable over the 40 cycles, reaching a re-oxidation of 99,93 % and 99,74 % after the 40^{th} cycle for 1Ms and 5Ms, respectively. The main explanation of this behavior might be attributed to the sintering effects found in those samples, which are much less intense compared to the other samples, being almost negligible in the 5Ms sample (Fig. 47). In this case, the particles do not show the characteristic coral-like array caused by sintering, instead the particles remain agglomerated maintaining approximately the starting particle size, which can be distinguished in the center of the picture of Fig. 5. In 1Ms and 5Ms samples, the particle size distribution is much more uniform compared to 1Mc and 5Mc samples, meaning that the sintering inhibition is more effective. Nevertheless, the XRD analysis presented in Fig. 47a shows traces of stable Mn_7SiO_{12} after the 40 redox cycles, while Fig. 47b shows a slight displacement of the peaks to higher 2θ angles, meaning that the solid solution is still forming during the redox cycles. These facts contribute to decrease the mass loss to 2.85 % and 2.46 % (for 1Ms and 5Ms), respectively. Additionally, the 5Ms sample present a slight decay in the reduction reaction extent during cycling, due to an excess of dopant which led to the formation of this undesirable phase Mn_7SiO_{12} found, while the 1Ms sample present a stable behavior during the 40 cycles and no more secondary phase is expected if the cycling program is extended.

Taking into account these results, where all the doped samples present lower sintering degree than pure sample, it can be concluded that Si doping is an effective technique to inhibit grain growth in Mn_2O_3.

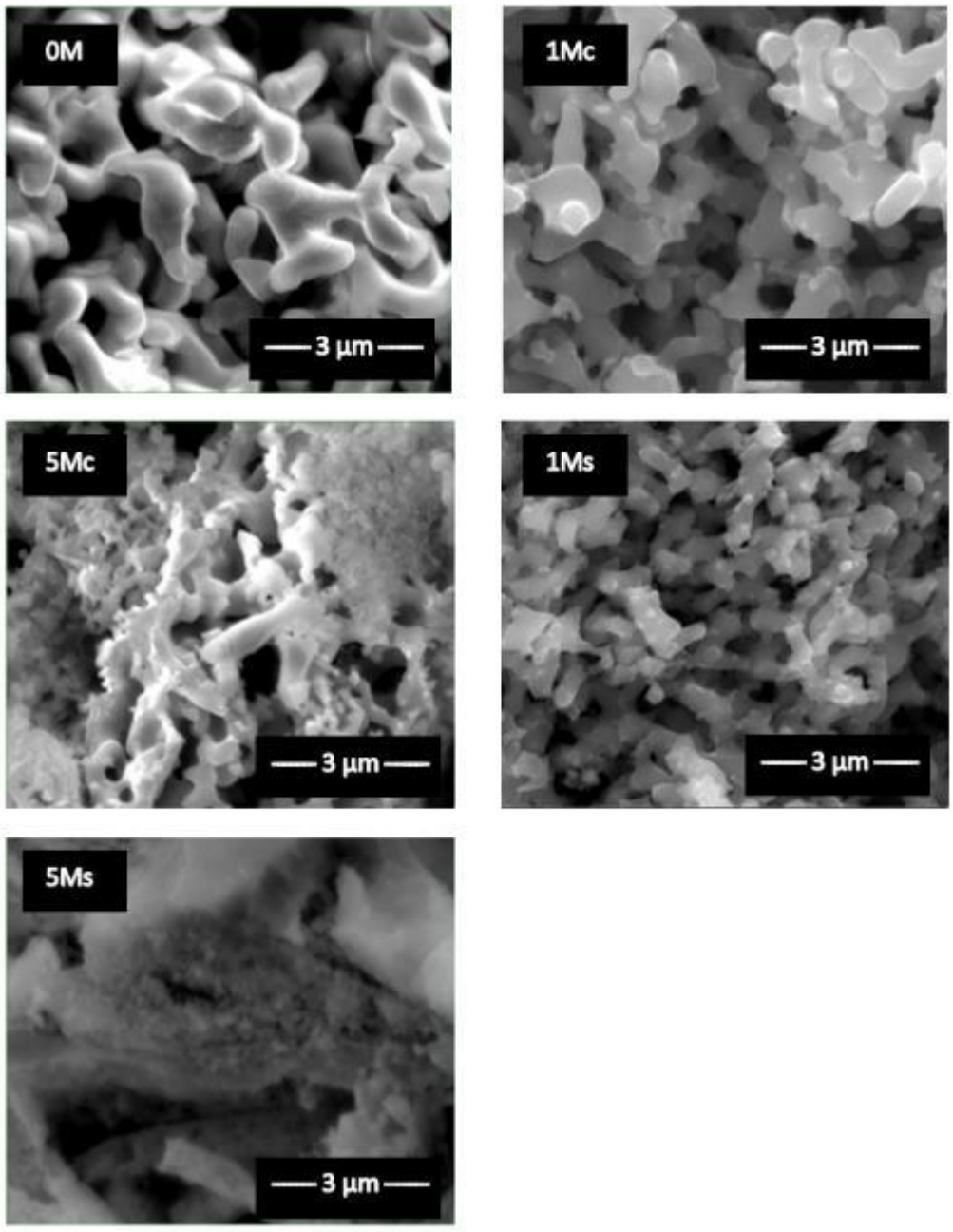

Figure 47. SEM images of samples after 40 cycles in TGA between 1050°C and 700°C.

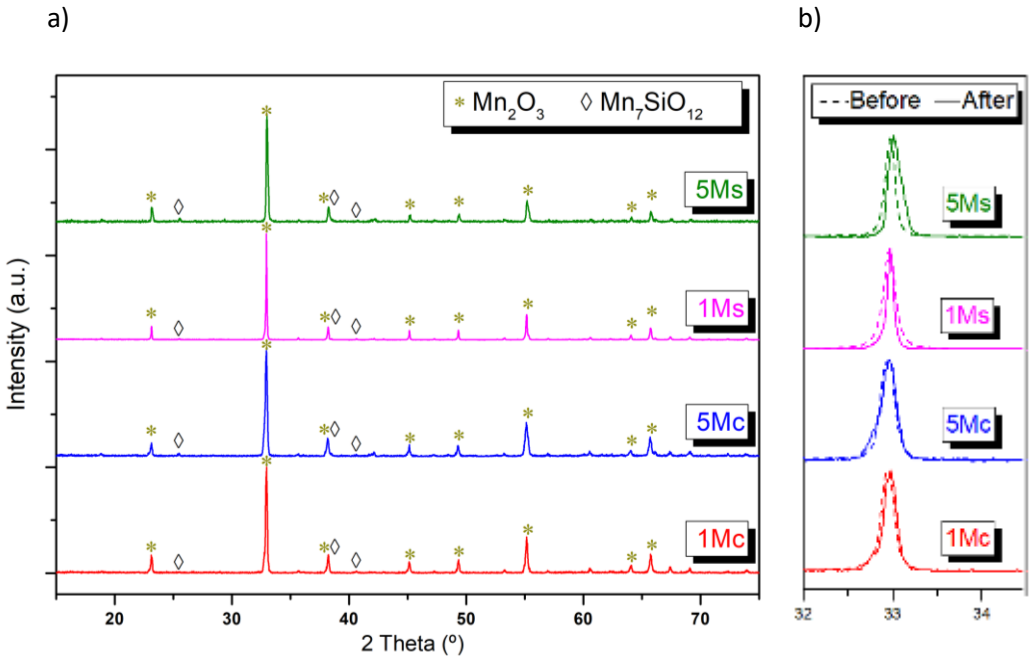

Figure 48. a) XRD patterns of the Si doped Mn_2O_3 samples in the oxidized state after 40 redox cycles program and b) details of XRD patterns showing the evolution of the peak in 32-34° region before and after the 40 redox cycles.

6.3.4 The role of Si doping in the cycling improvement

The sintering phenomenon in metal oxides for TES was already identified by B. Wong as the main reason of cyclability loss, stating a relationship between the grain growth and the decrease in the re-oxidation fraction over cycling, in most of the investigated pure oxides [30]. In regard to Mn_2O_3 material, Carrillo et al. studied the effect of the initial particle size on the cyclability, obtaining incomplete re-oxidation of the samples with the smallest particle sizes, while the largest ones presented complete cyclability during 30 redox cycles. Nevertheless, all the samples presented some re-oxidation kinetics deterioration over cycling. This deterioration was greater in the case of the smallest particles, having higher surface energy. This energy promotes mass diffusivity among grains which causes higher densification degree. This densification was presented as the main reason of the observed cyclability loss, representing a physical barrier which hinders the diffusion of O_2 into Mn_3O_4 molecules during the re-oxidation reaction [31].

Sintering is a well-known process in the manufacturing of metallurgical products to produce density-controlled materials. Sintering processes can be divided into two different sintering types: solid state sintering and liquid phase sintering. During solid state sintering two basic phenomena can be identified: densification and grain growth. Densification involves reducing the porosity of the powder, depending on mass transport along the grain boundaries between contacting particles. Whereas grain growth, also known as coarsening, involves that the smaller grains are consumed by the larger ones, depending on mass transport across the grain boundaries [32]. Both processes are competitive and depend on grain size and temperature but the laws that govern both of them are interrelated and not clear for certain. Nevertheless, one can conclude that the grain boundary becomes a critical factor to control the sintering effects, as it is the main mass diffusion path involved in both processes of solid state sintering. Liquid phase sintering occurs when a liquid phase is present in one or more components during sintering. In the case of Mn_2O_3 material, several chemical products

manufacturers provide 940°C as the melting point of the material and in that case, partial melting might occur during the temperature range used to complete the reduction reaction. This fact should be justified by an additional enthalpy due to the phase change of the non reduced part of the material. The enthalpy measurement of Mn_2O_3 has been reported in previous works by other researchers [112] [31] [124], presenting difficulties in obtaining accurate and reliable values. These results provide, in general, lower values than the theoretical 202 kJ/kg, obtained by S. Fritsch and A. Navrotski using transposed temperature drop calorimetry [125]. Furthermore, a much lower and even no measurable signal for the oxidation reaction enthalpy has been reported by the mentioned authors. In our work, we also obtained enthalpy values below the theoretical ones, but it was not possible to obtain accurate and stable enthalpy measurements by STA to support this statement. A first conclusion based on these findings is that melting of Mn_2O_3 is not likely to occur in the conditions assayed in this work, which was in agreement with the phase diagram provided by A. Cheraghi using FactSage 7.0 software [126] and thus, liquid sintering was not considered. Secondly, we found that reaction enthalpies measurement via DSC is strongly dependent on the experimental conditions and special attention must be paid to find out the appropriate conditions that provide accurate results, which will be presented in our upcoming research work.

A representation of the mass transport paths and the sintering effects between contacting particles can be observed in Fig. 49.

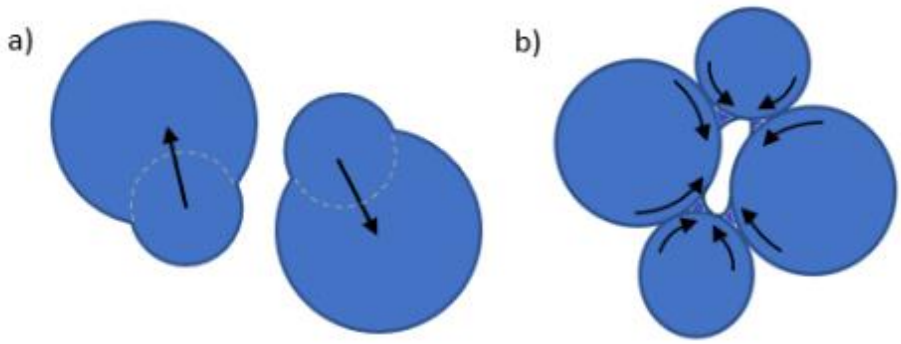

Figure 49. Basic material transport paths and effects during solid state sintering: a) grain growth via mass transport across grain boundaries and b) densification via mass transport along the grain boundaries

Doping of ceramic materials have been proven to be an effective technique to modify the grain growth and particle shrinkage in manufacturing of metallurgical products. When the amount of doping agent is higher than the bulk solubility limit, the excess cations may segregate forming dopant-rich phases at the grain boundaries (Fig. 50), contributing to change the grain boundary diffusivity and thus, the sintering conditions. In this work, segregation is a word that refers to an enrichment of molecules at a microscopic region. S. J. L. Kang stated that the sintering mechanism in most ceramic materials, particularly ionic compounds, is governed by ion diffusivity along and across the grain boundaries, being governed by the slowest moving species [38]. These ions diffuse by an interstitial mechanism that can be enhanced by the presence of oxygen vacancies. When cations of lower valence than the major component (acceptor dopants) are segregated at the grain boundaries, oxygen vacancies are created to maintain electrical neutrality providing faster ion diffusion pathways. On the other hand, when cations of higher valence than the major component (donor dopants) are segregated at the grain boundaries, oxygen interstitials inside the structure are created hindering the ion diffusion mechanisms. Most of this research has been focus on getting high dense materials with a fine grain structure for metallurgical applications, which are not desirable for TCES application.

Nevertheless, Pei-Lin Chen and I-Wei Chen found in their study of grain growth in CeO_2 [127] and Y_2O_3 [128], that an adequate selection of the dopant might contribute as well to decrease the sintering effects. In particular, they found a remarkable suppression in grain boundary mobility using Y^{3+} as a dopant in CeO_2 and Zr^{4+} in Y_2O_3. At the same time, the strengthening or weakening of ionic bonds, due to the greater or smaller dopant radius, respectively, might play a significant effect on diffusion mechanisms, even turning it into the governing diffusion mechanism. Chen et al. showed a diffusion increase with the addition of Nb^{5+} in CeO_2, even though it is expected to act as a donor hindering ion diffusion, the effect on lattice distortion found, caused by the smaller Nb^{5+} radius, was greater [128]. Finally, Lallemant et al. showed that an excess of dopant in alumina, caused a precipitation of a new phase in the grain boundaries, which contributes as well to disturb the grain mobility and reach even lower grain growth and densification rates [129]. A similar approach was recently proposed by Bagherisereshki et al., where SrO was doped with an inert material, finding some degree of sintering inhibition [130]. Confirming these findings, during the last years the effect of a numerous quantity of dopants and co-dopants have been reported, mainly in Al_2O_3 [129] and Y_2O_3 [131]. In general, doping of ceramics materials involves complex changes in grain boundaries and lattice diffusivity, grain boundary energy, surface energy and grain boundary mobility and it is often evaluated empirically.

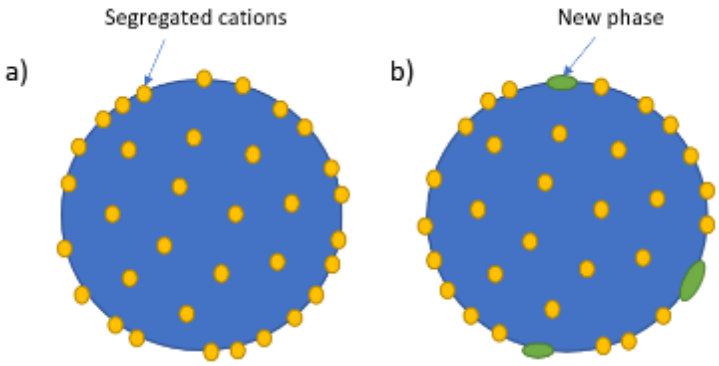

Figure 50. Different grain microstructures with the addition of dopants: a) dopant-rich phase segregated at the grain boundary and b) additional secondary new phase segregated at the grain boundary

The Si^{4+} doping agent used in this work presents a higher valence than Mn^{3+}, so in case of segregation on the grain boundaries, it is expected to act as a donor hindering the sintering effects. On the contrary, the Si^{4+} radius (0.4 Å) is smaller than the Mn^{3+} radius (0.645 Å) and thus, it may contribute to promote ion diffusion within the particles, counteracting the charge effects of the dopant. TEM images in all the doped samples investigated in this work, showed the presence of two different contrast areas (Fig. 51). The contrast between two adjacent areas in a TEM image can be attributed to differences in amplitude contrast, due to either thickness or crystallographic differences. In the surface of the grains of both types of synthesized samples, it can be observed a more brightness area, which corresponds to the same contrast of SiO_2 nanoparticles shown for 1Mc sample in Fig. 51. Therefore, it may indicate the presence of a Si^{4+}-rich solid solution on the surface of the particles, which comes to mean that the amount of Si^{4+} cation used is beyond the bulk solubility limits and different amounts of segregated cations are present on the grain boundaries.

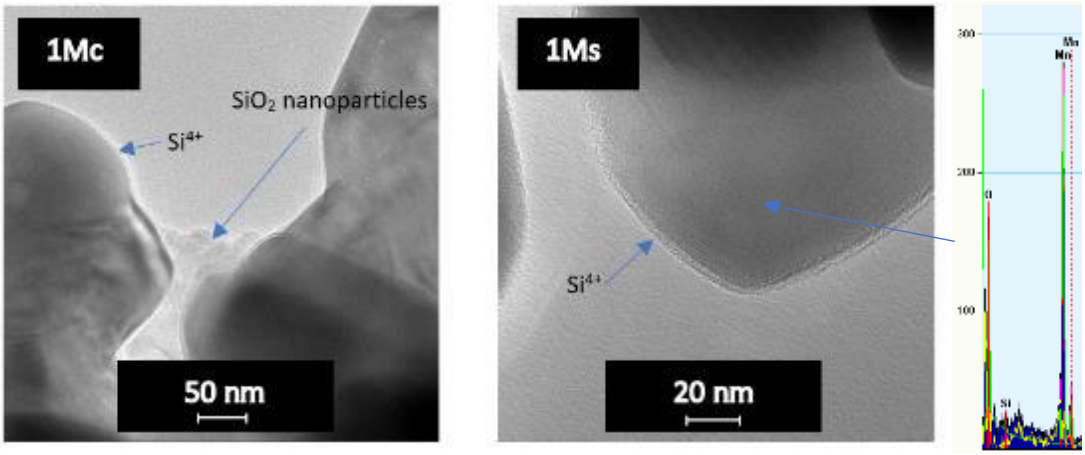

Figure 51. TEM images of the doped samples after cycling: 1Mc (left) and 1Ms (middle) and EDX analysis of 1Ms (right)

In order to identify the Si dopant effect in the densification phenomenon, the samples were subjected to dilatometry measurements. Pellets of 8 mm x 6.5 mm (diameter x width) of the samples, were prepared by uniaxial compression, applying a force of 100 N. The pellets were placed in a dilatometer and subjected to a pressure less heating program consisting of 4 cycles between 1050°C and 700°C, with a heating/cooling rate of 20°C/min, under air atmosphere. During the first heating step, all the samples suffered a strong shrinkage, attributable to particle rearrangement, likely due to insufficient preparation pressure and it was not taken into account for the present analysis.

In order to compare the behaviour of the samples when subjected to high temperature, the curves corresponding with the second heating step are plotted in Fig. 52. The 0M sample presented a deviation from the linear expansion approximately at 850°C, which can be considered as the sintering onset temperature. The sample presented a subsequent decrease on the slope of the expansion curve at approximately 950°C, which corresponds to the reduction reaction onset temperature. The reduced material density is higher than the oxidized form, 4.86 g/cm^3 compared to 4.5 g/cm^3, but taking into account the oxygen release during the reduction reaction, the observed shrinkage may be attributable to both structure change and sintering. Nevertheless, all the doped samples presented no deviation from the linear expansion until 950°C is reached, delaying the sintering effects to higher temperatures. The total length's variation of the samples during the 4 cycles program is shown in Fig. 53. In all samples, the final length at the end of each cooling down step are shorter than the corresponding length at the same temperature level of the previous cycle. This means that all the samples suffered some degree of shrinkage when subjected to redox cycles. The 0M sample presented the highest dimensional change, being $4.7 \cdot 10^{-3}$ % at the end of the temperature program. However, all the doped samples presented lower values at the end of the program, being $2.47 \cdot 10^{-3}$ % for 1Mc, $1 \cdot 10^{-3}$ % for 5Mc, $1.86 \cdot 10^{-3}$ % for 1Ms and $3.4 \cdot 10^{-3}$ % for 5Ms. The 1Ms sample provides the best performance among all the samples, presenting not only the lowest shrinkage value at the end of the program, but also the lowest shrinkage rate. Based on these results, it is suggested that the low densification degree found in 1MS sample is the main reason of the cyclability improvement found in the TGA measurements (Fig. 46h). Summarizing, these results show the positive effect of Si doping on reducing the densification effect on Mn_2O_3, in which the sintering protection effect of the Si^{4+} dopant charge counteracts the diffusion enhancement induced by the smaller size effect.

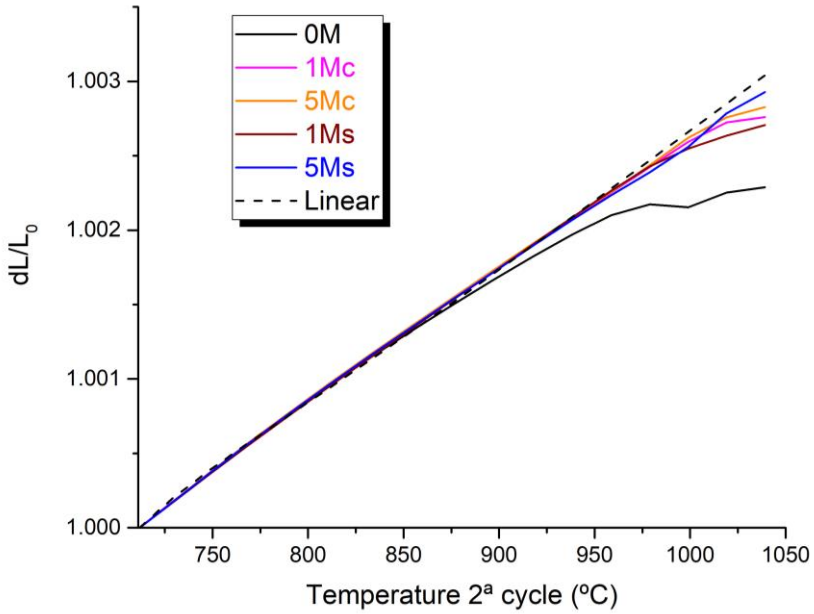

Figure 52. Dilatometry results for all the samples during the 2nd heating step of a 4 cycles redox program from 700°C to 1050°C, with 20°C/min in air

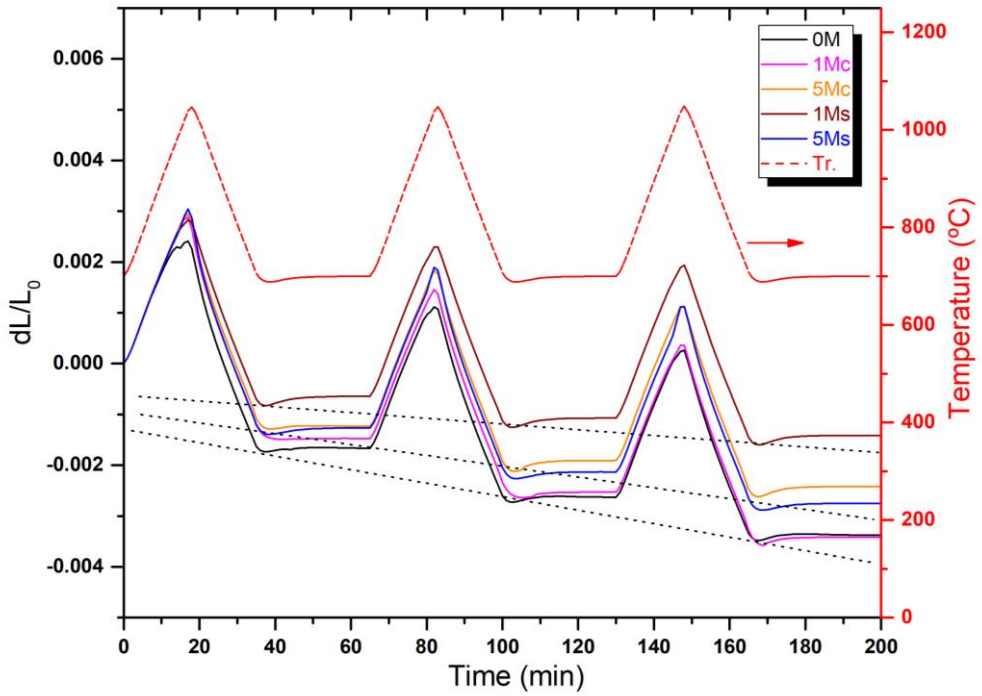

Figure 53. Dilatometry results for all the samples during a pressureless 4 cycles program between 1050°C and 700°C, with 20°C/min, in air atmosphere (1st cycle is not included).

It should be noted that the dopant effects found in the re-oxidation kinetics and sintering improvement are competitive and the amount of dopant might vary the equilibrium of the governing effect. According to Fig. 45, samples doped with 1% Si present faster re-oxidation kinetics than samples doped with 5% Si, whereas the latter may present lower degree of sintering and might be more reliable in a long-term use. Therefore, the selection of the appropriate amount of dopant for the given application should be selected carefully.

6.4 Conclusions

It has been observed that doping Mn_2O_3 with Si cations significantly improves the redox performance of this material for thermochemical energy storage applications. Compare to iron addition, it has been shown that Si doping presents a stable re-oxidation reaction rate and no increase in the reaction temperatures. It has been confirmed under a 40 redox cycles program that Mn_2O_3 material behaviour is highly affected by sintering, presenting a slow oxidation reaction kinetics and a continuous decrease in the re-oxidation rate. We observed that the sintering rate in Mn_2O_3 is controlled by ion grain boundary diffusivity, which can be hindered by Si^{4+} dopant segregation at the grain boundaries. Nevertheless, doping effects on the material behaviour depend on the charge, size and amount of dopant, so it must be taken into account when selecting the appropriate dopant. In the case of Si^{4+} dopant, its smaller size, compared to that of Mn^{3+}, contributes to improve the re-oxidation kinetics, while the higher valence contributes to decrease the sintering effects. This synergistic effect provides a constant energy storage capacity over a 40 redox cycles test in a TGA experiment. It is worth noting that increasing the quantity of Si^{4+} dopant decreases the sintering effects but at the same time, presents slower oxidation reaction kinetics. Therefore, selecting the appropriate amount of dopant becomes critical to obtain the best material performance. Additionally, it was also observed that in order to get an effective doping of the material, an appropriate synthesis method shall be applied. In this work, doping Mn_2O_3 with low Si content (x = 0.02) via sol-gel method obtained the TCES material with the fastest oxidation reaction rate and complete reversibility, over 40 redox cycles, presenting a slight increase on the particle size and low degree of densification. The combination of these two improvements, namely, increased cycle stability and enhanced re-oxidation kinetics, together with the low cost of Mn_2O_3 and Si dopant, render such a material an attractive option for further study and implementation in a thermochemical energy storage system.

6.5 Supplementary information

In 54a the TGA results of Mn_2O_3 reduction programs using different maximum temperatures are plotted. It is shown in Figure 54b that a temperature up to 1040°C is required to get the stoichiometry full reduction of the sample (3.38%). Neither the use of slower heating rates nor isothermal step at lower temperature than 1040ºC get complete reduction of the sample. A possible explanation of this behaviour is due to the configuration of the experiment, in which the air flow is passing around the sample from the bottom to the top, without going through it, hindering the oxygen release and increasing locally the partial pressure of the oxygen, thus slowing down the reduction reaction and displacing the equilibrium temperature upwards. In Figure 55 the photographs of the samples 0M and 1Ms after being subjected to 1 redox cycle, up to 1050°C and down to 700°C are shown. Sample 0M suffered a noticeable shrinkage and presented a compact pellet shape structure while sample 1Ms remained similar to the starting form.

a)

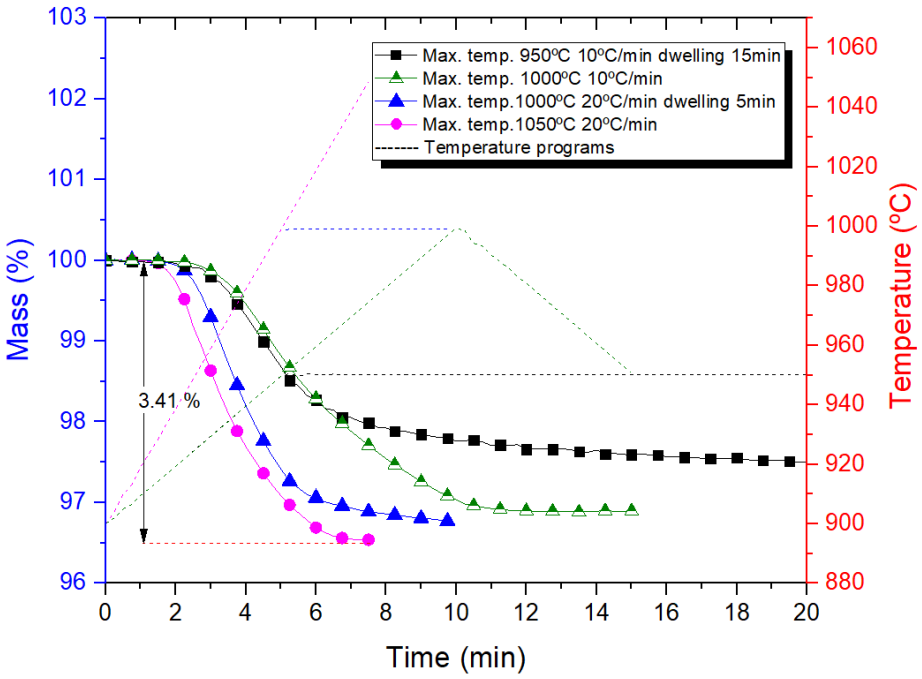

b)

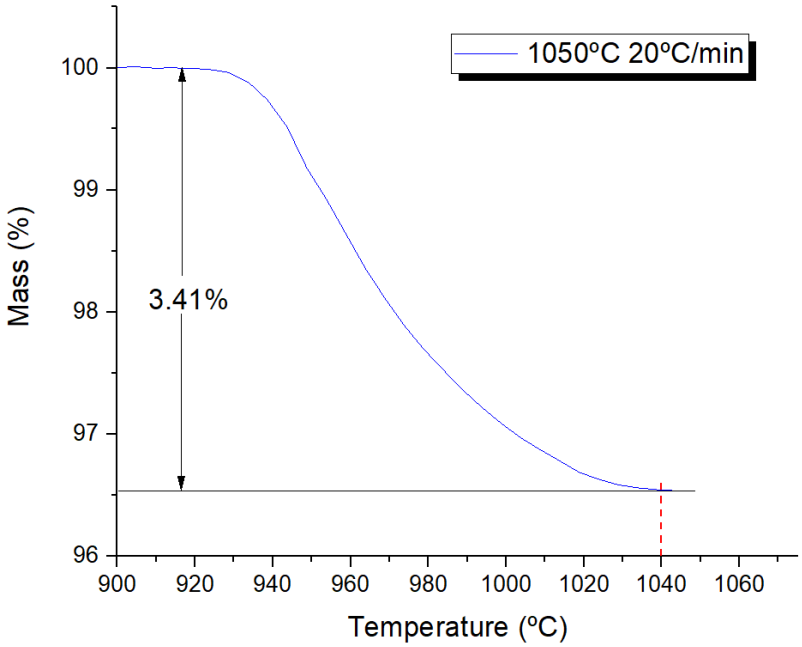

Figure 54. TGA results of Mn_2O_3 reduction programs using different temperature programs under 60 ml/min air flow: a) 950°C at 10ºC/min with 15 min isothermal, 1000°C at 10ºC/min, 1000ºC at 20ºC/min with 5 min isothermal and 1050°C with 20°C/min, and b) magnification of heating program to 1050ºC at 20ºC/min

a) b)

Figure 2S

Figure 55. Photographs of the samples after being subjected to 1 redox cycle between 1050°C and 700°C: a) 0M, b)1Ms

In Figure 56, a magnification of the XRD patterns of 1Ms and 5Ms samples after preparation is shown. In these magnifications the presence of Mn_3O_4 phase may be confirmed by the identification of small peaks in the corresponding 2θ angles.

a)

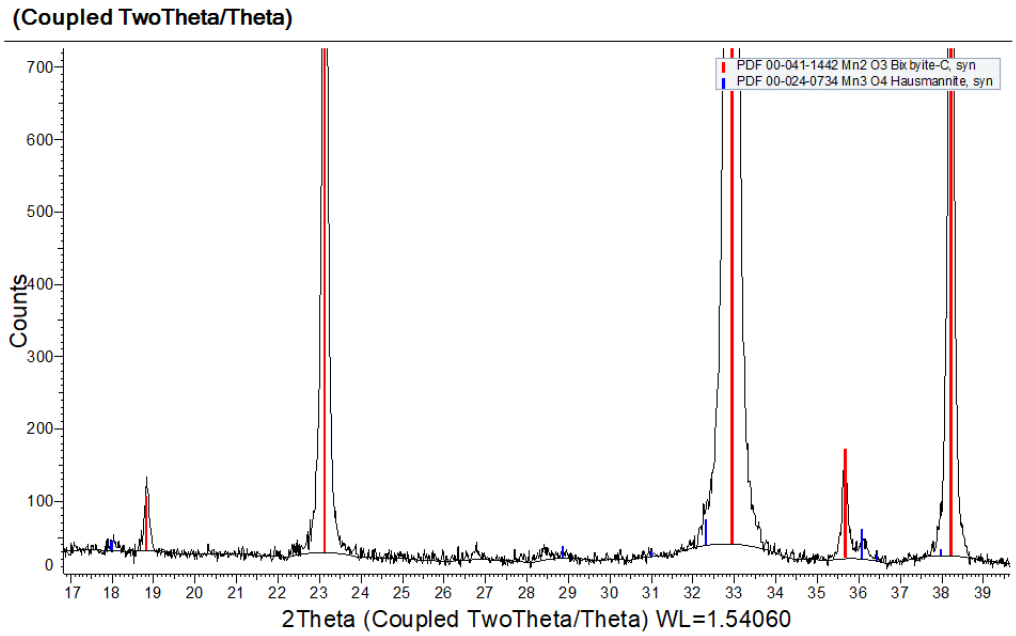

b)

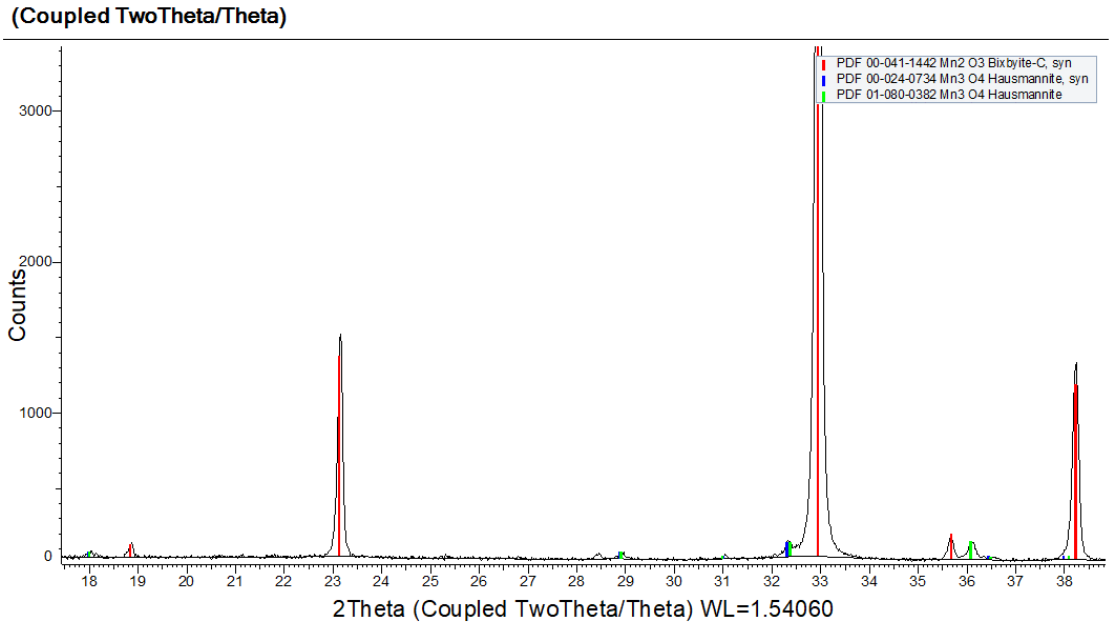

Figure 56. Details of XRD patterns of the samples in the oxidized state showing the presence of small peaks corresponding to Mn_3O_4 phase, a) 1Ms sample (red corresponding to Mn_2O_3 peaks and blue corresponding to Mn_3O_4 peaks) and b) 5Ms sample (red corresponding to Mn_2O_3 peaks and blue and green corresponding to Mn_3O_4 peaks)

CHAPTER 7. Development of the reaction kinetic model of Si-doped Mn_2O_3

The whole content of this subclause was published in Journal of Energy Storage in November of 2021, with the tittle: ' Development of a kinetic reaction model for reduction and oxidation of Si doped Mn_2O_3 for thermochemical energy storage in concentrated solar power plants', https://doi.org/10.1016/j.est.2021.103271.

7.1 Introduction

The study of the reduction and oxidation kinetics represents an important issue to determine empirical rate laws for TcES reactor design and to proceed to the next step of technological development. Nevertheless, redox kinetic studies have been scarcely reported for TcES, especially considering the effect of the pressure of the gas phase in the oxidation kinetics. Several authors have reported the kinetic study of the first step of the Mn_2O_3/Mn_3O_4 thermochemical cycle for hydrogen production, which involves Mn_2O_3 reduction to Mn_3O_4 under inert atmosphere. Francis et al., provided a calculation of a constant reaction rate of the reduction reaction of Mn_2O_3, assuming that the reaction proceeds via an Avrami–Erofeev mechanism [132]. Botas et al. obtained an accurate prediction model using a combination of isoconversional methods for the estimation of realistic activation energy values and a multivariate nonlinear regression procedure for the determination of the best kinetic model and pre-exponential factor [133]. Alonso et al. showed the kinetic study of the Mn_2O_3 reduction reaction using a solar-driven thermogravimeter, determining that the reaction rate fitted to a nth-order reaction rate [134]. Considering TcES applications, F. Pestalozzi developed a kinetic model for the reduction and oxidation of Mn_2O_3 in a packed bed reactor, under isothermal conditions, finding out that the experimental results did not fit with an Avrami model, so, a combined Sestak model was used to obtain satisfactory results [95]. A similar approach was applied by Carrillo et al., trying to explain the mechanisms involved in the reduction and oxidation of $(Mn_{0.8}Fe_{0.2})_2O_3$ in a thermobalance. They considered that the reactions followed nucleation and growth models, described by Avrami-Erofeev mechanisms, although they used a Sestak model to get more accurate results [113]. Al-Shankiti et al. studied the oxidation kinetics of $MnFe_2O_4$ using solid-state kinetics theory and XRD analysis. They found that the reaction proceeded according to two different reaction mechanisms, a diffusion-controlled reaction mechanism followed by a nucleation-growth reaction mechanism [135]. Nevertheless, even though several studies revealed that the gas partial pressure may have a significant effect on the reaction kinetics of these materials [136], little work can be found in the literature regarding modelling its effect over Mn-based oxides for TcES applications. Wokon et al. developed a kinetic model of $(Mn_{0.75}Fe_{0.25})_2O_3$ reduction and oxidation reactions, including the determination of the pressure dependence term. They found that the reactions follow an Avrami-Erofeev model. In the case of the oxidation reaction, they found model deviations when approaching to equilibrium, so it was not possible to determine a reaction rate expression within a certain temperature range called 'thermal hysteresis zone' [107]. Other study comprising the effect of the pressure term was published by Hamidi et al., devoted only to the study of the reduction reaction kinetics of $(Mn_{0.33}Fe_{0.67})_2O_3$, using air and argon as the reducing gas environments. Due to the low porosity of the prepared particles, they applied a shrinking core model to describe the reaction kinetics, finding the internal oxygen diffusion as the prevalent rate controlling mechanism. They developed a completely different reaction rate expression compared to the model of Wokon et al., ascribing this disagreement to the different materials used [108].

To the best of our knowledge, up to date no work has been reported regarding a complete kinetic study of reduction and oxidation of Si-doped manganese oxide for TcES. Due to the improved redox behavior of Si-doped Mn oxide, the identification of the main kinetic parameters (the activation energy E_a, the preexponential factor A, the kinetic model $f(\alpha)$ and the pressure dependent term $h(p_{gas})$), of the reduction and oxidation reactions is of relevant importance to set the basis for future upscaling of this technology. In addition, the effect of the oxygen partial pressure on the reaction kinetics of these materials has been barely reported, leading to models with restricted application in terms of operating temperature or pressure ranges. In order to optimize the future integration of the manganese oxide TcES system into a power plant, looking at the poor material oxidation behavior close to equilibrium and the degradation effect caused by the high temperature, it might be useful to charge and discharge the system using different gas partial pressures, since these pressures are directly related with the reaction onset temperature and kinetics. Therefore, the present study aims to provide new insights into the gas pressure relevance on the oxidation kinetic model, especially in the hysteresis zone, which has been ignored in most of the reported kinetic studies.

In this work, we have investigated for the first time the reduction and oxidation kinetics of $(Mn_{0.99}Si_{0.01})_2O_3/(Mn_{0.99}Si_{0.01})_3O_4$. In the first part of the work, we present a thermogravimetric and stability analysis of the redox cycle by simultaneous thermal analysis (STA), stating the main advantages of $(Mn_{0.99}Si_{0.01})_2O_3$ compared to pure Mn_2O_3. The second part of the work consists on the determination of the reduction and oxidation kinetics models of $(Mn_{0.99}Si_{0.01})_2O_3$, applying isoconversional methods from thermogravimetric experimental data to obtain the kinetic parameters. In this part, we provide a new proposal to gather the effect of the oxygen partial pressure into the oxidation reaction kinetics. Finally, as a means of validation, the kinetic equations obtained are successfully compared against experimental thermogravimetric measurements, providing further understanding on the reaction mechanisms involved.

7.2 Material preparation

$(Mn_{0.99}Si_{0.01})_2O_3$ samples were synthesized by a sol-gel method, following the procedure described in a previous work [137], which showed improved material redox reversibility compared to Mn_2O_3. First, a mixture of $Mn(NO_3)_2{\cdot}1H_2O$ (98%, Sigma Aldrich) and citric acid (99+%, Alfa Aesar) at a molar proportion 1:5 was dissolved in a solution of 20 ml of deionized water and ethanol (96%. Scharlau). Subsequently, the appropriate quantity of $Si(C_8H_{20}O_4)$ (98%, Sigma Aldrich) was added to the solution. Then, after stirring for 2 h, the mixture was dried at 120˚C and the resulting material was calcined at 800°C for 15 h and ground by means of a mortar until getting fine powder.

Similar process was used for the synthesis of the manganese oxides samples. In this case, ethylene glycol (99.8%, Sigma Aldrich) was added to the solution of $Mn(NO_3)_2{\cdot}1H_2O$ (98%, Sigma Aldrich) and citric acid (99+%, Alfa Aesar), at a molar ratio 3:5:1 (EG:CA:MN). Subsequently, the solution was dried at 120˚C until the gel was formed. Then, the resulting material was calcined at 800°C for 15 h and ground by means of a mortar until getting fine powder.

7.3 Results and discussion

7.3.1 Redox cycle and cycling behavior

The thermogravimetric analysis of the reduction/oxidation cycle of $(Mn_{0.99}Si_{0.01})_2O_3$, together with pure Mn_2O_3, is shown in Fig. 57. The reported measurements have been performed in air at a heating/cooling rate of 10˚C/min from 600˚C to 1050˚C (reduction reaction) and back to 600˚C (oxidation reaction). The reactions are reversible, although in the case of pure Mn_2O_3, the oxidation reaction kinetics was not fast enough to get full re-oxidation during the cooling step. The samples presented a weight change of 3.36 % for Mn_2O_3 and 3.01 % for $(Mn_{0.99}Si_{0.01})_2O_3$. The latter represents a lower value compared to the stoichiometry of Mn_2O_3 redox reaction (3.38 %). This difference is attributable to the partial deactivation of Mn-O bonds due to the introduction of Si into the structure [137]. The incorporation of Si also affected slightly the temperatures at which the reduction and oxidation take place, although in a previous work no significant differences were found [137]. Mn_2O_3 presents a reduction and oxidation onset temperatures of 910˚C and 712˚C, respectively, while $(Mn_{0.99}Si_{0.01})_2O_3$ presents a reduction onset temperature of 921˚C and an oxidation onset temperature of 768˚C (Fig. 57). We were not able to identify the reason of these deviations, which may be ascribed to differences in the measuring conditions induced by the testing instruments used in the previous and present studies (TGA and STA). In the following part of the work, the thermodynamic data is analyzed in order to obtain a hypothesis that might explain the observed reactions onset temperature increase in the Si-doped samples. Reaction enthalpies were retrieved from the areas under the DSC curves of the STA experiments and are plotted in Fig. 58a and 58b. The reduction enthalpy of Mn_2O_3 found was 147.15 J/g, however the oxidation reaction is so slow that the reaction enthalpy could not be obtained. In the case of $(Mn_{0.99}Si_{0.01})_2O_3$, its associated reduction enthalpy was 149,32 J/g and the oxidation one 17.99 J/g. These results are lower than the theoretical 210.5 kJ/kg, obtained by Fritsch and Navrotsky using transposed temperature drop calorimetry [138], but are close to the reported values using the same measurement technique (see Table 11). The determination of the reaction enthalpy of Mn_2O_3 redox material via STA measurement has been reported as a complex issue, attributable to its slow reaction kinetics [112]. Si doping in the conditions assessed in this work causes a slight reduction on the reduction reaction kinetics, which causes a peak broadening in the DSC signal, making it more difficult to obtain an accurate value for the reaction enthalpy. Nevertheless, the reduction reaction enthalpy measured for $(Mn_{0.99}Si_{0.01})_2O_3$ presents a very similar value compared to Mn_2O_3 sample, thus, no change on the energy storage density can be expected. In the case of the oxidation reaction, the kinetic improvement observed by Si doping was not enough to reach the theoretical values of the oxidation reaction enthalpy and the obtained value follows the trend reported in other works, where much lower value compared to the reduction one is showed, so other means shall be used to determine the oxidation reaction enthalpy.

In order to evaluate the cycling ability of the $(Mn_{0.99}Si_{0.01})_2O_3$ sample over a relevant number of charging and discharging cycles, it was subjected to 80 redox cycles under air between 1050°C and 700°C, with a heating rate of 20°C/min for the reduction reaction, followed by an oxidation isothermal step at 700˚C. The results depicted on Fig. 59a indicate good material stability under cycling, obtaining a measured recovered mass above 99.9 % over the whole cycling program. It should be pointed out that the initial mass of the sample was not recovered, likely ascribed to some impurities collected within the preparation process, lost in the first heating ramps, which was also observed by other

authors [139] [137]. For that reason, the initial sample mass considered for the stability assessment was the sample mass at the end of the 5th redox cycle. This cycling stability represents a significant improvement compared to Mn_2O_3 pure sample, already showed in a previous work [137] and was attributed to both the re-oxidation kinetics improvement and to the sintering protection given by Si doping, which hinders particle growth. Whereas Mn_2O_3 particles after 40 redox cycles presented a homogeneous coral-like array of particles approaching to the micro-size scale [137], $(Mn_{0.99}Si_{0.01})_2O_3$ particles after the 80 redox cycles carried out in this work present a much less degree of sintering, as it can be observed in Fig. 59b. All particles remain in the nano-size scale with some of them that seem not to be affected at all by sintering (e. g. at the center of Fig. 59b).

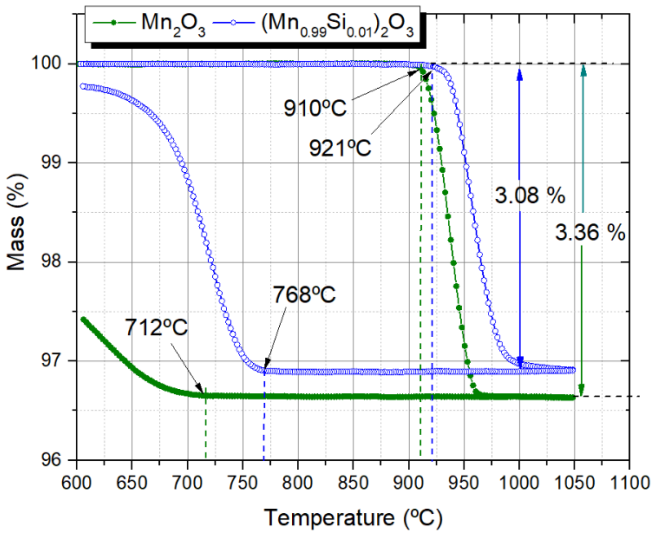

Figure 57. Reduction and oxidation cycle of Mn_2O_3 and $(Mn_{0.99}Si_{0.01})_2O_3$, applying a heating/cooling rate of 10˚C/min up to 1050˚C in air

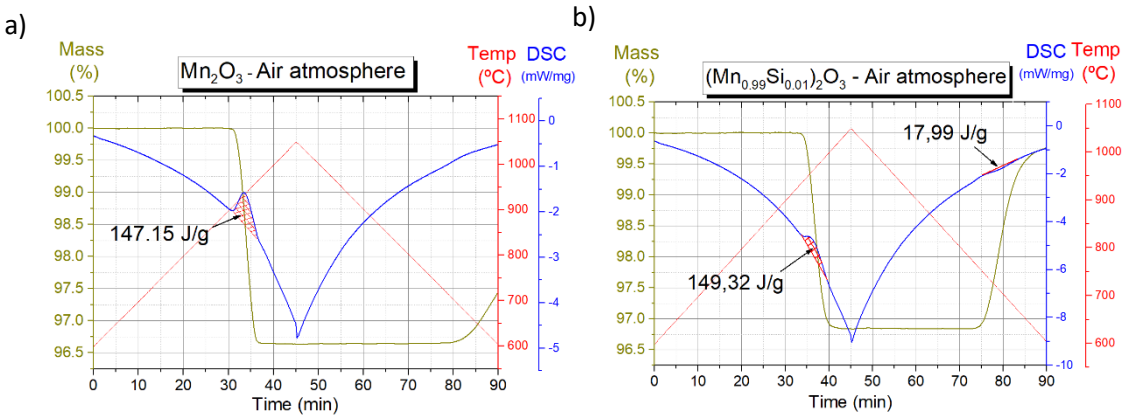

Figure 58. Reduction and oxidation enthalpy measurement results via STA using 60 ml/min of air at a heating/cooling rate of 10˚C/min: a) Mn_2O_3 and b) $(Mn_{0.99}Si_{0.01})_2O_3$.

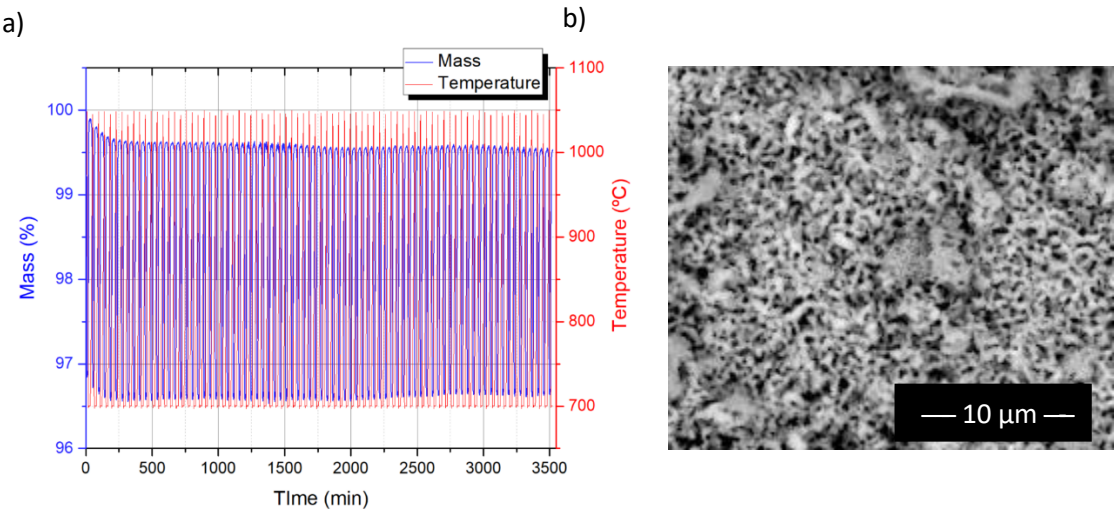

Figure 59. Cycling stability over 80 reduction and oxidation cycles to $(Mn_{0.99}Si_{0.01})_2O_3$ using 60 ml/min of air at a heating rate of 20˚C/min up to 1050˚C followed by an isothermal step at 700˚C: a) weight changes in the TGA and b) SEM photograph after cycling

Table 11. Reduction and oxidation reaction enthalpies of Mn_2O_3 found in literature and the ones obtained in this work for Mn_2O_3 and $(Mn_{0.99}Si_{0.01})_2O_3$

Authors	Experimental technique	Material	Gas flow [ml/min]	Reduction enthalpy [J/g]	Oxidation enthalpy [J/g]
S. Fritsch and A. Navrotsky [138]	transp. temp. drop calorimetry	Mn_3O_4	-	-	210.5 ± 7.6
V. Berbenni and A. Marini [140]	DSC	Mn_3O_4	100 – Air	127.84	124.96
Carrillo et al. [141]	DSC	Mn_2O_3	100 – Air	161.69	79.29
Carrillo et al. [139]	DSC	Mn_2O_3	100 – Air	160 - 170	130 - 60
Agrafiotis et al. [124]	DSC	Mn_2O_3	Air	138.6 - 84.6	-
Block et al. [112]	DSC	Mn_2O_3	80/20 - N_2/O_2	231	-
Agrafiotis et al. [142]	DSC	Mn_2O_3	Air	191 - 50	-
André et al. [35]	DSC	Mn_2O_3	20% O_2/Ar	148	-
This work	DSC	Mn_2O_3	60 - Air	147.15	-
This work	DSC	$(Mn_{1.98}Si_{0.01})_2O_3$	60 - Air	149.32	17.99

7.3.2 Kinetic analysis methodology

Reduction and oxidation reactions of metal oxides involve the absorption and desorption of oxygen, respectively and therefore, it involves a sample mass change. The plot of mass change with time *α(t),* is the common procedure used to analyse the reactions kinetics, which may have different shapes in direct relationship with the different mechanisms involved in the reactions.

A complete kinetic study requires the determination of the main kinetic parameters; namely, the activation energy E_a, the preexponential factor A, the reaction model $f(\alpha)$ and the pressure dependent term $h(p_{O2})$, which is related to the partial pressure of the oxygen [143]. The pressure dependence term $h(p_{O2})$ is ignored in most kinetic studies, but several studies showed how the oxygen partial pressure, P_{02}, in manganese oxide-based material may have a significant influence on reaction

onset temperatures, reaction rate ($d\alpha/dt$) and E_a [107] [144]. The reaction rate is commonly described by the following equations [143]:

$$\frac{d\alpha}{dt} = \boldsymbol{k}\,(\boldsymbol{T}) \times \boldsymbol{f}(\boldsymbol{\alpha}) \times \boldsymbol{h}(\boldsymbol{p_{O_2}}), \qquad \textbf{Eq. 23}$$

$$\boldsymbol{k}\,(\boldsymbol{T}) = \boldsymbol{A}\boldsymbol{e}^{-\frac{E_a}{RT}}, \qquad \textbf{Eq. 24}$$

where R is the universal gas constant (8.314 J mol^{-1} K^{-1}) and T [K] the temperature.

The reaction rate model can be determined by different kinetic analysis methods, such as model-fitting methods, generalized kinetic models and model-free methods, being the latter the most used method in studies concerning metal oxides for TcES. Model-free methods, also called isoconversional methods, allow the determination of the activation energy E_a without previous knowledge of the kinetic model $f(\alpha)$ that fits the reaction mechanism. The isoconversional principle assumes that the reaction rate is only function of the temperature for a given extent of conversion (α). The Friedman method is the most commonly used isoconversional method that provides accurate values of the activation energies [145]. This method states that if the pressure term is avoided using an inert gas atmosphere, Eq. 23 can be written in logarithmic form as follows:

$$\ln\left(\frac{d\alpha}{dt}\right) = \ln\left(\boldsymbol{A}\boldsymbol{f}(\boldsymbol{\alpha})\right) - \frac{E_a}{RT}. \qquad \textbf{Eq. 25}$$

Then, at a constant value of α, $f(\alpha)$ would also be constant and provided that A is also constant, the activation energy E_a at a constant α value can be determined from the slope of the plot of the left-hand side of Eq. 25 against the inverse of the temperature, at different heating/cooling rates.

The next step is the determination of $f(\alpha)$, that is often obtained by a combination of model-Fitting with model-Free methods, which requires using the previously calculated E_a and some experimental data, obtained from TGA measurements under different heating rates with a predetermined set of kinetic models. The use of master plots is a well-known method to apply this methods combination. Master plots are reference theoretical curves only dependent on the kinetic model. The method consists in obtaining an experimental master plot from the TGA measurements. Thereafter, it is compared with the theoretical master plots, which reflects certain kinetics mechanisms and the closets are used to determine the kinetics mechanisms of the studied sample. Some of these kinetic mechanisms are order-based, nucleation, diffusion and geometrical contraction models, shown in Table 12.

Table 12. Algebraic Expressions for the *f(α)* functions for the most common mechanisms in Solid-State Reactions

Reaction model	Code	Mechanism	f(x)
Mampel (n^{th} order)	F1	Random nucleation followed by an instantaneous growth of nuclei	1-α
	F2		$(1-\alpha)^2$
	F3		$(1-\alpha)^3$
Power law	P2	Random nucleation and growth of nuclei through different nucleation and nucleus growth models	$2\alpha^{1/2}$
	P3		$3\alpha^{2/3}$
	P4		$4\alpha^{3/4}$
Avrami-Erofeev	A2		$2(1-\alpha)[-\ln(1-\alpha)]^{1/2}$
	A3		$3(1-\alpha)[-\ln(1-\alpha)]^{2/3}$
	A4		$4(1-\alpha)[-\ln(1-\alpha)]^{3/4}$
Diffusion	D1	Based on the penetration of reactant molecules through a layer of product	$1/2\alpha-1$
	D2		$[-\ln(1-\alpha)]^{-1}$
	D3		$3/2(1-\alpha)^{2/3}[1-(1-\alpha)1/3]^{-1}$
	D4		$3/2[(1-\alpha)-1/3-1]$
Contracting cylinder	R2	Phase boundary-controlled reaction	$2(1-\alpha)^{1/2}$
Contracting sphere	R3		$3(1-\alpha)^{2/3}$

Finally, the most common pressure dependence rate of many of reversible solid-state decompositions, applicable to metal oxides redox reactions can be presented as Eq. 26 [136]:

$$h(p) = (1 - \frac{P_{O2}}{P_{O2eq(T)}})^m , \qquad \textbf{Eq. 26}$$

where P_{O2} is the experimental oxygen partial pressure, $P_{O2eq}(T)$ is the oxygen equilibrium pressure, that only depends on the reaction temperature and the material under study, and the exponent *m* is the order of the pressure dependence term.

The exponent *m* can be determined by taking natural logarithms in both sides of Eq. 23, which leads to Eq. 27. Thereafter, applying the isoconversional method for a given *α* at different gas pressures and plotting both sides of Eq. 27, it is possible to obtain the exponent *m* from the slope of the plot.

$$\ln\left(\frac{d\alpha}{dt}\right) - \ln(A) + \frac{E_a}{RT} - \ln(f(\alpha)) = m \cdot \ln\left(1 - \frac{P_{O2}}{P_{O2eq}}\right). \qquad \textbf{Eq. 27}$$

7.3.3 Reduction reaction rate modelling

In order to determine the kinetic parameters of the reduction reaction of $(Mn_{0.99}Si_{0.01})_2O_3$ two different programs were carried out. The first program consisted in five runs at different heating ramps under N_2 atmosphere (p_{O2} approaching to zero) (Fig. 60a). Inert atmosphere was used to avoid the influence of the pressure term *h(p)* on the reaction rate. The second program consisted in five runs at 10 ˚C/min using different oxygen partial pressures, ranging from 0.8 to 0.1 bar (Fig. 60b), aimed to determine the influence of the pressure term *h(p)* on the reaction rate.

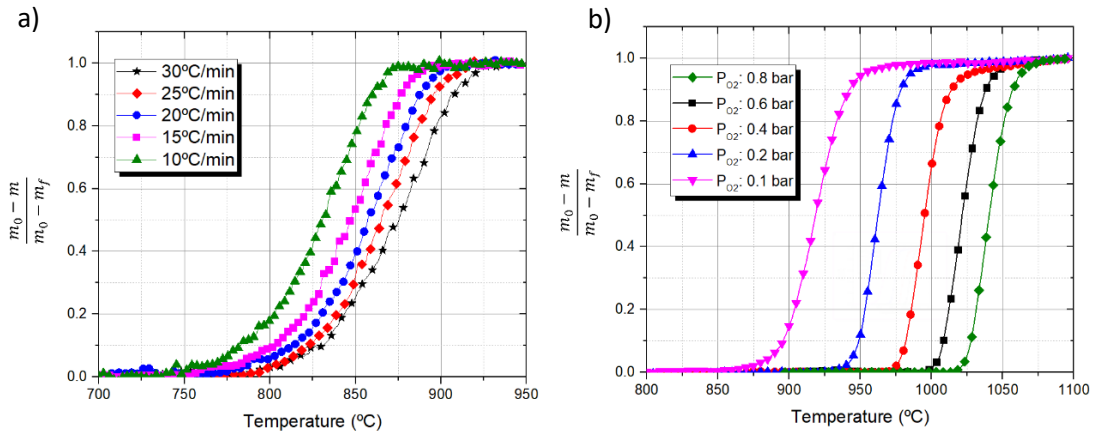

Figure 60. Reduction of $(Mn_{0.99}Si_{0.01})_2O_3$: a) at 10, 15, 20, 25 and 30˚C/min heating rates in N_2 and b) under O_2 partial pressures ranging from 0.1 bar to 0.8 bar at 10˚C/min

Then, using the STA experimental data and applying the Friedman isoconversional method, it was possible to determine the E_a value. Fig. 6 plots the left term of Eq. 4 against 1000/T at different extent of reduction reaction (α) and heating rates. E_a was determined from the slope of the curves.

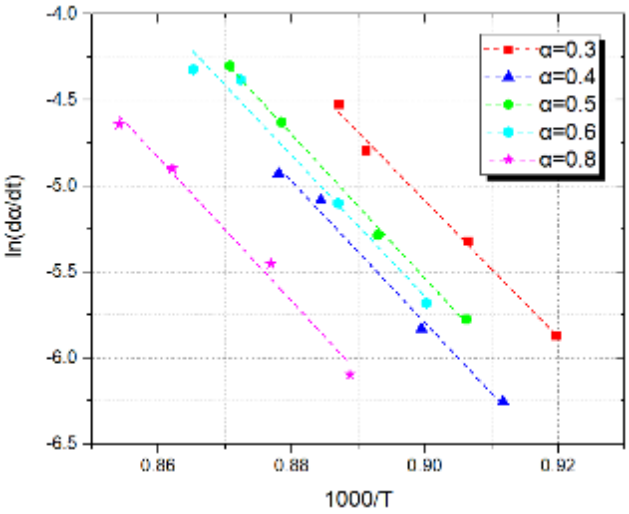

Figure 61. Friedman plots of $(Mn_{0.99}Si_{0.01})_2O_3$ reduction reaction at different reaction extents (α).

All the plots were almost linear and independently of the conversion extent the corresponding activation energy showed quite stable values with an average value of 341.726 ± 11.3 kJ/mol (Fig. 70). This value is higher to the ones reported by Francis et al. (106.36 kJ/mol) [132], Botas et al. (254.14 kJ/mol) [133] and Alonso et al. (303 kJ/mol) [134] for Mn_2O_3. However, a slightly higher value was reported by Carrillo et al. for a Mn-Fe mixed structure (371.2 kJ/mol), linking it to the observed 47˚C reduction onset temperature increase [113]. This fact is also consistent with the 26˚C increase on the reduction onset temperature observed in our samples. In order to provide more insights into this onset temperature increase, the reduction of $(Mn_{0.99}Si_{0.01})_2O_3$ was compared to the reduction of pure Mn_2O_3 using the same temperature program under N_2 atmosphere in the STA. We observed that the reduction onset temperature difference disappears in these conditions, occurring approximately at 740°C in both samples. Taking into consideration that almost no oxidation is expected during this temperature programs, the reduction onset temperature increase observed under air atmosphere in the Si-doped sample (Fig. 57), may be explained by the counteracting effect caused by the

improvement of the oxidation reaction kinetics, which delays the oxygen release detection to a higher temperature value during the heating program.

Once the E_a was determined, it was possible to assess the reaction mechanism using the so-called experimental master plots. Comparing the different theoretical reaction models given in Table 2 with the data gathered during thermogravimetric experiments, it could be observed that it did not agree with any theoretical model (Fig. 62). The same observation was reported by Pestalozzi and Carrillo et al., who proposed the use of the Sestak-Berggren (SB) model to achieve better accuracy [95] [113]. The SB model is a mathematical description of most of the possible solid-state reaction mechanisms, proposed by Sestak and Berggren in 1971 [146]. It uses an empirical formula with three exponents (n, m, and p), which are properly selected to fit the resulting model curve to the experimental results. In general, the SB model does not provide information regarding the mechanisms involved in the reaction but it constitutes a flexible tool to model almost any reaction process [147]. On the other hand, the sigmoid-shape of the α plots shown in Fig. 60a and 60b are commonly related to nucleation and growth mechanisms, which was also observed by Francis and Alonso in their kinetic study of Mn_2O_3 reduction reaction [132] [134]. Nevertheless, further investigation is required to ascertain the reaction mechanisms involved in the reduction reaction of $(Mn_{0.99}Si_{0.01})_2O_3$. Applying the SB model to our experimental data, it can be observed that the SB function fits the experimental data when m = 0.1, n = 1.15 and p = 0.05. Thus, *f(α)* can be written as:

$$f(\alpha)_{red} = \alpha^{0.1} \cdot (1-\alpha)^{1.15} \cdot [-\ln(1-\alpha)]^{0.05}. \qquad \textbf{Eq. 28}$$

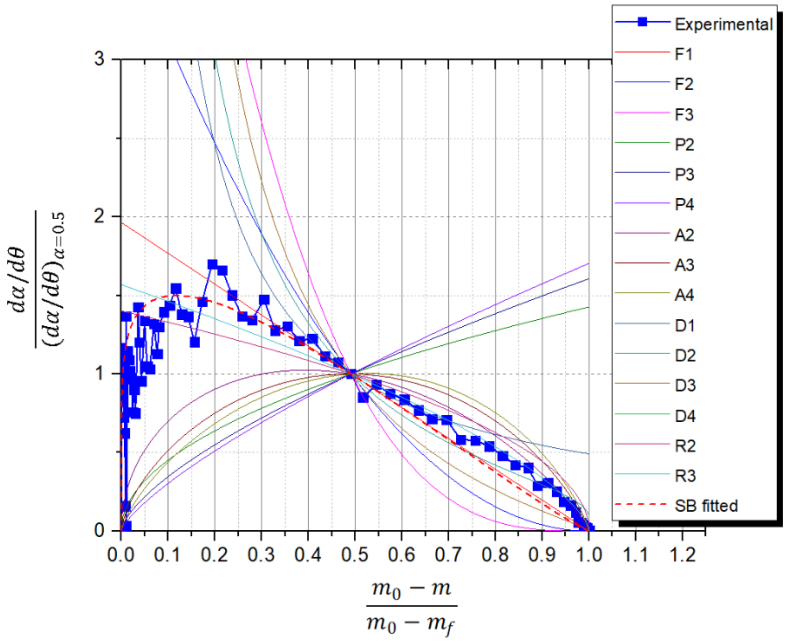

Figure 62. Theoretical master plot curves based on the differential form and experimental data from TGA run at 20˚C/min fitted to SB function with m = 0.1, n = 1.15 and p = 0.05.

Once *f(α)* was determined, it was possible to calculate the last term of the so-called "kinetic triplet" from Eq. 25, which is the pre-exponential factor *A*. It was determined by numerical curve fitting based on a minimization of the sum of error squares, resulting in an average value equal to $3.8 \cdot 10^{15}$ min^{-1}.

In the final step, the dependence of the reaction rate on the gas pressure, associated to the exponent *m* in the term *h(p,)* was identified using dynamic measurements in different O_2/N_2 gas atmospheres. In order to get different O_2 partial pressures, O_2 and N_2 different gas flows were introduced in the STA instrument at the same time. The total gas flow rate used was 100 mL/min, varying the O_2 and N_2 gas flow rates from 100 ml/min to 10 ml/min, resulting in a $O_2/(N_2+O_2)$ content ratio variation from 1 to 0.1. Firstly, it was required to identify the denominator of Eq. 5 ($P_{O2\ eq(T)}$), which correlates the oxygen partial pressure and the equilibrium temperature. For that purpose, six runs at 20˚C/min, 2˚C/min and 1˚C/min at different partial pressures were carried out. The equilibrium temperature of the reaction was calculated plotting the different curves at the same partial pressure and extending the resulting trend to a heating rate close to 0˚C/min (Fig. 71). In a similar approach, Wokon et al. used an exponential trend plot [107], nevertheless we found that a power function trend given by Eq. 29 fitted better with the equilibrium temperatures given by Mattison et al. for Mn_2O_3 [148].

$$P_{O2\ eq\ red} = 8 \cdot 10^7 \cdot e^{-23.13\left(\frac{1000}{T}\right)}. \qquad \textbf{Eq. 29}$$

The corresponding results of Eq. 29 at different temperatures are showed in a Van't Hoff plot (Fig. 63), together with the values reported by Mattisson et al. for Mn_2O_3. The resulting onset temperatures of the reduction reactions present very similar values compared to the values reported by Mattisson et al., nevertheless, taking into consideration the methodology used, these values should be taken only as an approximation for the purpose of the present work.

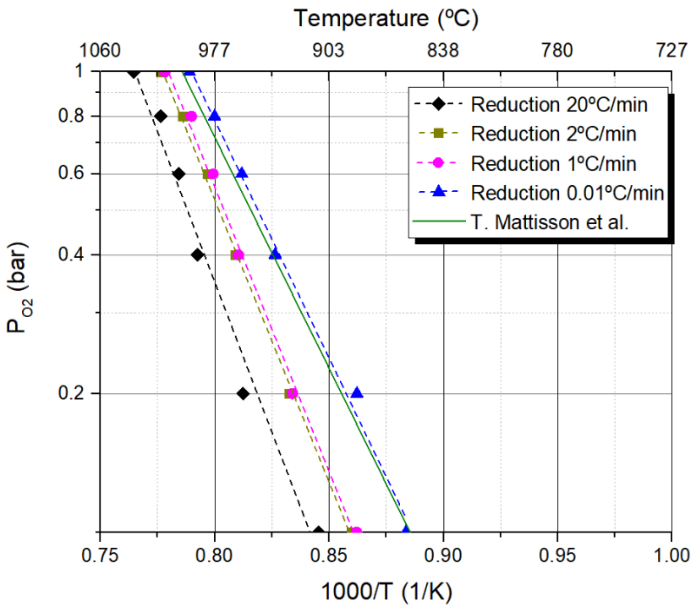

Figure 63. Correlation between oxygen partial pressures and experimental reduction reaction onset values for $(Mn_{0.99}Si_{0.01})_2O_3$ at different heating rates vs thermodynamic equilibrium temperatures for Mn_2O_3 given by Mattisson et al. **[148]**.

Henceforth and in order to determine the exponent *m*, dynamic measurements at 10˚C/min at several oxygen partial pressures ranging from 0.8 to 0.1 bar have been used in this work (Fig. 58b). Plotting both sides of Eq. 27 and applying the isoconversional method for different α, the exponent *m* was obtained from the slope of the resulting curve (Fig. 72), returning an average value of 7.05.

Based on the previous calculations, the resulting reaction rate model equation for the reduction step of $(Mn_{0.99}Si_{0.01})_2O_3$ is represented by the following expression:

$$\frac{d\alpha_{red}}{dt} = 3.8 \cdot 10^{15}\ min^{-1} \cdot e^{\left(-\frac{341.72\frac{kJ}{mol}}{RT}\right)} \alpha^{0.1} \cdot (1-\alpha_{red})^{1.15} \cdot [-\ln(1-\alpha_{red})]^{0.05} \cdot \left(1-\frac{P_{O2}}{8\cdot10^7 \cdot e^{-23.13\left(\frac{1000}{T}\right)}}\right)^{7.05} \quad \textbf{Eq. 30}$$

Thereafter, Fig. 64a illustrates the corresponding comparison between the experimental results and the predictions obtained from Eq. 30, concerning the reduction of $(Mn_{0.99}Si_{0.01})_2O_3$ in N_2 at different heating rates. On the other hand, Fig. 64b depicts the comparison between the model predictions and the experimental results at different O_2 partial pressures. From the plots, we can extract that the model predictions fit correctly during most of the reaction conversion extent, without significant errors on the predictions. We found small deviations of the predicted values for α > 0.8, which increase with increasing oxygen partial pressure. These deviations may be explained by the fact that initially, the reaction rate may be controlled mainly by nucleation and growth mechanisms, but as reaction proceeds, if the oxygen is not properly removed by the flowing gas, there is an increase in the oxygen concentration around the particles. Therefore, the oxygen partial pressure increases locally inside the sample and the reaction becomes closer to the equilibrium, turning the slower external oxygen diffusion into the controlling reaction mechanism, decreasing the reaction rate. As the difference to equilibrium decreases with increasing gas partial pressure (see Fig. 63), this effect is larger in the case of oxygen rich environments. This fact was also reported by Hamidi et al. [108], Varsano et al. [37] and Schoenfelder and Swisher [149] and may be attributable to the measuring conditions induced by the common laboratory analyzers used (TGA and STA).

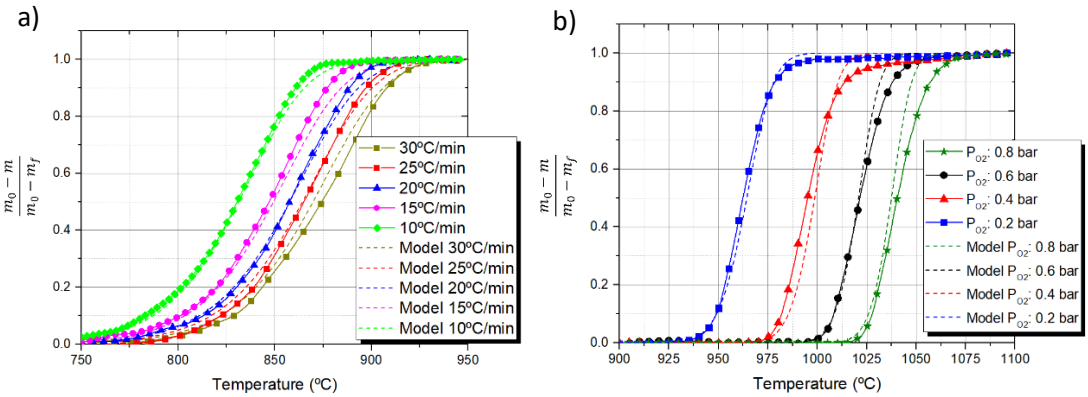

Figure 64. Comparison between experimental data and model prediction results for reduction of $(Mn_{0.99}Si_{0.01})_2O_3$: a) at different heating rates in N_2 (P_{O2}=0), and b) at different O_2 partial pressures. Continuous lines correspond to experimental data and doted lines to model predictions.

7.3.4 Oxidation reaction rate modelling

In order to obtain the kinetic parameters concerning the oxidation reaction of $(Mn_{0.99}Si_{0.01})_2O_3$, two sets of isothermal programs were used. The first one consisted on five oxidation isothermal steps at different temperatures ranging from 650˚C to 750˚C under O_2 atmosphere (p_{O2} approaching to 100%). The α-time plots of the oxidation reactions are illustrated in Fig. 65a. The second program consisted on six isothermal oxidation steps at 675˚C under different oxygen partial pressures, ranging from 1 bar to 0.1 bar (Fig. 65b). In both set of programs, to prevent any material oxidation during the

cooling step, the material was reduced firstly under N_2 atmosphere and the gas was switched to the relevant N_2/O_2 mixture once the isothermal condition was stabilized, 5 min after reaching the target temperature.

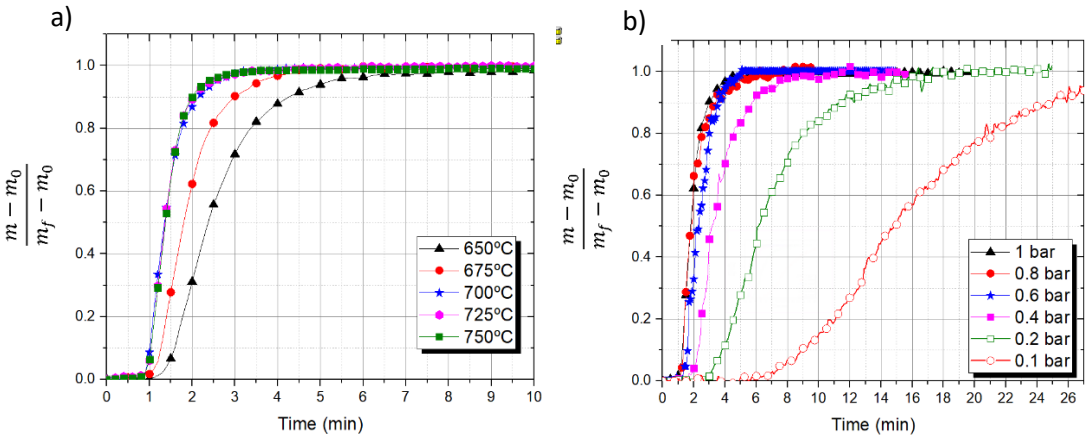

Figure 65. Oxidation of $(Mn_{0.99}Si_{0.01})_2O_3$: a) at 750, 725, 700, 675 and 650˚C in O_2 and b) at 1, 0.8, 0.6, 0.4, 0.2 and 0.1 bar of oxygen partial pressure at 675˚C

In case of isothermal experiments, the reaction model can be assessed by applying the master plots method regardless of the E_a [143]. Hence, comparing the different theoretical reaction models in the differential form (Table 2) with the thermogravimetric experimental data, no good match is found in the whole extent of reaction. This fact raises some difficulties to determine a reliable reaction mechanism from these plots (Fig. 73). The experimental curve approximates to an Avrami-Erofeev model during the first 2/3 of reaction, while for higher extent of conversion, it fits better to a diffusion model, meaning that there may be a change on the reaction controlling step for $\alpha > 0.8$. The particular configuration of the testing instrument and crucible geometry where the oxygen intake proceeds only through the top of the sample, may be one of the reasons behind this change in the reaction controlling step. Pestalozzi demonstrated how different crucible geometries and gas flow directions may alter the reaction kinetics of Mn_2O_3 [95]. To confirm this statement, a homemade tubular reactor will be constructed and tested in a following work. In order to find a single and accurate expression for *f(α)*, a SB empiric model was used to approach to the oxidation experimental data. Fig. 66 depicts the comparison of the oxidation at 700˚C between the experimental master plots with theoretical A2, D3 and SB model (fitted with $m = 2.7$, $n = 0.5$ and $p = -1.85$). As can be deduced from the plots, the SB model gets a better match with the experimental data. Therefore, *f(α)* can be written as Eq. 31.

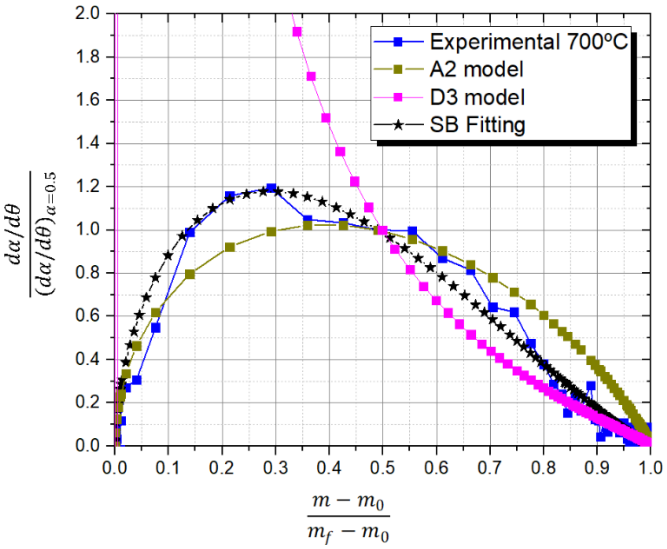

Figure 66. Comparison between master plot built with oxidation experimental data from STA at 700˚C and theoretical Avrami-Erofeev A2 model, D3 model and SB function with m = 2.7, n = 0.5 and p = -1.85.

$$f(\alpha)_{ox} = \alpha^{2.7} \cdot (1-\alpha)^{0.5} \cdot [-\ln(1-\alpha)]^{-1.85}. \qquad \text{Eq. 31}$$

In the case of the oxidation reaction, the determination of a unique E_a value for a broad range of temperatures using the Friedman isoconversional method may lead to an inaccurate kinetic model. Nonlinearity of Arrhenius plots close to the equilibrium temperature has been reported for nucleation driven phase transitions in reversible processes [150]. Carrillo et al. observed, in their work regarding the investigation of $(Mn_{0.8}Fe_{0.2})_2O_3$ reaction kinetics in air, a significant kinetic deceleration of the oxidation reaction when approaching to the reaction equilibrium conditions. In their Friedman isoconversional plot, the curve presented two different behavior zones, one up to 725˚C following an Arrhenius behavior with an average E_a value of 74 kJ/mol, and another from 725˚C up to 800˚C with a positive slope, turning into a negative E_a value [113]. Considering these results, they provided a SB kinetic model only valid for temperatures below 725˚C, far from equilibrium conditions, corresponding to the Arrhenius behavior. This zone close to the equilibrium conditions belongs to the so-called 'technical hysteresis' and is characteristic of some metal oxides. In this zone, the effective reaction rate is almost negligible meaning that the forward and backward reaction rates become similar. In addition, it has been shown that the reaction behavior under the technical hysteresis zone maintains a strong relationship with the oxygen partial pressure, especially significant in the case of the oxidation reaction [107]. This material behavior in the hysteresis zone has been barely studied, Shenouda and Aziz ascribed it mainly to particle shrinkage [151], where oxygen diffusion into the lattice encounters physical barriers that limit the rate of the reactions, but further work is required to find an appropriate model to replicate the material response within this zone. Studying a similar manganese-iron oxide composition, Wokon et al. deduced a SB oxidation reaction kinetic model for $(Mn_{0.75}Fe_{0.25})_2O_3$, providing satisfactory predictions in a higher temperature range than Carrillo, between 805.2 and 891.2˚C and pressures between 0.15 and 0.4 bar. In this temperature range, the material still presented an Arhenious behavior providing an E_a value in air of 463.53 kJ/mol. It is worth to say that Wokon et al. used granulated particle sizes between 1 to 3 mm, while the material used by Carrillo et al. was in the form of fine powder. Higher particle size has been shown to increase the oxidation reaction onset temperature [139] and therefore, it may become the main reason of the technical hysteresis reduction observed in the work of Wokon et al.. On the other hand, the E_a was obtained at

temperatures 3 times closer to equilibrium compared to that of Carrillo, which may explain the high difference in the E_a value. These results are in agreement with the work of Liavitskaya and Vyazovkin where they demonstrated the dependencies between the activation energy and temperature, over dehydration reversible reactions [152]. In order to reproduce this relationship in a prediction model, they introduced the isoconversional activation energy value $E_{\alpha,}$ according to Eq. 11, which permits establishing a link between the effective activation energy of the overall process and other parameters of the individual steps such as temperature and pressure.

$$E_{a(p)} = E_a + \Delta H_r \frac{P_{O2eq}}{P_{O2eq} - P_{O2}} \qquad \text{Eq. 32}$$

Considering these findings, in our work, to determine an effective activation energy representing a broader range of temperatures and partial pressures, we applied the isoconversional activation energy concept to our results. Firstly, we followed the Friedman isoconversional method to obtain the E_a in a temperature range far from the equilibrium (954˚C in O_2), trying to avoid the effect of the technical hysteresis zone. Then, to include the effect of the partial pressure, we applied the correction factor given by Liavitskaya and Vyazovkin in Eq. 32 to obtain E_α. The determination of the correction factor requires previous determination of the oxidation reaction equilibrium pressures and reaction enthalpy (ΔH_r).

Then, in order to obtain an E_a value far from equilibrium, we applied the Friedman isoconversional method using the experimental oxidation results at different isothermal conditions under O_2. Fig. 67 depicts the left term of Eq. 25 versus 1/T at different α values, E_a is obtained from the slope of the curve. Regardless of the conversion state, all the curves present a kinetic exponential trend up to ≈700˚C, followed by a slope change at 730˚C, which means entering into the hysteresis zone, similar to the behavior reported by Carrillo et al. in their study concerning a similar sample morphology [113]. E_a is determined from the slope of the Arrhenius zone, before the slope starts to decay, corresponding to temperatures below 700˚C and presented a stable value of 120.42 ±17 kJ/mol (Fig. 74). The E_a values reported by Wokon et al. (463.53 kJ/mol) and Carrillo et al. (74 kJ/mol) corresponded to manganese iron oxides, so they can be taken only as a reference. Compared to our measurements, they were measured closer and farther to equilibrium conditions, respectively, so our result that lies in between, may agree with the statement given by Liavitskaya and Vyazovkin, regarding the decrease of the E_a with increasing temperature difference to the equilibrium.

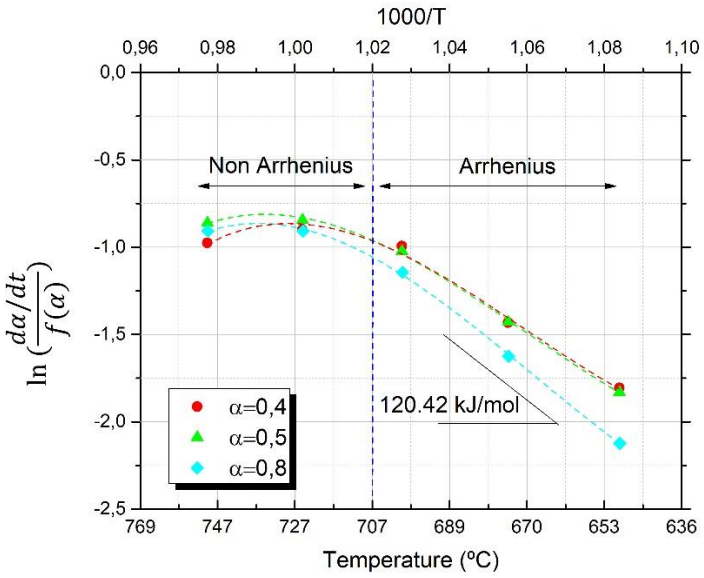

Figure 67. Friedman plots of $(Mn_{0.99}Si_{0.01})_2O_3$ oxidation reaction at different reaction extents (α).

To determine the reaction enthalpy (ΔH_r), it is necessary to identify the oxidation reaction equilibrium conditions. For this purpose, several programs at different cooling rates under different oxygen atmospheres were launched. The corresponding correlations between oxygen partial pressures and experimental reaction temperature threshold values at different cooling rates are plotted in Fig. 75 and derives to the power function formula showed in Eq. 33. Extrapolating the power trend to a cooling rate approaching 0˚C/min, we obtained the equilibrium temperature at different oxygen partial pressures depicted in a Van't Hoff diagram (Fig. 68) together with the equilibrium values reported by Mattisson et al. for Mn_2O_3 [148]. It can be observed that the resulting onset temperatures of the oxidation reaction of $(Mn_{0.99}Si_{0.01})_2O_3$ are far away from the values reported by Mattisson et al., which was also observed by Wokon et al. in their kinetic study of $(Mn_{0.75}Fe_{0.25})_2O_3$. They attributed this difference to a profound slowdown of the oxidation reaction when approaching to the equilibrium [107], which was also observed in our work (Fig. 68). Hence, the parametrization of $P_{O2eq}(T)$ proposed and represented by Eq. 33, cannot be identified as thermodynamic equilibrium of the $(Mn_{0.99}Si_{0.01})_2O_3$ system and it is only used for the purpose of this work.

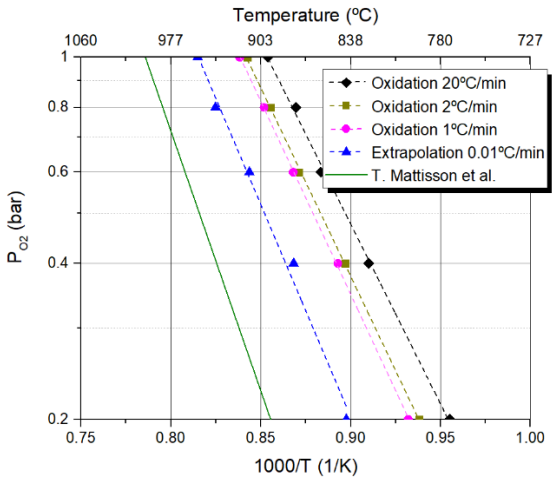

Figure 68. Correlation between oxygen partial pressures and experimental oxidation reaction onset values for $(Mn_{0.99}Si_{0.01})_2O_3$ at different cooling rates. Thermodynamic equilibrium temperatures for Mn_2O_3 given by Mattisson are included **[148]**.

$$P_{O2\ eq\ ox} = 5 \cdot 10^6 \cdot e^{-18.87\left(\frac{1000}{T}\right)}. \qquad \textbf{Eq. 33}$$

Thereafter, using the equilibrium approximation values given by Eq. 33, ΔH_r has been calculated plotting the logarithmic partial pressures (P_{O2eq}/P_{O2}) against the reciprocal temperatures at thermodynamic equilibrium, according to Van't Hoff equation (Fig. 76). This plot gives a linear plot, which slope is proportional to the standard reaction enthalpy, obtaining a value of 156.88 kJ/mol, which is very similar to the values obtained in the STA measurements.

Based on these results, $E_{\alpha(P)}$ can be represented by the following expression:

$$E_{\alpha(P)} = -120.42 + 156.88\frac{P_{O2eq}}{P_{O2eq}-P_{O2}}\ . \qquad \textbf{Eq. 34}$$

Finally, introducing the previous calculations in Eq. 23, the oxidation reaction rate model returns the following expression:

$$\frac{d\alpha_{ox}}{dt} = 1.7 \cdot 10^7\ min^{-1} \cdot e^{\left(-\frac{E_{\alpha(P)}}{RT}\right)} \cdot {\alpha^{2.7}}_{ox} \cdot (1-\alpha_{ox})^{0.5} \cdot [-\ln(1-\alpha_{ox})]^{-1.85}\ . \qquad \textbf{Eq. 35}$$

Fig. 69a and 69b illustrate the corresponding experimental results and the predictions obtained from Eq. 69 concerning the oxidation of $(Mn_{0.99}Si_{0.01})_2O_3$ in O_2 at different isothermal programs (Fig. 65a) and at different O_2 partial pressures under isothermal conditions at 675˚C (Fig. 65b). Examining the model results, there is a good match between the experimental and model results even at temperatures closer to the equilibrium. The model is able to predict the reaction kinetics in the whole range of examined temperatures and partial pressures, modelling accurately the kinetics acceleration and deceleration when approaching to the hysteresis zone. Nevertheless, the effective reaction rate undergoes a strong deceleration for temperatures above 750°C that may not be reproduced by Eq. 35, so a deeper insight into the hysteresis zone would be required to get a model able to accurately represent the material behavior under the whole hysteresis zone. It is worth to add, that the model predictions present small deviations for $\alpha > 0.8$, which may be attributable to the identified change in the reaction controlling mechanism. We found that for a high extent of conversion

the diffusion mechanism may become the controlling step of the reaction, where applying SB models have been shown to lead to some inaccuracies [153].

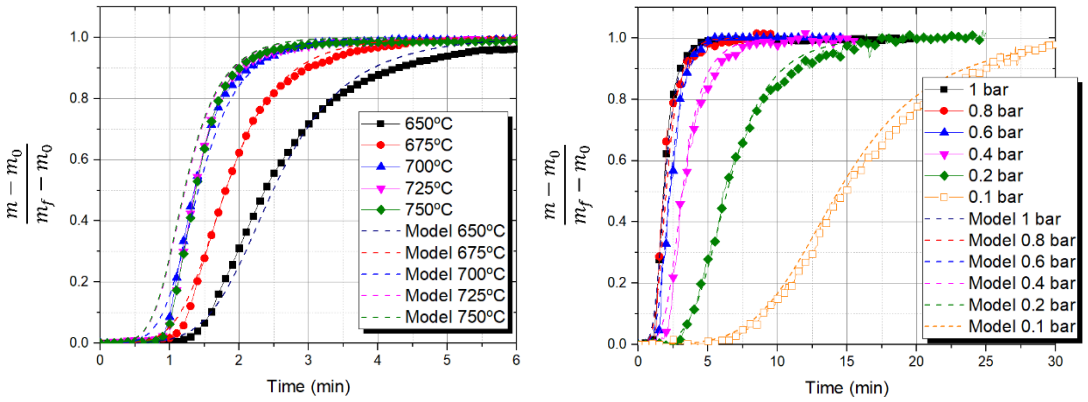

Figure 69. Comparison between experimental data and model prediction results during oxidation of $(Mn_{0.99}Si_{0.01})_2O_3$: a) at different isothermal programs in O_2 (P_{O2}=100), and b) at different O_2 partial pressures at 675˚C. Continuous lines correspond to experimental data and doted lines to model predictions applying Eq. 35

7.4 Conclusions

In this work, $(Mn_{0.99}Si_{0.01})_2O_3$ was studied for thermochemical energy storage in concentrated solar power plants. The results from thermogravimetric analysis were compared to the behaviour of pure Mn_2O_3, showing a slight increase in the reaction onset temperatures with no significant variation of the energy storage density (147.15 – 149.32 J/g). Nevertheless, the main difference observed was the much faster and stable oxidation reaction kinetics of $(Mn_{0.99}Si_{0.01})_2O_3$ under air atmosphere, which led to a consistent reversibility under an 80 redox cycles program in a thermobalance. Subsequently, a complete study of reduction and oxidation kinetics of $(Mn_{0.99}Si_{0.01})_2O_3$ was carried out, trying to ascertain accurately the three components of the reaction rate equation, namely k(T), f(α) and h(P). The resulting modelling expressions showed a satisfactory kinetic parametrization of each process, suitable for future thermochemical reactor modelling. Our modelling results show that nucleation and growth mechanism is the controlling step of the reduction and oxidation reactions up to 80% conversion. After that, the reaction rates are either controlled by the slower external or internal diffusion of oxygen, that may be imposed by the limited capacity of the testing crucibles and instruments to bring or remove oxygen in and out the sample, which would probably not happen in a tubular reactor. The oxidation kinetics is highly affected by the equilibrium conditions and presents a temperature threshold while cooling with a substantial change on the activation energy. This fact can lead to inaccurate models if a unique value of the activation energy is selected and used for parametrization of the reaction rate and reactor modelling. For an accurate determination of the oxidation kinetic model, the recent developed concept of 'isoconversional activation energy' has been applied, obtaining accurate results in the whole range of temperatures and pressures studied in this work. Overall, the developed methodology demonstrates a full flexibility, accuracy and improved capabilities able to simulate different operation conditions, in novel concentrated solar power plants environments with the corresponding boundaries and requirements. In addition, the methodology and findings showed in this work may be applicable not only to the material under study, but also to other similar systems and thermochemical energy storage materials as well.

7.5 Supplementary information

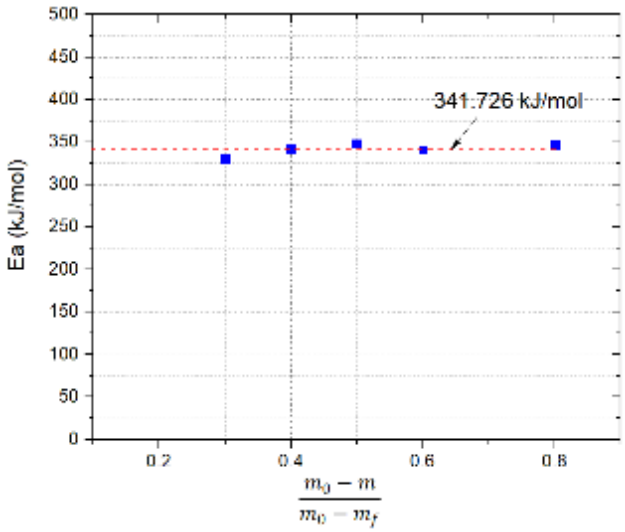

Figure 70. E_a values at different degrees of conversion for $(Mn_{0.99}Si_{0.01})_2O_3$ reduction reaction.

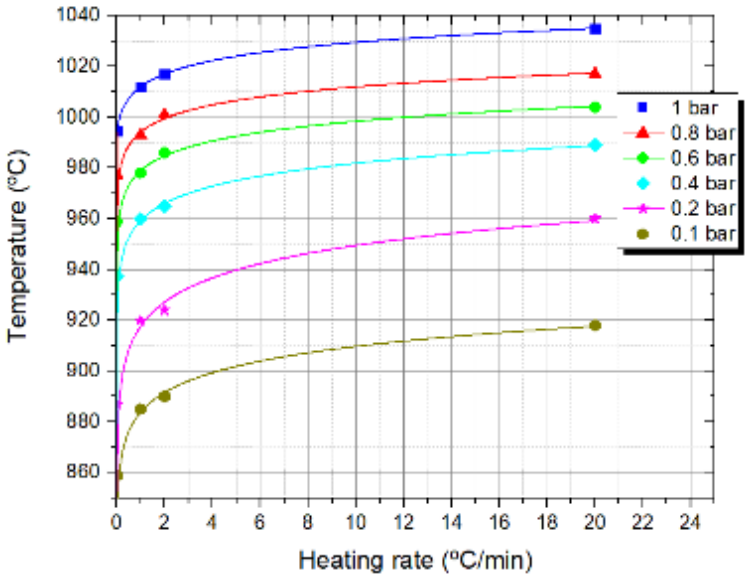

Figure 71. Experimental onset temperatures of the reduction reaction for various oxygen partial pressures vs different heating rates and extrapolated temperature value for a heating rate of 0.01˚C/min.

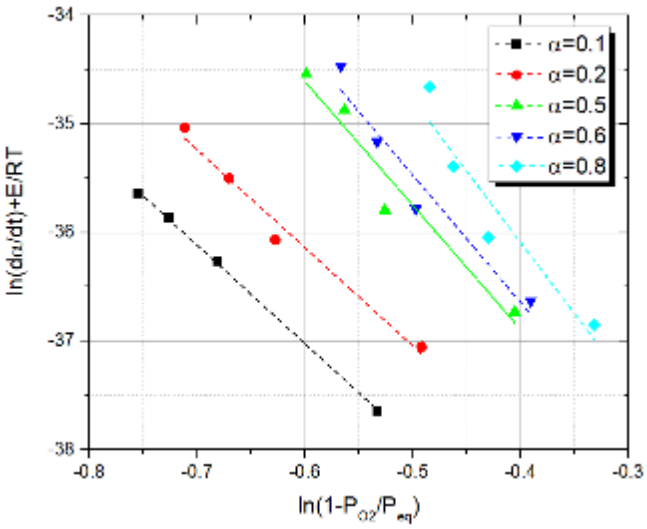

Figure 72. Double logarithmic plot of Eq. 6 corresponding to dynamic measurements of $(Mn_{0.99}Si_{0.01})_2O_3$ reduction at 30˚C/min at oxygen partial pressures between 0.8 and 0.1.

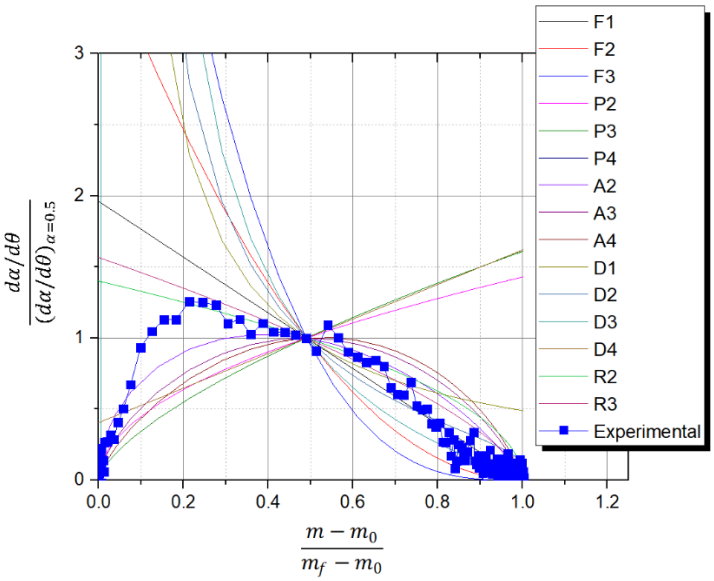

Figure 73. Theoretical master plot curves based on the differential form and experimental data from oxidation reaction run at 700˚C in the STA

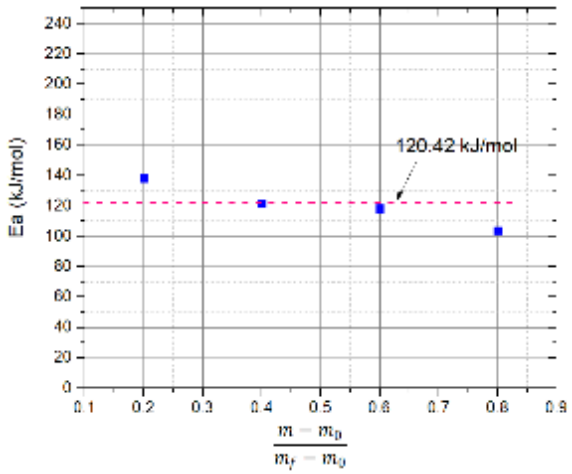

Figure 74. E_a values at different degrees of conversion for $(Mn_{0.99}Si_{0.01})_2O_3$ oxidation reaction below 700˚C.

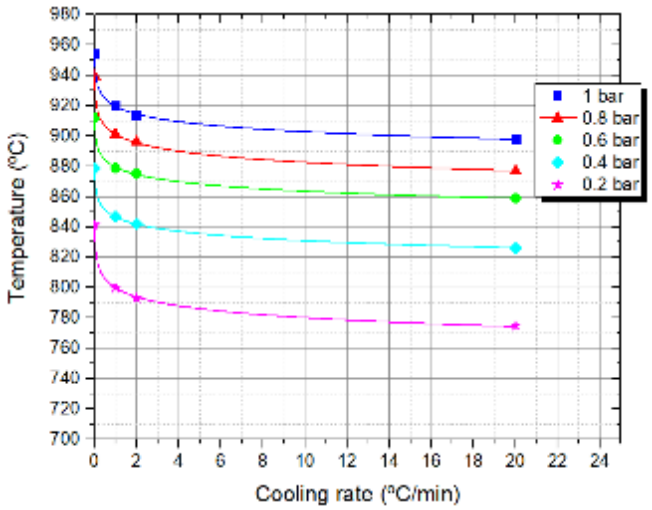

Figure 75. Experimental onset temperatures of the oxidation reaction for various oxygen partial pressures vs different heating rates and extrapolated temperature value for a cooling rate of 0.01˚C/min.

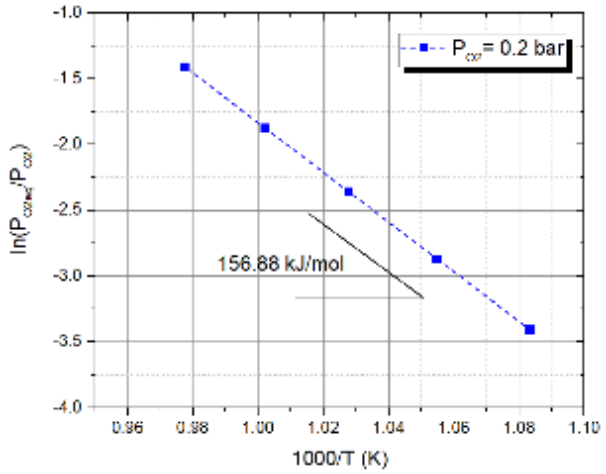

Figure 76. Correlation between logarithmic partial pressures ($P_{O2}eq/P_{O2}$) against the reciprocal temperatures for the oxidation reaction of $(Mn_{0.99}Si_{0.01})_2O_3$

CHAPTER 8. Development of the granulation process and experimental tests

The whole content of this subclause has been recently sent for publication to Solar Energy journal, with the tittle: '*New insights into Mn_2O_3 based metal oxide granulation technique with enhanced chemical and mechanical stability for thermochemical energy storage in packed bed reactors*', currently under the peer review process.

8.1 Introduction

The step from the lab-scale experiments to prototyping requires finding out a proper preparation route which allows the transformation of the thermochemical metal oxide from the powder state to a consistent material unit, in order to make feasible its utilization into a real scale thermochemical reactor. Considering that adding a support material decreases the volumetric energy storage density and may deactivate the thermochemical material by undesired chemical reactions, we present a comprehensive study of the granulation technique proposed by Gigantino et al. [70] and we applied it to Si-doped manganese oxide. This method allows the preparation of spherical porous granules of the active material from powder, which showed satisfactory behavior for the redox pair CuO/Cu_2O. In a previous work we demonstrated the improved kinetics and chemical stability of Si-doped manganese oxide in powder state, representing a promising material candidate for technology upscaling [137], which stores and releases heat according to the following equation:

$$\mathbf{6}(Mn_{0.99}Si_{0.01})_2O_3(s) + \mathbf{149}\ J/g \leftrightarrow \mathbf{4}(Mn_{0.99}Si_{0.01})_3O_4\ (s) + \ O_2\ (g) \qquad \text{Eq. 36}$$

The investigation carried out in the present work aims to identify all the effects of the different granulation synthesis parameters on the material behavior, paying special attention to the chemical and mechanical stability and to increase the active material content of the granules, providing new insights into a potential TcES material preparation route for large scale packed bed thermochemical reactors. In the first part of the work, we evaluate the influence of the different synthesis route parameters on the material behavior, from the kinetics to the chemical stability and mechanical behavior of the granules. Subsequently, granules exhibiting the most promising properties were selected for the upscaling study where 8 g of the material was subjected first to 50^{th} redox cycling study in a lab-scale packed bed reactor. Finally, a sample of the tested granules were subjected to additional 50 redox cycles in a STA to analyze in detail their chemical stability after a total of 100 redox cycles. The satisfactory results observed concerning granules mechanical and chemical stability represent a step forward in high temperature thermochemical energy storage upscaling, that can be applicable not only to the material under study but to other metal oxides.

8.2 Granules synthesis route

The synthesis process applied, based on the methodology developed by Gigantino et al. [70], consists of the following three steps: i) synthesis step, where the precursors are transformed in a fine powder of the desired material, ii) granulation step, where spherical granules are produced, and iii) hardening step, consisting in a sintering process to enhance the mechanical stability of the granules.

First, Si-doped manganese oxide samples were synthesized by a sol-gel method, following the procedure described in a previous work [154]. The subsequent granulation technique is based on preparing a mixture of this metal oxide powder and a solution of a polymeric binder and a solvent.

Subsequently the mixture is introduced dropwise through a syringe into a precipitating bath, where the drops harden while the solvent leaves the granule. After drying, the granules are calcined to remove the remaining organic matter and to enhance their mechanical stability. As a consequence, the space occupied by the binder becomes empty and then, porous solid granules are obtained. The following two conditions shall be met: the solvent must be miscible with the precipitation bath and the polymeric binder must be soluble in the solvent and insoluble in the precipitation bath. The preparation steps are illustrated in Fig. 77.

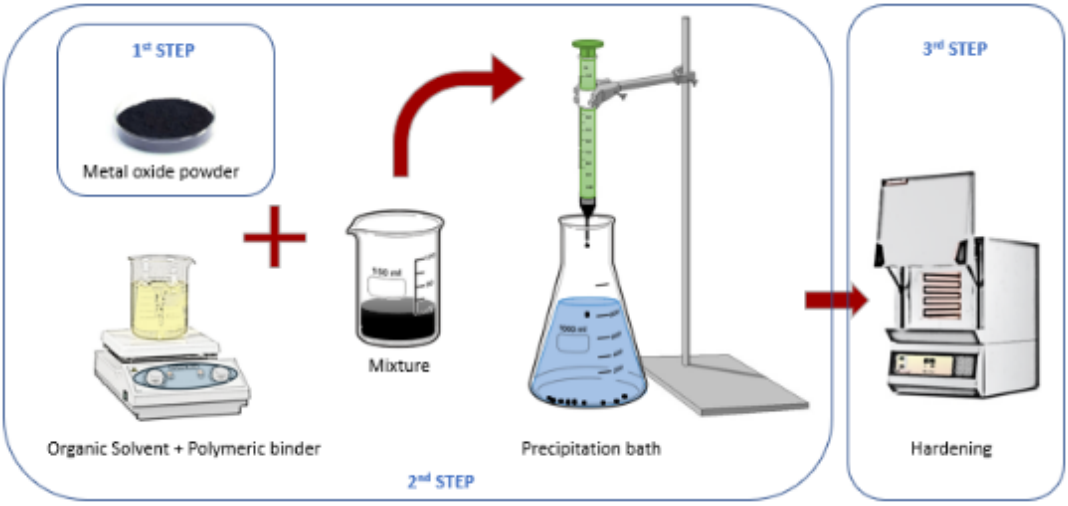

Figure 77. Metal oxide spherical granules preparation route

Various granules of Si-doped Mn_2O_3 were prepared varying the proportions of the metal oxide (MO), organic solvent (OS) and polymeric binder (PB) with the aim of finding the best preparation route giving spherical shape granules with good mechanical and chemical stability. The PB used was ethyl cellulose (Sigma Aldrich) and the OS 1-methyl 2-pyrrolidinone (>99% Sigma Aldrich). The precipitation bath was made of deionized water, mixed with a surfactant (Tween 80, Sigma Aldrich) to reduce its high surface tension and to promote the solvent exit from the granule.

It was found that for the amounts of MO used (< 1 g), the ratio OS:PB shall be maintained in the range 9:1. Lower and higher OS:PB ratio led to inconsistent granules in the precipitation bath and after the hardening step, respectively. In principle, the amount of MO in the granules is important because it might affect directly to the energy storage density, so high proportions are preferred. Nevertheless, high MO proportions (MO/MO+PB > 0.7) increase the viscosity of the mixture resulting in tile-like granules (Fig. 78a), being not practical to increase the MO proportion above 0.8, since the viscosity imposes significant difficulties to the solution to flow out of the syringe. In order to reduce the viscosity and maintain a high MO content, the OS+PB mixture was heated at 40°C, contributing to improve the sphericity of the granules (Fig. 78b). The distance between the precipitation bath and the syringe tip affected the granules in two ways: distances > 5cm resulted in coin-shape granules due to high mechanical shock when the granules reached the precipitation bath surface, and distances < 2 cm do not allow the granules to penetrate the bath and remain floating in the surface for some time. Therefore, a distance of 3 cm was selected for all the samples. The diameter of the syringe tip has a strong influence on the final size of the granules, which should be maintained below 1:10-20 of the reactor diameter in order to avoid gas channelling inside the thermochemical reactor [155]. Therefore, a tip diameter of 2 mm was used, resulting in granules within the average diameter range of 3-4 mm after step 2. Removing the water during the drying step became critical, since it was observed that the

water content after the synthesis process may reach up to 80 wt% of the total granule mass and its extraction can destroy the granule sphericity, unless it is carried out slowly. For that reason, the granules were dried at room temperature until the water content was almost totally removed. Subsequently, the granules were subjected to a temperature program consisting in heating up to 450°C at 1°C/min, followed by an isothermal step for 4 h to remove the organic matter (Fig. 78c). The final hardening step consisted in another heating step at 2°C/min up to the corresponding calcination temperature, where different isothermal steps were used to promote particle sintering. A noticeable granule shrinkage was observed during the water and organic matter removal steps, being greater the fewer the content of MO, resulting in granules with a final size of around 1-3 mm of diameter. Table 13 shows the different materials prepared in this work.

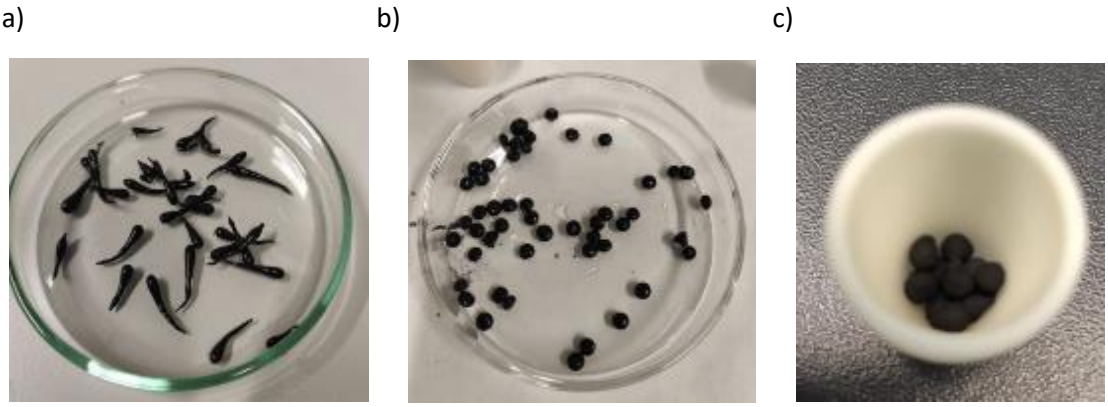

Figure 78. Granules of Mn_2O_3 prepared by the drop technique: a) pronounced tile-like granules, b) spherical granules and c) granules after the calcination step at 450°C

Table 13. Description of materials prepared in this work

Description	MO Proportion (wt %)*	Diameter (mm)
Powder	1	N/A
MO 50	50	1,83
MO 70	70	2,34
MO 80	80	2,46

*MO proportion (wt %) = MO/(MO+PB)

8.3 Experimental setup

The experimental test rig consists of two main parts: the heating setup and the thermochemical reactor (Fig.79a). The generation of a controlled gas flow rate above 800°C required to carry out the reduction and oxidation of the material may become a complex issue and therefore, a furnace placed around the thermochemical reactor carries out the heating/cooling process. The furnace setup temperature was varied between 550°C and 800°C at a heating/cooling rate of 20°C/min and the reactions were conducted switching the gas flow between N_2 and O_2. The thermochemical reactor consists on an AISI 304 metal tube of 15 mm of inner diameter and 400 mm length. Around 8 g of MO were placed in the middle of the tube length. Silicon carbide particles were placed below and above the MO, filling completely the reactor, preventing any movement or fluidization of the MO. Once the gas stream crosses the reactor, it is cooled down in a water bath and subsequently, the oxygen content is measured by means of a zirconia gas analyzer KCD-ON320 (Sensorstecnics). The

reactor includes five temperature measuring points at different heights: T2, T3 and T4 placed inside the reactor at the positions indicated in Fig. 79a and $T2_{out}$ and $T4_{out}$ placed on the exterior surface of the reactor at the same height of T2 and T4, respectively. The signals were collected with an acquisition system type ABSD-MD832-81-23-HLP (Yunrunyn) and registered by a homemade Labview app. The complete set-up is illustrated on Fig. 79b.

a) b)

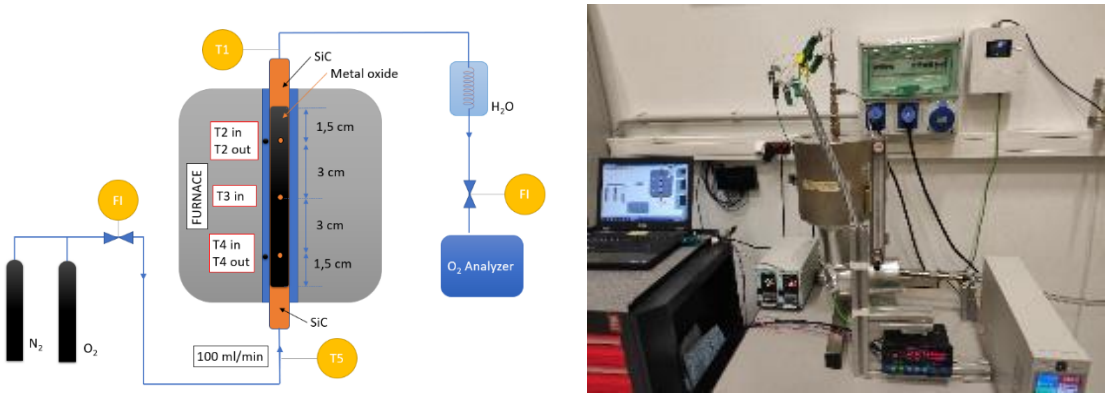

Figure 79. Thermochemical experimental setup: a) components diagram and b) setup photography

8.4 Results and discussion

8.4.1 Effects of the synthesis parameters on the granules behavior

A comprehensive study was made to assess the influence of the granule conformation, the MO content and the hardening step on the chemical and mechanical behavior of Si-doped Mn_2O_3 granules. In order to identify the influence of the granule conformation on the chemical behavior, the comparison of the mass loss/gain rate between the sample in powder and granule form during one redox cycle is plotted on Fig. 80a. In order to avoid the effects of the hardening step, the granules were subjected to a restricted temperature program up to 450°C for 4 h, aimed to remove the organic matter. As can be inferred from the TGA plot, the reduction reaction kinetics remains similar whereas the oxidation onset temperature is delayed to a lower temperature with a slight slow-down of the reaction kinetics. This effect cannot be attributed to particle sintering during the preparation of the granules since sintering of Mn_2O_3 becomes significant at temperatures above 900°C [137] and these granules were subjected to significantly lower temperature. Therefore, the results suggest that the particle densification in the granule may have a slight negative impact on the oxygen diffusion rate. This phenomenon, however, does not affect the reversibility of the samples, since after the redox cycle the mass of both samples was equal to their respective initial masses.

Considering that it has been shown that the sintering is the main reason of the cyclability loss in these materials [96], the hardening program shall be carefully selected to get enough mechanical stability of the granules avoiding critical thermochemical cyclability loss. The resulting granules should have enough mechanical stability to withstand the mechanical stresses occurring in a packed bed reactor while their porous structure should facilitate oxygen diffusion and exchange during system charging and discharging. The influence of the hardening step on the chemical performance of the granules was studied by subjecting the samples to three different temperature programs: 1050°C for

4h, 1050°C for 8h and 1100°C for 4h, and observing their behaviour under 1 redox cycle (Fig. 80b). Again, the reduction reaction did not show any significant variation caused by the hardening step. It should be noted that the granular samples presented a slight decrease on the reduction extent compared to the sample in powder state. This fact can be attributed to an incomplete Si-doping during the synthesis process of the powder, which is further developed during the hardening step of the granules, leading to the formation of more inactive Mn-Si-O bonds and thus, reaching a more chemically stable structure. The same effect was observed in a previous work [137]. On the other hand, the harsh temperature conditions applied caused an additional slow-down on the oxidation reaction kinetics, more pronounced at the second half of the reaction, which will be further analyzed in the cyclability studies. Nevertheless, similar mass gain profiles were observed independently of the hardening program used. This fact may suppose an important advantage since increasing the temperature or the time exposure does not affect negatively the chemical performance, whereas it is expected to significantly improve the mechanical stability.

a) b)

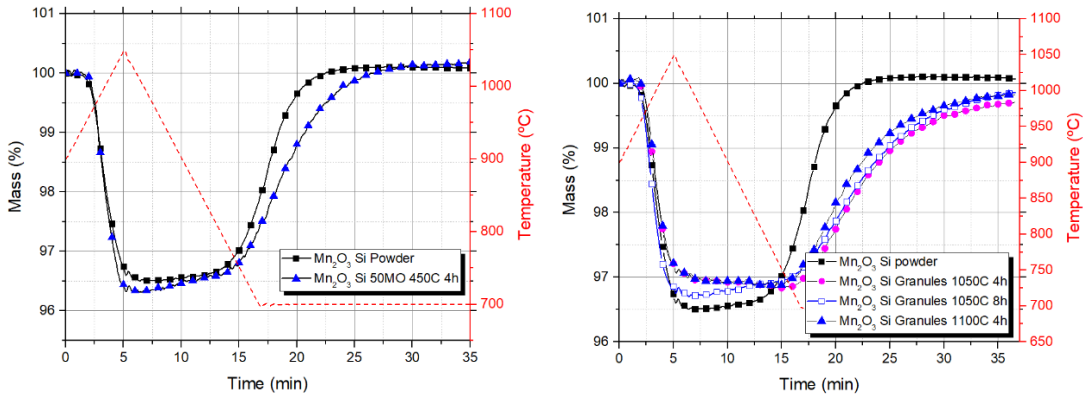

Figure 80. TGA plot of 1 redox cycle to: a) Mn_2O_3-Si powder and Mn_2O_3-Si granules calcined at 450°C for 4h and b) Mn_2O_3-Si powder and Mn_2O_3-Si granules calcined at 1050°C for 4h, 1050°C 8h and 1100°C for 4h.

The effect on the chemical behavior of the MO content in the granules was studied over three samples with the following MO:PB ratios: 50:50, 70:30 and 80:20, calcined at 1050°C for 4h. The three samples together with the sample in powder state were subjected to one redox cycle and the TGA results were overlapped and plotted in Fig. 81a. As can be observed, the reduction reaction kinetics for the three granular samples remains is comparable to the the powder sample. However, the oxidation reaction kinetics exhibits remarkable differences. The higher the MO content the faster the oxidation kinetics, with the sample containing 80% of MO exhibiting a similar performance to the powder sample. It would be expected that the granules with the lowest MO content and consequently, the highest PB content, would present higher voids after PB removal and thus, the oxygen diffusion would encounter less obstacles leading to a faster kinetics. Nevertheless, the removal of water, OS and PB led to a significant decrease of the granule size, as can be observed in Fig.81b and consequently, of the porous volume. This reduction in volume was greater with the decrease of MO content, leading to lower pore volume, which would hinder the oxygen diffusion into the particles.

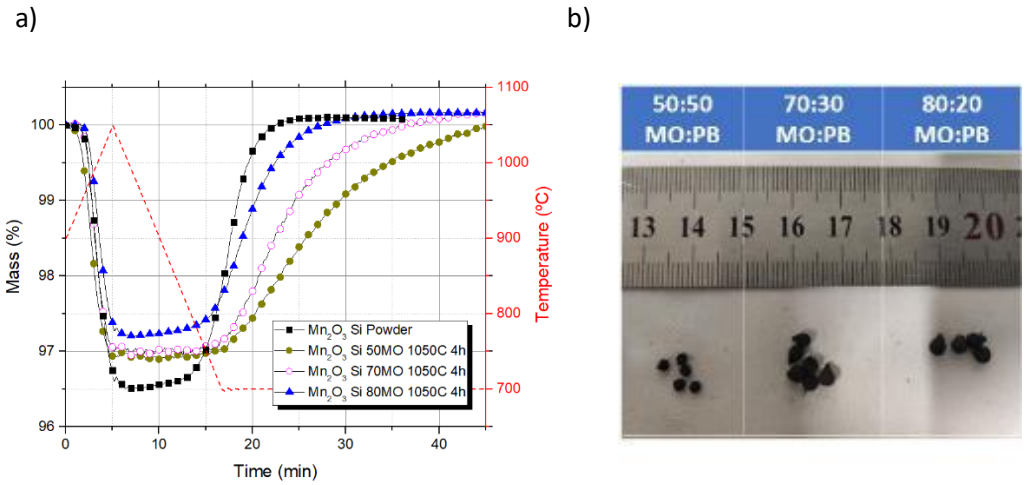

Figure 81. a) TGA plot of 1 redox cycle to Mn_2O_3-Si powder and Mn_2O_3-Si granules calcined at 1050°C 4h with different MO:PO proportions (80:20, 70:30 and 50:50) and b) Mn_2O_3-Si granules picture with different MO:PO proportions (80:20, 70:30 and 50:50)

In a previous work, Mn_2O_3 1% Si-doped material showed good chemical stability over 40 redox cycles in the form of powder. Nevertheless, taking into consideration the results observed in the TGA measurements, the influence of both the particle densification in the granules and the hardening step will be evaluated prior to upscale the solution to the thermochemical lab-scale reactor. For this purpose three batches of granules were prepared with a MO content ratio 70:30 (MO:PB) and calcined at 1050°C for 4h, 1050°C for 8h and 1100°C for 4h. The chemical stability of the three samples together with the sample in the form of powder were studied over 10 redox cycles in a thermobalance. In this case, Mn_2O_3 Si-doped sample in the form of powder showed a significant reversibility improvement compared to that of pure Mn_2O_3 sample (Fig. 82a and 82b), similar behavior was observed in a previous work, where Si acted as a sintering inhibitor and oxidation accelerator [137]. The three granular samples showed complete reversibility over 10 redox cycles (Fig. 82c, 82d and 82f), meaning that neither the granule shape nor the hardening program have a significant negative impact on the reversibility of the material, as was the case of Mn_2O_3 pure samples. In this case, the positive effects of doping Mn_2O_3 with Si, counteracted the barriers imposed by the granulation and the hardening program to the oxygen diffusion inside the material, improving the material chemical stability. This effect is confirmed if the oxidation reaction kinetics is analyzed in detail throughout the 10 redox cycles, where it can be observed that applying any of the hardening programs led to a negligible slowdown of the oxidation reaction kinetics no matter what calcination temperature or isothermal exposure time were used (Fig. 83). The dependence between the temperature program and the oxidation rate decay on manganese oxide was observed by Carrillo et al., where using 1050°C instead of 1000°C as the maximum temperature of the redox cycles led to a significant sintering of the particle grains and a complete deactivation of the manganese oxide sample studied [156]. Therefore, the observed tolerance of the Si-doped granules to high temperatures may represent a significant advantage to improve the mechanical stability without decreasing the chemical performance.

In order to provide more insights into the chemical stability of the granules, the particle morphology and the sintering effects were studied by SEM. Sintering effects on metal oxides are particle growth and densification. Both have been shown to constitute physical barriers that hinder the oxygen diffusion and thus, the reversibility of the reactions is deteriorated [30]. This deterioration is especially significant in the case of the oxidation reaction. Carrillo et al. attributed these negative consequences to the material exposition to the high temperatures required to carry out the redox reactions, causing an evolution from nano-sized particles to particles of several micrometers just after

30 redox cycles [96]. In the present work, the samples were exposed to a first isothermal high temperature hardening program during the granules preparation route to increase the granules crushing strength, followed by a second variable temperature program during cycling to check their chemical stability, involving reduction and oxidation of the sample. The SEM micrographs after the two thermal processes are presented in Fig. 84. As can be inferred from the SEM images, the particle morphology and particle size seem not to be affected by either the calcination temperature or the isothermal exposure time. This fact can be deduced from the similar TG measurement profiles of the three granular samples during the first redox cycle. Furthermore, the particle size remains stable after 10 redox cycles, which comes to confirm an effective sintering protection by Si-doping process.

Nevertheless, the resulting particle morphology after the redox cycles indicates that the sintering pathways during both temperature programs differ at some extent. Particle morphology after the hardening program presents a more loose and non-uniform size distribution of coarsened particles, whereas after the cycling program the particle morphology turned into a higher degree of coral-like array interconnected particles of similar size without a noticeable particle growth from the previous step. It has been observed, that after the 10^{th} redox cycle, the three samples presented a slight oxidation rate decay. This suggests that the woven net formed during the coral sintering pathway hinders the oxygen diffusion into the inner particles, causing a slight slow-down of the oxidation rate. It was shown that the material in the form of powder calcined at 800°C did not present neither this particle morphology evolution nor the oxidation rate decay over a 40 redox cycle program [137], which may significate that the particle morphology changes induced by the hardening program might weaken the sintering protection given by the Si-doping process. It is worth noting that the operating conditions imposed by the TGA laboratory instrument used can differ from the ones expected in a real packed bed reactor, being considerably less severe for the material. In order to get a complete reduction of the material in the TGA it was required to reach a maximum temperature more than 100°C above the reduction onset temperature of the material. This fact was already observed in a previous work, where isothermal programs did not get further material reduction once the isothermal temperature was reached [157]. The authors attributed to a deficient oxygen gas removal from the particles, caused by the specific configuration of the experiment, where the material is placed in a cylindrical crucible with just one open face. This arrangement may cause an oxygen partial pressure increase and consequently, as the distance to equilibrium decreases with increasing gas partial pressure, it requires a continuous temperature increase to keep reducing the material. A similar behavior was reported by Hamidi [108], Varsano [37] and Schoenfelder and Swisher [149]. Furthermore, the difficulties observed regarding the oxygen diffusion within the particles in the TGA instrument, of critical importance to carry out the oxidation reaction, should present evident improvements in a thermochemical reactor where the gas is pumped through the whole sample in a bottom-up flow. Therefore, the assessment of the chemical stability of the material shall be complemented with a study in a packed bed laboratory set-up.

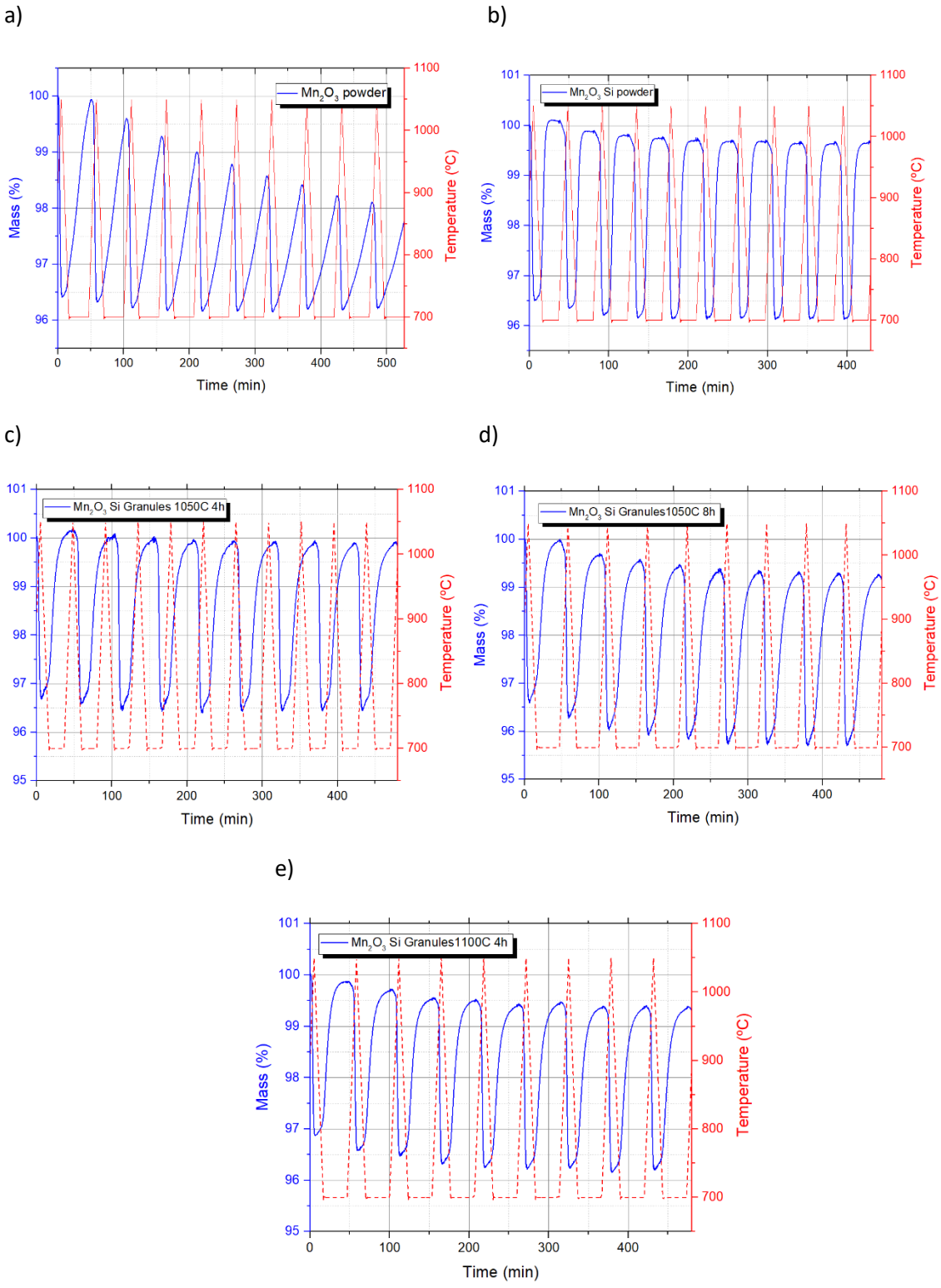

Figure 82. 10 Redox cycles of several Mn_2O_3-Si doped samples sintered at different temperatures: a) Mn_2O_3 powder, b) Mn_2O_3-Si powder, c) Mn_2O_3-Si granules sintered at 1050°C for 4h, d) Mn_2O_3-Si granules sintered at 1050°C for 8h, e) Mn_2O_3-Si granules sintered at 1100°C for 4h.

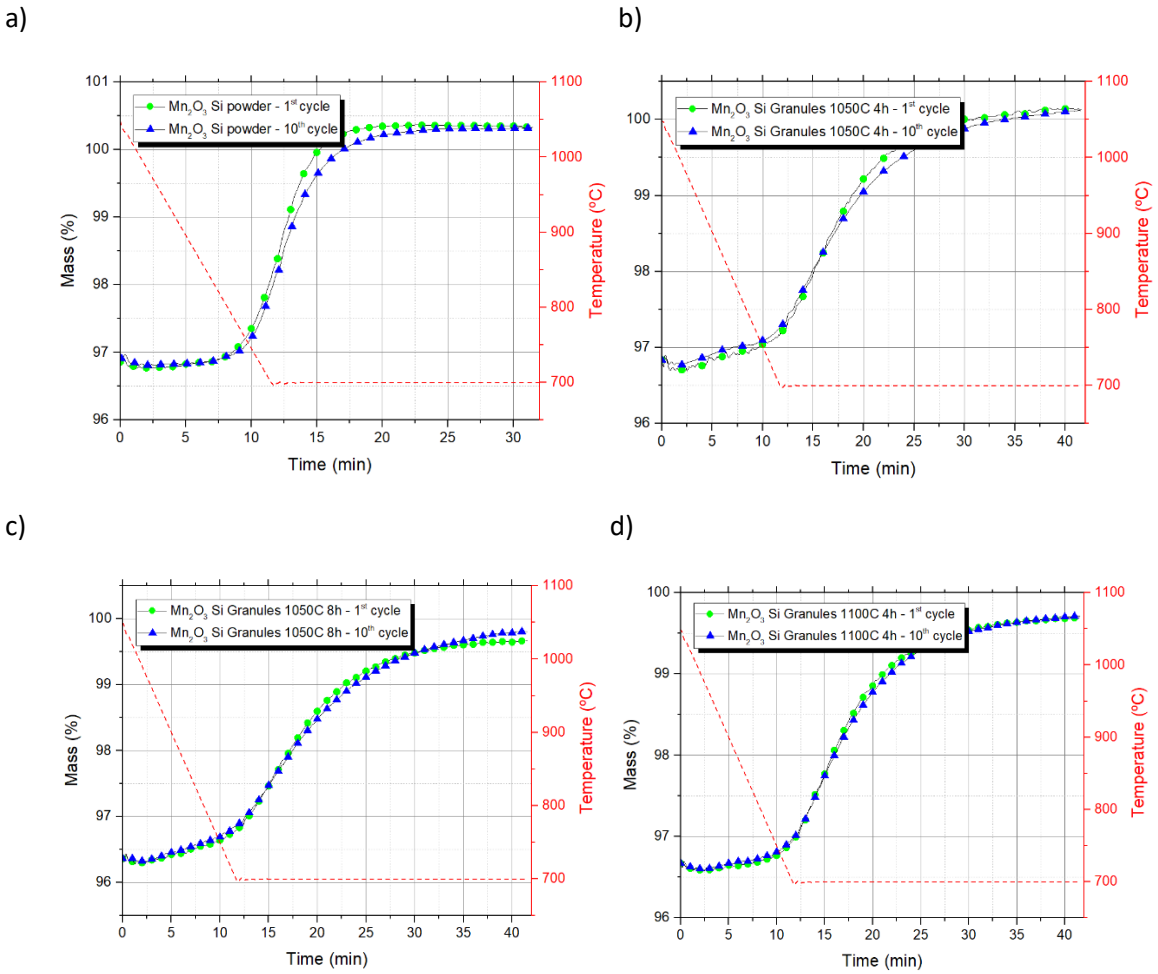

Figure 83. Oxidation reaction TGA plots during the 1st and 10th redox cycle of several Mn_2O_3-Si doped samples sintered at different temperatures: a) Mn_2O_3-Si powder, b) Mn_2O_3-Si granules sintered at 1050°C for 4h, c) Mn_2O_3-Si granules sintered at 1050°C for 8h, d) Mn_2O_3-Si granules sintered at 1100°C for 4h.

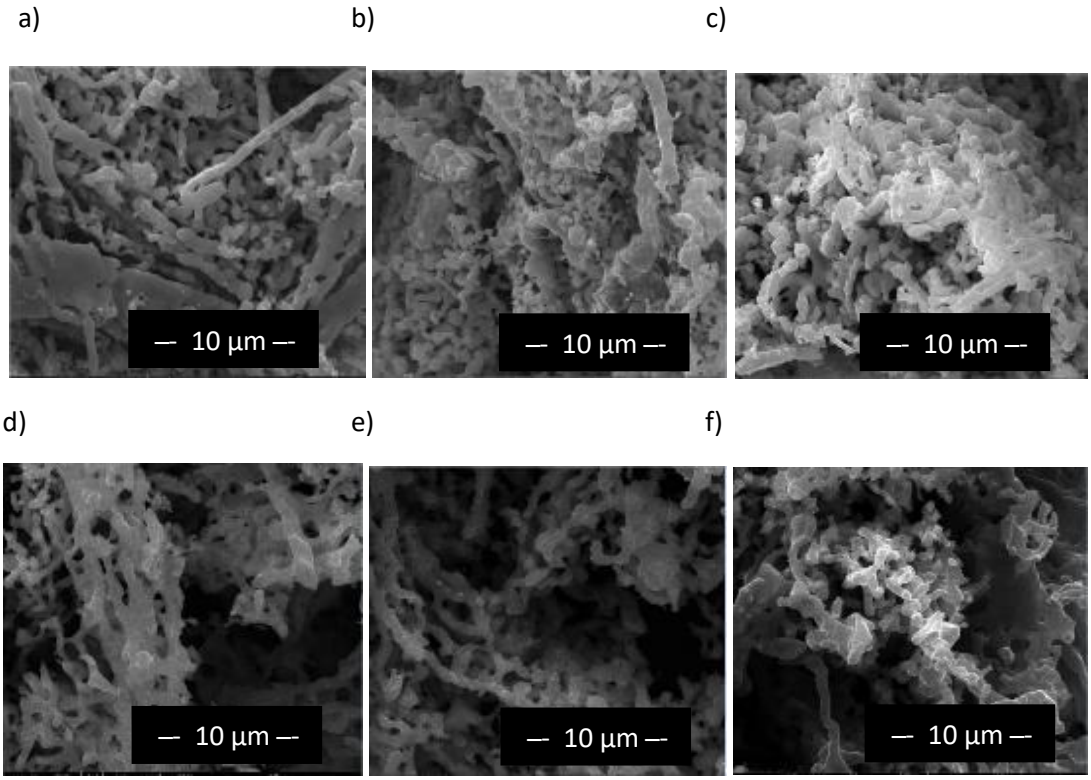

Figure 84. SEM images of the different Mn_2O_3-Si 70MO granules after exposition at different temperature programs: a) 1050°C for 4h, b) 1050°C for 8h, c) 1100°C for 4h, d) 1050°C for 4h and 10 redox cycles, e) 1050°C for 8h and 10 redox cycles and, f) 1100°C for 4h and 10 redox cycles

8.4.2 Packed bed thermochemical reactor experiments

8.4.2.1 Granules mechanical stress assessment

In order to assess the mechanical capability of the different calcined granules to withstand the mechanical stresses imposed by the lab-scale packed bed reactor set-up, a layer composed of 3 of the different set of granules was submitted to an increased weight through a flat plate until failure. The crushing strength results are shown in Table 14 and shall be taken only as a reference value for the particular configuration tested in the present work. To obtain an accurate value for the crushing strength specific lab device should be used (e. g. standard compression testing machine).

Table 14. Crushing strength of the granules calcined at different temperature programs

Sample id	Hardening program	Maximum weight	Crushing strength
MO 50	1050°C 4h	38 g	0,126 N
MO 50	1050°C 8h	44 g	0,146 N
MO 50	1100°C 4h	50 g	0,166 N

8.4.2.2 Selection of the granules for the packed bed reactor experiments

The reactor consisted on a stainless-steel tube of 13 mm of internal diameter and 90 mm height, turning into an effective volume of 11,9 cm^3. In order to determine the energy density contained in this volume it is necessary to measure the actual metal oxide content in the granules and the packed bed void fraction. The metal oxide content in the granules was determined using a reference volume of 1 cm^3. This volume was filled with granules of the different MO:PB ratios used and the bulk density and true density were measured using a helium pycnometer AccuPyc II 1340. It was observed that the maximum MO in the granules reached only 16.94%, likely caused by a deficient dissolution of the OS in the precipitation bath. In order to get an increase on the MO content another batch of granules was prepared decreasing the temperature of the bath by using ice in order to reduce the solubility of the PB (MO 50-c). The resulting granules got a significant MO content increase. The results are showed in the following table.

Table 15. Samples properties measurement over a reference volume of 1 cm^3

Description	Mass granule g	Diameter mm	Bulk density g/cm^3	True density g/cm^3	MO content %
Powder	N/A	N/A	0,3345	5,3236	N/A
MO 50	0,0023	1,835	0,735	5,116	14,38
MO 70	0,0055	2,342	0,828	5,0047	16,56
MO 80	0,0066	2,466	0,846	5,253	16,94
MO 50-c	0,002	1,396	1,402	5,653	24,81

Considering the size of the lab-scale reactor and the granules with the highest bulk density, the maximum amount of material that can be introduced in the reactor without applying pressure was a maximum of 8 g. Therefore, according to the data provided in Table 14, the three hardening programs provide to the granules with enough mechanical stability to withstand the mechanical stress imposed by the weight of the packed bed. Consequently, the granules with the highest MO content (MO 50-c) calcined at 1050°C for 4h, which in addition present a more homogeneous sphericity, were selected and synthesized for further cycling tests in the lab-scale reactor (Fig. 85).

Figure 85. Mn_2O_3 Si-doped granules 50:50 (MO:PB) for reactor testing: a) After step 2 of the synthesis route and b) After hardening at 1050°C for 4 h.

8.4.2.3 Packed bed reactor experimental results

A summary of the main reactor parameters is presented in Table 16.

Table 16. Lab-scale reactor parameters

Description	Value
Reactor radius	13 mm
Reactor length	90 mm
Particle diameter (d_p)	1,39 mm
Reactor mass	7,96 g
Bulk density	1,402 g/cm^3
Void fraction (ε)	0,59
Material storage density	149 J/g [154]
Storage capacity	0,33 Wh

In order to evaluate the chemical and mechanical stability of the granules in a packed bed arrangement, the reactor was subjected to 50 redox cycles consisting in of: i) a heating step up to 800°C at 20°C/min under 100 mL/min of N_2, ii) an isothermal step at 800°C for 20 min to ensure complete reduction of the material, since in a previous study, the reduction onset temperature in N_2 was identified at approximately 775°C [154], and iii) a cooling step down to 550°C with a cooling rate of 20°C/min under a gas flow of 10%/90% (N_2/O_2). In the same work it was observed that in such conditions, oxidation takes place in less than 5 min, so complete material oxidation is expected during the cooling step, before starting the following redox cycle. The temperature evolution at different points of the reactor and the oxygen content in the gas stream flowing out of the reactor were recorded by the instrumentation during the 50 redox cycles and are plotted in Fig. 86a. For better understanding, the same parameters comprising only the 3rd and 4th cycles are plotted in Fig. 86b.

In regard of the reduction reaction, it is difficult to obtain useful information from the temperature profiles of Fig. 86b, since it seems that reduction takes place when the furnace reaches the temperature set point and reduces the power input, which is followed by an abrupt temperature slowdown that makes it difficult to distinguish the effect of the endothermic reduction reaction in the temperature profiles of the internal thermocouples. The reaction occurrence can be ascertained from the oxygen variation measurement, since an increase of the oxygen content in the gas stream reaching a peak of 5% was detected. Nevertheless, the extent of the reaction cannot be evaluated, since integrating the area under the curve, it results in a value reaching only 6% of the theoretical oxygen release expected, considering a theoretical mass loss of 3%. In the case of the oxidation reaction, the internal recorded temperatures (T2, T3 and T4) present a slightly lower cooling rate than the temperatures recorded outside the reactor ($T2_{out}$ and $T4_{out}$) at the beginning of the cooling step. This fact can be caused by the exothermic nature of the oxidation reaction, even though the starting and finishing point of the reaction cannot be distinguished. Regarding the oxygen concentration, a slight variation during the oxidation reaction can be observed. The exact oxygen decrease cannot be accurately determined as a consequence of the poor sensor resolution. However, both evidences suggests that during the heating step reduction of the material is taking place, while in the cooling step the material is being oxidized.

The morphological evolution and physical integrity of the granules after the 50 redox cycles in the reactor was analyzed both by visual inspection (Fig. 86c) and SEM (Fig. 86d). None of the granules presented the reddish color typical of the reduction phase and thus, showing incomplete oxidation, maintaining their spherical shape after removing them from the reactor. As can be observed from the

SEM image, the particles have not suffered from noticeable sintering, since their size remain similar to their initial sate after the hardening step (Fig. 84a). Therefore, no reversibility loss would be expected. To confirm this statement three granules of the already cycled material in the reactor were subjected to an additional 50 redox cycles in the STA, using the same temperature program, completing a total program of 100 redox cycles. The mass loss/gain during the STA program together with a SEM image of the particles after the 100 redox cycles are shown in Fig. 87a and Fig. 87b, confirming no loss of the chemical stability of the granules with no noticeable change on the particle morphology.

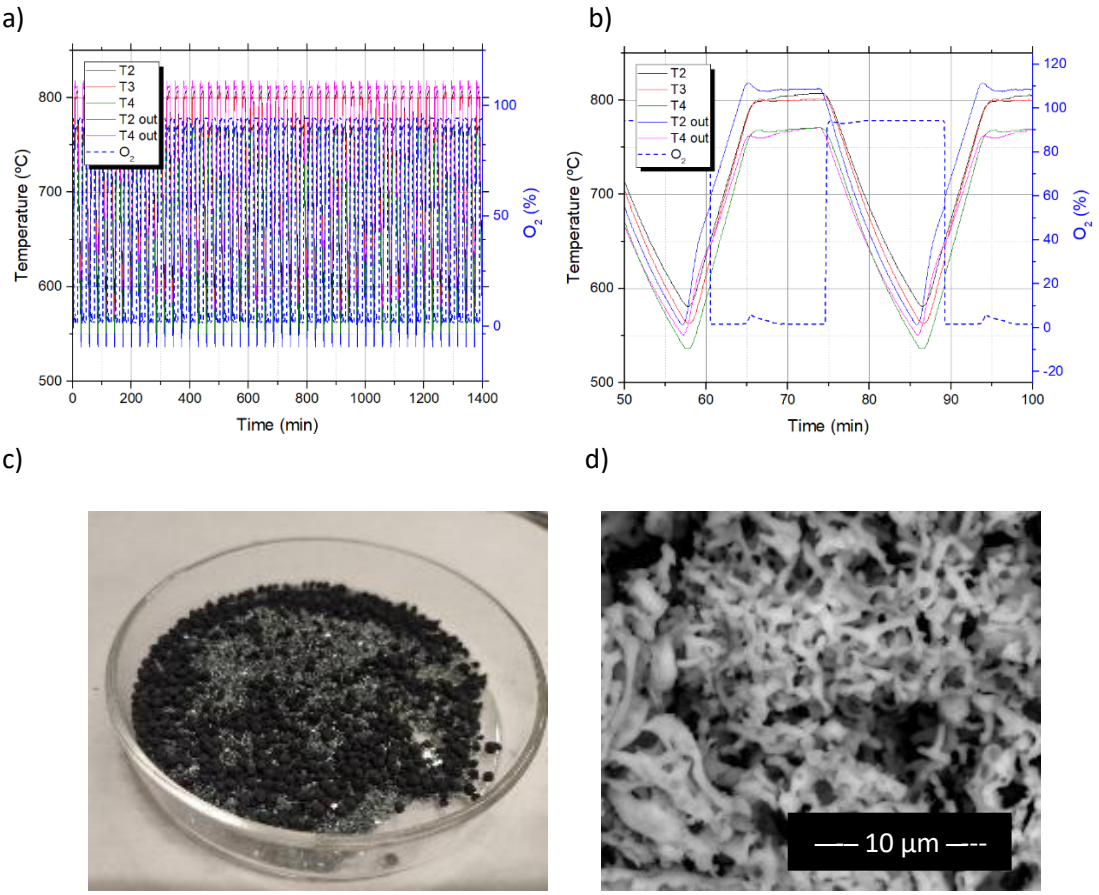

Figure 86. Si-doped Mn_2O_3 granules redox cycling in the thermochemical reactor: a) thermocouples signals record during the whole 50 redox program, b) magnification of the thermocouple signals and oxygen sensor during the 3rd and 4th redox cycle, c) Si-doped granules together with SiC particles appearance after cycling and removing from the reactor, and d) SEM image showing the morphological evolution after the 50th redox cycle

a) b)

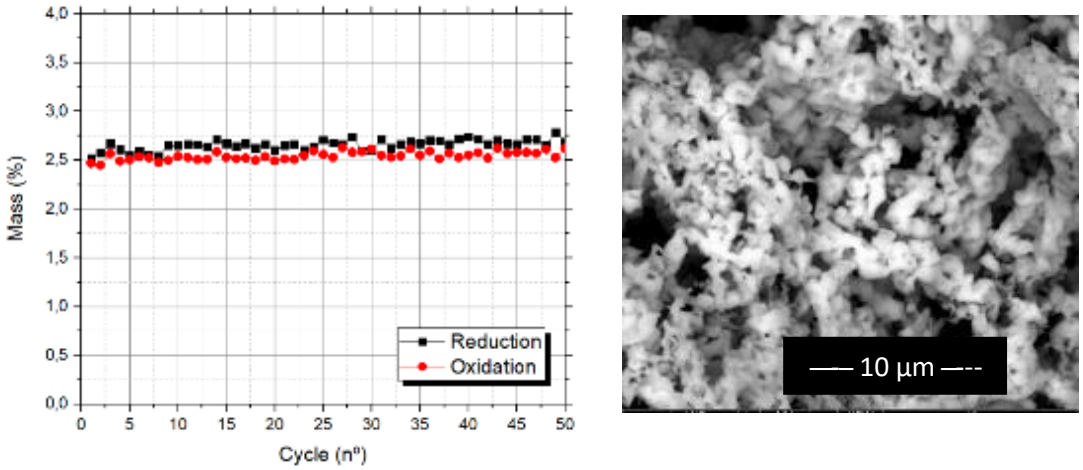

Figure 87. Si-doped Mn_2O_3 granules subjected to 50 additional redox cycles in the STA: a) mass loss/gain recorded in the STA, and b) SEM picture after the 50 additional redox cycles

8.5 Conclusions

In this work, a granule preparation route was studied for thermochemical energy storage upscaling using a novel Si-doped manganese oxide for concentrated solar power plants. The research work comprises material preparation and thermochemical performance evaluation in a lab-scale packed bed reactor. The process succeeded in obtaining spherical porous granules of 1-2 mm with different active material content. The results identify the critical parameters of the synthesis process which provide the best mechanical and chemical stabilities of the granules in order to be used in a thermochemical packed bed reactor. It was observed that the hardening step aimed to increase the mechanical stability of the granules does not affect significantly their chemical stability. This fact confirms that the severity of the hardening process could be further increased, leading to more mechanically stable granules, required for larger scale reactors. Furthermore, we observed that decreasing the solubility of the polymeric binder in the synthesis bath almost double the active material content in the granules and consequently, enhances the volumetric energy storage capacity. We achieved an active material content of 24.81%, and this result suggests that there is a way to keep increasing the energy storage density of the granules, which need to be further developed. In addition, 8 g of Si-doped granules were subjected to 50 redox cycles in a lab-scale packed bed reactor, showing satisfactory mechanical and chemical stability, which was confirmed over additional 50 redox cycles in a thermobalance, with complete re-oxidation over the whole program. In summary, both the Si-doped manganese oxide and the granule preparation route conducted have demonstrated enough reliability to be used on a larger scale and thus, contribute to push the high temperature thermochemical storage technology for a next generation of concentrated solar power plants

CHAPTER 9. Thesis conclusions

9.1 General conclusions

The research and technological communities rely on thermochemical energy storage as a step forward in the development of thermal energy storage technologies for new generation of concentrated solar power plants. Nevertheless, the technology is still on an early stage of development, facing unsolved issues mainly related with the material degradation over multiple charge and discharge cycles. The present thesis was focused on the development of a new approach to minimize this degradation, which would allow a significant progress on the development of the technology. In order to carry out the research work, metal oxides were selected, mainly due to the fact that air can be used both as heat transfer fluid and reactant. More specifically, we chose the redox pair Mn_2O_3 /Mn_3O_4 as the base of the work, since its toxicity is low and it is highly available becoming a low-cost material.

Firstly, the reduction and oxidation reactions of Mn_2O_3 were investigated under different conditions aimed to characterize and assess the kinetics and cycling behavior of this thermochemical material. The pair Mn_2O_3 /Mn_3O_4 is distinguished for a high temperature gap between reduction and oxidation reactions. Reduction takes place in the temperature range between 950°C and 1050°C in air, whereas oxidation takes place in the temperature range between 550°C and 750°C. Furthermore, **Mn_2O_3 presents a clear trend to sinter when it is subjected to the high temperatures required for redox cycling, hindering the reversibility of the material**. This fact was already shown by other authors, even though not always a reversibility loss was observed. Considering the results of this work, we observed in the STA that the heat storage capacity after 10 cycles was almost reduced to the half, caused by a continuous slowdown of the oxidation reaction which prevented the material to be completely oxidized during the temperature program. Overall, it was identified that the performance of the Mn_2O_3/Mn_3O_4 needs to be clearly improved, in order to have any opportunities to be upscaled.

The most studied approach to improve the cyclability of metal oxides have been creating a mixed structure with other metals. The resulting structure generates lattice distortions which facilitate the oxygen diffusion in an out of the particles, improving the kinetics of the redox reactions. Following this approach, in a second part of this work, a comprehensive study searching for an adequate dopant for Mn_2O_3 was carried out, comprising using different quantities of Co, Ni, Cr and Fe. It was observed that apart from Fe, none of the other metals provide any significant improvement either on the kinetics of Mn_2O_3 or cyclability. The positive effect on the oxidation kinetics of iron addition was already studied by many authors, reporting great improvements on the material behavior. Nevertheless, the chemical deterioration caused by sintering was not avoided in none of the studied samples. In the case of iron, the oxidation kinetics improvement compensates the negative effects caused by sintering, which in the long-term will undoubtedly lead to a complete material deactivation. Consequently, **a new approach other than Co, Ni, Cr or Fe addition must be studied to obtain a Mn_2O_3-based thermochemical candidate for future CSP plants**.

In order to tackle the negative effects caused by sintering, a new approach consisting of doping Mn_2O_3 with Si was studied. The thermochemical behaviour and cycling stability over 10 redox cycles were compared to pure Mn_2O_3 and Fe-doped Mn_2O_3. The re-oxidation kinetics of a 15% Fe doped sample showed a considerably improvement in the redox behavior compared to Mn_2O_3, although it was observed that the sintering effects were not completely avoided. Nevertheless, **doping Mn_2O_3 with Si presented different positive effects**. The comparison between the thermogravimetric and SEM data of pure Mn_2O_3, $Mn_{1.7}Fe_{0.3}O_3$ and Mn_2O_3 doped with 1% Si, confirmed the positive effect of

Si doping, which unlike pure and Fe doped samples, led to a negligible grain growth after a 10 redox cycles test. Furthermore, the Si doped sample presented the fastest oxidation kinetics of the three tested samples, although the slight decay observed at the end of the oxidation reaction could indicate an incomplete doping of the material, revealing a need to improve the synthesis route.

Subsequently, further insights into the synthesis routes of the Si-doped Mn_2O_3 material and into the sintering inhibition process nature was carried out. We observed Si^{4+} dopant segregation at the grain boundaries, caused by exceeding Si solubility, which hinders the sintering rate, since it is controlled by ion diffusivity at the grain boundaries. Furthermore, Si^{4+} dopant becomes especially adequate because of its smaller size, compared to that of Mn^{3+}, which contributes to improve the re-oxidation kinetics, while the higher valence contributes to decrease the sintering effects. This synergistic effect provides a great improvement of the material behaviour. On the other hand, using the right amount of dopant is of paramount importance, in order to obtain the best material behaviour, since it was observed that exceeding 1% led to the formation of a secondary stable phase. Overall, **doping Mn_2O_3 with low Si content (x = 0.02) via sol-gel method is the most adequate way to obtain the material with the fastest oxidation reaction rate and most stable reversibility**, decreasing significantly the negative sintering effects.

In a subsequent activity further insights into the characterization and reaction kinetics modelling of $(Mn_{0.99}Si_{0.01})_2O_3$ material were studied. The main thermodynamic features did not differ substantially to those of Mn_2O_3, providing similar reaction onset temperatures and similar energy storage density (147.15 – 149.32 J/g). Subsequently, a kinetic model for the reduction and the oxidation reactions was developed, obtaining the three kinetic parameters, namely k(T), f(α) and h(P), essential for a thermochemical reactor design. The resulting modelling expressions showed a satisfactory kinetic parametrization of each process. The oxidation kinetics is highly affected by the equilibrium conditions and presents a temperature threshold while cooling with a substantial change on the activation energy. This fact can lead to inaccurate models if this is not taken into consideration and therefore, **the recent developed concept of 'isoconversional activation energy' has been applied, obtaining a very accurate model results in the whole range of temperatures and pressures studied in this work**. Overall, the developed methodology and model can provide the required tools for upscaling the technology to a thermochemical reactor.

Finally, since it is not practical to use the material in powder state in a real scale thermochemical reactor, the study and design of a methodology to prepare granules of $(Mn_{0.99}Si_{0.01})_2O_3$ material was assessed. The process succeeded in obtaining spherical porous granules of 1-2 mm with different active material contents. It was observed that the hardening step aimed to increase the mechanical stability of the granules does not affect significantly their chemical stability. This fact confirms that the severity of the hardening process could be further increased, leading to stable granules showing a higher mechanical stability, required for large scale reactors. Furthermore, we observed that decreasing the solubility of the polymeric binder in the synthesis bath almost doubles the active material content in the granules and consequently, enhances the volumetric energy storage capacity. We achieved an active material content of 24.81%, and it could be likely increased. In the final part of the work, **a laboratory setup was constructed and 8 g of Si-doped granules with the best thermochemical properties were subjected to 50 redox cycles in a lab-scale packed bed reactor of around 0,33 Wh**. The results showed satisfactory mechanical and chemical stability of the granules, which was confirmed over additional 50 redox cycles in a thermobalance, with **complete re-oxidation over the whole 100 cycles temperature program**.

In summary, we have demonstrated a novel successful approach to overcome one of the main drawbacks of the metal oxides for thermochemical energy storage. Both this new Si-doped material

and the study concerning the granule preparation route have demonstrated enough reliability to be used on a larger scale and thus, contribute to push the high temperature thermochemical storage technology for a next generation of concentrated solar power plants.

9.2 Further work

In the following paragraphs some of the ideas that can be tackled in the future to keep improving the findings observed in the present work are summarized.

- It was suggested that the main reason of the oxidation kinetics improvement observed was an enlargement and weaken of Mn-O bonds caused by the addition of Si of smaller radius. Nevertheless, a detailed characterization of the Si-doped Mn_2O_3 crystalline structure transition by adequate techniques at atomic scale was not carried out and it would help to understand the reasons behind the improvement found.

- An effective sintering inhibition caused by Si doping was observed, nevertheless it was found that the protection was not complete, since at the end of a cycling program part of the particles remained at their initial size, whereas others suffered from some degree of sintering. It would be helpful to improve, or study and design a proper synthesis route to provide almost all the particles with the sintering inhibition given by Si segregation.

- There is a clear temperature gap around equilibrium temperature where the material remains almost inactive (~150°C). It became difficult to determine the phenomenon taking place in this temperature range and may represent significant exergy losses. Furthermore, it was not possible to determine a mathematical model to represent the behaviour in this zone. In order to accurately represent the material behaviour during charge and discharge, which happens around equilibrium, and to improve the material energy efficiency, it would be helpful to further study the chemical processes happening within this temperature gap.

- The reaction kinetics mathematical model developed was obtained from the material behaviour in powder state. In order to provide useful data to thermochemical reactor engineering at relevant scale, this model must be adjusted to the behaviour corresponding to the material in granular shape, since it may differ at some extent.

- The crushing strength of the granules produced was enough to withstand the mechanical stresses that occur in the lab-scale packed bed reactor used in this work. Nevertheless, this property was not measured with adequate laboratory equipment and moreover, its relationship with the hardening step must be determined in order to provide the granules with sufficient crushing strength for a real scale packed bed reactor.

- The actual MO content in the granules is of paramount importance due to its direct relationship with the storage energy density. We found a way to promote the solvent exchange in the synthesis bath and increase the MO content up to 24.81% (x 1,7). We think that this amount might be further increased by studying carefully this process, achieving higher energy densities.

- In order to observe more accurately the charge and discharge process in a thermochemical reactor a higher amount of material must be prepared and tested, using a larger scale reactor than the one used in this work. It would be helpful to study the reaction onset temperatures and reaction kinetics, since it may differ from the ones obtained in the different laboratory instruments (TGA and STA).

BIBLIOGRAPHY

[1] D. Hahn, "How much energy does the sun produce? (and other fun facts)," 30 10 2020. [Online]. Available: https://www.solarreviews.com/blog/how-much-energy-does-the-sun-produce. [Accessed 11 2021].

[2] Ken Butti and John Perlin, A Golden Thread: 2500 Years of Solar Architecture and Technology, Chesire Books, 1980.

[3] Protermosolar, "Centrales Termosolares Situación a nivel mundial," [Online]. Available: https://www.protermosolar.com/la-energia-termosolar/situacion-internacional/. [Accessed 11 10 2021].

[4] H. Muller-Steinhagen and F. Trieb, "Concentrating solar power: A review of the technology," Institute of Technical Thermodynamics, German Aerospace Centre (DLR), Stutgart, 2004.

[5] M. Liu, N.H. Steven Tay, S. Bell, M. Belusko, R. Jacob, G. Will, W. Saman and F. Bruno, "Review o nconcentrating solar power plants and new developments in hightemperature thermal energy storage technologies," *Renewable and Sustainable Energy Reviews,* vol. 53, p. 1411–1432, 2016.

[6] J. Lilliestam and R. Pitz-Paal, "Concentrating solar power for less than USD 0.07 per kWh: finally the breakthrough?," *Renewable Energy Focus,* vol. 25, pp. 17-21, 2018.

[7] A. J. Schrader, A. P. Muroyama, P.G. Loutzenhiser, "Solar electricity via an Air Brayton cycle with an integrated two-step thermochemical cycle for heat storage based on Co3O4/CoO redox reactions: Thermodynamic analysis," *Solar Energy,* vol. 118, pp. 485-495, 2015.

[8] S. Polimeni, M. Binotti, L. Moretti, G. Manzolini, "Comparison of sodium and KCl-MgCl2 as heat transfer fluids in CSP solar tower with sCO2 power cycles," *Solar Energy,* vol. 162, pp. 510-524, 2018.

[9] B. Sakadjian, S. Hu, M. Maryamchik, T. Flynn, K. Santelmann and Z. Ma, "Fluidized-bed Technology Enabling the Integration of High Temperature Solar Receiver CSP Systems with Steam and Advanced Power Cycles," *Energy Procedia,* vol. 69, pp. 1404-1411, 2015.

[10] A. Palacios, A. Calderón, C. Barrenechea, J. Bertomeu, M. Segarra, A. Inés Fernández, "Study on solar absorptance and thermal stability of solid particles materials used as TES at high temperature on different aging stages for CSP applications," *Solar Energy Materials and Solar Cells,* vol. 201, p. 110088, 2019.

[11] M. Binotti, M. Astolfi, S. Campanari, G. Manzolini, P. Silva, "Preliminary Assessment of sCO2 Power Cycles for Application to CSP Solar Tower Plants," *Energy Procedia,* vol. 105, pp. 1116-1122, 2017.

[12] A H Abedin, M A Rosen, "A critical review of Thermochemical Energy Storage Systems," *The Open Renewable Energy Journal,* vol. 4, pp. 42-46, 2011.

[13] G. Alva, L. Liu, X. Huang, G. Fang, "Thermal energy storage materials and systems for solar energy applications," *Renewable and Sustainable Energy Reviews,* vol. 68, pp. 693-706, 2017.

[14] P. Krishnamurthy, S. Mishra, R. Banerjee, "An analysis of costs of parabolic trough technology in India," *Energy Policy,* vol. 48, p. 407–419, 2012.

[15] C. Kutscher, M. Mehos, C. Turchi, G. Glatzmaier, T. Moss, "Line-Focus Solar Power Plant Cost Reduction Plan (Milestone Report)," U.S. Department of Energy, https://doi.org/10.2172/1001434, 2010.

[16] M. Goldstein, "Some physical chemical aspects of heat storage," in *United nations conference on new sources of energy*, Rome, 1961.

[17] A. J. Carrillo, J. González-Aguilar, M. Romero, and J. M. Coronado, "Solar Energy on Demand: A Review on High Temperature Thermochemical Heat Storage Systems and Materials," *Chem. Rev.,* vol. 119, no. 7, p. 4777–4816, 2019.

[18] W. E. Wentworth and E. Chen, "Simple thermal decomposition reactions for storage of solar thermal energy," *Solar Energy,* vol. 18, pp. 205-2014, 1976.

[19] P Pardo, A Deydier, Z Anxionnaz-Minvielle, P Cognet, "Review on high temperature thermochemical heat energy storage," *Renewable and Sustainable Energy Reviews,* vol. 32, p. 591–610, 2014.

[20] B. Bogdanovic, A. Ritter, B. Splietthoff, "Active MgH2-Mg systems for reversible chemical energy storage," *Angewandte Chemie,* vol. 29, no. 3, pp. 223-34, 1990.

[21] D. Harries, M. Paskevicius, D. A. Sheppard, C. E. Buckley, "Concentrating Solar Thermal Heat Storage using metal hydrides," *Proceedings of the IEEE,* pp. 539-549, 2012.

[22] M. N. Azpiazu, J. M. Morquillas, A. Vazquez, "Heat recovery from a thermal energy storage based on the Ca(OH)2/CaO cycle," *Applied thermal engineering,* vol. 23, pp. 733-741, 2003.

[23] G. Ervin, "Solar Heat Storage using chemical reactions," *Journal of solid state chemistry,* vol. 22, pp. 51-61, 1977.

[24] J M Criado, M Macias, A Macias-Machin, "Analysis of the system CaO□CO2□H2O for storage of solar thermal energy," *Solar Energy,* vol. 49, no. 2, pp. 83-86, 1992.

[25] N. R. Rhodes, A. Barde, K. Randhir, L. Li, D. W. Hahn, R Mei, J. K. Klausner, N. AuYeung, "Solar Thermochemical Energy Storage Through Carbonation Cycles of SrCO3/SrO Supported on SrZrO3," *ChemSusChem,* vol. 8, no. 22, p. 3793–379, 2015.

[26] B. Wong, *Thermochemical heat storage for concentrated solar power - Phase II Final report for the period September 30, 2008 through April 30, 2011,* General Atomics, 2011.

[27] T Block, M Schmücker , "Metal oxides for thermochemical energy storage: A comparison of several metal oxide systems," *Solar Energy,* vol. 126, p. 195–207, 2016.

[28] P. O. Carden, "Energy corradiation usign the reversible ammonia reaction," *Solar Energy,* vol. 19, pp. 365-378, 1977.

[29] M. Levy, R. Levitan, H. Rosin and R. Rubin, "Solar energy storage via a closed-loop chemical heat pipe," *Solar Energy,* vol. 50, no. 2, pp. 179-189, 1993.

[30] B. Wong, "Thermochemical Heat Storage for Concentrated Solar Power. Final Report for the U.S. Department of Energy," in *http://www.osti.gov/scitech/*, Berlin, 2010.

[31] A J Carrillo, D P Serrano, P Pizarro, J M Coronado, "Thermochemical heat storage based on the Mn2O3/Mn3O4 redox couple: Influence of the initial particle size on the morphological evolution and cyclability," *Journal of Materials Chemistry ,* vol. 2, pp. 19435-19443, 2014.

[32] R. M. German, "Coarsening in Sintering: Grain Shape Distribution, Grain Size Distribution, and Grain Growth Kinetics in Solid-Pore Systems," *Critical Reviews in Solid State and Materials Sciences,* vol. 35, p. 263–305, 2010.

[33] A J Carrillo, D P Serrano, P Pizarro,J M Coronado, "Improving the Thermochemical Energy Storage Performance of the Mn2O3/Mn3O4 Redox Couple by the Incorporation of Iron," *ChemSusChem,* vol. 8, no. 11, p. 1947–1954, 2015.

[34] A J Carrillo, D P Serrano, P Pizarro, J M Coronado, "Understanding Redox Kinetics of Iron-Doped Manganese Oxides for High Temperature Thermochemical Energy Storage," *The journal of physical chemistry,* vol. 120, no. 49, pp. 27800-27812, 2016.

[35] L. André, S. Abanades, L. Cassayre, "High-temperature thermochemical energy storage based on redox reactions using Co-Fe and Mn-Fe mixed metal oxides," *Journal of Solid State Chemistry,* vol. 253, p. 6–14, 2017.

[36] M. Wokon, A. Kohzer, M. Linder, "Investigations on thermochemical energy storage based on technicalgrade manganese-iron oxide in a lab-scale packed bed reactor," *Solar Energy,* vol. 153, pp. 200-214, 2017.

[37] Francesca Varsano, Carlo Alvani, Aurelio La Barbera, Andrea Masi, Franco Padella, "Lithium manganese oxides as high-temperature thermal energy storage system," *Thermochimica Acta,* vol. 640, pp. 26-35, 2016.

[38] S. J. L. Kang, "Sintering: Densification, Grain Growth & Microstructure.," 2005.

[39] H. Beidaghy Dizajia and H. Hosseinib, "A review of material screening in pure and mixed-metal oxide thermochemical energy storage (TCES) systems for concentrated solar power (CSP) applications," *Renewable and Sustainable Energy Reviews,* vol. 98, p. 9–26, 2018.

[40] S. Wu, C. Zhou, E. Doroodchi, R. Nellore, B. Moghtaderi, "A review on high-temperature thermochemical energy storage based on metal oxides redox cycle," *Energy Conversion and Management,* vol. 168, p. 421–453, 2018.

[41] J. M. Hildebrand, "The thermal dissociation of barium peroxide," *The Journal of the American Chemical Society ,* vol. 34, no. 3, pp. 246-258, 1912.

[42] L. Till, "Thermochemical data of barium peroxide from thermogravimetric measurements," *Journal of Thermal Analysis ,* vol. 3, no. 2, pp. 177-180, 1971.

[43] M A Fahim, J D Ford, "Energy storage using the BaO2BaO reaction cycle," *The Chemical Engineering Journal,* vol. 27, no. 1, pp. 21-28, 1983.

[44] R G Bowrey, J Jutsen, "Energy storage using the reversible oxidation of barium oxide," *Solar Energy,* vol. 21, no. 6, p. 523–525, 1978.

[45] C Agrafiotis, M Roeb, C Sattler, "Exploitation of thermochemical cycles based on solid oxide redox systems for thermochemical storage of solar heat. Part 2: Redox oxide-coated porous ceramic structures as integrated thermochemical reactors/heat exchangers," *Solar Energy,* vol. 114, p. 440–458, 2015.

[46] C Agrafiotis, M Roeb, C Sattler, "Exploitation of thermochemical cycles based on solid oxide redox systems for thermochemical storage of solar heat. Part 4: Screening of oxides for use in cascaded thermochemical storage concepts," *Solar Energy,* vol. 139, p. 695–710, 2016.

[47] C Jin, T Hirose, M Koto, "Effect of barium content and sample size of BaO2-MgO oxygen acceptor on reaction rate," *Industrial and Engineering Chemistry Research ,* vol. 44, no. 9, pp. 2942-2947, 2005.

[48] X Chen, T Jung, J Park, W S Kim, "Preparation of Tunable (BaSrMg)O for Oxygen Chemisorption: Formation Mechanism and Characterization," *INORGANIC CHEMISTRY ,* vol. 54, no. 11, pp. 5419-5425, 2015.

[49] A J Carrillo, D Sastre, D P Serrano, P Pizarro, J M Coronado, "Revisiting the BaO2/BaO redox cycle for solar thermochemical energy storage," *Physical Chemistry Chemical physics,* vol. 18, pp. 8039-8048, 2016.

[50] G Karagiannakisa, C Pagkouraa, A Zygogianni, S Lorentzou, A G Konstandopoulos, "Monolithic Ceramic Redox Materials for Thermochemical Heat Storage Applications in CSP Plants," *Energy Procedia,* vol. 49, pp. 820-829, 2014.

[51] A J Carrillo, J Moya, A Bayon, P Jana, V A de la Peña, M Romero, J Gonzalez-Aguilar, D P Serrano, P Pizarro, J M Coronado, "Thermochemical energy storage at high temperature via redox cycles of Mn and Co oxides: Pure oxides versus mixed ones," *Solar Energy Materials & Solar Cells,* vol. 123, pp. 47-57, 2014.

[52] S. A. d. Miguel, "Analysis of redox reactions in a fluidized/fixed bed reactor for thermochemical energy storage in solar thermal power plants," Thesis. Universidad Politecnica de Madrid, 2017.

[53] W R Ott, D T Rankin , "Oxidation of Sintered Cobalt Oxide," *Journal of the American Ceramic Society ,* vol. 62, no. 3-4, pp. 203-205, 1979.

[54] H S Hsu, G J Yurek , "Kinetics and mechanisms of the oxidation of cobalt at 600-800°C," *Oxidation of Metals ,* vol. 17, no. 1-2, pp. 55-76, 1982.

[55] K N Hutchings, M Wilson, P A Larsen, R A Cutler, "Kinetic and thermodynamic considerations for oxygen absorption/desorption using cobalt oxide," *Solid State Ionics,* vol. 177, no. 1-2, pp. 45-51, 2006.

[56] C. Pagkoura, G.Karagiannakis, A. Zygogianni, S. Lorentzou, M. Kostoglou, A. G. Konstandopoulos, M. Rattenburry, J. W. Woodhead, "Cobalt oxide based structured bodies as redox thermochemicalheat storage medium for future CSP plants," *Solar Energy,* vol. 108, pp. 146-163, 2014.

[57] G. Karagiannakisa, C. Pagkoura, A. Zygogianni, S. Lorentzou and A. G. Konstandopoulos, "Monolithic ceramic redox materials for thermochemical heat storage applications in CSP plants," *Energy Procedia,* vol. 49, p. 820 – 829, 2014.

[58] C Pagkoura, G Karagiannakis, A Zygogianni, S Lorentzou, M Kostoglou, A G Konstandopoulos, M Rattenburry, J W Woodhead, "Cobalt oxide based structured bodies as redox thermochemical heat storage medium for future CSP plants," *Solar Energy,* vol. 108, p. 146–163, 2014.

[59] C Pagkoura, G Karagiannakis, A Zygogianni, S Lorentzou, A G Konstandopoulos, "Cobalt oxide based honeycombs as reactors/heat exchangers for redox thermochemical heat storage in future CSP plants," *Energy Procedia,* vol. 69, p. 978 – 987, 2015.

[60] M Neises, S Tescari, L de Oliveira, M Roeb, C Sattler, B Wong, "Solar-heated rotary kiln for thermochemical energy storage," *Solar Energy,* vol. 86, no. 10, p. 3040–3048, 2012.

[61] M. Neises, S. Tescari, L. de Oliveira, M. Roeb, C. Sattler, B. Wong, "Solar-heated rotary kiln for thermochemical energy storage," *Solar Energy,* vol. 86, p. 3040–3048, 2012.

[62] S Tescari, C Agrafiotis, S Breuer, L de Oliveira, M Neises-von Puttkamer, , "Thermochemical solar energy storage via redox oxides: materials and reactor/heat exchanger concepts," *Energy Procedia,* vol. 49, p. 1034 – 1043, 2014.

[63] C Agrafiotis, M Roeb, M Schmücker, C Sattler, "Exploitation of thermochemical cycles based on solid oxide redox systems for thermochemical storage of solar heat. Part 1: Testing of cobalt oxide-based powders," *Solar Energy,* vol. 102, pp. 189-211, 2014.

[64] C Agrafiotis, M Roeb, M Schmücker, C Sattler, "Exploitation of thermochemical cycles based on solid oxide redox systems for thermochemical storage of solar heat. Part 2: Redox oxide-coated porous ceramic structures as integrated thermochemical reactors/heat exchangers," *Solar energy,* vol. 114, pp. 440-458, 2015.

[65] C Agrafiotis, M Roeb, C Sattler, "Hybrid Sensible/Thermochemical Solar Energy Storage Concepts Based on Porous Ceramic Structures and Redox Pair Oxides Chemistry," *Energy Procedia,* vol. 69, pp. 706-715, 2015.

[66] C Agrafiotis, S Tescari, M Roeb, M Schmücker, C Sattler, "Exploitation of thermochemical cycles based on solid oxide redox systems for thermochemical storage of solar heat. Part 3: Cobalt oxide monolithic porous structures as integrated thermochemical reactors/heat exchangers," *Solar Energy,* vol. 114, p. 459–475, 2015.

[67] C Agrafiotis, A Becker, M Roeb, C Sattler, "Exploitation of thermochemical cycles based on solid oxide redox systems for thermochemical storage of solar heat. Part 5: Testing of porous ceramic honeycomb and foam cascades based on cobalt and manganese oxides for hybrid sensible/thermochemical heat," *Solar Energy,* vol. 139, p. 676–694, 2016.

[68] S. Tescari, A. Singh, C. Agrafiotis, L. de Oliveira, S. Breuer, B. Schlögl-Knothe, M. Roeb, C. Sattler, "Experimental evaluation of a pilot-scale thermochemical storage system for a concentrated solar power plant," *Applied Energy,* vol. 189, p. 66–75, 2017.

[69] E Alonso, C Perez-Rabago, J Licurgo, E Fuentealba, C A Estrada, "First experimental studies of solar redox reactions of copper oxides for thermochemical energy storage," *Solar Energy,* vol. 115, pp. 297-305, 2015.

[70] M. Gigantino, S. Sas Brunser, and A. Steinfeld, "High-Temperature Thermochemical Heat Storage via the CuO/Cu2O Redox Cycle: From Material Synthesis to Packed-Bed Reactor Engineering and Cyclic Operation," *Energy & Fuels,* vol. 34, no. 12, pp. 16772-16782, 2020.

[71] A J Carrillo, D P Serrano, P Pizarroa, J M Coronado, "Thermochemical heat storage at high temperatures using Mn2O3/Mn3O4 system: narrowing the redox hysteresis by metal codoping," *Energy Procedia,* vol. 73, p. 263 – 271, 2015.

[72] S Alvarez de Miguel, S Bellan, J M Garcia de Maria, J Gonzalez-Aguilar, M Romero, "Numerical Modelling of a 100-Wh Lab-Scale Thermochemical Heat Storage System for Concentrating Solar Power Plants," in *21st International Conference on Concentrating Solar Power and Chemical Energy Systems (SolarPACES)* , Cape Town, SOUTH AFRICA , 2016.

[73] T Block, N Knoblauch, M Schmücker, "The cobalt-oxide/iron-oxide binary system for use as high temperature thermochemical energy storage material," *Thermochimica Acta,* vol. 577, p. 25– 32, 2014.

[74] N. C. Preisner and M. Linder, "A Moving Bed Reactor for Thermochemical Energy Storage Based on Metal Oxides," *Energies,* vol. 13, no. 1232, p. doi:10.3390/en13051232, 2020.

[75] M. Hamidi, V. M. Wheeler, X. Gao, J. Pye, K. Catchpole, A. W. Weimer, "Reduction of iron–manganese oxide particles in a lab-scale packed-bed reactor for thermochemical energy storage," *Chemical Engineering Science,* vol. 221, p. 115700, 2020.

[76] N. C. Preisner, T. Block, M. Linder, H. Leion, "Stabilizing particles of manganese-iron oxide with additives for thermochemical energy storage," *Energy Technol.,* p. 10.1002/ente.201800211, 2020.

[77] P Hallberg, D Jing, M Rydén, T Mattisson, A Lyngfelt, "Chemical Looping Combustion and Chemical Looping with Oxygen Uncoupling Experiments in a Batch Reactor Using Spray-Dried CaMn1–xMxO3−δ (M = Ti, Fe, Mg) Particles as Oxygen Carriers," *Energy & Fuels,* vol. 27, no. 3, p. 1473–1481, 2013.

[78] P Hallberg, M Hanning, M Rydén, T Mattison, A Lyngfelt, "Investigation of a calcium manganite as oxygen carrier during 99 h of operation of chemical-looping combustion in a 10 kW(th) reactor unit," *INTERNATIONAL JOURNAL OF GREENHOUSE GAS CONTROL,* vol. 53, pp. 222-229, 2016.

[79] N Galinsky, A Mishra, J Zhang, F Li, "Ca1−xAxMnO3 (A = Sr and Ba) perovskite based oxygen carriers for chemical looping with oxygen uncoupling (CLOU)," *Applied Energy,* vol. 157, p. 358–367, 2015.

[80] T Masunaga, J Izumi, N Miura, "Relationship between oxygen sorption properties and crystal structure of Fe-based oxides with double perovskite composition," *Chemical Engineering Science,* vol. 84, p. 108–112, 2012.

[81] Q Shen, Y Zheng, C Luo, C Zheng , "Characteristics of SrCo1-xFexO3-δ Perovskite Powders with Improved O2/CO2 Production Performance for Oxyfuel Combustion," *Bulletin of the Korean Chemical Society,* vol. 35, no. 6, pp. 1613-1618 , 2014.

[82] J R Sheffe, D Weibel, A Steinfel, "Lanthanum–Strontium–Manganese Perovskites as Redox Materials for Solar Thermochemical Splitting of H2O and CO2," *Energy & Fuels,* vol. 27, no. 8, p. 4250–4257, 2016.

[83] S M Babiniec, E N Coker, J E Miller, A Ambrosini, "Investigation of LaxSr1-xCoyM1-yO3-d (M = Mn, Fe) perovskite materials as thermochemical energy storage media," *Solar Energy,* vol. 118, p. 451–459, 2015.

[84] S M Babiniec, E N Coker, A Ambrosini, J E Miller, "ABO(3) (A = La, Ba, Sr, K; B = Co, Mn, Fe) Perovskites for Thermochemical Energy Storage," in *21st International Conference on Concentrating Solar Power and Chemical Energy Systems (SolarPACES)*, Cape Town, SOUTH AFRICA , OCT 13-16, 2015 .

[85] S M Babiniec, E N Coker, J E Miller, A Ambrosini, "Doped calcium manganites for advanced high temperature thermochemical energy storage," *INTERNATIONAL JOURNAL OF ENERGY RESEARCH,* vol. 40, p. 280–284, 2016.

[86] Zi Zhang, L Andre, S Abanades, "Experimental assessment of oxygen exchange capacity and thermochemical redox cycle behavior of Ba and Sr series perovskites for solar energy storage," *Solar Energy,* vol. 134, p. 494–502, 2016.

[87] M. Schmidt and M. Linder, "Power generation based on the Ca(OH)2/ CaO thermochemical storage system – Experimental investigation of discharge operation modes in lab scale and corresponding conceptual process design," *Applied Energy,* vol. 203, p. 594–607, 2017.

[88] U. Pelay, L. Luo, Y. Fan, D. Stitou, C. Castelain, "Integration of a thermochemical energy storage system in a Rankine cycle driven by concentrating solar power: Energy and exergy analyses," *Energy,* vol. 167, pp. 498-510, 2019.

[89] S. Ströhle, A. Haselbacher, Z. R. Jovanovic, A. Steinfeld, "The Effect of the Gas-Solid Contacting Pattern in a High-Temperature Thermochemical Energy Storage on the Performance of a Concentrated Solar Power Plant," *Energy & Environmental Science,* vol. 9, no. 4, p. 1375–1389, 2016.

[90] X. Peng, M. Yao, T. W. Root, C. T. Maravelias, "Design and analysis of concentrating solar power plants with fixed-bed reactors for thermochemical energy storage," *Applied Energy,* vol. 262, p. 114543, 2020.

[91] R. Buck, C. Agrafiotis, S. Tescari, N. Neumann, M. Schmücker, "Techno-Economic Analysis of Candidate Oxide Materials for Thermochemical Storage in Concentrating Solar Power Systems," *Frontiers in Energy Research,* vol. 694248, p. 9, 2021.

[92] G. Zsembinszki, A. Solé, C. Barreneche, C. Prieto, A. Inés Fernández and Luisa F. Cabeza, "Review of Reactors with Potential Use in Thermochemical Energy Storage in Concentrated Solar Power Plants," *Energies,* vol. 11, p. 2358, 2018.

[93] E. Alonso and M. Romero, "Review of experimental investigation on directly irradiated particles solar reactors," *Renewable and Sustainable Energy Reviews,* vol. 41, pp. 53-67, 2015.

[94] G. Zsembinszki, A. Solé, C. Barreneche, C. Prieto, A. I. Fernández and L. F. Cabeza, "Review of Reactors with Potential Use in Thermochemical Energy Storage in Concentrated Solar Power Plants," *Energies,* vol. 2358, p. 11, 2018.

[95] F. Pestalozzi, Master Thesis: Experimental Investigation of Mn-Based Redox Reaction Kinetics for Thermochemical Energy Storage, ETH, March 2013.

[96] A. J. Carrillo, D. P. Serrano, P. Pizarro and J. M. Coronado, "Thermochemical heat storage based on the Mn2O3/Mn3O4 redox couple: influence of the initial particle size on the morphological evolution and cyclability," *J. Mater. Chem. A,,* vol. 2, p. 19435–19443, 2014.

[97] Pagkoura, C., Karagiannakis, G., Zygogianni, A., Lorentzou, S., Konstandopoulos, A.G., "Cobalt oxide based honeycombs as reactors/heat exchangers for redox Thermochemical Heat Storage in Future CSP Plants," *Energy Procedia,* vol. 69, pp. 978-987, 2015.

[98] Karagiannakis, G., Pagkoura, C., Halevas, E., Baltzopoulou, P., Konstandopoulos, A.G., "Cobalt/cobaltous oxide based honeycombs for thermochemical heat storage in future concentrated solar power installations: Multi-cyclic assessment and semi-quantitative heat effects estimations," *Solar Energy,* vol. 133, pp. 394-407, 2016.

[99] A. Singh, S. Tescari, G. Lantin, C. Agrafiotis, M. Roeb, C. Sattler, "Solar thermochemical heat storage via the Co3O4/CoO looping cycle: Storage reactor modelling and experimental validation," *Solar Energy,* vol. 144, p. 453–465, 2017.

[100] Agrafiotis, C., Roeb, M., Schmuecker, M., Sattler, C., "Exploitation of thermochemical cycles based on solid oxide redox systems for thermochemical storage of solar heat. Part 2: Redox oxide-coated porous ceramic structures as integrated thermochemical reactors/heat exchangers," *Solar Energy,* vol. 114, pp. 440-458, 2015.

[101] C. Agrafiotis, M. Roeb, C. Sattler, "Hybrid sensible/thermochemical solar energy storage concepts based on porous ceramic structures and redox pair oxides chemistry," *Energy Procedia,* vol. 69, p. 706 – 715, 2015.

[102] C. Agrafiotis, A. Becker, M. Roeb and C. Sattler, "Exploitation of thermochemical cycles based on solid oxide redox systems for thermochemical storage of solar heat. Part 5: Testing of porous ceramic honeycomb and foam cascades based on cobalt and manganese oxides for hybrid sensible/thermochemical heat s," *Solar Energy,* vol. 139, pp. 676-694, 2016.

[103] G. Azimi, T. Mattisson, H. Leion, M. Rydén, A. Lyngfelt, "Comprehensive study of Mn–Fe–Al oxygen-carriers forchemical-looping with oxygen uncoupling (CLOU)," *International Journal of Greenhouse Gas Control,* vol. 34, pp. 12-24, 2015.

[104] G. Azimi, H. Leion, T. Mattisson, M. Rydén, F. Snijkers, and A. Lyngfelt, "Mn–Fe Oxides with Support of MgAl2O4, CeO2, ZrO2 and Y2O3–ZrO2 for Chemical-Looping Combustion and Chemical-Looping with Oxygen Uncoupling," *Ind. Eng. Chem. Res.,* vol. 53, no. 25, p. 10358–10365, 2014.

[105] M. Abián, A. Abad Secades, M. T. Izquierdo Pantoja, P. Gayán Sanz, L. F. Diego Poza, F. García Labiano, J. Adánez Elorza, "Titanium substituted manganese-ferrite as an oxygen carrier with

permanent magnetic properties for chemical looping combustion of solid fuels," *Fuel,* vol. 195, pp. 38-48, 2017.

[106] I. A. Al-Shankiti, B. D. Ehrhart, B. J. Ward, A. Bayon, M. A. Wallace, R. Bader, P. Kreider, A. W. Weimer, "Particle design and oxidation kinetics of iron-manganese oxide redox materials for thermochemical energy storage," *Solar Energy,* vol. 183, p. 17–29, 2019.

[107] M. Wokon, T. Block, S. Nicolai, M. Linder, M. Schmücker, "Thermodynamic and kinetic investigation of a technical grade manganese-iron binary oxide for thermochemical energy storage," *Solar Energy 153,* p. 471–485, 2017.

[108] M. Hamidi, A. Bayon, V.M. Wheeler, P. Kreider, M. A. Wallace, T. Tsuzuki, K. Catchpole, A. W. Weimer, "Reduction kinetics for large spherical 2:1 iron–manganese oxide redox materials for thermochemical energy storage," *Chemical Engineering Science,* vol. 201, pp. 74-81, 2019.

[109] Tor Olav Løveng Sunde, Tor Grande and Mari-Ann Einarsrud, "Modified Pechini Synthesis of Oxide Powders and Thin Films," *Handbook of Sol-Gel Science and Technology,* pp. 1-30, 2016.

[110] P. Jana, V, A. de la Peña O'Shea, J. M. Coronado, D. P. Serrano, "Cobalt based catalysts prepared by Pechini method for CO2-free hydrogen production by methane decomposition," *International journal of hydrogen energy,* vol. 35, pp. 10285-10294, 2010.

[111] B. Wong, L. Brown, F. Schaube, R. Tamme, C. Sattler, "Oxide Based Thermochemical Heat Storage," in *Proceedings of 16th SOLAR PACES,* , Perpignan, France, 2010.

[112] T. Block and M. Schmücker, "Metal oxides for thermochemical energy storage: A comparison of several metal oxide systems," *Solar Energy,* vol. 126, p. 195–207, 2016.

[113] A. J. Carrillo, D. P. Serrano, P. Pizarro, and J. M. Coronado, "Understanding Redox Kinetics of Iron-doped Manganese Oxides for High Temperature Thermochemical Energy Storage," *The Journal of Physical Chemistry C,* vol. 120 (49), pp. 27800-27812, 2016b.

[114] YU. V. GOLIKOV, S. YA. TUBIN, V. P. BARKHATOV and V. F. BALAKIREV, "PHASE DIAGRAMS OF THE Co-Mn-O SYSTEM IN AIR," *J Phys Chem Solids,* vol. 46, no. 5, pp. 539-544, 1985.

[115] Yu. V. G~LIKOV and V. F. BALAKIREV, "PHASE EQUILIBRIUM DIAGRAM OF THE SYSTEM Ni-Mn-O," *J. Phys. Chem. Solids,* vol. 49, no. 4, pp. 329-332, 1988.

[116] YU. V. GOLIKOV AND V. F. BALAKIREV, "Phase Equilibrium Diagram of the System Mn-Cr-0," *JOURNAL OF SOLID STATE CHEMISTRY,* vol. 71, pp. 562-565, 1987.

[117] Jarrod V. Crum, Brian J. Riley, and John D. Vienna, "Binary Phase Diagram of the Manganese Oxide–Iron Oxide System," *J. Am. Ceram. Soc,* vol. 92, no. 10, p. 2378–2384, 2009.

[118] Bertolini J.C., Rousset J.L., Reactivity of Metal Nanoparticles, Berlin, Heidelberg : Springer, 2008.

[119] S. Esposito, "“Traditional” Sol-Gel Chemistry as a Powerful Tool for the Preparation of Supported Metal and Metal Oxide Catalysts," *Materials,* vol. 12, no. 668, 2019.

[120] A. Muan, "Phase equilibria in the system manganese oxide-SiO2 in air," *American Journal of Science,* vol. 252, pp. 297-315, 1959.

[121] M. Rydén, H. Leion, T. Mattisson, A. Lyngfelt, "Combined oxides as oxygen-carrier material for chemical-looping with oxygen uncoupling," *Applied Energy,* vol. 113, p. 1924–1932, 2014.

[122] R. D. Shannon, "Revised Effective Ionic Radii and Systematic Studies of Interatomie Distances in Halides and Chaleogenides," *Acta Cryst.,* vol. A32, pp. 751-767, 1976.

[123] R. Chaim, M. Levin, A. Shlayer and C. Estournes, "Sintering and densification of nanocrystalline ceramic oxide powders: a review," *Advances in Applied Ceramics,* vol. 107, no. 3, pp. 159-169, 2008.

[124] C. Agrafiotis, M. Roeb, C. Sattler, "Exploitation of thermochemical cycles based on solid oxide redox systems for thermochemical storage of solar heat. Part 4: Screening of oxides for use in cascaded thermochemical storage concepts," *Solar Energy,* vol. 139, p. 695–710, 2016.

[125] S. Fritsch, A.Navrotsky, "Thermodynamic properties of manganese oxides," *J. Am. Ceram. Soc.,* vol. 79, p. 1761–1768, 1996.

[126] A. Cheraghi, H. Yoozbashizadeh and J. Safarian, "Gaseous Reduction of Manganese Ores: A Review and Theoretical Insight," *Mineral Processing and Extractive Metallurgy Review,* vol. DOI: 10.1080/08827508.2019.1604523, 2019.

[127] P. L. Chen and I. W. Chen, "The role of defect interaction in boundary mobility and cation diffusivity of CeO2," *Journal of the american ceramic society,* vol. 7, no. 9, pp. 2289-2297, 1994.

[128] P.L. Chen, I.W. Chen, "Grain Growth in CeO2: Dopant Effects, Defect Mechanism, and Solute Drag," *Journal of the American Ceramic Society,* vol. 79, no. 7, pp. 1793-1800, 1996.

[129] L. Lallemant, N. Roussel, G. Fantozzi, V. Garnier, G. Bonnefont, T. Douillard, B. Durand, S. Guillemet-Fritsch, J.Y. Chane-Ching, D. Garcia-Gutierez, J. Aguilar-Garib, "Effect of amount of doping agent on sintering, microstructure and optical properties of Zr- and La-doped alumina sintered by SPS," *Journal of the European Ceramic Society,* vol. 34, no. 5, pp. 1279-1288, 2014.

[130] E. Bagherisereshki, J. Tran, F. Lei, N. AuYeung, "Investigation into SrO/SrCO3 for high temperature thermochemical energy storage," *Solar Energy,* vol. 160, pp. 85-93, 2018.

[131] C. Kim, D. Lee, J. A. Lee, J. H. Lee, Y. W. Heo, J. J. Kim, "Effect of ZnO and TiO2 doping on the sintering behavior of Y2O3 ceramics," *Ceramics International,* 2019.

[132] T. M. Francis, P. R. Lichty, A. W. Weimer, "Manganese oxide dissociation kinetics for the Mn2O3 thermochemical water-splitting cycle. Part 1: Experimental," *Chemical Engineering Science,* vol. 65, p. 3709–3717, 2010.

[133] J. A. Botas, J. Marugan, R. Molina, C. Herradon, "Kinetic modelling of the first step of Mn2O3/MnO thermochemical cycle for solar hydrogen production," *International journal of hydrogen energy,* vol. 37, pp. 18661-18671, 2012.

[134] E. Alonso, C. Hutter, M. Romero, A. Steinfeld, and J. Gonzalez-Aguilar, "Kinetics of Mn2O3−Mn3O4 and Mn3O4−MnO Redox Reactions Performed under Concentrated Thermal Radiative Flux," *Energy Fuels,* vol. 27, no. 8, pp. 4884-4890, 2013.

[135] I. A. Al-Shankiti, B. D. Ehrhart, B. J. Ward, A. Bayon, M. A. Wallace, R. Bader, P. Kreider, A. W. Weimer, "Particle design and oxidation kinetics of iron-manganese oxide redoxmaterials for thermochemical energy storage," *Solar Energy,* vol. 183, pp. 17-29, 2019.

[136] S. Vyazovkin, "Kinetic effects of pressure on decomposition of solids," *International Reviews in Physical Chemistry,* vol. 39, no. 1, pp. 35-66, 2020.

[137] D. Bielsa, A. Zaki, Pedro L. Arias, A. Faik, "Improving the redox performance of Mn2O3/Mn3O4 pair by Si doping to be used as thermochemical energy storage for concentrated solar power plants," *Solar Energy,* vol. 204, pp. 144-154, 2020.

[138] S. Fritsch and A. Navrotski, "Themodinamic properties of manganese oxides," *J. Am. Ceram. Soc.,* vol. 79, no. 7, pp. 1761-68, 1996.

[139] A. J. Carrillo, D. P. Serrano, P. Pizarro and J. M. Coronado, "Thermochemical heat storage based on the Mn2O3/Mn3O4 redox couple: influence of the initial particle size on the morphological evolution and cyclability," *J. Mater. Chem. A,,* vol. 2, p. 19435–19443, 2014b.

[140] V. Berbenni and A. Marini, "Oxidation behaviour of mechanically activated Mn3O4 by TGA/DSC/XRPD," *Materials Research Bulletin,* vol. 38, p. 1859–1866, 2003.

[141] A. J. Carrillo, J. Moya, A. Bayón, P. Jana, V. A.de la Peña O'Shea, M. Romero, J. Gonzalez-Aguilar, D. P.Serrano, P. Pizarro, J. M.Coronado, "Thermochemical energy storage at high temperature via redox cycles of Mn and Co oxides: Pure oxides versus mixed ones," *Solar Energy Materials & Solar Cells,* vol. 123, p. 47–57, 2014a.

[142] C. Agrafiotis, T. Block, M. Senholdt, S. Tescari, M. Roeb, C. Sattler, "Exploitation of thermochemical cycles based on solid oxide redox systems for thermochemical storage of solar heat. Part 6: Testing of Mn-based combined oxides and porous structures," *Solar Energy,* vol. 149, p. 227–244, 2017.

[143] Vyazovkin, S., Burnham, A.K., Criado, J.M., Pérez-Maqueda, L.A., Popescu, C., Sbirrazzuoli, N, "ICTAC Kinetics Committee recommendations for performing kinetic computations on thermal analysis data," *Thermochim. Acta ,* vol. 520, pp. 1-19, 2011.

[144] J. Marugan, J. A. Botas, M. Martın, R. Molina, C. Herradon, "Study of the first step of the Mn2O3/MnO thermochemical cycle for solar hydrogen production," *international journal of hydrogen energy,* vol. 37, pp. 7017-7025, 2012.

[145] H. Friedman, "Kinetics of thermal degradation of char-forming plastics from thermogravimetry. Application to a phenolic plastic," *Polym. Sci.,* vol. Part C 6, p. 183–195, 1964.

[146] J. Šesták and G. Berggren, "Study of the kinetics of the mechanism of solid-state reactions at increasing temperatures," *Thermochimica Acta,* vol. 3, no. 1, pp. 1-12, 1971.

[147] P. Simon, "Fourty years of the Sesták–Berggren equation," *Thermochimica Acta,* vol. 520, pp. 156-157, 2011.

[148] T. Mattisson, A. Lyngfelt, H. Leion, "Chemical-looping with oxygen uncoupling for combustion of solid fuels," *International journal of greenhouse gas control,* vol. 3, p. 11 – 19, 2009.

[149] C.W. Schoenfelder and J.H. Swisher, "Kinetics of Thermal Decomposition of TiH2," *J Vac Sci Technol,* vol. 10, p. 862–870, 1973.

[150] S. Vyazovkin, "Recent Advances, Techniques and Applications, Vol.5," in *The Handbook of Thermal Analysis & Calorimetry, 1st ed.*, Amsterdam, Elsevier, 2008.

[151] F. Shenouda and S. Aziz, "Equilibria and hysteresis in the system Mn2O3-Mn3O4-O2," *Journal of Applied Chemistry,* vol. 17, p. 258–262, 1967.

[152] T. Liavitskaya and S. Vyazovkin, "Delving into the Kinetics of Reversible Thermal Decomposition of Solids Measured on Heating and Cooling," *J. Phys. Chem. C,* vol. 121, no. 28, pp. 15392-15401, 2017.

[153] N. Sbirrazzuoli, "Determination of pre-exponential factors and of the mathematical functions f(ɑ) or G(ɑ) that describe the reaction mechanism in a model-free way," *Thermochimica Acta,* vol. 564, pp. 59-69, 2013.

[154] D. Bielsa, A. Zaki, P. L. Arias and A. Faik, "Development of a kinetic reaction model for reduction and oxidation of Si doped Mn2O3 for thermochemical energy storage in concentrated solar power plants," *Journal of Energy Storage,* 2020.

[155] F. S. Mederos, J. Ancheyta, J. Chen, "Review on criteria to ensure ideal behaviors in trickle-bed reactors," *Applied Catalysis A: General,* vol. 355, pp. 1-19, 2009.

[156] A. J. Carrillo, D. P. Serrano, P. Pizarro and J. M. Coronado, "Improving the Thermochemical Energy Storage Performance of the Mn2O3/Mn3O4 Redox Couple by the Incorporation of Iron," *ChemSusChem,* vol. 8, p. 1947 – 1954, 2015.

[157] D. Bielsa, A. Zaki, A. Faik, and P. L. Arias, "Efficiency improvement of Mn2O3/Mn3O4 redox reaction by means of different operation strategies," *AIP Conference Proceedings,* vol. 2126, p. 210001, 2016.

[158] A J Carrillo, D Sastre, D P Serrano, P Pizarro, J M Coronado, "Revisiting the BaO2/BaO redox cycle for solar thermochemical energy storage," *Physical Chemistry Chemical physics,* vol. 18, pp. 8039-8048, 2016a.

[159] Laurie André, Stéphane Abanades, Laurent Cassayre, "High-temperature thermochemical energy storage based on redox reactions using Co-Fe and Mn-Fe mixed metal oxides," *Journal of Solid State Chemistry,* vol. 253, p. 6–14, 2017.

[160] D. Jing, E. Y.S.I.M. Hermans, H. Leion, M. Rydén, T. Mattisson, J. Van Noyen, A. Lyngfelt, "Manganese-silica combined oxides as oxygen carrier for chemical-looping combustion," in *2nd International Conference on Chemical Looping*, Darmstadt, Germany, 26-28 September 2012.

[161] A. Shulman, E. Cleverstam, T. Mattisson, A. Lyngfelt, "Manganese/Iron, Manganese/Nickel, and Manganese/Silicon Oxides Used in Chemical-Looping With Oxygen Uncoupling (CLOU) for Combustion of Methane," *Energy Fuels ,* vol. 23, p. 5269–5275, 2009.

[162] R. A. Robie, J. S. Huebner, B. S. Hemingway, "Heat capacities and thermodynamic properties of braunite (Mn 7 SiO 12) and rhodonite (MnSiO 3)," *American Mineralogist,* vol. 80, pp. 560-575, 1995.

INDEX OF FIGURES

INDEX OF TABLES

INDEX OF EQUATIONS

PUBLICATIONS

This thesis has contributed to the following scientific publications:

- Daniel Bielsa, Abdelali Zaki, Abdessamad Faik, and Pedro L. Arias, "*Efficiency improvement of Mn_2O_3/Mn_3O_4 redox reaction by means of different operation strategies*", AIP Conference Proceedings 2126, 210001 (2019); https://doi.org/10.1063/1.5117750.

- Abdelali Zaki, Daniel Bielsa, and Abdessamad Faik, "*Development of a continuous solid solution with extended Red-Ox temperature range and unexpected high reaction enthalpies for thermochemical energy storage",* AIP Conference Proceedings 2126, 210010 (2019); https://doi.org/10.1063/1.5117759.

- Daniel Bielsa, Abdelali Zaki, Abdessamad Faik and Pedro L. Arias, "*Thermochemical Heat Storage for CSP Using Mn_2O_3/Mn_3O_4: Effects of Si Doping in Cyclability Improvement*", AIP Conference Proceedings 2303, 200001 (2020); https://doi.org/10.1063/5.0028737.

- Abdelali Zaki, Andrea Gutierrez, Matthias Schmidt, Daniel Bielsa, Marc Linder, Abdessamad Faik, "*Investigation of $Ca_{12}Al_{14}O_{33}$ Mayenite for hydration/dehydration thermochemical energy storage*", Journal of Energy Storage 31 (2020) 101647; https://doi.org/10.1016/j.est.2020.101647.

- Daniel Bielsa, Abdelali Zaki, Pedro L. Arias, Abdessamad Faik, "*Improving the redox performance of Mn_2O_3/Mn_3O_4 pair by Si doping to be used as thermochemical energy storage for concentrated solar power plants*", Solar Energy 204 (2020) 144–154; DOI: 10.1016/j.solener.2020.04.073.

- Abdelali Zaki, Javier Carrasco, Daniel Bielsa, and Abdessamad Faik, "*Tunable Redox Temperature of a $Co_{3-x}Mn_xO_4$ ($0 \leq x \leq 3$) Continuous Solid Solution for Thermochemical Energy Storage*", ACS Applied Materials & Interfaces, 12-6, (2020) 7010-7020; https://doi.org/10.1021/acsami.9b14369.

- Daniel Bielsa, Abdelali Zaki, Pedro L. Arias, Abdessamad Faik, "*Development of a kinetic reaction model for reduction and oxidation of Si doped Mn_2O_3 for thermochemical energy storage in concentrated solar power plants*", Journal of Energy Storage 43 (2021) 103271; https://doi.org/10.1016/j.est.2021.103271.

- Daniel Bielsa, Mikel Oregui and Pedro L. Arias, "*New insights into Mn_2O_3 based metal oxide granulation technique with enhanced chemical and mechanical stability for thermochemical energy storage in packed bed reactors*", Submitted *to Solar Energy* in November 2021, currently under peer review.